

UNIVERSITY OF CALGARY

Synthesis and Electron Transfer Studies of Anthraquinones

by

Anusha Dilhani Abhayawardhana

A THESIS

SUBMITTED TO THE FACULTY OF GRADUATE STUDIES
IN PARTIAL FULFILMENT OF THE REQUIREMENTS FOR THE
DEGREE OF MASTER OF SCIENCE

DEPARTMENT OF CHEMISTRY

CALGARY, ALBERTA

JANUARY, 2010

© ANUSHA DILHANI ABHAYAWARDHANA 2010



Library and Archives
Canada

Published Heritage
Branch

395 Wellington Street
Ottawa ON K1A 0N4
Canada

Bibliothèque et
Archives Canada

Direction du
Patrimoine de l'édition

395, rue Wellington
Ottawa ON K1A 0N4
Canada

Your file Votre référence
ISBN: 978-0-494-62048-9
Our file Notre référence
ISBN: 978-0-494-62048-9

NOTICE:

The author has granted a non-exclusive license allowing Library and Archives Canada to reproduce, publish, archive, preserve, conserve, communicate to the public by telecommunication or on the Internet, loan, distribute and sell theses worldwide, for commercial or non-commercial purposes, in microform, paper, electronic and/or any other formats.

The author retains copyright ownership and moral rights in this thesis. Neither the thesis nor substantial extracts from it may be printed or otherwise reproduced without the author's permission.

AVIS:

L'auteur a accordé une licence non exclusive permettant à la Bibliothèque et Archives Canada de reproduire, publier, archiver, sauvegarder, conserver, transmettre au public par télécommunication ou par l'Internet, prêter, distribuer et vendre des thèses partout dans le monde, à des fins commerciales ou autres, sur support microforme, papier, électronique et/ou autres formats.

L'auteur conserve la propriété du droit d'auteur et des droits moraux qui protègent cette thèse. Ni la thèse ni des extraits substantiels de celle-ci ne doivent être imprimés ou autrement reproduits sans son autorisation.

In compliance with the Canadian Privacy Act some supporting forms may have been removed from this thesis.

While these forms may be included in the document page count, their removal does not represent any loss of content from the thesis.

Conformément à la loi canadienne sur la protection de la vie privée, quelques formulaires secondaires ont été enlevés de cette thèse.

Bien que ces formulaires aient inclus dans la pagination, il n'y aura aucun contenu manquant.


Canada

UNIVERSITY OF CALGARY
FACULTY OF GRADUATE STUDIES

The undersigned certify that they have read, and recommend to the Faculty of Graduate Studies for acceptance, a thesis entitled " Synthesis and Electron Transfer Studies of Anthraquinones " submitted by Anusha Dilhani Abhayawardhana in partial fulfilment of the requirements of the degree of Master of Science.

*Supervisor, Dr. Todd C. Sutherland
Department of Chemistry*

*Dr. Thomas G. Back
Department of Chemistry*

*Dr. Viola I. Birss
Department of Chemistry*

*Dr. Douglas Storey
Department of Biological Sciences*

Date

Abstract

Electron transfer reactions of anthraquinone at a modified electrode interface and the role hydrogen bonds play in the electron transfer reaction were investigated. Two classes of redox active anthraquinones were synthesized, first to probe electronic communication through hydrogen bonds and second to form redox-active self-assembled monolayers (SAMs). The synthesized compounds were subjected to cyclic voltammetry (CV) and electrochemical impedance spectroscopy (EIS) experiments. Formation of the SAMs on Au electrodes was confirmed by a surface FTIR method. Electrochemical studies involving variable temperature and pH provided evidence that SAMs of anthraquinones undergo proton-coupled electron transfer with electron transfer rates of approximately 7 s^{-1} in acidic media. The formal potential of an anthraquinone SAM at different pH follows the Nernst equation with $60 \text{ mV}\cdot\text{pH}^{-1}$ gradient consistent with a 2 electron, 2 proton redox mechanism.

Acknowledgements

First and foremost, I would like to thank my supervisor, Dr. Todd C. Sutherland, for giving me the opportunity to work in these interesting and challenging projects and also for his patience, guidance, and support.

I thank my committee members Dr. T.G Back, Dr. V.I Birss and the external examiner Dr. D. Storey for evaluating my work.

Many thanks to my group members, Sandra and Raphy, for the good times spent inside and outside the lab.

I thank Dr. Raghav Yamdagni, Qiao Wu, Dorothy Fox, Jian Jun Li and Wade White for their immense technical support in characterizing compounds.

I greatly appreciate the support of the administrative staff, particularly Bonnie King for her excellent secretarial work, my fellow graduate students, Mark Toonen at the glass blowing shop, staff of the chemistry store and electronics group.

I owe my deepest gratitude to my family, especially to my husband and my sister who always encourage me to follow my passion in research.

This work was supported by the Canada Foundation for Innovation, the Natural Science and Engineering Research Council of Canada, and the Institute for Sustainable Energy, Environment, and Economy.

Table of Contents

Approval Page.....	ii
Abstract.....	iii
Acknowledgements.....	iv
Table of Contents.....	v
List of Tables.....	viii
List of Figures and Illustrations.....	ix
List of Abbreviations.....	xiv
CHAPTER ONE: INTRODUCTION.....	1
1.1 Electron Transfer.....	1
1.2 Methods for measuring ET.....	15
1.2.1 Cyclic Voltammetry.....	15
1.2.2 Electrochemical Impedance Spectroscopy.....	21
1.3 Self Assembled Monolayer Preparation and Characterization.....	36
1.4 Thesis Overview.....	39
CHAPTER TWO: EXPERIMENTAL.....	40
2.1 Synthesis.....	40
2.1.1 Synthesis of 1-Acetylenylanthraquinone (2).....	41
2.1.2 Synthesis of 2,6-di-N-acetylamino-4-bromo-pyridine (3).....	42
2.1.3 Synthesis of 2,6-diacetylamino-4-ethynylpyridine (3').....	42
2.1.4 Synthesis of Chelidonic Acid (4-oxo-4H-pyran-2,6-dicarboxylic acid) (4).....	43
2.1.5 Synthesis of Chelidamic Acid (1,4-dihydro-4-oxo-2,6-pyridinedicarboxylic acid) (5).....	44
2.1.6 Synthesis of Dimethyl-4-bromo-2,6-pyridinedicarboxylate (6a).....	45
2.1.7 Synthesis of Diethyl-4-bromo-2,6-pyridinedicarboxylate (6b).....	46
2.1.8 Synthesis of Dimethyl 4-iodopyridine-2,6-dicarboxylate (7a).....	47
2.1.9 Synthesis of 4-bromo-2,6-pyridinedicarboxylic acid (8a).....	48
2.1.10 Synthesis of 4-iodo-pyridine-2,6-dicarboxylic acid (8b).....	48
2.1.11 Synthesis of 2,6-di-tert-butoxycarbonylamino-4-bromo-pyridine (9a).....	49
2.1.12 Synthesis of 4-bromopyridine-2,6-dicarboxamide (10a).....	50
2.1.13 Synthesis of 4-iodopyridine-2,6-dicarboxamide (10b).....	51
2.1.14 Synthesis of 4-bromo-2,6-diaminopyridine (11).....	51
2.1.15 Synthesis of 2,6-dibromopyridine-1-oxide (12).....	52
2.1.16 Synthesis of 2,6-dibromo-4-nitropyridine-1-oxide (13).....	53
2.1.17 Synthesis of 2,4,6-tribromopyridine-1-oxide hydrobromide (14).....	54
2.1.18 Synthesis of 4-bromo-1-oxypyridine-2,6-diamine (15).....	55
2.1.19 Synthesis of 1-iodoanthraquinone (16).....	55
2.1.20 Synthesis of 1-(trimethylsilylacetylenyl)anthraquinone (17).....	56
2.1.21 Synthesis of 2,6-diacetylamino-4-[(trimethylsilyl)ethynyl]pyridine (18).....	57
2.1.22 Synthesis of 1-(10-iododecylamino)anthracene-9,10-dione (20).....	58
2.1.23 Synthesis of S-10-(9,10-dioxo-9,10-dihydroanthracen-1-ylamino)decyl ethanethioate (21).....	59

2.1.24 Synthesis of 1-(10-(2-(10-(9,10-dioxo-9,10-dihydroanthracen-1-ylamino)decyl)disulfanyl)decylamino)anthracene-9,10-dione (22)	60
2.1.25 Synthesis of 1-hydroxy-9,10-anthraquinone (23).....	61
2.1.26 Synthesis of Potassium salt of 1-hydroxyanthraquinone (24) and Synthesis of 1-(10-iodododecanoyl)-anthraquinone (25)	62
2.1.27 Synthesis of S-10-(9,10-dioxo-9,10-dihydroanthracen-1-yloxy)decyl ethanethioate (26).....	64
2.1.28 Synthesis of 1-(9-(2-(10-(9,10-dioxo-9,10-dihydroanthracen-1-yloxy)decyl)disulfanyl)nonyloxy)anthracene-9,10-dione (27).....	65
2.2 Electrochemistry	67
2.2.1 Buffer and Electrolyte solution preparation	67
2.2.2 Instrument and Method.....	68
2.2.3 Preparation of electrodes and Self Assembled Monolayer (SAM) Deposition on Au Electrodes	70
2.3 Spectroelectrochemistry.....	73
2.4 Infrared Measurements- Photoelastic modulation Infrared Reflection Absorption Spectroscopy (PEMIRRAS) and Fourier Transform Infrared Spectroscopy (FT-IR)	73
2.5 Theoretical Calculation.....	74
CHAPTER THREE: RESULTS AND DISCUSSION.....	75
3.1 Electron transfer studies in Solution.....	75
3.1.1 Material Synthesis	75
3.1.2 Solution electrochemical studies	93
3.2 Electron transfer studies at a Au surface	101
3.2.1 Material Synthesis	101
3.2.2 Monolayer preparation and SAM Characterization.....	106
3.2.3 Surface Electrochemical Studies	109
3.2.3.1 Electron Transfer studies of SAM of 1-aminoAQ disulfide (22)	109
3.2.3.2 Electron Transfer studies of 1-hydroxyAQ disulfide (27).....	131
3.2.4 DFT Calculations.....	171
3.2.5 Spectroelectrochemistry	176
CHAPTER FOUR: CONCLUSION.....	179
CHAPTER FIVE: FUTURE WORK.....	181
CHAPTER SIX: REFERENCES.....	185
CHAPTER SEVEN: APPENDIX	190
7.1 ¹ H and ¹³ C NMR Spectra of Compounds.....	190
7.2 CV data of SAM of 1-hydroxyAQ disulfide (27).....	219
7.3 Plots of peak current as a function of scan rate – For SAM of 1-hydroxyAQ disulfide (27).....	232
7.4 Plots of [Difference in Peak Potentials (ΔE_p) – Equilibrium Potential (E^0)] as a function of scan rate (ν) – For SAM of 1-hydroxyAQ disulfide (27)	236
7.5 Eyring plots for SAM of 1-hydroxyAQ disulfide (27) from EIS data.....	239

7.6 DFT coordinate files for compound EtNHAQ, EtNH ₂ ⁺ AQ, EtOAQ	242
7.7 Potential scan EIS (Brevnov Protocol) data of SAM of 1-aminoAQ disulfide (22).....	250

List of Tables

Table 1	Composition of Buffer Solution for various pH.	68
Table 2	Optimization of yield of 2,6-Di-acetylamino-4-bromo-pyridine (3) from pyridine 11.....	82
Table 3	Attempted synthesis of 1 using 1-Acetylenylantraquinone (2) and 2,6-di-N-acetylamino-4-bromo-pyridine (3).....	88
Table 4	Yield optimization of 2,6-diacetylamino-4-ethynylpyridine (3').....	91
Table 5	Summary of electrochemical parameters for compounds 1-Acetylenylantraquinone (2).....	93
Table 6	Hydrolysis of S-10-(9,10-dioxo-9,10-dihydroanthracen-1-ylamino)decyl ethanethioate (21) at various conditions.....	104
Table 7	Fitting analysis results of SAMs of 1-aminoAQ disulfide (22).....	117
Table 8	ET rate constant (k_{app}) for 1-aminoAQ disulfide (22)	120
Table 9	Extracted thermodynamic parameters from CV for 1-hydroxyAQ disulfide (27) at $50\text{mV}\cdot\text{s}^{-1}$ at $25\pm 0.5\text{C}$ as a function of pH.....	134
Table 10	Extracted thermodynamic parameters from CV for 1-hydroxyAQ disulfide (27) at $50\text{mV}\cdot\text{s}^{-1}$ at $15\pm 0.8\text{C}$ as a function of pH.....	135
Table 11	Extracted thermodynamic parameters from CV for 1-hydroxyAQ disulfide (27) at $50\text{mV}\cdot\text{s}^{-1}$ at $5\pm 1\text{C}$ as functions of pH.....	137
Table 12	Extracted thermodynamic parameters from CV for 1-hydroxyAQ disulfide (27) at $50\text{mV}\cdot\text{s}^{-1}$ at $35\pm 0.5\text{C}$ as functions of pH.....	137
Table 13	Fitting analysis results of SAMs of 1-hydroxyAQ disulfide (27)	158
Table 14	k_{app} obtained by CV and EIS as function of temperature and pH.....	164
Table 15	Thermodynamic parameters extracted from Eyring plots.	167

List of Figures and Illustrations

Figure 1-1 Comparison of ET through various bond types	3
Figure 1-2 Structures of self and hetero dimerized Donor-HB-Acceptor assembly of Anthraquinone diamidopyridine derivative (1).....	5
Figure 1-3 Self Assembled Monolayers of compound 22 (1-aminoAQ disulfide) and 27 (1-hydroxyAQ disulfide).....	8
Figure 1-4 Typical Quinone reduction/Oxidation a) aprotic solvent b) aqueous medium.....	9
Figure 1-5 Nine member square scheme for stepwise quinone reduction / oxidation.....	10
Figure 1-6 A typical excitation triangular waveform	16
Figure 1-7 A typical cyclic voltammetry response for a quasi reversible redox reaction	17
Figure 1-8 Anodic (v_a) and cathodic (v_c) critical scan rates.....	21
Figure 1-9 Phasor diagram for an alternating voltage	23
Figure 1-10 Phasor diagram for an alternating current and voltage with phase angle ϕ at frequency ω	24
Figure 1-11 Rectangular coordinates diagram of Impedance (Z).....	27
Figure 1-12 Small AC perturbation super-imposed on a DC voltage.....	28
Figure 1-13 (a) Bode plots for a parallel RC circuit (b) Nyquist plot for a parallel RC circuit.....	30
Figure 1-14 Equivalent circuit diagrams for a) general electrochemical cell; b) diffusion control cell; c) SAM cell.....	32
Figure 1-15 a) Nyquist plot, b) Bode plot, and c) Equivalent circuit for diffusion controlled cell.....	33
Figure 1-16 s and p components of polarized light.....	37
Figure 3-1 Retrosynthetic scheme for target compound 1 (anthraquinone diamidopyridine derivative)	75
Figure 3-2 Synthesis scheme of 4-halo-2,6-pyridinediester (6).....	76
Figure 3-3 Synthesis of 4-halopyridine-2,6-diester (7).....	77

Figure 3-4 Synthesis of 2,6-di-tert-butoxycarbonylamino-4-halo-pyridine (9).....	78
Figure 3-5 Attempted synthesis of 4-bromo-2,6-diaminopyridine (11) via Hoffmann rearrangement.....	79
Figure 3-6 Mechanism for Hoffmann rearrangement.....	80
Figure 3-7 Synthesis of 4-bromo-2,6-diaminopyridine (11).....	81
Figure 3-8 Synthesis of 2,6-Di-acetylamino-4-bromo-pyridine (3)	82
Figure 3-9 Synthesis of 1-Acetylenylantraquinone (2).....	83
Figure 3-10 Catalytic cycle for Sonogashira reaction.....	86
Figure 3-11 Attempted Sonogashira coupling of 1-Acetylenylantraquinone (2) and 2,6-Di-acetylamino-4-bromo-pyridine (3)	87
Figure 3-12 Revised retrosynthetic approach of Anthraquinone diamidopyridine derivative (1)	90
Figure 3-13 Synthesis of compound 2,6-diacetylamino-4-ethynylpyridine (3'), 1-Iodoanthracene (2') and unfinished work.....	92
Figure 3-14 Cyclic voltammogram of 1-Acetylenylantraquinone (2).	94
Figure 3-15 Bode and Nyquist plots of 1-Acetylenylantraquinone (2)	97
Figure 3-16 A plot of variation of anodic and cathodic peak current for 1-Acetylenylantraquinone (2) vs. square root of scan rates ($v^{1/2}$).....	98
Figure 3-17 Structures of anthraquinone derivatives 1-aminoAQ disulfide / 1-aminoAQ thiol (22/22') and 1-hydroxyAQ disulfide /1-hydroxyAQ thiol 27/27' for Self- assembled monolayer.	101
Figure 3-18 Synthesis scheme of compound 1-aminoAQ disulfide (22) and 1-aminoAQ thiol (22').....	103
Figure 3-19 Synthesis scheme of 1-hydroxyAQ disulfide /1-hydroxyAQ thiol (27/27').....	105
Figure 3-20 PEM-IRRAS spectrum of SAM of 1-aminoAQ disulfide (22).....	108
Figure 3-21 PEM-IRRAS spectrum of SAM of 1-hydroxyAQ disulfide (27)	108
Figure 3-22 Example cyclic voltammograms of 1-aminoAQ disulfide (22)	111
Figure 3-23 Slow scan rate CV of 1-aminoAQ disulfide (22) in 0.1M H ₂ SO ₄ at 24.8°C.	112

Figure 3-24 Background-subtracted peak current at various scan rates and temperatures	112
Figure 3-25 Charge transfer analysis of a SAM of 1-aminoAQ disulfide (22) using Laviron formalism.....	113
Figure 3-26 Nyquist plot for 1-aminoAQ disulfide (22) at different temperatures	115
Figure 3-27 EIS Bode plots for SAMs of 1-aminoAQ disulfide (22).....	116
Figure 3-28 Three equivalent circuits used to fit impedance data of 1-aminoAQ disulfide (22).	117
Figure 3-29 Admittance for SAM of 1-aminoAQ disulfide (22) at 3.2 Hz and 24.8 °C.....	121
Figure 3-30 Equivalent circuits of a) common electrolytic cell with electroactive monolayer and b) simple RC circuit.....	122
Figure 3-31 Impedance spectra of SAMs of 1-aminoAQ disulfide (22) at various DC potentials.	123
Figure 3-32 Bode plots of SAMs of 1-aminoAQ disulfide (22) at various DC potentials.	124
Figure 3-33 Proposed reactions occurring on SAMs of 1-aminoAQ disulfide (22) on Au surface under 3 applied potential regions.	127
Figure 3-34 Cyclic voltammograms of SAMs of 1-aminoAQ disulfide (22) at different pHs.....	128
Figure 3-35 Eyring and Arrhenius plots of charge transfer reaction for 1-aminoAQ disulfide (22)..	129
Figure 3-36 ¹ H-NMR of 1-aminoAQ disulfide (22) in CDCl ₃ of the amine and aromatic regions at various concentrations	130
Figure 3-37 Example cyclic voltammograms of 1-hydroxyAQ disulfide (27).....	131
Figure 3-38 Cyclic voltammograms of 1-hydroxyAQ disulfide (27) at scan rate 50 mV·s ⁻¹ as a function of pH at 15±0.8°C	132
Figure 3-39 Formal potential of SAM of 1-hydroxyAQ disulfide (27) vs. Ag AgCl NaCl _{3M} as a function of pH at 25°±0.5C.....	135
Figure 3-40 Background-subtracted peak current at various scan rates and temperatures in pH 1.66 buffer solution for SAM of 1-hydroxyAQ disulfide (27)	140

Figure 3-41 EIS Bode plots for SAMs of 1-hydroxyAQ disulfide (27) in pH 1.66 buffer solution	148
Figure 3-42 EIS Bode plots for SAMs of 1-hydroxyAQ disulfide (27) in pH 3.34 buffer solution.	149
Figure 3-43 EIS Bode plots for SAMs of 1-hydroxyAQ disulfide (27) in pH 5.50 buffer solution.	150
Figure 3-44 EIS Bode plots for SAMs of 1-hydroxyAQ disulfide (27) in pH 7.51 buffer solution.	151
Figure 3-45 EIS Bode plots for SAMs of 1-hydroxyAQ disulfide (27) in pH 9.52 buffer solution.	152
Figure 3-46 EIS Bode plots for SAMs of 1-hydroxyAQ disulfide (27) in pH 11.61 buffer solution.	153
Figure 3-47 EIS Bode plots for SAMs of 1-hydroxyAQ disulfide (27) in pH 13.18 buffer solution	154
Figure 3-48 Two equivalent circuits used to fit impedance data of SAM of 1-hydroxyAQ disulfide (27).....	155
Figure 3-49 Nyquist plot for 1-hydroxyAQ disulfide (27) at different temperatures. A) pH 1.66, B) pH 3.34, C) pH 5.50, and D) pH 7.51	156
Figure 3-50 Nyquist plot for 1-hydroxyAQ disulfide (27) at different temperatures. E) pH 9.52, F) pH 11.61.....	157
Figure 3-51 ET rate analysis of a SAM of 1-hydroxyAQ disulfide (27) using Laviron's formalism	160
Figure 3-52 ET rate constant obtained by CV at various temperature and pH for SAM of 1-hydroxyAQ disulfide (27).....	161
Figure 3-53 ET rate constants obtained by EIS as function of temperature and pH for SAM of 1-hydroxyAQ disulfide (27).....	162
Figure 3-54 α vs. pH at various temperatures SAM of 1-hydroxyAQ disulfide (27) ...	163
Figure 3-55 Eyring plots of SAM of 1-hydroxyAQ disulfide (27) at selected pH and temperatures	166
Figure 3-56 Laviron's proposed 9-member square scheme.....	169
Figure 3-57 Laviron's proposed 6-member square scheme.....	170

Figure 3-58 Optimized ground-state geometries of N-Ethyl-aminoAQ in its oxidized, reduced and amine protonated forms calculated with Gaussian 03 using DFT methods [B3LYP/6-31G+(d,p)].....	174
Figure 3-59 Optimized ground-state geometries of EtOAQ in its oxidized, and reduced forms calculated with Gaussian 03 using DFT methods [B3LYP/6-31G+(d,p)].....	175
Figure 3-60 UV-VIS-NIR spectra obtained during in-situ reduction of 1-hydroxyAQ disulfide (27)	178
Figure 3-61 Absorption difference spectra obtained from UV-VIS-NIR spectra of 1-hydroxyAQ disulfide (27) during in-situ reduction	178
Figure 5-1 Anthraquinone diamidopyridine derivative (Compound 1) binds with self assembled flavin derivative through hydrogen bonds.	183
Figure 5-2 SAM mixed with diluents	184

List of Abbreviations

Symbol	Definition
AC	Alternative Current
AQ	Anthraquinone
Boc	t-Butoxycarbonyl
CDCl ₃	Deuterated chloroform
CHCl ₃	Chloroform
CI	Chemical ionization
CV	Cyclic Voltammetry
DAP	Diamidopyridine
DC	Direct Current
DCM	Dichloromethane
DFT	Density Functional Theory
DMF	<i>N,N'</i> -Dimethylformamide
DMSO	Dimethylsulfoxide
EI	Electron Impact
EIS	Electrochemical Impedance Spectroscopy
ESI	Electron Spray Ionization
ET	Electron Transfer
Et ₂ O	Diethyl ether
Et ₃ N	Triethyl amine
EtOAc	Ethylacetate
EtOH	Ethanol
FWHM	Full-Width-at-Half-Maximum
HB	Hydrogen Bond
MeOH	Methanol
MS	Mass Spectroscopy
NMR	Nuclear Magnetic Spectroscopy
Oxd	Oxidized species
PCET	Proton Coupled Electron Transfer
PEMIRRAS	Photo Elastic Modulated Infra Red Reflection Absorption Spectroscopy
Red	Reduced species
SAM	Self Assembled Monolayer
TFA	Trifluoroacetic acid
THF	Tetrahydrofuran
TLC	Thin Layer Chromatography
UV-VIS-NIR	Ultra Violet visible Near Infra Red Spectroscopy

Chapter One: Introduction

1.1 Electron Transfer

Electron transfer is one of the elementary steps in chemical processes, but undoubtedly a crucial process, and plays a pivotal role in many biological processes, such as photosynthesis and respiration. In biology, electrons are transferred at various sites such as at cell membranes and in cell matrices. In these sites, nature uses different modes to transfer electrons from one place to another, efficiently and controllably. For example, in the mitochondrial respiratory chain, membrane bound ubiquinone transfers electrons and protons from NADH to oxidoreductase. Another step involves non-covalent interactions such as hydrogen bonding, π stacking etc., between ubiquinone and redox reaction receptor sites to regulate the electron transfer in the same respiratory chain.^{1,2} Understanding the fundamental features that underlie these electron transfer processes is greatly advantageous not only to develop the technologies but also to develop comprehensive theories.

As pointed out by Marcus³, the wide spectrum of electron transfer (ET) aspects have been studied since 1940. Of those aspects, ET mediated by hydrogen bonds (HBs) between two redox molecules (represented by Donor-HB-Acceptor), and ET at membrane bound redox molecules or surface ET has attracted attention because they play a vital role in natural energy producing systems.³

It is relatively well established that ET between two redox centres mediated through HBs is faster than that mediated by saturated bonds.³⁻⁶ The pioneering comparative study was

undertaken by de Rege *et al.*⁵, in which they compared three Zn(II)-porphyrin-bridge-Fe(III)porphyrin dyads (**Figure 1-1**). As shown in **Figure 1-1**, dyad 1 (HB bridge) and dyad 2 (π bond bridge) have almost similar photo induced ET rate constant values whereas dyad 3 (σ bond bridge), the ET rate constant is half the value of other two. Not only de Rege *et al.* but also Hao *et al.*⁴ recently claimed, that they observed better electronic communication between two ferrocenes, assessed by cyclic voltammetry when they were H-bonded together. These results are surprising since it is established that the electronic communication through a HB is weaker than that through a saturated C-C bond.⁷ Faster ET through HBs could be a result of strongly organized multiple HB arrays assembled between redox centres; binding energies of those assemblies ranges from 4 to 120 kJ·mol⁻¹.⁸ Moreover, the specificity and the high degree of the directionality of the HB network assists efficient ET. Another explanation is, as in the case of the proton coupled electron transfer mechanism, that the motion of the proton in the HB may accompany the ET.⁷

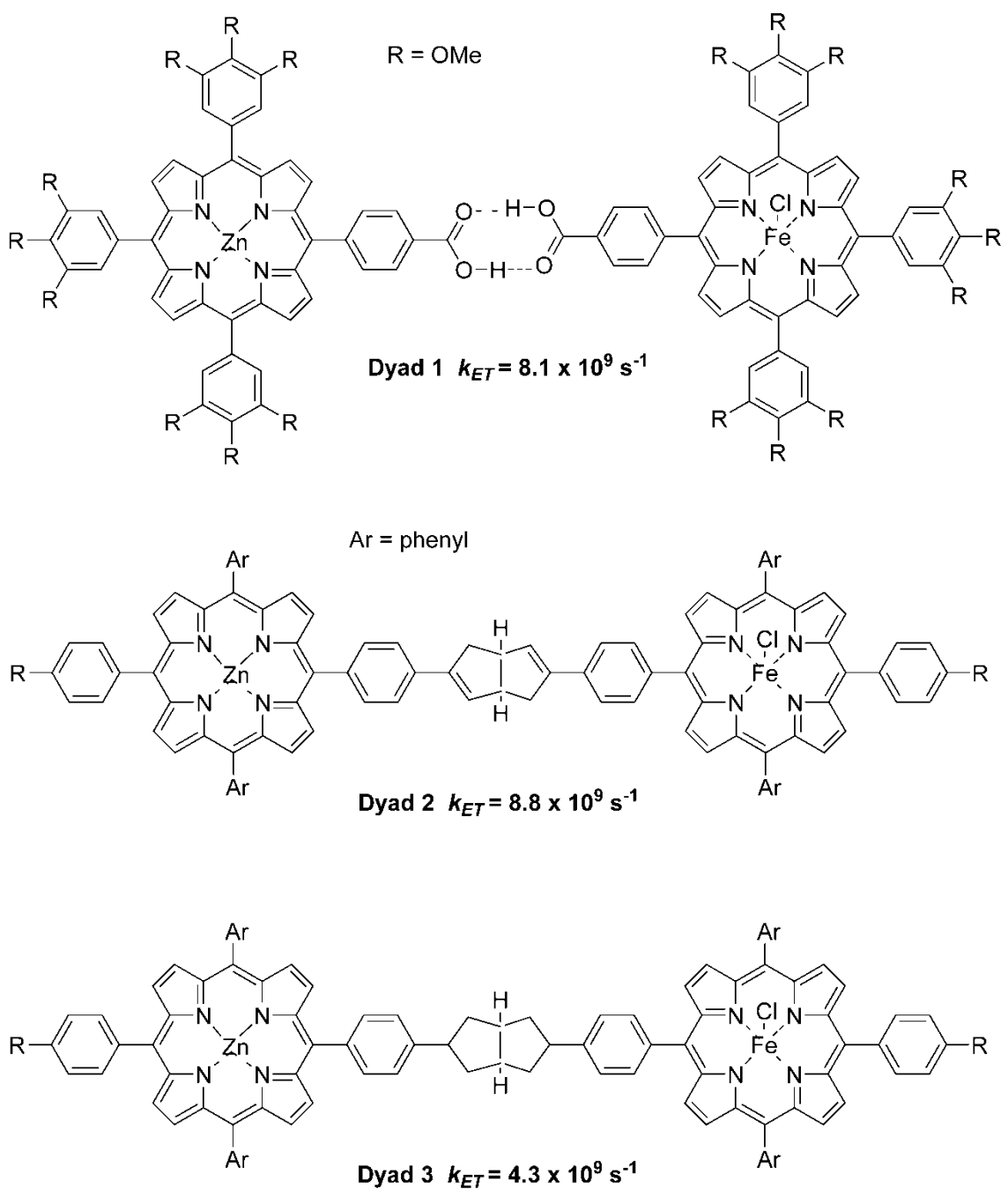


Figure 1-1 Comparison of ET through various bond types

Still, ET through HBs is a relatively new area of research, and new systems with Donor-HB-Acceptor assemblies continue to emerge and provide insight into the participation of

HBs in ET. A new anthraquinone- diamidopyridine **1** (AQ-DAP) with HB motifs (**Figure 1-2**) was designed and synthesized to join the frontiers of the Donor-HB-Acceptor assemblies and explore the solution phase self-assembling and ET through HBing. Compound **1** has a three point HBing motif (Donor-Acceptor-Donor or D-A-D; **Figure 1-2**), and using two HB points **1** can form a self dimer. A complementary three point HB compound such as flavin could form a dimer with compound **1** using all three of its HB sites. It is necessary to study the dynamics of the association of the dimers or assemblies in order to understand ET mediated by HBs. Therefore, first the association constant has to be established by spectroscopic techniques such as ^1H NMR, then ET can be studied using electrochemical methods, such as cyclic voltammetry.

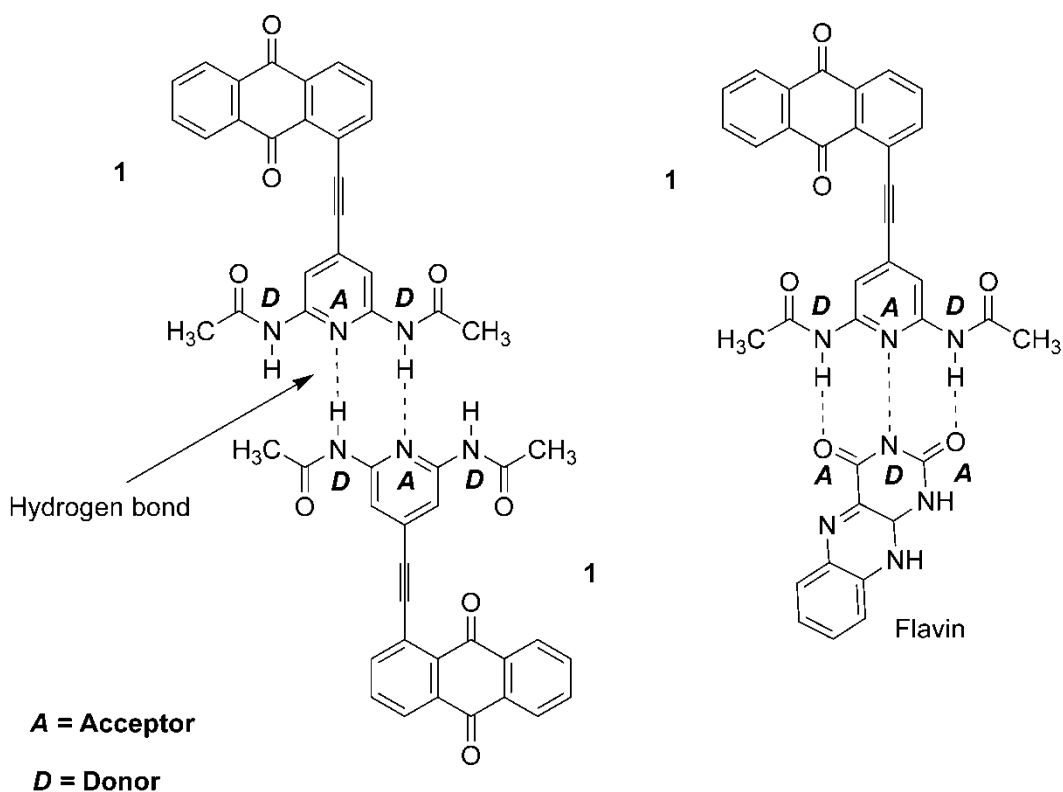


Figure 1-2 Structures of self and hetero dimerized Donor-HB-Acceptor assembly of **1**.

Natural energy producing systems, for instance respiration and photosynthesis, extensively use membrane bound redox molecules for ET processes between the aqueous|biomembrane interface. The redox centres at the interface experience different microenvironments compared to the non- membrane bound redox centres. The dynamics of the ET process is controlled by additional parameters such as the restricted motion of the redox probe, solvation of the redox probe at the hydrophilic and hydrophobic interface, local neutralization by counter ions, etc. For example, a benzoquinone at physiological pH has a formal potential ($E^0 / E_{1/2}$) of -0.122 V vs. Ag|AgCl|KCl in an unbuffered solution,⁹ whereas the same benzoquinone redox group that has formed a

self-assembled monolayer (SAM) using Au-thiol chemistry has a formal potential (E^0) of +0.04 V vs. Ag|AgCl|KCl.¹⁰ The difference in free energies between solution redox and surface bound redox ($\Delta\Delta G$) is 31 kJ·mol⁻¹, which demonstrates that the interface can influence the redox thermodynamics. This simplified comparison between solution and surface-bound benzoquinone redox chemistry does not take into account the alkyl thiol spacer group, (CH₂)₈, which may exert a large solvation difference and a small electronic effect on the benzoquinone. Understanding ET at this particular environment is of interest for the development of technologies such as molecular electronics and bioelectronics and for the fundamental study of redox reactions.

A well-characterized electro active monolayer (monolayer bearing redox centre) on gold surfaces mimics the properties of the redox centres bound to organized hydrocarbon chains of the biomembrane. The electron-supplying source for the reduction or oxidation of the redox pendant is the applied potential to the gold surface. Such a system is proven to be ideal for studying membrane bound ET process.¹¹

Many experiments relevant to the research area are reported, but there remain unexplored areas, such as detailed kinetics of the ET in surface bound redox centres. Therefore, 1-aminoanthraquinone derivative (1-aminoAQ disulfide or Compounds **22**) and 1-hydroxyanthraquinone derivative (1-hydroxyAQ disulfide or Compounds **27**) were designed, synthesized, and then self assembled monolayers (SAM) were formed on gold surfaces to study the surface ET process (**Figure 1-3**). Details of the SAM, such as definition and formation, are given in the section **1.3**.

Quinone was chosen as the redox probe in this series of ET studies because of its extensive occurrence in nature and variety of roles it plays, particularly participating in

the energy production systems in living organisms. Ubiquinone, vitamin K, plastoquinone, and tocopherylquinone are the main four groups of naturally occurring quinones, and the majority of them are membrane bound. They all participate in ET processes coupled with energy production as well.¹² In addition, quinones have a broad array of other uses such as dyes, oxidizing and reducing agents, and medicines.⁹ Most importantly, it has been used as a prototypical organic redox couple for electrochemical studies, which means the electrochemistry of quinones is well studied and debated alike in the literature.¹³

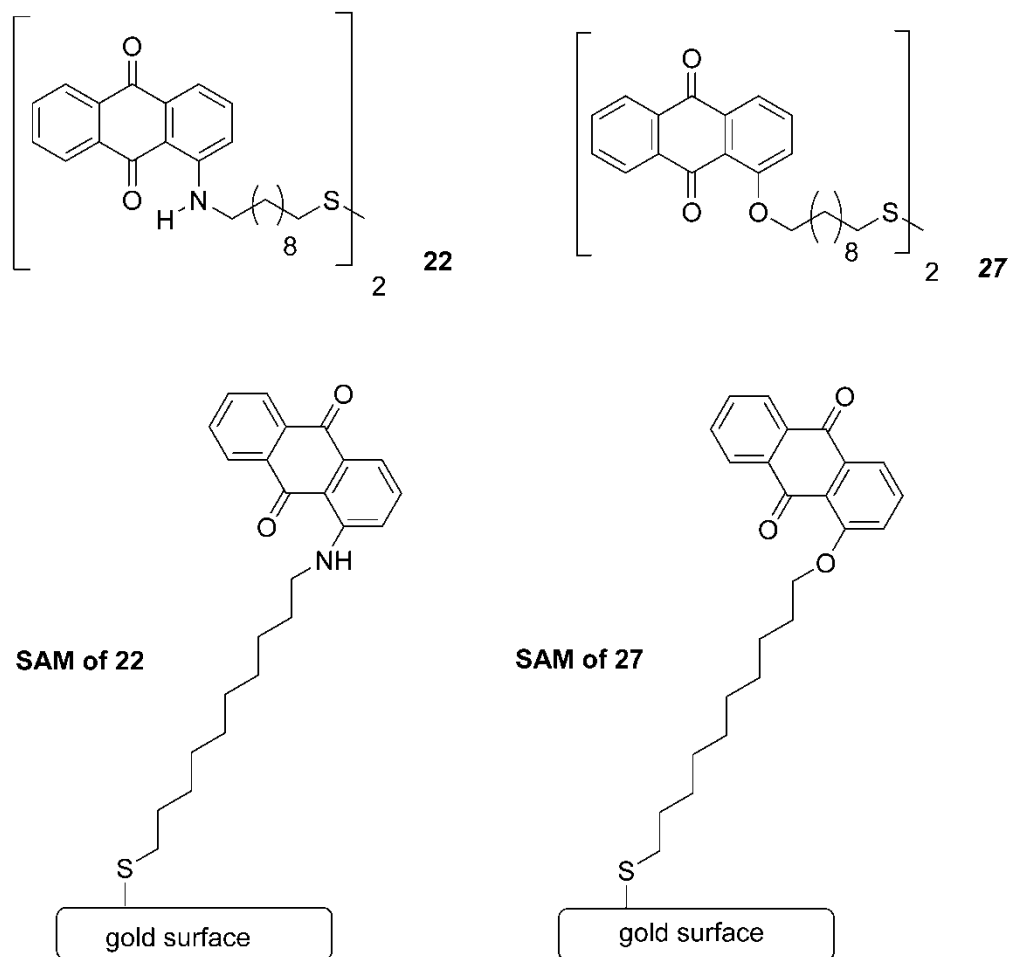


Figure 1-3 Self Assembled Monolayers of compound **22** (1-aminoAQ disulfide) and **27** (1-hydroxyAQ disulfide)

Electrochemistry of quinones belongs to a subclass of ET processes called proton coupled electron transfers (PCET). As implied by the name, the electron transfer is coupled with proton transfer, and the mechanistic details of the process are largely unresolved.¹⁴ Stepwise addition of electron and proton was accepted earlier, but recent work by Savéant¹⁵⁻¹⁷ suggests that a concerted mechanism for electron and proton transfer could be operating in several natural processes, such as cytochrome *c* oxidase,¹⁸ ribonucleotide reductase¹⁹ and superoxide dismutase.²⁰ Quinones PCET mechanism, theoretically,

should involve 2 electrons and 2 protons ($2e, 2H^+$). However, the redox mechanism is dependent on solvent, supporting electrolyte, electrode material, and pH.¹⁴ In a dry, aprotic solvent a cyclic voltammogram (CV; shown in **Figure 1-4a**) shows that the quinones undergo two consecutive redox steps attributed to a $2e$ redox process, according to the following scheme.^{9,21,22}

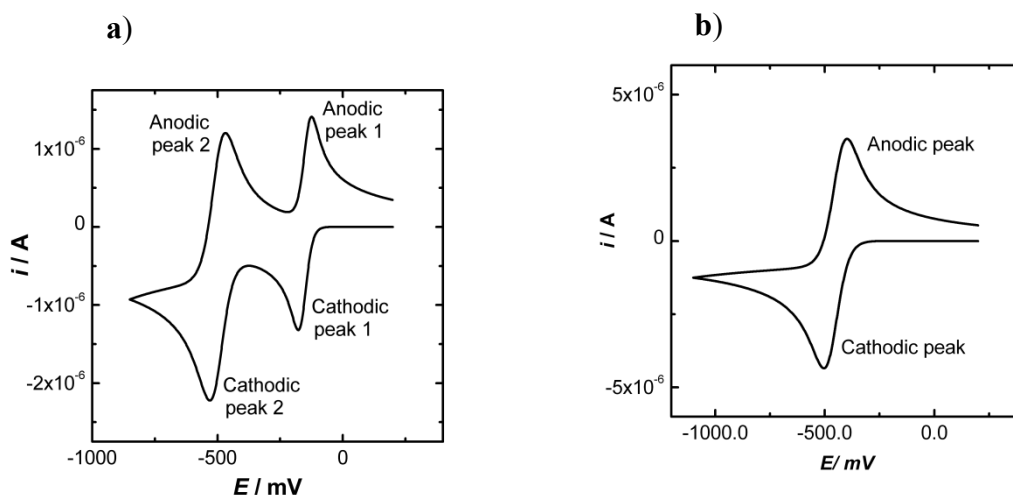
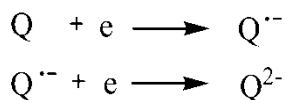


Figure 1-4 Typical Quinone reduction/Oxidation **a)** aprotic solvent^{9,21,22} **b)** aqueous medium^{9,14,23}

In an aqueous medium, the CV (**Figure 1-4b**) shows a single $2e$ redox wave for the quinone redox process, which is attributed to $2e, 2H^+$ to produce hydroquinone.



The two redox waves seen in the dry aprotic environment amalgamated to give a single peak in aqueous medium as a result of strong hydrogen bonding which stabilizes Q^{2-} over

the $Q^{\cdot-}$.⁹ Studies of the fate of the ET in response to proton transfer in quinone electrochemistry show that in aprotic solvents, reduced quinone is stabilized either by HBing or protonation depending on the nature of the proton donor solvents.^{9,14,23} Protonation is promoted by strong acids whereas HB agents, such as alcohols, promote HB formation. In addition, the basicity of the quinone anion also affects the proton transfer.¹⁴ In aqueous media, protonation / deprotonation prevails, but buffered or unbuffered media complicate the situation. Recent studies reveal that the strong HBs stabilize the reduced quinone anions in unbuffered aqueous solution,⁹ a situation similar to that in aprotic solvents with addition of acid or HBing agents. The possible stepwise electron transfer (horizontal transformation of **Figure 1.5**) and proton transfer (vertical transformation of **Figure 1.5**) of quinone electrochemistry is summarized in the following 9-membered square scheme.

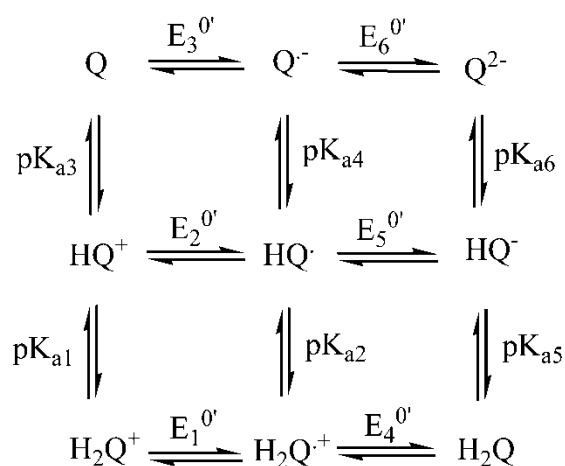


Figure 1-5 Nine member square scheme for stepwise quinone reduction / oxidation

The electrochemical thermodynamic parameter, equilibrium potential ($E^{0'}$), of the quinone reduction depends on the nature of the compound and can generally be obtained by CV. Steric effects and the substituent groups also play an important role in determining $E^{0'}$.²⁴ In an aprotic solvent, a highly solvated quinone redox probe changes its $E^{0'}$ toward the anodic region if any acidic or HBing additive is present.^{9,14,23,25}

Quinones electrochemical behaviour is completely different in aqueous media. As mentioned earlier, the single peak for quinone reduction is observed and the $E^{0'}$ of the redox couple follows a Nernstian response, hence the response can be predicted from the Nernst equation, shown as **Equation 1**. The Nernstian equation relates the variation of electrode potential to the activity of the reactants and products of the system. When the concentrations of the components are very low, the activity is replaced with concentration. A typical form of the Nernst equation under a set of equilibrium conditions is given by,

$$E = E^{0'} + \frac{2.303RT}{nF} \log \frac{[Oxd]}{[Red]} \quad \text{Equation 1}$$

Where E is the standard electrode potential; $E^{0'}$ is the apparent equilibrium potential; [Oxd] is the oxidant concentration; [Red] is the reductant concentration; R is the universal gas constant; T is the absolute temperature; F is the Faraday constant; n is the number of electrons involved in the redox process.

Generally, a pH dependent redox couple has an electrochemical reaction according to the following equation.



The apparent equilibrium potential ($E^{0'}$) can be calculated using the Nernst equation when the system is at equilibrium, i.e. [Oxd] = [Red], and the equation assumes the following form.

$$E^{0'} = E^0 - \left(\frac{0.059m}{n} \right) pH$$

Equation 2

Where, n and m are the number of electrons and protons transferred, respectively.

The nine member square scheme (**Figure 1-5**) is frequently used by researchers to understand the microscopic kinetics of electron and protons transfers in aqueous media for the quinone reduction regardless whether it is in solution or surface bound.^{9,26-29} The $2e$ and $2H^+$ electrochemistry of quinone is extremely complex with varying pH, but Laviron has developed and tested theories for kinetics of quinones at variable pHs.²⁶ In these theories, two basic assumptions were made. First, when the electrochemistry is under kinetic control the protonation is at equilibrium and second, side reactions, such as disproportionation and dimerization, are absent. Laviron *et al.* studied quinone electrochemistry using literature polarographic data and equations pertinent to the relevant calculation of ET rate constants are given in the CV section. Usually, the values for the acid / base equilibrium constant (pK_a) (**Figure 1-5**) are obtained by curve fitting the experimental apparent ET rate constant (k_{app}) data to the theoretical data, and once these are known ET and proton transfer (PT) sequences can be predicted. For example, the benzoquinone / hydroquinone couple literature polarographic data were analyzed using the theory, and it showed good agreement with the microscopic rate constants between pH 0 to 7.²⁶ The study also highlights that within this pH range, both QH_2^{2+} and Q^{2-} species are not involved in the quinone electrochemistry, and the order of electron

and proton addition for the reduction reaction is, H^+eH^+e , eH^+H^+e , and eH^+eH^+ for low pH (0 to 2), intermediate pH (3.5 to 5.5), and high pH (6 to 8), respectively.²⁶

The redox chemistry of quinone in solution is well documented, and the electrochemistry of quinone discussed thus far is for well solvated diffusing redox probes. However, similar analyses can be applied to surface bound or tethered quinone redox couples. Tethered quinones, or quinones covalently attached to an electrode to form SAMs (also called electro active monolayer) not only mimic the biomembrane redox environment, but also provide specific advantages that are relevant for studying ET at interfaces. The advantage is that there is no mass transfer current, which diminishes the time constant and double layer effects of the electrochemical cell, greatly simplifying the components in the electrochemical equations.³⁰ There are different ways to attach the redox probe to the alkanethiol chain, but attaching the quinone prior to the SAM formation is believed to be the best method because the final target compound can be fully characterized before tethering on gold.

PCET of SAMs of different quinones (benzoquinone, naphthoquinone, anthraquinone, etc) at various pHs were explored by several groups.^{4,10,28,29,31-37} The $E^{0'}$ of the quinone is affected by the surface attachment, and Nernstian behaviour is observed when the pH is changed, *i.e.* $E^{0'}$ in basic pH is more negative than that in acidic pH, consistent with **Equation 2**. The surface pK_a of the phenolic hydrogen is expected to be higher than that of the solution counterpart.²⁸ Usually, CVs of quinones in acidic buffer pH show larger peak separation than in basic buffer pH for a given scan rate indicating sluggish electron kinetics. Although other methods are available to analyze the ET kinetics of the quinone,³ Laviron's formalism, based on Butler-Volmer kinetics, is mainly used. In addition to the

pH of the medium, the ET kinetics is affected by the distance,³³ type of bridge between the electrode and redox centre quinone,³⁸ and functional group present in the quinone.²⁸ Furthermore, plots of k_{app} vs. pH show a 'W'-shaped curve when the quinone undergoes $2e$ and $2H^+$ reduction based on Laviron's stepwise treatment. Nevertheless, some quinone systems do not obey this theory. For example, March *et al.*²⁸ recently published kinetics of the naphthaquinone system as a function of pH, which show that the kinetics remain constant up to pH 7 then increase with increment of pH. The authors attributed the unusual change to an intramolecular HB between the adjacent phenoxide anion and the hydroquinone. Trammell *et al.* benzoquinone systems also show frequent deviation from theory.²⁹

The literature precedence for electrochemistry of quinone SAMs clearly shows that understanding the kinetics of the quinones may be a challenging task but a clear fundamental understanding is necessary considering its importance in the chemical and biological energy conversion strategies.

Our group is interested in making functional supramolecular materials using quinone derivatives for applications such as photovoltaic cells, and the focus of this thesis is to understand the quinone ET at the hydrophobic|hydrophilic interface and ET mediated by HBs.

1.2 Methods for measuring ET

There are several techniques, such as spectroscopic methods and electrochemical methods available to measure ET in different systems. Typical electrochemical methods are chronoamperometry (CA), cyclic voltammetry (CV), and electrochemical impedance spectroscopy (EIS). Of those techniques, CV and EIS were used for the present series of ET studies, and in the following paragraphs those techniques and analysis of data is discussed.

1.2.1 Cyclic Voltammetry^{39,40}

Cyclic voltammetry is a simple, flexible electro analytical technique to characterize the electrochemical behaviour of a redox couple, such as apparent rate constant and equilibrium potential.

In cyclic voltammetry, current through a working electrode (WE) is recorded as a function of time, while the potential (E) is swept linearly. During the experiments, the working electrode is kept stationary and the electrolyte solution is unstirred. The potential of the WE is swept, or scanned, from a starting potential (E_s) to a certain potential called the switching potential (E_λ) then scanned back to the starting potential or end potential; the two scans are often called a cycle. The end potential is not necessarily the starting potential, but can extend past the starting potential. CV experiments can be single scans or multiscans. **Figure 1-6** shows typical excitation triangular wave form used in CV.³⁹

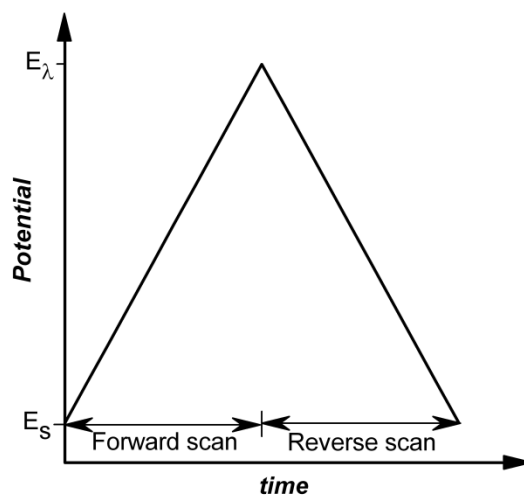


Figure 1-6 A typical excitation triangular waveform

The current response of the redox probe at various scan rates, either in solution or at a surface, is obtained as a cyclic voltammogram (**Figure 1-7**). The rate at which the potential is changed is called scan rate ($v/V \cdot s^{-1}$). **Figure 1-7** shows that the scanning starts at 0.25V (E_s) and a constant current flows through the WE until -0.25V, indicating the charging of the double layer of the WE. Onset of the cathodic faradaic current can be seen nearing -0.5V. Eventually, as the potential scan passes $E^{0'}$ the current reaches a maximum value of E_{pc} at -0.5V and thereafter the current decreases to a steady state at -1.1V. On the reverse scan, the same process is repeated with a maximum at E_{pa} , but the faradaic current is due to oxidation of the redox couple.

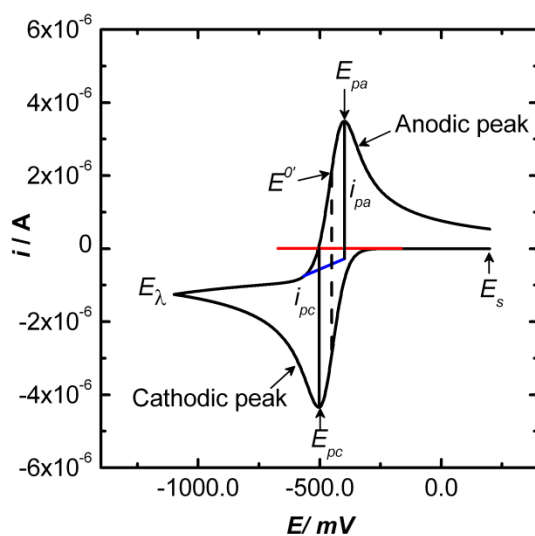


Figure 1-7 A typical cyclic voltammetry response for a quasi reversible redox reaction

The acquired CV can then be analyzed to extract the thermodynamic and kinetic parameters. At sufficiently low scan rates, the redox response of a quasi reversible system is dictated by thermodynamic factors, resulting in peak current (i_p) and peak potential (E_p) of cathodic and anodic peaks, area under the peaks and the peak's full width at half maximum height (FWHM) are obtained with assistance of GPES 4.9 software. Solution phase or diffusion controlled, and surface bound redox centres have different electrochemical responses due to their environment. As a result, correct analytical equations for current – potential (i - E) should be used to extract the thermodynamic parameters.

For solution phase systems, the following equations are used to characterize the system.

Equilibrium potential ($E^{0'}$) of the system is given by,

$$E^{0'} = E_{\frac{1}{2}} = \frac{E_{pa} + E_{pc}}{2} \quad \text{Equation 3}$$

The relationship between ΔE_p and number of e (n) transferred for reversible redox reaction at 25°C,

$$\Delta E_p = E_{pa} - E_{pc} = \frac{58}{n} mV \quad \text{Equation 4}$$

From the Randles- Sevcik equation, the diffusion coefficient (D) can be calculated.

$$i_p = 2.69 \times 10^5 n^{3/2} A C_{ox}^0 (\nu D_{ox})^{1/2} \quad \text{Equation 5}$$

Where A is the area of the electrode in cm^2 , i_p is the peak current in amperes; D_{ox} is the diffusion coefficient of the oxidized component in $cm^2 \cdot s^{-1}$; ν is the scan rate in $V \cdot s^{-1}$; C_{ox}^0 is the bulk concentration of the oxidant in $mol \cdot cm^{-3}$.

The following equations and descriptions are used for the electrochemical characterization of a surface bound redox centre in CV.

Equation 3 will again be used for the calculation of the equilibrium potential. Ideally, ΔE_p should be zero because the surface bound redox centre's equilibrium potential is equal to the E_p . The full-width-at-half-maximum (FWHM) is a measure of the broadness of the faradaic peak, and its ideal value is given by **Equation 6**,

$$FWHM = \frac{90.6}{n} mV \quad \text{Equation 6}$$

The other important parameter is surface coverage (Γ in mol·cm⁻²), which is obtained by integrating the area under the faradaic peak or total charges passed through electrode and substituting it to the following **Equation 7**. The software (GPES 4.9) provided with the instrument was used to correct the background current and to integrate the peak.

$$\Gamma = \frac{Q}{nF} \quad \text{Equation 7}$$

Here, F is the Faradaic constant (96485 C·mol⁻¹).

The peak current response of the strongly adsorbed monolayer of electro active species is given by **Equation 8**.

$$i_p = \frac{n^2 F^2}{4RT} \nu A \Gamma_o^* \quad \text{Equation 8}$$

Kinetics of the ET studies were performed only for the Self Assembled monolayers (SAMs) of compounds **22** and **27**. Theory and equations pertinent to surface confined redox couples are explained in the following section.

A widely cited theoretical treatment by Laviron⁴¹ to measure the kinetics of ET by cyclic voltammetry was used. The basis for the theory is based on Butler-Volmer kinetics. However, other treatments of CV data to extract kinetics parameters, based on Marcus's density of State theory, are available.³

Laviron's theory deals primarily with peak separation ΔE_p ($E_{pc} - E_{pa}$) as a function of scan rate ν . The best experimental condition for obtaining k_{app} and the transfer coefficient (α) is when $\Delta E_p > 200/n$ mV. The CV data that fulfill the above condition are used for determination of kinetics by the **Equations 9 and 10**.

$$E_{pc} = E^{0'} - \frac{RT}{\alpha nF} \ln \left(\frac{\alpha nF \nu}{RTk_c} \right) \quad \text{Equation 9}$$

$$E_{pa} = E^{0'} - \frac{RT}{(1-\alpha)nF} \ln \left(\frac{(1-\alpha)nF \nu}{RTk_a} \right) \quad \text{Equation 10}$$

E_{pc} and E_{pa} are the cathodic and anodic peak potentials, respectively. $E^{0'}$ is the formal potential; n is the number of electron transferred; R is the gas constant; T is the absolute temperature and F is the faraday constant. The transfer coefficient (α) is usually determined from the gradient of the linear portion of the graph of $\Delta E_p - E^{0'}$ vs. $\ln \nu$. The transfer coefficient (α) is a measure of the activation energy barrier,^{39,42} and when the transition state is approximately halfway between the reactant and product, the value of α tends to be 0.5. Most often, symmetric cathodic and anodic peaks give an indication that the transfer coefficient is 0.5. The slope of the linear part of the graph at higher scan rates provides α , and once α is known, k_{app} can be found. There are two ways that can be used to determine k_{app} , either by substituting the α value to the **Equation 8** or **9** and then solving them, or obtaining the critical scan rate, when $\Delta E_p - E^{0'} = 0$, and then substituting the critical scan rate into **Equation 11**.

$$k = \alpha nF \nu_c / RT = (1-\alpha)nF \nu_a / RT \quad \text{Equation 11}$$

Where ν_a and ν_c are critical scan rates (**Figure 1-8**) for anodic and cathodic reactions, respectively, as shown in **Figure 1-8**.

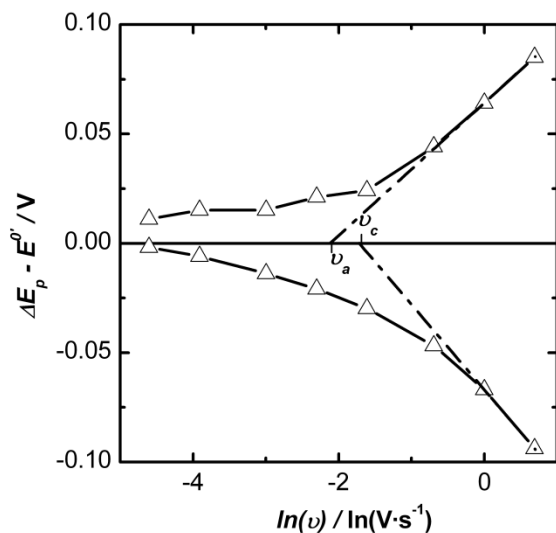


Figure 1-8 Anodic (v_a) and cathodic (v_c) critical scan rates

1.2.2 Electrochemical Impedance Spectroscopy^{39,43}

Electrochemical Impedance Spectroscopy (EIS) is used to characterize many of the electrical properties of interfaces with electronically conducting electrodes. Modern advance in electronics have led to the development of sophisticated experimental equipment to measure and analyze the frequency response to a small amplitude ac signal for a wide range of frequencies normally between 10^{-3} to 10^6 Hz.

Although there are several types of excitation methods available, in standard EIS a small voltage with different frequencies is applied to the interface and amplitude and phase shift, or real and imaginary parts, of the resulting current is measured. Impedance at the interface as a function of the frequency is then calculated; hence, it can be used to obtain electrochemical reaction details of the interface. In order to obtain meaningful experimental data from EIS, the interfacial (electrode-material interface) response needs

to be linear. However, it is well known that, the interface response is nonlinear to most external electrical stimuli, especially for large input of current or voltage. According to MacDonald,⁴³ the nonlinearity in the response can be overcome by applying a potential difference that is smaller than the thermal voltage. Thermal voltage is defined as $V_T \equiv RT/F \equiv k_b T/e$, and has a value close to 25mV at 25°C. Here, k_b is the Boltzmann constant; e is the electron charge; other symbols have their usual meanings.

Electrical impedance is a more general term than the resistance because it takes the phase difference between resulting and applied signals into account. Phase is a parameter of a sinusoidal (alternative) signal, when represented as a vector, given by the multiplication of angular velocity of the signal with time. This signal is generally referred to as an AC (Alternative Current) signal. When the angular velocity is zero, the signal is a “DC” (Direct Current) signal, and the impedance can be given as resistance. The relationship between impedance and the electrical elements are explained in the following section.

A sinusoidal (alternative) voltage can be represented as a vector with amplitude E and angular frequency ω , and real and imaginary components are,

$$e(\text{real}) = E \sin \omega t \text{ and } e(\text{imaginary}) = E \cos \omega t$$

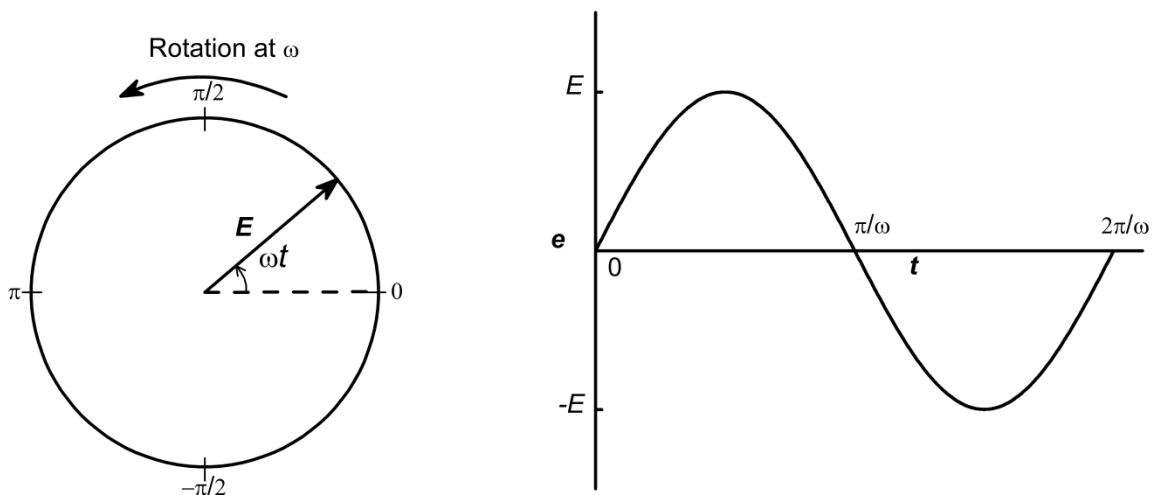


Figure 1-9 Phasor diagram for an alternating voltage, $e = E \sin \omega t$

Figure 1-9 shows the voltage as a rotating vector (phasor) and the real part of the voltage is $E \sin \omega t$ and imaginary part is $E \cos \omega t$. An alternate current can also be represented by phasor I , which can be rotating at the same frequency ω , but these phasors may not be in the same phase and are separated by a phase angle, ϕ , which is explained in **Figure 1-10**.

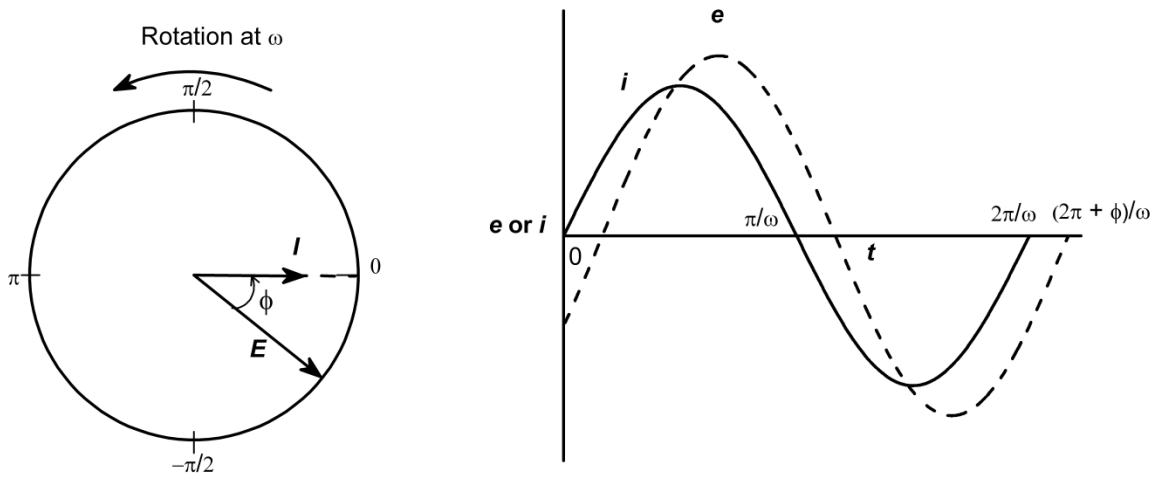


Figure 1-10 Phasor diagram for an alternating current and voltage with phase angle ϕ at frequency ω

Figure 1-10 shows single frequency voltage and current signals where current phasor leads the voltage phasor by an angle of ϕ . Thus the current signal can be written as,

$$i = I \sin (\omega t + \phi)$$

When an alternative voltage $e = E \sin \omega t$ is applied across a pure resistor R , according to Ohm's law, the current across the resistor is,

$$i = E \sin \omega t / R = E/R \sin \omega t$$

Here, voltage and current phasors are in the same phase and the phase angle between them is zero, i.e. the phase shift is zero. When the same alternative voltage $e = E \sin \omega t$ applied across a pure Capacitor C , charge accumulation (q) on the capacitor is,

$$q = Ce$$

Hence the current across the capacitor, dq/dt is,

$$i = C (de/dt)$$

Differentiation gives,

$$i = CE\omega \cos \omega t$$

This can be written as,

$$i = E\omega C \sin (\omega + \pi/2)t$$

The phase angle is $\pi/2$ (phase shift of 90°), which means the current leads the voltage by $\pi/2$.

Impedance of a system is given by,

$$Z = E/I$$

Where Z is impedance; I is current; E is potential.

Impedance of a resistor for an AC signal, $e = E \sin \omega t$ and $i = E/R \sin \omega t$, is,

$$Z = R$$

Impedance of a pure capacitor for an AC signal, $e = E \sin \omega t$ and $i = E\omega C \sin (\omega + \pi/2)t$, is,

$$Z = -1/\omega C$$

The phasor is represented in terms of complex notation j , which has value $\sqrt{-1}$, in order to keep the vector components straight. In this conversion, the component of the phasor along the ordinate is multiplied by $j = \sqrt{-1}$ and is referred to as the “Imaginary” part. The component along the abscissa is referred as the “Real” part. Both parts are real, because phase angle between “Imaginary” and “Real” parts can be measured. Thus for a pure capacitor, in complex notation,

$$E = -jI/\omega C$$

Therefore, the impedance of a capacitor is,

$$Z = -1/j\omega C$$

In the above final form of the equation, the impedance of the capacitor not only has a numerical value, which changes with frequency, but also takes phase angle into account by incorporating complex notation.

Since impedance can be represented as a planar vector, it can be represented as the sum of vector components along imaginary (y -axis) and real (x -axis) axes,

$$Z(\omega) = Z' + jZ''$$

Where Z' and Z'' represent real and imaginary components of the impedance, respectively. **Figure 1-11** shows rectangular coordinates of the two vector components of the impedance, and their values are,

$$\text{Re}(Z) = Z' = |Z| \cos\phi \text{ and } \text{Im}(Z) = Z'' = |Z| \sin\phi$$

With the phase angle,

$$\phi = \tan^{-1}(Z''/Z')$$

and the magnitude of the total impedance is,

$$|Z| = [(Z'')^2 + (Z')^2]^{1/2}$$

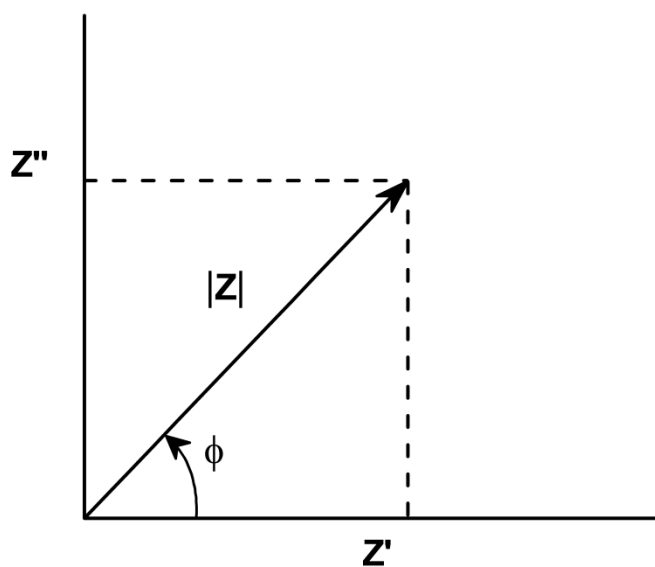


Figure 1-11 Rectangular coordinates diagram of Impedance (Z)

In the present study of the EIS applications, two methods are adopted. In the first method, a DC voltage equivalent to the equilibrium potential of the system is applied. Then a small AC voltage (10mV at different frequencies) is super-imposed on to the DC voltage as shown in **Figure 1-12**. The second method is similar to the first, but in addition to the AC excitation at different frequencies, DC potentials are scanned over a range, usually $E^0 \pm 0.25V$.

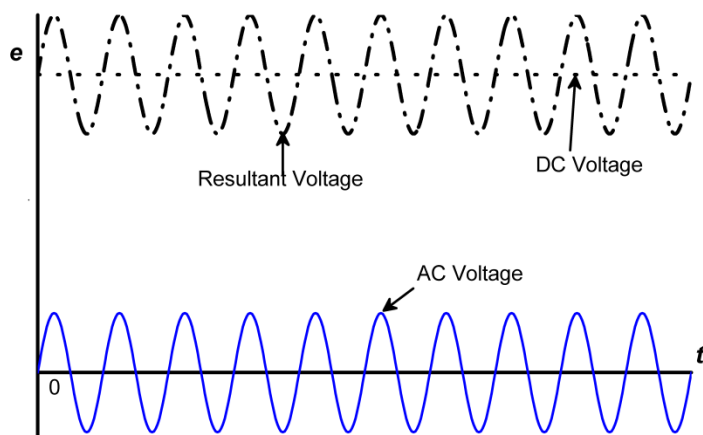


Figure 1-12 Small AC perturbation super-imposed on a DC voltage

The gathered impedance data of the system is presented as both Bode and Nyquist plots. A Bode plot is the plot of $\log|Z|$ and phase angle of the impedance against the log frequency of the applied voltage. A Nyquist plot is the plot of the imaginary part of the impedance (Z'') against the real part of the impedance (Z') at different frequencies of the applied voltage. **Figure 1-13** shows samples of Bode and Nyquist plots.

Although there are several methods to analyze the impedance data, only two of them were used in the present study.

I. Complex plane analysis

In complex plane analysis, a network of electrical circuit elements or an equivalent circuit is used for modelling the electrochemical process of the system. The choice of the circuit elements and their combinations are based on the understanding of the molecular level electrochemical processes, otherwise more than one combination of elements is possible for a set of impedance data. For example, **Figure 1-13** shows the Nyquist and Bode plots

of an equivalent circuit with parallel RC elements. Once the correct combination of elements is selected, the experimental impedance data is curve fitted by using the complex nonlinear least square (CNLS) method. It is important to obtain meaningful values for each element. In addition, χ^2 of the curve fit needs considerable attention, because it provides the information about goodness of the fit, and usually, a better fit result in a χ^2 value of less than 0.1. Finally, with the aid of these numerical values of elements, electrochemical characterization of the system can be done.

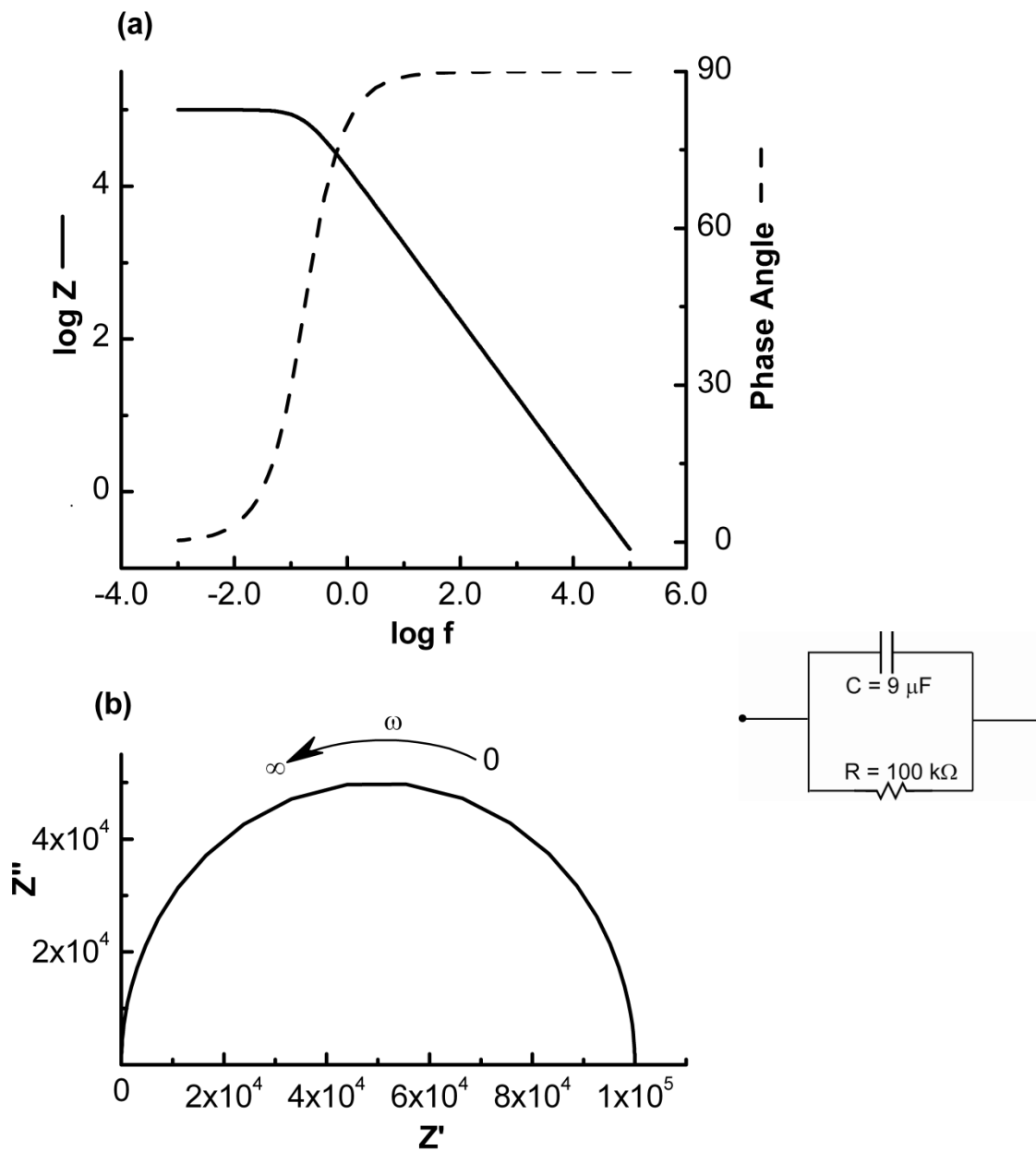


Figure 1-13 (a) Bode plots for a parallel RC circuit with $R = 100 \text{ k}\Omega$ and $C = 9 \text{ }\mu\text{F}$. (b) Nyquist plot for a parallel RC circuit, shown in the picture with $R = 100 \text{ k}\Omega$ and $C = 9 \text{ }\mu\text{F}$.

In this study, impedance data of both the solution phase (solvated redox probe) and solid phase (electro active SAM) were analyzed using the complex plane method. Understanding the two electrochemical systems in terms of the model equivalent circuit is necessary to interpret the impedance data. For example, an equivalent circuit of a general electrochemical cell appears in **Figure 1-14a**, where R_s is solution resistance, C_{dl} is double layer capacitance, and Z_f is faradaic impedance, which describes the frequency dependant faradaic process. It is convenient that the Z_f is interpreted in terms of a pure resistor R_{CT} (charge transfer resistance) and general impedance Z_g . These three common elements (R_s , C_{dl} , Z_f) are present in both systems studied. However, in the solution phase, Z_g is replaced with *Warburg impedance* (Z_w), which is caused by the diffusion of the redox probe and it represents a type of resistance to mass transfer. **Figure 1-14b** shows the circuit diagram and **Figure 1-15** shows Nyquist and Bode plots of a system under diffusion control. In the Nyquist plot, the intercept of the x -axis at high frequency represents the solution resistance (**Figure 1-15b**), the diameter of the semicircle gives R_{CT} , and the straight line with the slope of 1 indicates a purely diffusion controlled faradaic process at the low frequency limit.

The kinetic parameter, rate of ET (k_{app}) can be determined by solving **Equation 12** and **13**.

$$i_0 = \frac{RT}{nFR_{CT}}$$

Equation 12

$$i_0 = nFk_{app}\Gamma$$

Equation 13

$$k_{app} = \frac{RT}{\Gamma n^2 F^2 R_{CT}}$$

Equation 14

Where Γ is the surface coverage of a redox probe determined from the CV; other symbols have their usual meanings.

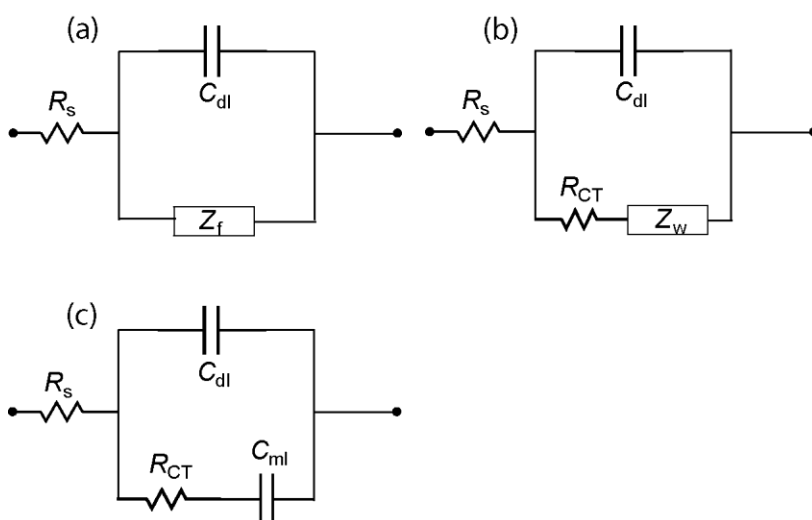


Figure 1-14 Equivalent circuit diagrams for a) general electrochemical cell; b) diffusion control cell; c) SAM cell

In an electro active SAM system, the general impedance Z_g is replaced with capacitance of the monolayer (C_{ml}) as shown in **Figure 1-14c**³⁰ and k_{app} can be determined from **Equation 13**.

It is important to note here that all capacitive elements (C_{dl} and C_{ml}) are treated as pure electrical capacitive elements, but McDonald⁴³ claims that such treatment does not properly represent the actual situation of the electrochemical cell. Therefore, the

capacitance is replaced with a distributed element called a constant phase element (CPE).

A constant phase element impedance is defined as,

$$Z_{\text{CPE}} = 1 / Q^{\circ}(j\omega)^n$$

Where Q° is the numerical value of the admittance at $\omega = 1$ rad/s.

Phase angle of a CPE remains constant for any frequency, but depends on n . When $n = 1$

CPE is a pure capacitor (phase angle 90 deg) and when n is 0, CPE is a pure resistor

(phase angle 0 deg).

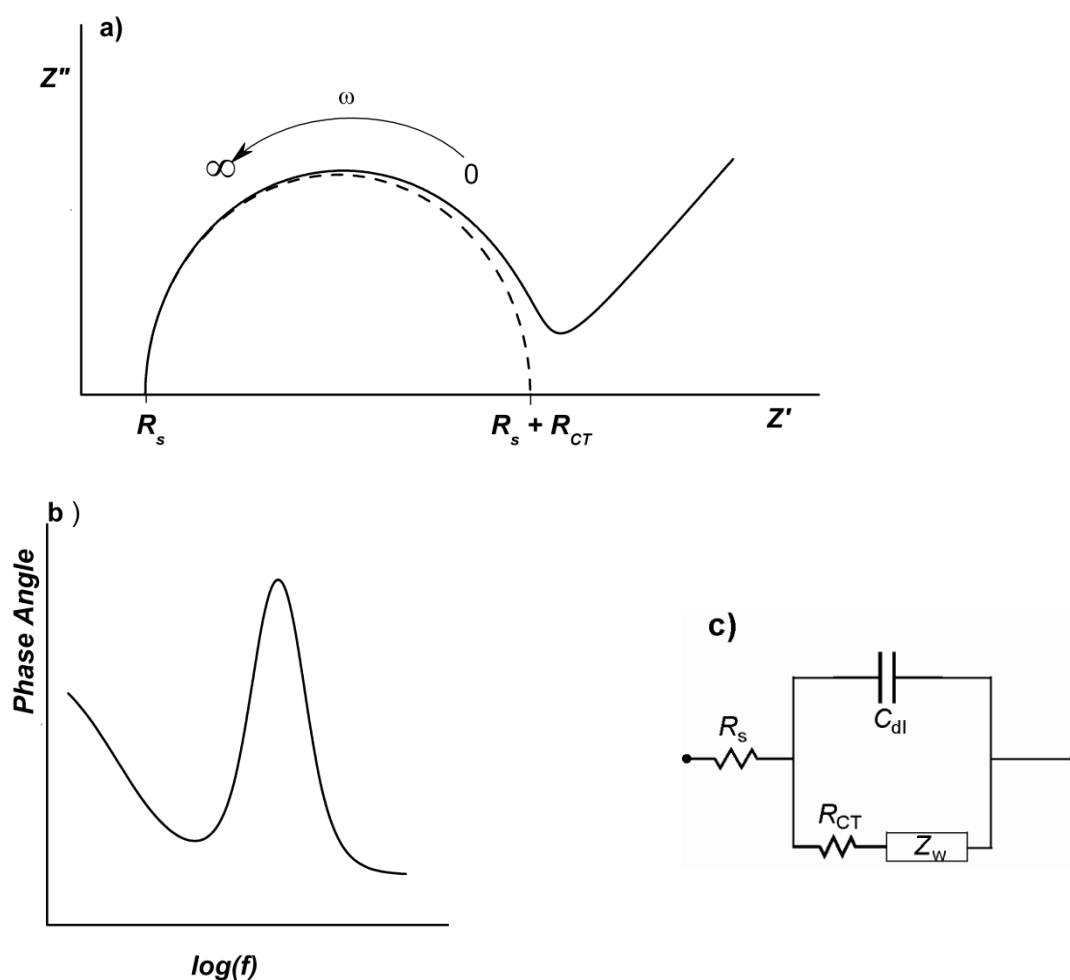


Figure 1-15 a) Nyquist plot, b) Bode plot, and c) Equivalent circuit for diffusion controlled cell.

II. Brevnov *et al.* Protocol⁴⁴

This method is similar to AC voltammetry,³⁹ but the y axis has admittance instead of current i in the AC voltammogram. Laviron's faradaic admittance theory for strongly adsorbed electroactive species obeying the Langmuir isotherm was used to analyze the data.⁴⁵

According to admittance theory, components of faradaic impedance can be designated as adsorption resistance (R_{CT}) and adsorption capacitance (C_{ml}), which are frequency independent and defined as

$$R_{CT} = (RT/n^2 F^2 A k_{app}) [\alpha \Gamma_o \eta^{-\alpha} + (1-\alpha) \Gamma_R \eta^{(1-\alpha)}]^{-1} \quad \text{Equation 15}$$

$$C_{ml}^{-1} = k_{app} R_{CT} (\eta^{-\alpha} + \eta^{(1-\alpha)}) \quad \text{Equation 16}$$

Where, η is overpotential ($E^0 - E^{0'}$); A is the electrode area.

It is assumed that the surface coverage of the electrode remains constant during the data acquisition; total surface coverage (Γ_{Total}) is given by,

$$\Gamma_{Total} = \Gamma_o + \Gamma_R \quad \text{Equation 17}$$

Γ_o and Γ_R are the surface coverage of the oxidized and reduced compounds, respectively, and if they obey the Langmuir isotherm and the redox reaction is reversible, the Nernst equation holds true. Therefore, the relationship between overpotential and surface coverage is given by,

$$\Gamma_o/\Gamma_R = \eta = \exp [(nF/RT) (E_{DC} - E^{0'})] \quad \text{Equation 18}$$

And the faradaic admittance of the cell is defined as

$$Y^{faradaic} = [R_{CT} - j/(\omega C_{ml})]^{-1} \quad \text{Equation 19}$$

The stepwise procedure that was used to extract faradaic admittance from cell admittance is outlined in the following section.

After acquiring the cell's total admittance ($Y^{totalcell}$) as a function of DC potential, the second step is to correct for R_s to obtain the interfacial admittance (Y^{inter}) from the $Y^{totalcell}$.

Y^{inter} is defined as

$$Y^{inter} = [(Y^{Totalcell})^{-1} - R_s]^{-1} \quad \text{Equation 20}$$

The R_s is obtained from the high frequency x intercept of the complex plane plot of the impedance. The third step involves extracting faradaic admittance ($Y^{faradaic}$) from the Y^{inter} . This was done by subtracting nonfaradaic admittance (CPE baseline) from Y^{inter} . At the DC potential well away from the $E^{0'}$ ($E^{0'} \pm 0.25V$), the faradaic admittance is negligible. Therefore, extrapolation of the Y^{inter} 250 mV before $E^{0'}$ provides a value for the nonfaradaic admittance. All three steps were separately repeated for the imaginary and real part of the cell admittance.

Finally, a theoretical simulation based on **Equation 15-20** was curve fitted to experimental curves while optimizing the ET coefficient (α), $E^{0'}$, and the total electrode coverage ($\Gamma_{Total} A$), to obtain the ET rate constant k_{app} using a custom Microsoft Office Excel[®] work sheet.

1.3 Self Assembled Monolayer Preparation and Characterization

The process of formation of self-assembled monolayers (SAM) of alkanethiols/ alkane disulfides on gold surfaces is described as a spontaneous formation of the gold thiol bond, driven by the interplay of non-covalent interaction of alkane chains with themselves and with solvent molecules. These intramolecular and intermolecular interactions direct the sulfur atom to be bonded with the gold. As a result, only defined-organized- monolayers are formed after incubation in solution of alkanethiols/ alkane disulfides. The formed monolayer is in thermodynamic equilibrium under the experimental conditions.⁴⁶ These organized molecular assemblies on surfaces have gained great attention owing to their potential application in several areas such as electronics, electrochemistry, biological studies, and ultimately in forming molecular devices. Of all the methods available to prepare these kinds of structures, self-assembling of alkanethiols on gold surfaces is the most simple and cheapest method. Furthermore, incorporation of well-defined redox centres on to the self-assembled monolayers provides materials that can be tuned for external stimulus for an intended purpose.

The Nuzzo and Allara method for⁴⁷ SAM preparation has become the most widely used for solution phase SAM preparation. Usually, a pre cleaned gold surface is used, and it is incubated in a solution of electro active alkanethiol or disulfide. Gold (0) is chosen because the zero valent gold is probably one of the most inert substrates toward oxidation.⁴⁷ Chemical, electrochemical, or a combination of both methods is used for the precleaning of gold, and the choice of the cleaning method depends on the nature of the organosulfur compound. The concentration of organosulfur compound is generally in the

range of 0.01-1mM.³⁰ The incubation time depends on the nature of the alkanethiol and the expected use of the SAM. After formation, the characterization of the SAM is done by using photo elastic modulator Fourier-transform-infrared-reflection-absorption spectroscopy (PEMIRRAS/PEMFTIRRAS). The technique involved with PEMIRRAS is described in the following section.

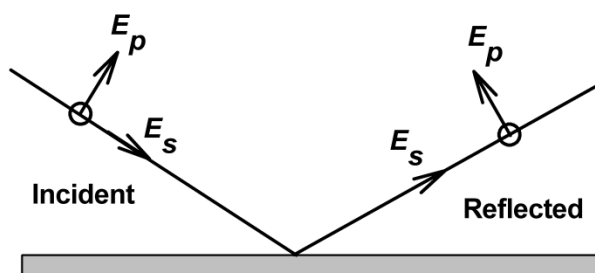


Figure 1-16 *s* and *p* components of polarized light

Polarized light consists of *s* and *p* components; the *s* component is the radiation perpendicular to the plane of incidence whereas radiation parallel to the incident plane is the *p* component (**Figure 1-16**). According to the surface selection rule, only the *p* component of the light interacts with the dipole moment of the molecules on the surface when the polarized light shines on a metal surface at high angle of incidence ($\sim 80 \pm 5^\circ$). The intensity of the reflected light of the *p* component is close to twice the intensity of the incident light,^{48,49} which can be used for obtaining differential spectra ($\Delta R/R$) of *s* and *p* components, and ($\Delta R/R$) is defined as

$$\frac{\Delta R}{R} = \frac{I_p - I_s}{I_p + I_s}$$

Where I_p and I_s are the intensities of the p and s components of the polarized light, respectively. Moreover, since differential spectra of the s and p components are obtained and the intensity of the p components is larger than s components, background correction is not necessary.⁴⁸

After obtaining the spectrum, the region of interest lies mainly in the methylene symmetric ($\sim 2850\text{cm}^{-1}$) and antisymmetric ($\sim 2919\text{cm}^{-1}$) stretching frequency and any other functional group stretching frequency such as carbonyl stretching ($\sim 1700\text{ cm}^{-1}$).⁵⁰⁻⁵²

More detailed discussion of this is given in the results and discussion part.

1.4 Thesis Overview

Two categories of electron transfer (ET) studies of anthraquinones are described in this thesis. The first is ET between the redox active anthraquinones mediated by hydrogen bonds, which is named as solution based ET studies. The second is ET of surface confined anthraquinones by using electro active self-assembled monolayers (SAMs), which is named as surface ET studies.

For surface ET studies, two surface-active anthraquinones were synthesized. These surface-active anthraquinones form self-assembled monolayers (SAMs) on gold surfaces by the spontaneous formation of the Au-S bond, enabling the formation of tailored surfaces and permitting detailed electrochemical investigations. Thorough electrochemical studies involving variable temperature and pH are provided.

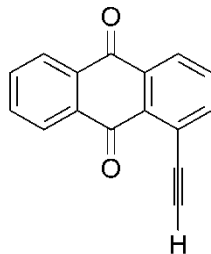
For solution based ET studies, the synthesis of a covalently linked anthraquinone to diaminopyridine through an ethynyl linkage was attempted. The target compound will assess the assembling dynamics and electronic communication mediated through hydrogen bonds. Electrochemistry of the intermediates in solution is studied.

Chapter Two: Experimental

2.1 Synthesis

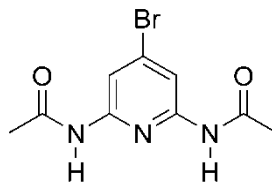
Unless otherwise stated, all chemicals were purchased commercially and were used without further purification. All common solvents were purchased from commercial sources and purified with MBRAUN purification system. Purification and recovery of certain solvents (ethanol, Acetone, Et₃N) were carried out according to procedures described in Perrin.⁵³ Reactions were carried out in oven-dried glassware under N₂ atmosphere. Column chromatography was carried out on silica (40- 63µm 60Å). ¹H and ¹³C NMR spectra were recorded on Bruker AC 200, Bruker Avance DMX 300, Bruker Avance 400 Ultrashield, Bruker AMX 300, Bruker UGI 300 and 400 machines. Operating frequencies of these machines range from 400 MHz- 200 MHz for ¹H nucleus and from 50 MHz- 101 MHz for ¹³C nucleus. FTIR and UV-VIS spectra were recorded on a Varian FTS 7000 FTIR spectrophotometer and a Cary 5000 UV-VIS-NIR spectrophotometer, respectively. MS spectrum was obtained on Bruker esquire 300, fennigan SSQ7000. Elemental analysis was done on PerkinElmer Series II CHNO/S analyzer.

2.1.1 Synthesis of 1-Acetylenylantraquinone (2)



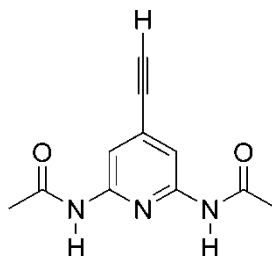
1-(Trimethylsilylacetylenyl)anthraquinone (**17**) (0.4008 g, 1.31 mmol) was dissolved in 26 mL of CHCl_3 and heated to reflux. To this mixture, a solution of tetrabutylammonium fluoride (4 mL, 1 M in THF) in 13 mL of CHCl_3 was added drop wise over 2.5 h and the refluxing was continued for another 3 h. After cooling to room temperature, water (30 mL) was added. The organic layer was washed with brine (30 mL), and with water (30 mL). The solvent was removed under reduced pressure to afford a dark green colour solid. The solid was washed thoroughly with MeOH, and dried to yield 0.2420 g (79%) of desired product. ^1H NMR (300 MHz, CDCl_3) δ 8.42- 8.28 (m, 2H), 7.99 (d, 1H, J (Hz) = 7.8), 7.87- 7.71 (m, 4H), 3.63 (s, 1H). ^{13}C NMR (101 MHz, CDCl_3), δ 182.64, 182.13, 141.35, 134.59, 134.55, 134.20, 134.08, 133.73, 132.83, 128.07, 127.66, 127.04, 122.55, 83.79, 82.68.⁵⁴

2.1.2 Synthesis of 2,6-di-N-acetylamino-4-bromo-pyridine (3)



4-bromo-2,6-diaminopyridine (**11**) (0.2003g, 1.1 mmol) was dissolved in 3.0 mL of triethylamine and 15 mL of dry THF. The resulting solution was chilled to 0°C, and acetic anhydride (1.0 mL, 10 mmol) was added. The mixture was stirred at room temperature for >24 h and the solvent was concentrated *in vacuo*. The product was isolated by trituration with Et₂O. Yield was 57.5% (0.1664 g). ¹H NMR (300 MHz, CDCl₃) δ 8.13 (s, 2H), 7.53 (s, 2H), 2.20 (s, 6H). ¹³C NMR (75 MHz, CDCl₃) δ 168.47, 149.82, 136.35, 112.61, 24.83.⁵⁵

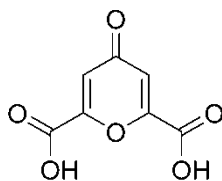
2.1.3 Synthesis of 2,6-diacetylamino-4-ethynylpyridine (3')



To a solution of 2,6-diacetylamino-4-[(trimethylsilyl)ethynyl]pyridine (**18**) (0.0788 g, 0.27 mmol) in MeOH (3.0 mL) 3.0 mL of 1M aqueous potassium hydroxide solution was

added and the mixture was stirred at room temperature for 2h. 5 mL of water was added and the aqueous phase was extracted with CHCl_3 (3×5 mL). The combined organic phases were dried over MgSO_4 , filtered, and the solvent was evaporated *in vacuo* to yield the mixture of compound with desired product. ^1H NMR (300 MHz, CDCl_3) δ 7.64 (s, 2H), 4.21 (s, 5H), 3.21 (s, 1H), 1.98 (s, 7H). Some NMR data is not consistent with previously reported synthesis by Llanes- Pallas *et. al.*⁵⁶ and Inouye *et. al.*⁵⁷

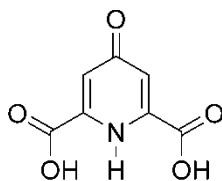
2.1.4 Synthesis of Chelidonic Acid (4-oxo-4H-pyran-2,6-dicarboxylic acid) (4)



Sodium ethoxide (37.6 g) was dissolved in 126 mL of dry ethanol and was warmed to 60°C . Approximately 60 mL of sodium ethoxide solution was transferred to a three-neck flask charged with a stirrer bar and a reflux condenser; the other half was kept warm. The first half of the solution was allowed to cool until solids began to appear, then 14.5 g of dry acetone mixed with 38.9 g of ethyl oxalate was added once and stirred. Heat was evolved, and the solution turned brown, but remained clear. As soon as turbidity appeared, the other half of the sodium ethoxide solution was added together with 38.9 g of ethyl oxalate and mixed in the flask. Initially, the solution was clear, and brown in colour, but, after stirring for 0.5h, it became solid. Around 30 mL of ethanol was distilled, and the flask was cooled to 20°C . The sodium salt was removed to a beaker, and

was treated with a mixture of 75 mL of concentrated hydrochloric acid and 200 g of crushed ice. After crushing all lumps, the creamy yellow suspension of acetonedioxalic ester was collected by vacuum filtration. The residue was removed from filter, stirred with about 25 mL of water, and filtered again. The ester was hydrolyzed by heating at 100°C in 50 mL of concentrated HCl for 20 h. After cooling to 20°C, the hydrated acid was vacuum filtered, and washed with two 10 mL portion of ice water and dried to yielded 16.41 g (35.6% yield) of desired product as off-white solid. ^1H NMR (200 MHz, DMSO- D_6) δ 6.9 (s, 1H). ^{13}C NMR (50 MHz, DMSO- D_6), δ 180, 161, 154, 118. ⁵⁸

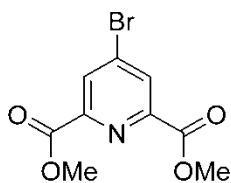
2.1.5 Synthesis of Chelidamic Acid (1,4-dihydro-4-oxo-2,6-pyridinedicarboxylic acid) (5)



Chelidonic acid (16.41 g) was dissolved in 28% aqueous ammonia solution, and heated to reflux for 5h with occasional addition of ammonium hydroxide. Progress of the reaction was monitored by analytical TLC. Once the reaction was completed, the mixture was neutralized with 37% HCl. The precipitate was filtered and washed with water. The precipitate was redissolved in 28% aqueous ammonium hydroxide, and heated to reflux for a second time 5h this was followed by acidification, filtration, washing, and drying to

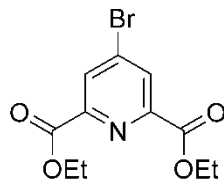
afford 15.31 g (0.0841 mol, 94.3% yield) of white solids. ^1H NMR (200 MHz, DMSO- D_6) δ 7.55 (s, 1H). ^{13}C NMR (50 MHz, DMSO- D_6) δ 167, 161, 149, 115.⁵⁹

2.1.6 Synthesis of Dimethyl-4-bromo-2,6-pyridinedicarboxylate (6a)



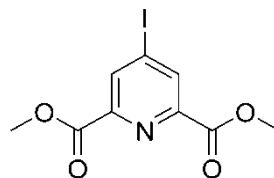
Phosphorous pentabromide (18 g, 42 mmol) and Chelidamic acid were charged into a round bottom flask equipped with magnetic stir bar. This mixture was subsequently fitted with a reflux condenser and heated to 90°C. The resulting melt was then stirred for 3h. The mixture was allowed to cool to room temperature and the residue was taken up in 600 mL of chloroform, and the resulting solution was filtered. The filtrate was cooled to 0°C, whereupon 90 mL of Methanol was added drop wise over a period of 1h. The solution was concentrated *in vacuo* to one third of the original volume then refrigerated overnight. The precipitate formed was collected via vacuum filtration and washed with cold methanol (5 mL \times 3) then with hexanes (5 mL). Yield of pure product was 82% (2.46 g). ^1H NMR (300 MHz, CDCl_3) δ 8.47 (s, 2H), 4.04 (s, 6H). ^{13}C NMR (75 MHz, CDCl_3) δ 164.08, 149.17, 135.19, 131.38, 53.56.⁶⁰

2.1.7 Synthesis of Diethyl-4-bromo-2,6-pyridinedicarboxylate (6b)



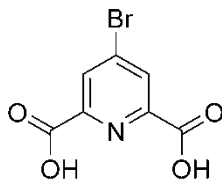
Chelidamic monohydrate (0.3170 g, 2.73 mmol) and phosphorus pentabromide (5.87 g, 13.6 mmol) were heated to 90°C, where solids formed a melt. This melt was stirred at 90°C for 2h. After the solution was cooled, 4 mL of chloroform was added and the crude product was filtered. The filtrate was cooled in a ice bath, while 6.5 mL ethanol was slowly added to the solution. The solvent was evaporated and crude compound was purified on silica gel column eluting with ethyl acetate and chloroform (1:20, v/v; $R_f = 0.31$). The pure product was obtained as a pale- white solid in 32% (0.26 g) yield. ^1H NMR (300 MHz, CDCl_3) δ 8.33 (s, 1H), 4.40 (q, 3H, J (Hz)= 7.1), 1.36 (t, 4H, J (Hz)= 7.1). ^{13}C NMR (75 MHz, CDCl_3) δ 163.32, 149.35, 134.71, 130.88, 62.53, 14.06. ⁶¹

2.1.8 Synthesis of Dimethyl 4-iodopyridine-2,6-dicarboxylate (7a)



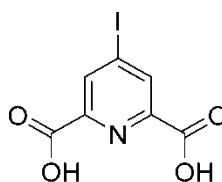
Acetyl chloride (0.4 mL, 5.4 mmol) was added to a mixture of bromo pyridine **6a** (0.5 g, 1.8 mmol) and sodium iodide (5.5 g, 36.5 mmol) in dry acetonitrile (12.5 mL) at 0°C. The reaction mixture was sonicated for 5h under N₂ atmosphere maintaining bath temperature below 50°C. After cooling to 0°C, saturated sodium carbonate solution (10 mL) and DCM (25 mL) were added. The aqueous layer was extracted with dichloromethane (2 × 10mL) and the combined organic layers were washed with saturated sodium thiosulphate (2 × 5 mL), water (2 × 10 mL), and dried over MgSO₄. The solvent was removed under reduced pressure. The crude product was recrystallized from hot MeOH and the desired compound was obtained in 71% (0.4137 g) yield. ¹H NMR (300 MHz, CDCl₃) δ 8.68 (s, 2H), 4.04 (s, 6H). ¹³C NMR (75 MHz, CDCl₃) δ 163.9, 148.4, 137.2, 107.0, 53.5. The Crystal structure of this compound was published in *Acta Crystallographica section E*.

2.1.9 Synthesis of 4-bromo-2,6-pyridinedicarboxylic acid (8a)



To a solution of diethyl-4-bromo-2,6-pyridinedicarboxylate (0.3768 g, 1.3 mmol) in 9 mL of THF was added a solution of lithium hydroxide (0.0759 g, 3.1 mmol) in 1 mL of water. This mixture was stirred for 3.5h, during which precipitate formed. Upon acidification to pH 0-1 with concentrated HCl, the precipitate dissolved. THF was removed *in vacuo*, and water was added to the residue to obtain desired product. The product was dried under high vacuum at 50°C and yielded 78% (0.3178 g) of pure product. ¹H NMR (300 MHz, DMSO- d₆) δ 11.16 (br, s, 2H), 8.87 (s, 1H), 8.72 (s, 1H).⁶¹

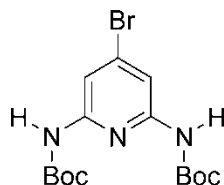
2.1.10 Synthesis of 4-iodo-pyridine-2,6-dicarboxylic acid (8b)



To a solution of dimethyl-4-iodo-2,6-pyridinedicarboxylate (0.6955 g, 2.2 mmol) in 16.5 mL of THF was added a solution of lithium hydroxide (0.1468 g, 5.4 mmol) in 1.8 mL of water. This mixture was stirred for 3.5h, during which a precipitate formed. Upon

acidification to pH 0-1 with concentrated HCl, the precipitate dissolved. THF was removed *in vacuo*, and water was added to residue to obtain desired product. The product was dried under high vacuum at 50°C and yielded 91% (0.5778 g) of pure product. ¹H NMR (300 MHz, DMSO- d₆) δ 8.52 (s, 2H), 3.33 (br, s, 2H). ¹³C NMR (75 MHz, DMSO- d₆) δ 164.50, 148.75, 135.88, 107.0, 108.68.⁶¹

2.1.11 Synthesis of 2,6-di-tert-butoxycarbonylamino-4-bromo-pyridine (9a)

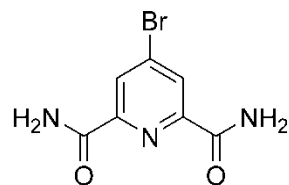


To a solution of 4-bromo-pyridine-2,6-dicarboxylic acid (0.32 g, 1.3 mmol) in benzene (3.5 mL) was added one drop of DMF and oxalyl chloride (1.0 mL, 11.8 mmol). The mixture was heated to reflux for 12h. The solvent was removed and the obtained diacid chloride was used without further purification.

A solution of the diacid chloride in 3 mL of dichloromethane was added to a mixture of tetrabutylammonium bromide (1 mg) saturated aqueous solution of sodium azide (6.4 M, 6 eq), and dichloromethane (1.5 mL) at -5°C over 10 min. The mixture was further stirred for 10 min at 0°C. The organic layer was separated. The aqueous layer was washed with cold dichloromethane (2x10 mL) and the combined organic fractions were washed with cold water (2x10 mL) and cold brine (1x10 mL). The solution was dried over MgSO₄ at 0°C for 10 min and filtered. The filtrate was dried with CaH at 0°C for 30 min and then

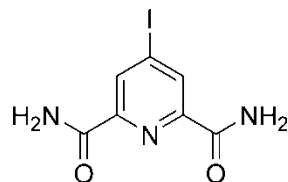
filtered through a pad of celite. To the filtrate was added dry tert butanol (3 mL) and the mixture was heated to reflux for 24h. The solution was cooled to room temperature and solvent was removed *in vacuo*. The crude product was purified on silica gel column eluting with EtOAc: Hexanes = 1:20 to 1:10. Yield of mixture of product was 16% (0.0779 g). ^1H NMR (200 MHz, Acetone- d_6) δ 8.74 (br, s, 2H), 7.84 (s, 1H), 7.67 (s, 1H), 1.49 (s, 18H).⁵⁵

2.1.12 Synthesis of 4-bromopyridine-2,6-dicarboxamide (10a)



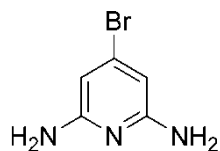
4-bromopyridine-2,6-bisdimethylester [**6a**; 0.1761 g (0.64 mmol)] was dissolved in a minimum volume of hot MeOH. A stream of ammonia gas was slowly bubbled through the solution and the reaction progress was monitored by analytical TLC (eluting solvent system Hexanes: EtOAc = 1:1, R_f = 0.38) until all the starting material was consumed. 0.0931 g (0.38 mmol) of yield was obtained. ^1H NMR (300 MHz, DMSO- d_6) δ 8.87 (s, 2H), 8.48 (s, 2H), 7.80 (s, 2H).⁶⁰

2.1.13 Synthesis of 4-iodopyridine-2,6-dicarboxamide (10b)



4-iodopyridine-2,6-bisdimethylester [**7a**; 1.0645 g (3.3 mmol)] was dissolved in a minimum volume of hot MeOH. A stream of ammonia gas was slowly bubbled through the solution and the reaction progress was monitored by analytical TLC (eluting solvent system Hexanes: EtOAc = 1:1, R_f = 0.38) until all starting material was consumed. Quantitative yield (0.9650 g, 3.3 mmol) was obtained. ^1H NMR (300 MHz, DMSO- d_6) δ 8.88 (s, 2H), 8.48 (s, 2H), 7.81 (s, 2H). ^{13}C NMR (75 MHz, DMSO- d_6) δ 164.07, 149.34, 132.83, 109.23.⁶⁰

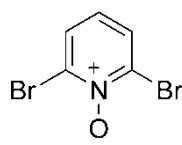
2.1.14 Synthesis of 4-bromo-2,6-diaminopyridine (11)



A mixture of 1.3216 g (6.5 mmol) of 4-bromo-1-oxypyridine-2,6-diamine (**15**) and 0.4592 g (8.2 mmol) of iron powder in 13 mL of Acetic acid : water (1:1) solution was stirred at 100°C for 2h. The mixture was cooled to room temperature, diluted with 30 mL

of EtOAc, and neutralized with 28% sodium hydroxide solution. To remove solids, the solution was filtered over a pad of silica gel. The aqueous layer was extracted with 5×10 mL of EtOAc. The combined organic layers were washed with brine (3×25 mL), dried over MgSO_4 , and filtered. The solvent was evaporated to yield crude material. This crude solid was dissolved in dichloromethane and the same volume of 28% Sodium hydroxide was added, and the resultant two layers were left in the refrigerator for 3 days. After 3 days, the aqueous layer was extracted with dichloromethane. The combined organic layers were washed with brine, dried over MgSO_4 , and filtered. The solvent was evaporated. The solid crude product was sublimed at $40^\circ\text{C}/0.15$ torr to yield 0.9185 g (75%) of desired product as a white to pale-white solid. ^1H NMR (300 MHz, CDCl_3) δ 6.06 (s, 2H), 4.26 (br, s, 4H). ^{13}C NMR (100 MHz, CDCl_3) δ 158.27, 134.59, 100.79.

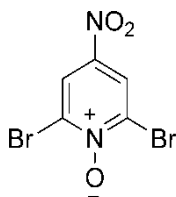
2.1.15 Synthesis of 2,6-dibromopyridine-1-oxide (12)



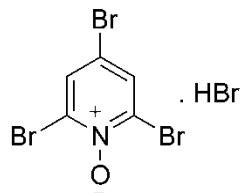
To a solution of 20 g (84 mmol) of 2,6-dibromopyridine in 100 mL of trifluoroacetic acid was added 22 mL of aqueous hydrogen peroxide (33%, 212 mmol) over 1h. The mixture was heated to $95\text{-}100^\circ\text{C}$ for 4h. The progress of the reaction was monitored by analytical TLC. The mixture that contained small amount of starting material was cooled to room temperature and diluted with 50 mL of water, whereupon the starting material formed a

white precipitate, which was filtered. The product was extracted from the aqueous phase with 5 x 200 mL portions of dichloromethane. To remove all acid, the organic phase was washed with 3 x 50 mL of 0.5 M potassium carbonate solution. Dichloromethane was evaporated under addition of Hexanes at atmospheric pressure and the suspension was filtered on a Buchner funnel, yielding 1.9 g (75%) of product as diamond shaped white crystals. ^1H NMR (300 MHz, CDCl_3) δ 7.66 (d, 2H, J (Hz) = 8.1), 6.94 (t, 1H, J (Hz) = 8.1). ^{13}C NMR (100 MHz, CDCl_3) δ 133.69, 129.64, 124.97.⁶⁴

2.1.16 Synthesis of 2,6-dibromo-4-nitropyridine-1-oxide (13)

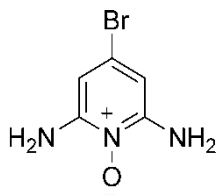


To a mixture of 52.8 mL of concentrated sulphuric acid and 28.4 mL of concentrated nitric acid was added all at once 15.9 g (63.4 mmol) of 2,6-dibromopyridine-1-oxide, and the mixture was stirred for 20h at 60°C. After completion of the reaction, which was monitored by analytical TLC (EtOAc: Hexane = 1: 10 (v/v); R_f = 0.66), the mixture was neutralized with 28% ammonium hydroxide and ice. The precipitate was filtered and dried to yield 14.8 g (77.6%) of product as a white powder. ^1H NMR (300 MHz, CDCl_3) δ 8.54 (s). ^{13}C NMR (75 MHz, CDCl_3) δ 140.25, 134.02, 123.59.⁶⁴

2.1.17 Synthesis of 2,4,6-tribromopyridine-1-oxide hydrobromide (14)

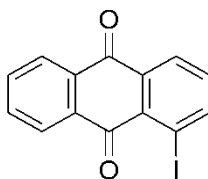
A suspension of 3.0g (10.1 mmol) of 2,6-dibromo-4-nitropyridine-1-oxide in 30 mL of acetic acid was warmed to 60°C, and 0.6 mL (8.1 mmol) of acetyl bromide was added. The mixture was stirred at 80°C for 2h. An additional 0.6 mL of acetyl bromide was added and stirred for 5h. The progress of the reaction was monitored by analytical TLC (EtOAc: Hexane = 1: 10 (v/v); R_f = 0.51). After completion of the reaction, the mixture was cooled to 15°C and the product was isolated by filtration. The precipitate was washed with diethyl ether (3 × 10 ml) and dried to yield 3.2664 g (78%) of the hydrobromide of the product as a light-yellow colour solid. ^1H NMR (300 MHz, DMSO- d_6) δ 8.30 (s). ^{13}C NMR (75 MHz, DMSO- d_6) δ 133.28, 132.04, 116.40. ⁶⁴

2.1.18 Synthesis of 4-bromo-1-oxypyridine-2,6-diamine (15)



A suspension of 0.40 g (10 mmol) of 2,4,6-tribromopyridine-1-oxide hydrobromide in 5.9 mL of 28% aqueous ammonia solution was placed in an Acid Digestion Bomb (Parr instrument). This bomb was heated in an oven at 220°C for 8h. After cooling to room temperature, the slurry was filtered on a Buchner funnel, washed with ice water (3 x 5 mL), and dried to yield 0.18 g (86% yield) of the desired product as a pale-white needles. ¹H NMR (300 MHz, DMSO- d₆) δ 6.78 (s, 4H), 6.11 (s, 2H). ¹³C NMR (75 MHz, DMSO- d₆) δ 150.03, 119.87, 96.58.

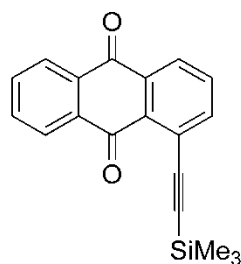
2.1.19 Synthesis of 1-iodoanthraquinone (16)



1-aminoanthraquinone (1.0 g) was dissolved in 7.4 g of concentrated sulphuric acid. To this solution, 0.4 g of sodium nitrite was added slowly over one hour. The mixture was

stirred during the addition of the sodium nitrite and for an additional two-hour period, then poured slowly into 50mL of ice water with continuous stirring and stirred for one-hour. Next, the solution was filtered and to the filtrate, 0.5 g of potassium iodide was added; the mixture was allowed to stand at room temperature for three hours and heated for reflux for one hour. After adding 10 mL of sodium bisulfite solution, the mixture was filtered, and the residue was washed with distilled water and dried *in vacuo* at 40°C. The crude product was purified by recrystallizing it twice from nitrobenzene yielded 0.2709 g of (18 %) brown solid. $^1\text{H NMR}$ (CDCl_3 , 300MHz) δ 8.46-8.26 (m, 4H), 7.86-7.77(m, 2H), 7.41(t, 1H, J (Hz) = 7.78). MS (EI, 70eV): m/z Calcd 333.95 $[\text{M}]^+$; found 333.9; relative peak intensity 100%.⁶⁵ $^1\text{H NMR}$ data is consistent with previously reported synthesis by Ma *et.al.*⁶⁶

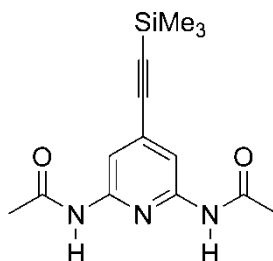
2.1.20 Synthesis of 1-(trimethylsilylacetylenyl)anthraquinone (17)



The mixture of 1-iodoanthraquinone (0.2709 g, 0.81 mmol), trimethylsilylacetylene (0.14 mL, 0.97 mmol), $\text{Pd}(\text{PPh}_3)_2\text{Cl}_2$ (0.1138 g, 20% mol), Copper iodide (0.0309 g, 20% mol), and triphenylphosphene (0.0043 g, 2% mol) in diisopropylethylamine (2 mL) and THF (2 mL) was heated at 40°C overnight, while protecting the flask from light. The

solvent was evaporated and the dark solid was dissolved in dichloromethane. The organic layer was extracted with saturated ammonium chloride (10 mL), water (2x 10 mL), and brine (10 mL). Drying of the solution over MgSO_4 followed by evaporation gave a solid, which was purified by flash chromatography (silica, Hexanes : EtOAc = 20:1) to afford the desired product as a bright yellow solid (0.1763 g, 72%). ^1H NMR (300 MHz, CDCl_3) δ 8.36- 8.24 (m, 3H), 7.94 (d, 1H, J (Hz) = 7.73), 7.84-7.76 (m, 3H), 0.37 (s, 9H). MS (EI, 70 eV): m/z Calcd 304.09 $[\text{M}]^+$; found 304.1; relative peak intensity 55%. ^1H NMR data is consistent with previously reported synthesis by Ma *et.al.*⁶⁶

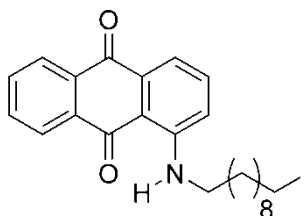
2.1.21 Synthesis of 2,6-diacetylamino-4-[(trimethylsilyl)ethynyl]pyridine (18)



Dry triethylamine (10 mL), dry THF (1.5 mL) and DMF (0.25 mL) were added to a Schlenk flask and the solution was degassed by one “freeze-pump-thaw” cycle. 4-bromo-2,6-diacetylamino-pyridine (0.0976 g, 0.36 mmol), $[\text{Pd}(\text{PPh}_3)_4]$ (0.0462g, 0.04 mmol), and copper iodide (0.0152 g, 0.08 mmol) were added and the resulting mixture was degassed for the second time. Trimethylsilyl acetylene (0.5 mL, 3.6 mmol) was then added and the reaction mixture was degassed one final time then the mixture was stirred at 85°C for overnight. The resulting dark mixture was filtered over celite and washed with toluene (5

mL), dichloromethane (10 mL), and MeOH (10 mL). Removal of the solvent under vacuum and purification of the crude by silica gel column chromatography (cyclohexane : EtOAc = 1:1) yielded the desired compound (0.0788 g, 64%) contaminated with PPh₃O. ¹H NMR (300 MHz, CDCl₃) δ 7.93 (br, s, 2H), 7.76 (br, s, 2H), 2.18 (s, 6H), 0.24 (s, 9H). ¹³C NMR (75 MHz, CDCl₃) δ 168.48, 149.48, 135.88, 111.90, 102.40, 99.92, 24.81, -0.25.⁵⁶

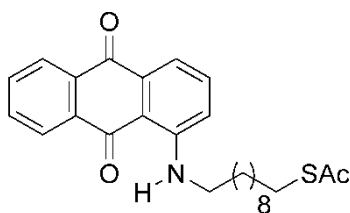
2.1.22 Synthesis of 1-(10-iododecylamino)anthracene-9,10-dione (20)



1-aminoanthraquinone (0.087g, 0.39 mmol) and 1,10-diiiododecane (0.614g, 1.56 mmol) were refluxed in 3 mL of acetonitrile for 5 days. The solution was concentrated under reduced pressure and purified by silica gel chromatography (hexanes: EtOAc=10:1, R_f = 0.36) to give the desired product (0.045g, 24% yield) as a maroon powder; mp 85-86°C. ¹H NMR (300 MHz, CDCl₃) δ 9.72 (s, 1H), 8.35 – 8.14 (m, 2H), 7.74 (td, 1H, *J* = 1.6, 7.5), 7.67 (td, 1H, *J* (Hz) = 1.5, 7.4), 7.62- 7.47 (m, 2H), 7.03 (dd, 1H, *J* (Hz) = 1.4,8.2), 3.30 (dd, 2H, *J* (Hz) = 6.9, 12.3), 3.16 (t, 2H, *J* (Hz) = 7.0), 1.88 – 1.66 (m, 4H), 1.60 – 1.12 (m, 15H). ¹³C NMR (75 MHz, CDCl₃) δ 184.93, 183.86, 151.80, 135.26, 135.05, 134.64, 133.91, 133.02, 132.85, 126.69, 126.62, 117.88, 115.50, 112.79, 42.97, 33.51,

30.47, 29.38, 29.32, 29.28, 29.08, 28.49, 27.14, 7.33. Anal. Calcd (%) for $C_{24}H_{28}INO_2$ (489.12): C, 58.9; H, 5.77; N, 2.86; found: C, 57.78; H, 6.44; N, 2.57. ESI-MS m/z : $[M+Na]^+$ Calcd 512.11; found 511.81; relative peak intensity 16.7%. IR (KBr) ν cm^{-1} 3419 (br), 3294 (w), 2930 (s), 2852 (s), 1664 (w), 1630 (s), 1592 (s), 1504 (w), 1269 (s), 1071 (w). UV/ VIS (THF) λ_{max} (ϵ) = 243 (35100), 272 (9600), 314 (5700), 504 (5700).⁶⁷

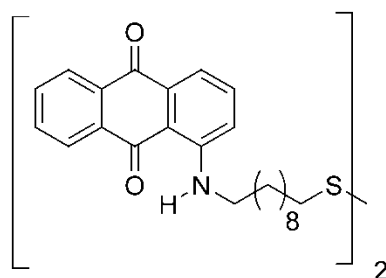
2.1.23 Synthesis of *S*-10-(9,10-dioxo-9,10-dihydroanthracen-1-ylamino)decyl ethanethioate (21)



Both compound **20** (0.024g, 0.049 mmol) and potassium thioacetate (0.027g, 0.24 mmol) were mixed in acetonitrile (24 mL) and refluxed for 6h under N_2 atmosphere. The acetonitrile was distilled off under reduced pressure and the residue was suspended in CH_2Cl_2 and filtered. The organic phase was concentrated under reduced pressure and purified by silica gel chromatography (Hexane:EtOAc=15:1, R_f = 0.19) to give the desired product (0.016g; 75% yield) as a red solid; mp 90-91°C. 1H NMR (300 MHz, $CDCl_3$) δ 9.73 (s, 1H), 8.32 – 8.13 (m, 2H), 7.73 (td, 1H, J (Hz) = 1.6, 7.5), 7.68 (td, 1H, J (Hz) = 1.6, 7.4), 7.61 – 7.45 (m, 2H), 7.04 (dd, 1H, J (Hz) = 1.5, 8.2), 3.39- 3.29 (m, 2H), 2.87 – 2.80 (t, 2H, J (Hz) = 7.4), 2.30 (s, 3H), 1.80 – 1.66 (m, 2H), 1.60 – 1.12 (m, 17H). ^{13}C NMR (75 MHz, $CDCl_3$) δ 196.08, 184.94, 183.89, 151.82, 135.26, 135.06,

134.64, 133.91, 133.02, 132.85, 126.69, 126.63, 117.90, 115.50, 112.79, 42.98, 30.64, 29.47, 29.40, 29.37, 29.29, 29.12, 29.09, 29.06, 28.78, 27.14. Anal. Calcd (%) for $C_{26}H_{31}NO_3S$ (437.20): C, 71.36; H, 7.14; N, 3.20; found: C, 70.85; H, 7.39; N, 2.84. ESI-MS m/z : $[M+Na]^+$ calcd 460.19; found 459.97; relative peak intensity 70%. IR (KBr) ν cm^{-1} 3419 (br), 3262 (w), 2923 (s), 2853 (s), 1690 (w), 1630 (s), 1594 (s), 1511 (w), 1270 (s), 1070 (w). UV/ VIS (THF) λ_{max} (ϵ) = 243 (39400), 272 (9600), 314 (5700), 504 (5700).⁶⁷

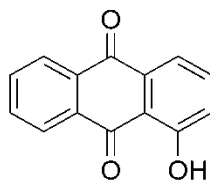
2.1.24 Synthesis of 1-(10-(2-(10-(9,10-dioxo-9,10-dihydroanthracen-1-ylamino)decyl)disulfanyl)decylamino)anthracene-9,10-dione (22)



Reagent grade acetone (2 mL) and 3 M NaOH (2 mL) were placed in a flame dried 25 mL flask that was then deoxygenated with N_2 gas purge for 20 minutes at $0^\circ C$. Under positive N_2 pressure, compound **21** (0.1g, 0.23 mmol) was added and stirred for 5 days at room temperature. 1 M HCl was added drop wise to neutralize the solution to pH 7 and the aqueous fraction was extracted three times with EtOAc. The combined organic extracts were washed with brine (10 mL), dried over $MgSO_4$ and solvent evaporated under reduced pressure. The remaining residue was purified by silica gel chromatography

(Hexane:THF= 1:1, R_f = 0.33) to give the desired product (0.086g; 48% yield) as a maroon powder; mp 115-116°C. ^1H NMR (300 MHz, CDCl_3) δ 9.72 (s, 1H), 8.28 (dd, 1H, J (Hz) = 1.4, 7.6), 8.24 (dd, 1H, J (Hz) = 1.4, 7.5), 7.79 – 7.61 (m, 2H), 7.61 – 7.44 (m, 2H), 7.03 (dd, 1H J (Hz) = 1.5, 8.2), 3.30 (dd, 2H, J (Hz) = 7.0, 12.2), 2.71 – 2.59 (t, 2H, J (Hz) = 7.4), 1.83- 1.62 (m, 2H), 1.54 – 1.16 (m, 19H). ^{13}C NMR (101 MHz, CDCl_3) δ 184.94, 183.84, 151.79, 135.25, 135.06, 134.65, 133.90, 133.03, 132.85, 126.70, 126.62, 117.88, 115.52, 112.83, 43.01, 39.18, 29.43, 29.42, 29.32, 29.19, 29.10, 28.49, 27.16. Anal. Calcd (%) for $\text{C}_{48}\text{H}_{56}\text{NO}_4\text{S}_2$ (788.37): C, 73.06; H, 7.15; N, 3.55; found: C, 72.14; H, 7.59; N, 3.35. ESI-MS m/z : $[\text{M}+\text{H}]^+$ calcd 789.38; found 789.04; relative peak intensity 11%. IR (KBr) ν cm^{-1} 3419 (br), 3275 (w), 2928 (s), 2852 (s), 1663 (s), 1629 (s), 1590 (s), 1507 (s), 1269 (s), 1071 (w). UV/ VIS (THF) λ_{max} (ϵ) = 243 (75500), 272 (19900), 316 (12000), 504 (12600).⁶⁸

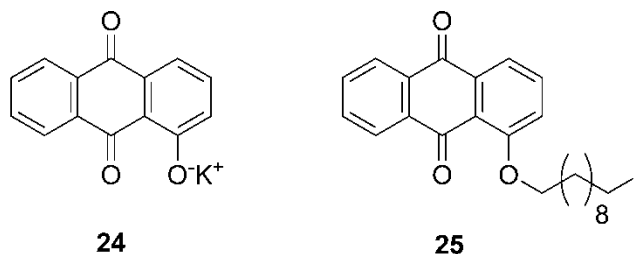
2.1.25 Synthesis of 1-hydroxy-9,10-anthraquinone (23)



1-Aminoanthraquinone (3.0007 g, 13.4 mmol) was dissolved in 98% H_2SO_4 (45 mL) at 70°C then cooled to 0°C. To this solution, Sodium nitrite (1.6500g, 23.9 mmol) was added portion wise with stirring, and the resulting mixture was warmed to room temperature. The stirring was continued for 3.5h at room temperature, and then poured

into ice (150 g). The resulting solution of Diazonium hydrogensulfate was heated to reflux for 1h during which an orange- yellow precipitate formed. After cooling to room temperature, the precipitate was collected by vacuum filtration, washed with water, and dried. The crude was purified by sublimation at 100°C/ 0.1 torr. Recrystallization from heptane-toluene (v/v: 1:10) afforded 1.2478 g (42%) of the desired product as yellow solid. ¹H NMR (CDCl₃, 300MHz) δ 12.64 (s, 1H), 8.33(td, 2H, *J* (Hz) =3.71, 5.68, 5.68), 7.89- 7.80(m, 3H), 7.70(t, 1H, *J* (Hz) =7.95), 7.33(d, 1H, *J* (Hz) =8.4). ¹³C NMR (CDCl₃, 75Hz) δ 116.22, 119.63, 124.43, 126.99, 127.5, 133.27, 133.51, 133.69, 134.25, 134.25, 136.82, 162.63, 182.43, 188.74.^{69,70}

2.1.26 Synthesis of Potassium salt of 1-hydroxyanthraquinone (24) and Synthesis of 1-(10-iodododecanoyl)-anthraquinone (25)

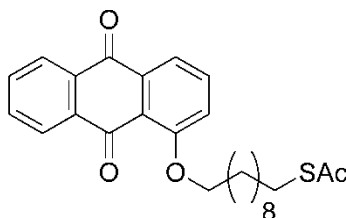


1-Hydroxyanthraquinone (0.5491 g, 2.5 mmol) and DMF (65 mL) were stirred in a 250 mL round bottom flask while heating at 60°C to dissolve the anthraquinone. Potassium *tert*-butoxide (0.3301 g, 2.9 mmol) was added to the reaction mixture over 30 min. The reaction mixture was allowed to cool for 1h and transferred to a freezer (-20°C). The

resulting precipitate was filtered and vacuum dried at 75°C for 12h. The Potassium salt of 1-hydroxyanthraquinone (a blackish-purple, 0.6117 g, 93%) was used without further purification. The compound was not characterized.⁷¹

The potassium salt of 1-hydroxyanthraquinone (0.0500 g, 0.19 mmol), 1,10-diiododecane (0.9061 g, 2.3 mmol) and 18-crown-6-ether (0.0503 g, 0.19 mmol) were heated at 100°C for 60h. The reaction mixture was allowed to cool. The CHCl₃ (15 mL) and 3M HCl (15 mL) were added, and the organic layer was extracted with brine (3x 15 mL), dried over MgSO₄, and filtered. The solvent was evaporated, and crude was purified by column chromatography (silica, Hexanes: EtOAc= 40:1 to 20:1) to yield the title compound **24** as a yellow solid (0.0716 g, 76%); mp 76-77°C. ¹H NMR (CDCl₃, 300 MHz) δ 8.25 (ddd, 2H, *J* (Hz) = 1.45, 7.67, 8.68), 7.94 (d, 1H, *J* (Hz) = 7.68), 7.82-7.64 (m, 3H) 7.33 (d, 1H, *J* (Hz) = 8.45) 4.16 (t, 2H, *J* (Hz) = 6.63), 3.18 (t, 2H, *J* (Hz) = 7.03), 2.03-1.89 (m, 2H), 1.88-1.75 (m, 2H), 1.69-1.51 (m, 2H), 1.48-1.22 (m, 12H). ¹³C NMR (101 MHz, CDCl₃) δ 183.64, 182.26, 160.05, 135.72, 135.11, 134.90, 134.24, 133.15, 132.52, 127.25, 126.57, 121.59, 119.60, 119.13, 69.71, 33.59, 30.55, 29.45, 29.39, 29.33, 29.16, 28.57, 25.96, 7.47. UV/ VIS (THF) λ_{max} (ε) = 255 (5400), 318 (750), 378 (1300). IR (KBr) ν cm⁻¹ 2923 (s), 2847 (s), 1665 (s), 1582 (s), 1263 (s), 712 (s). Anal. Calcd (%) for C₂₄H₂₇IO₃ (788.37): C, 58.78; H, 5.55; found: C, 61.08; H, 6.43. MS (CI) *m/z*: [M+H]⁺ calcd 491.1; found 490.97; relative peak intensity 100%.⁷²

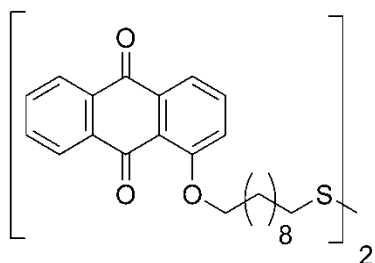
2.1.27 Synthesis of *S*-10-(9,10-dioxo-9,10-dihydroanthracen-1-yloxy)decyl ethanethioate (26)



A mixture of compound **25** (0.0427 g, 0.0871 mmol) and potassium thioacetate (0.0696 g, 0.6095 mmol) in dry acetonitrile (45 mL) was heated to reflux for 6h under N₂. After cooling to ambient temperature, the solvent was distilled under reduced pressure, and the residue was suspended in dichloromethane and filtered. The organic solvent was concentrated *in vacuo* and the crude product was purified by column chromatography (silica, Hexanes:EtOAc = 10:1; R_f = 0.42) to yield the title compound as a brownish-yellow solid (0.0244 g, 64%); mp 88-90°C. ¹H NMR (300 MHz, CDCl₃) δ 8.26 (ddd, 2H, *J* (Hz) = 1.51, 7.69, 8.78), 7.94 (dd, 1H, *J* (Hz) = 1.00, 7.68), 7.83-7.65 (m, 3H), 7.33 (d, 1H, *J* (Hz) = 8.45), 4.17 (t, 2H, *J* (Hz) = 6.66), 2.86 (t, 2H, *J* (Hz) = 7.32, 7.32), 2.32 (s, 3H), 2.04-1.90 (m, 2H), 1.66-1.50 (m, 5H), 1.48-1.23 (m, 12H). ¹³C NMR (101 MHz, CDCl₃) δ 196.09, 183.64, 182.25, 160.05, 135.71, 135.11, 134.86, 134.20, 133.11, 132.51, 127.23, 126.54, 121.61, 119.58, 119.15, 69.71, 29.72, 29.51, 29.45, 29.41, 29.31, 29.17, 29.13, 29.11, 28.83, 25.93. UV/ VIS (THF) λ_{max} (ε) = 255 (6100), 318 (750), 378 (1300). IR (KBr) ν cm⁻¹ 2920 (s), 2847 (s), 1688 (s), 1675 (s), 1582 (s), 1316 (s), 1266 (s), 708 (s). Anal. Calcd (%) for C₂₆H₃₀O₄S (438.19): C, 71.2; H, 6.89; found: C, 70.56;

H, 6.76. MS (CI) m/z : $[M+H]^+$ calcd 439.02; found 439.04; relative peak intensity 100%.⁶⁷

2.1.28 Synthesis of 1-(9-(2-(10-(9,10-dioxo-9,10-dihydroanthracen-1-yloxy)decyl)disulfanyl)nonyloxy)anthracene-9,10-dione (27)



THF (5 mL), and 3M NaOH (3 mL) in a 25 mL flame dried round bottom flask were deoxygenated with N₂ for 20 min at 0°C. Under positive N₂ pressure compound **26** (0.05 g, 0.114 mmol) was added. This reaction mixture was stirred at room temperature, until all the starting material was consumed. A solution of 1M HCl was added dropwise to neutralize the mixture. The aqueous phase was extracted with CHCl₃ (3x 10 mL), and the combined organic phases were washed with brine (30 mL), dried over MgSO₄, filtered, and the solution was concentrated *in vacuo*. The residue was dissolved in a minimum volume of CHCl₃, EtO₂ was added, and transferred to a freezer (-20°C). The resultant precipitate was filtered to afford the title compound as a light-yellow granules (0.0356 g, 40%); mp 124-126°C. ¹H NMR (300 MHz, CDCl₃) δ 8.26 (ddd, 2H, J 9Hz) = 1.59, 7.71, 9.03), 7.95 (dd, 1H, J (Hz) = 1.00, 7.68), 7.83-7.65 (m, 3H), 7.34 (d, 1H, J (Hz) = 7.59), 4.17 (t, 2H, J (Hz) = 6.65), 2.69 (t, 2H, J (Hz) = 7.32), 2.05-1.90 (m, 2H), 1.77-1.52 (m,

6H), 1.50-1.25 (m, 14H). ^{13}C NMR (101 MHz, CDCl_3) δ 183.71, 182.31, 160.13, 135.81, 135.20, 134.93, 134.19, 133.19, 132.60, 127.31, 126.63, 121.72, 119.67, 119.23, 69.81, 39.29, 29.79, 29.54, 29.41, 29.32, 29.23, 29.13, 28.63, 26.03. Anal. Calcd (%) for $\text{C}_{48}\text{H}_{54}\text{O}_6\text{S}_2$ (791.07): C, 72.88; H, 6.88; found: C, 72.67; H, 6.71. ESI-MS m/z : $[\text{M}+\text{Na}]^+$ calcd 813.33; found 813.15; relative peak intensity 55%. UV/ VIS (THF) λ_{max} (ϵ) = 255 (17100), 318 (2600), 380 (4600). IR (KBr) ν cm^{-1} 2923 (s), 2850 (s), 1675 (s), 1675 (s), 1582 (s), 1319 (s), 1266 (s), 708 (s).⁶⁸

2.2 Electrochemistry

2.2.1 Buffer and Electrolyte solution preparation

Buffer and aqueous electrolyte solutions were prepared with deionised water purified to a resistivity of $18.2 \text{ M}\Omega\text{cm}^{-1}$ with Mili-Q[®] water from Millipore water purification system. Protocols from CRC book of Chemistry and Physics⁷³ were followed to prepare buffer solutions from 1.5 to 13.5 at constant ionic strength. For solution electrochemistry, organic solvents from the MBRAUN[®] solvent purification system were used and the concentration ratio of analyte to supporting electrolyte was 1: 100. However, the actual electrolyte used will be documented in appropriate sections.

Table 1 Composition of Buffer Solution for various pHs.

pH	Compositions of Buffer Solutions	
1.66	25 ml of 0.2 molar KCl	+ 20.7 ml of 0.2 molar HCl
3.34	50 ml of 0.1 molar Potassium hydrogen phthalate	+ 8.2 ml of 0.1 molar HCl
5.5	50 ml of 0.1 molar Potassium hydrogen phthalate	+ 36.6 ml of 0.1 molar NaOH
7.51	50 ml of 0.1 molar Potassium dihydrogen phosphate	+ 40.9 ml of 0.1 molar NaOH
9.52	50 ml of 0.025 molar Borax	+ 8.8 ml of 0.1 molar NaOH
11.61	50 ml of 0.05 molar Disodium hydrogen phosphate	+ 11.1 ml of 0.1 molar NaOH
13.18	25 ml of 0.2 molar KCl	+ 66 ml of 0.2 molar NaOH

Final volume of mixtures = 100 ml.

2.2.2 Instrument and Method

The electrochemical experiments were performed using the potentiostat (Autolab PGSTAT 302) controlled by a PC and FRA/GPES 4.9 software package. Voltammetric experiments were conducted at different scan rates using an analog triangle waveform generator (Autolab PG 302, Scangen module). Electrochemical Impedance Spectroscopy experiments were carried out using the same instrument with different dc potential, different sweeping frequencies, and 10 mV ac excitation signal and 10 data points per decade of frequencies were collected.

The measurements were done at different temperatures (nominal values 5°C, 15°C, 25°C, 35°C) regulated by circulating water bath (Lauda, Ecoline Refrigerating Circulator RE-200 series). All experimental temperatures were reported as an internal solution temperature. A conventional three-electrode system was employed to study electrochemistry of the SAMs and solution. All compound **22** (1-AminoAQdisulfide) electrochemical studies were carried out in a custom- built glass cell consisting of a SAM modified Au bead as a working electrode (WE), a Pt mesh auxiliary/counter electrode (CE), and a custom-built Ag/AgCl/KCl_{3M} electrode isolated by a Vycor tip as a reference electrode (RE). The electrochemical studies of compound **27** (1-OxyAQdisulfide) were performed in glass cell vial purchased from Bioanalytical System Inc., BASi, West Lafayette, IN with a SAM modified Au disk working electrode (BASi), a Pt counter electrode (BASi), and a Ag/AgCl,NaCl_{3M} reference electrode (BASi). All solution-based electrochemistry was carried out in one of the same set ups described above, and unmodified clean gold bead was used as a WE. All potentials were reported against the above mentioned reference electrodes. The electrolyte solution was bubbled with Ar for 30 min prior to the each experiment to reduce the oxygen level, and a blanket of Ar was continuously maintained throughout each experiment. The Ohmic resistance of the solution was calculated from high frequency intercept of the Nyquist plot, and the value was fed into the GPES software for iR compensation during each measurement. The Counter electrode was always cleaned immediately prior to each experiment by flaming it in a butane flame and quenched in Mili-Q[®] water. These two steps were repeated for 5 min. Au wire (99.99%), Pt mesh and Ag wire (99.99%) were purchased from Alfa Aesar for preparation of electrodes.

2.2.3 Preparation of electrodes and Self Assembled Monolayer (SAM) Deposition on Au Electrodes

Two types of Au electrodes (Au bead and Au disk) were used to prepare SAMs of two types (compounds **22** and **27**) of compounds.

For the compound **22** SAMs preparation, a polycrystalline Au bead (3.5 mm diameter) was used. It was prepared by annealing the tip of gold wire in a butane flame. This bead was etched in aqua regia (HNO_3 : HCl = 1:3), flame annealed, and then quenched in Mili-Q[®] water. The flame annealing and quenching in Mili-Q[®] water were repeated several times. The deposition of monolayer of compound **22** on Au electrode was carried out by incubating freshly cleaned Au electrode in 1 mM solution of compound **22** in dry THF for 24h. The electrode was then rinsed with copious amount of dry THF and Mili-Q water to remove any weakly adsorbed organic matter. These modified electrodes were used immediately for measurements.

The cleaning of electrode and monolayer deposition method for used gold bead electrodes is described in the following section.

Au bead electrode was annealed in a butane flame, etched in aqua regia, flame annealed, quenched in Mili-Q[®] water, flame annealed, and quenched again in Mili-Q[®] water. The last two steps were repeated several times until a shiny surface of the gold ball was seen. Finally, the bead was dried in Ar, and immersed in compound **22** solution for 24h. After the required incubation was completed, the electrode was rinsed thoroughly with THF followed by Mili-Q[®] water to remove any weakly adsorbed material. The modified electrode was immediately used for experiments.

For the compound **27** SAMs preparation, Au disk electrodes purchased from Bioanalytical System Inc., USA were used. This electrode has geometrical diameter 1.6 mm. A Buehler MiniMet 1000 grinder/ Polisher was used for polishing the disk electrodes. New electrodes were cleaned by sequential mechanical polishing to a mirror surface on a polishing pad (Buehler, Microcloth) with diamond suspension (MetaDi diamond suspension, Buehler) of decreasing particle size (1 micron to 0.05 micron). After 5-10 min, the electrode was removed and rinsed extensively with ethanol and water. After polishing, the electrode was sonicated in ethanol for 1-2 min to remove any residual abrasive particles, rinsed again with ethanol from the squeeze bottle, and shook off any remaining ethanol. Next, the electrode was electrochemically polished by running 25 successive CV scans from -0.2 V to +1.5 V vs. Ag/AgCl/NaCl_{3M} in 0.1 M H₂SO₄ at 0.1 V·s⁻¹. The electrochemical stripping was carried out by running 10 scans of CV between 0.75 V and 0.2 V in the same solution and at the same sweep rate. The electrode was then washed thoroughly with Mili-Q water followed by ethanol, and dried in Ar. The final step of the cleaning is chemical reduction of Au oxide, which was done by static incubation of the electrode in absolute ethanol for 20 min. Then, it was dried in Ar and used immediately for SAM preparation. Compound **27** on Au electrode was prepared by incubating freshly cleaned Au electrode in 1 mM solution of compound **27** in dry THF and ethanol solution (v/v = 5:1) for 24h. The electrode was then rinsed with copious amount of dry THF and Mili-Q water to remove any weakly physisorped organic matter. This modified electrode was used immediately for measurements.

The cleaning of electrode and monolayer deposition method for used gold disk electrodes is described in the following section.

First, to remove all adsorbate from previous experiment, 200 scans of CV from -0.5 V to -1.5 V *vs.* Ag/AgCl/NaCl_{3M} at sweep rate of 1Vs⁻¹ were run in 0.1 M NaOH solution while bubbling with Ar. The electrode was cleaned by sequential mechanical polishing to a mirror surface on a polishing pad with diamond suspension of decreasing particle size (1 micron to 0.05 micron) for 5-10 min. The electrode was removed and rinsed extensively with ethanol and water. Now, the electrode was sonicated in ethanol for 1-2 min to remove any residual abrasive particles, rinsed again with ethanol from the squeeze bottle, and shook off any remaining ethanol. Next, electrode was electrochemically polished by running a 25 successive scans of CV from -0.2 V to +1.5 V *vs.* Ag/AgCl/NaCl_{3M}, in 0.1 M H₂SO₄ at 0.1 Vs⁻¹. The electrochemical stripping was carried-out by running 10 scans of CV between 0.75 V and 0.2 V in the same solution and at the same sweep rate. The electrode was then washed thoroughly with Mili-Q[®] water followed by ethanol, and dried in Ar. Final step of the cleaning is chemical reduction of Au oxide, which was done by static incubation of electrode in absolute ethanol for 20 min. Then, it was dried in Ar and used immediately for SAM preparation. The clean electrode was immersed in the solution of compound **27** for 24h. After the required incubation was completed, the electrode was rinsed thoroughly with Mili-Q[®] water followed by THF to remove any weakly adsorbed material. The modified electrode was immediately used for experiments.⁷⁴

2.3 Spectroelectrochemistry

In situ UV-VIS-NIR experiments were performed using a Cary 5000 UV-VIS-NIR Spectrophotometer in conjunction with thin layer quartz cuvette (path length 1 mm, BASi) at ambient temperature. The cell was filled with working solution (concentration ratio of analyte to supporting electrolyte was 1: 100), and it carried Pt gauze working electrode, Pt counter electrode, and Ag/AgCl/NaCl_{3M} reference electrode.

A general experimental procedure was, applying a DC potential to the system and holding the potential for required time (1-2 mins) then recording the UV-VIS-NIR spectra. The DC potential was scanned over a range that should fully reduce or oxidize the redox species completely.

2.4 Infrared Measurements- Photoelastic modulation Infrared Reflection Absorption Spectroscopy (PEMIRRAS) and Fourier Transform Infrared Spectroscopy (FT-IR)

A Varian FTS 7000 spectrophotometer was used in conjunction with PEMIRRAS accessory to study the IR absorption of monolayers on Au surface. PEMIRRAS accessory permitted external focusing of the beam, equipped with a liquid N₂ cooled Mercury-Cadmium-Telluride (MCT) detector, a UDR-4 filter, and a Au grid polarizer. The IR radiation was phase modulated at 800 Hz at amplitude of 1.0λ while stepping at 5 Hz. The IR spectra of adsorbate were recorded by reflecting of the incident beam at an angle of incidence of 80°-85° using *p*- polarized light, which was obtained by using a Au grid polarizer. The *p*-polarized light was modulated by a Hinds ZnSe PEM operating at

74 KHz at amplitude of 0.5λ before reflecting off the sample. The spectrum was taken at 2 cm^{-1} resolution at ambient temperature and usually 2-3 scans were averaged for acceptable result. The digital signal processing (DSP3) algorithm that is incorporated into the ResolutionPro software was used to collect the spectrum.

The following method was adopted to prepare sample for PEMIRRAS measurement. Monolayer was prepared on polycrystalline Au film. Au Oxides and any other surface contaminants were removed by static incubation of Au substrate in absolute ethanol for 30 min, and then it was dried in Ar. After subjected to chemical cleaning, the Au substrate was immersed in a freshly prepared 1 mM THF/ ethanol (5:1, v/v) solution of given disulfide for 24h at ambient temperature. After incubation, the substrate was rinsed with THF and vacuum dried and sample was immediately used for measurement.

Diffuse Reflection measurement method (incident angle 45°) was used to obtain bulk IR spectrum. Samples were prepared by finely grinding approximately 1% (w/w) of appropriate compound in KBr. Finely ground pure KBr served as the background reference.

2.5 Theoretical Calculation

The density functional theory calculations were carried out using the Gaussian 03 software. Geometries of molecules were optimized at the B3LYP/6-31G+(d,p) level of theory. The polarisable continuum model was used as the water solvent model in the process of optimizing the ground state energy of molecules.

Chapter Three: Results and Discussion

3.1 Electron transfer studies in Solution

3.1.1 Material Synthesis

Synthesis of target compound **1** (anthraquinone diamidopyridine derivative) had different approaches, but all these approaches had the basic idea of linking the redox moiety (anthraquinone derivative- AQ) with hydrogen bonding (diamidopyridine derivative- DAP) moiety by acetylene. Acetylene was chosen as the spacer unit, because it provides a planer molecular framework and unsaturation, which would enhance electronic communication between two redox ends when it dimerises in solution. **Figure 3-1** illustrates the initial retrosynthetic route to **1**, and here the ethynyl spacer unit was attached to the AQ moiety (**2**).

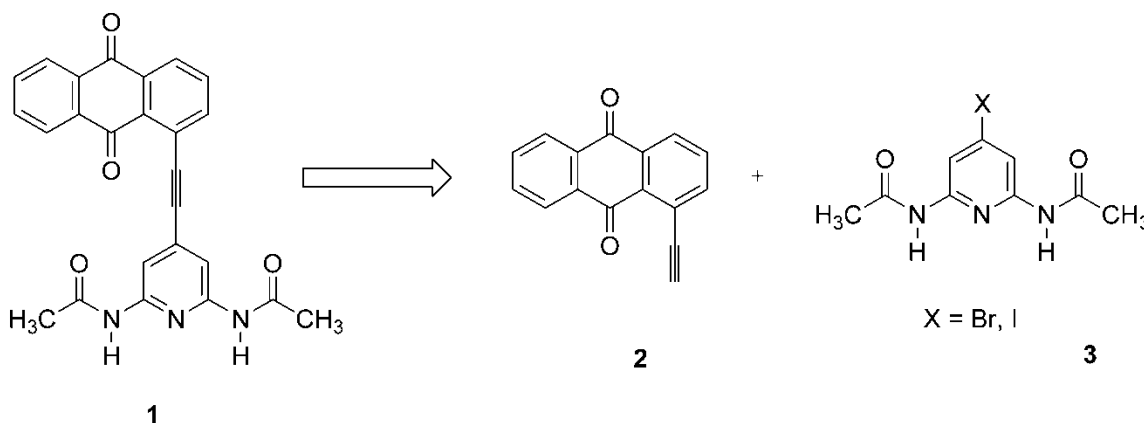


Figure 3-1 Retrosynthetic scheme for target compound **1** (anthraquinone diamidopyridine derivative)

A literature survey revealed preparation of **3** could be accomplished by several methods. However, at the outset of the synthesis, two key reactions, namely Hoffmann and Curtius rearrangement, were considered to make crucial intermediate 4-halo-2,6-diaminopyridine (**11**). The precursor for this intermediate was 4-halo-2,6-diesterpyridine (**6**), and the synthetic route is described in **Figure 3-2**. Condensation of acetone with ethyl oxalate produced acetone dioxalic ester, which was hydrolyzed to chelidonic acid (**4**) by concentrated HCl.⁵⁸ This was converted to chelidamic acid (**5**) by dissolving **4** in 28% aqueous ammonia and heating to reflux for 5h.⁵⁹ Chelidamic acid (**5**) is an important compound in ligand synthesis, and therefore extensive structural details are available. In solution, this exists largely in its keto tautomeric form.⁷⁵ Nevertheless, the solid state structure is a monohydrated zwitterionic species.⁷⁶ The fusion of **5** with phosphorus pentabromide at 90°C converted OH of **5** to Br, concurrently producing diacid dihalides, which were converted to esters with either methanol or ethanol to give **6a** and **6b**, respectively.

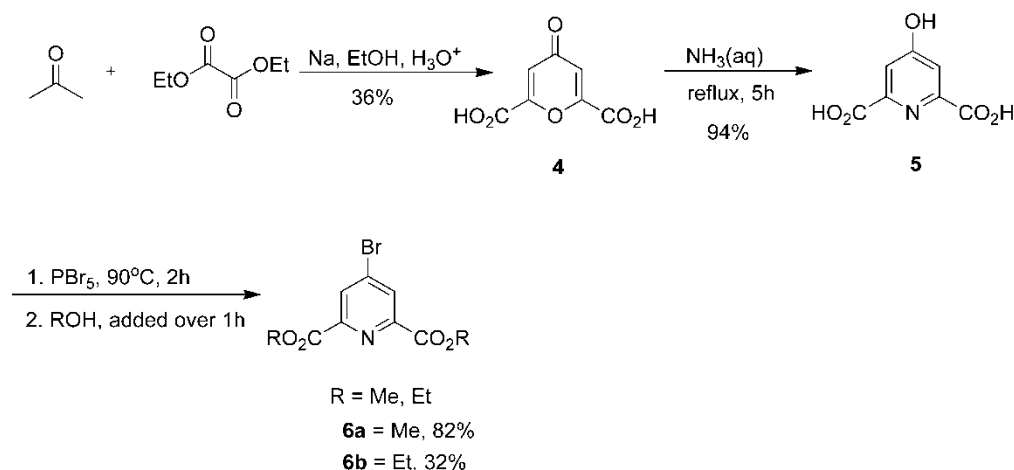


Figure 3-2 Synthesis scheme of compound **6**

The retrosynthetic plan was to perform the Sonogashira coupling at the last stage, it was necessary to have a more reactive aryl halide bond installed at the fourth position of DAP. Usually, Sonogashira coupling is efficiently performed with the more reactive heteroaryl iodide. **Figure 3-3** illustrates the attempted synthetic pathways to achieve the halogen exchange.

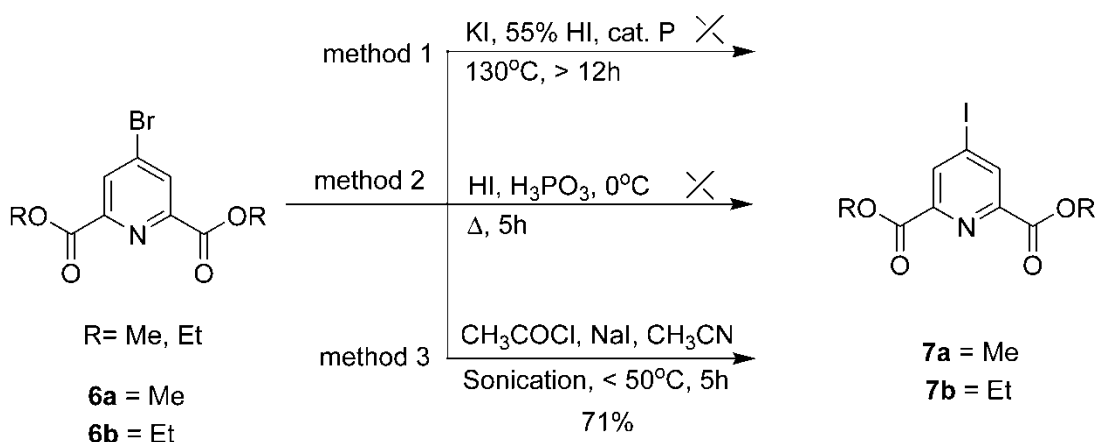


Figure 3-3 Synthesis of compound 7

As shown in **Figure 3-3**, trans-halogenation of compound **6** in the presence of excess iodide and phosphorus based compounds at high temperature were not successful. However, under mild conditions as in method 3 of the **Figure 3-3** the trans-halogenations proceeded cleanly in 71% yield.^{62,63} The role of P or phosphorus acid in halogen exchange is not clear. Halogen exchange takes place via an aromatic nucleophilic substitution pathway, and some conditions that give higher probability of success are, use of excess iodide nucleophile, activation of pyridine ring with protonation or acylation, and increased temperature.

The next step was the conversion of **6/7** to **9** via Hoffmann or Curtius rearrangements. **Figure 3-4** explains the Curtius rearrangement.⁵⁵ Esters (**6** or **7**) were converted to acids without much difficulty by treating them with aqueous LiOH, and bromide and iodide derivatives gave yields of 78% and 91%, respectively. The one pot synthesis of diacid (**8**) to diacid dichloride with oxalyl chloride and diacid dichloride to bis-acylazide with sodium azide was planned, because the by-product of the acid chloride conversion step is CO₂, which does not need any purification. The bis-acylazide compound was isolated but not characterized due to potential hazard of N₂ extrusion at increased concentration. Before triggering the Curtius rearrangement, the acylazides were dried thoroughly to prevent unnecessary side reactions of isocyanates. Curtius rearrangement converts the bis-acylazides functional group to isocyanates, and subsequently transformed to carbamates (**9**) in the presence of tertiary butanol under pyrolytic conditions. **9a** was obtained in 16% yield.

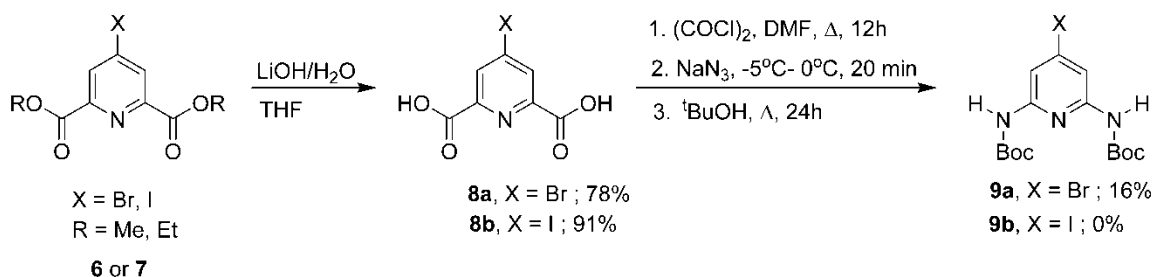


Figure 3-4 Synthesis of compound **9**

It was thought that the low yield obtained is because of the one pot synthesis of acyl azide. Splitting the steps, however, did not produce any favourable results. The reason for not having **9b** is currently unexplainable. An alternate route was needed due to the low

yield of the carbamate and due to safety hazards of a gram scale reaction of acylazides. It became apparent that the Hoffmann rearrangement was the best alternate, because the same starting material could be used to achieve the target.^{60,77} The Hoffmann pathway started with aminolysis of pyridinediester (**6** or **7**) to dicarboxamide (**10**), and subsequent rearrangement of dicarboxamide to diamine (**11**) was unsuccessful (**Figure 3-5**). The careful mechanistic analysis of the Hoffmann reaction (**Figure 3-6**) made clear that different reaction conditions needed to be investigated. The formation of compound **11** is the result of hydrolysis of isocyanate, which is the actual product but does not survive under the reaction conditions.

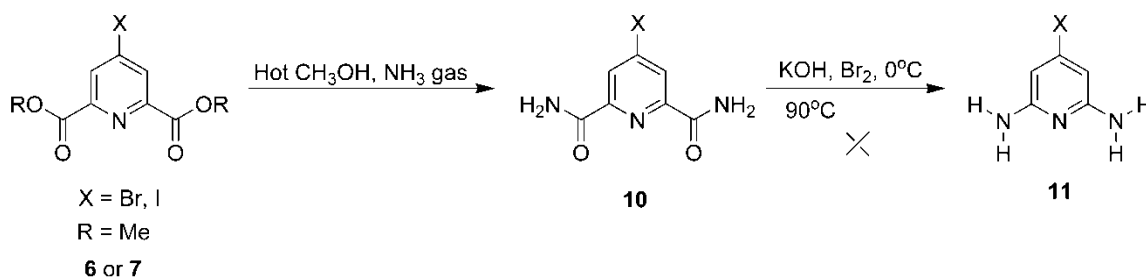


Figure 3-5 Attempted synthesis of compound **11** via Hoffmann rearrangement

Isocyanates could undergo side reactions producing urea and acylurea if low temperature and dilution conditions were not satisfied. The active brominating species potassium hypobromite was made *in-situ* by reacting aqueous KOH with Br₂ at 0°C, because at higher temperatures potassium hypobromite will disproportionate into bromide and bromate. This active species reacts with pyridine **10** to form N-bromo amide (**Figure 3-6**), and then to isocyanate, which subsequently hydrolyses to amine (**11**). The ratio of isocyanate to amine should be kept low to suppress the formation of urea, which could be

achieved when the reaction mixture is cold and diluted.^{78,79} After several attempts, complete dissolution of the starting material at 0°C was not observed, and temperature was increased to room temperature to see whether the hypothesis was correct. A ten- fold dilution also did not produce any favourable result. The low solubility of the starting material could be the reason for the failure of the reaction. It was decided to investigate the reaction with phase transfer catalyst- tetrabutyl ammonium bromide, because Sy *et al.*⁷⁸ and Rane *et al.*⁷⁹ reported that a phase transfer catalyst would increase the yield of isocyanate. Nevertheless, no effective results were obtained.

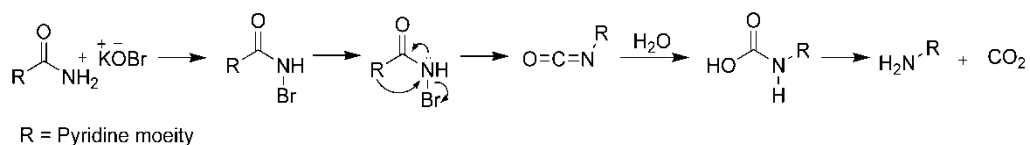


Figure 3-6 Mechanism for Hoffmann rearrangement

In view of this failure, there was a need for a method that produces **11** on a large scale without posing safety risks. As shown in **Figure 3-7**, the alternate route to synthesize compound **11** started with the oxidation of commercially available 2,6-dibromopyridine to yield pyridine N-oxide **12**.⁶⁴ Nitration of **12** with nitric acid and sulfuric acid afforded **13** without any purification involved. The subsequent nucleophilic substitution of the nitro group with bromine produced yields as low as 10%. Having a very low yield at an early stage of the synthesis would have serious effect later. Hence, it was decided to optimize the reaction conditions.

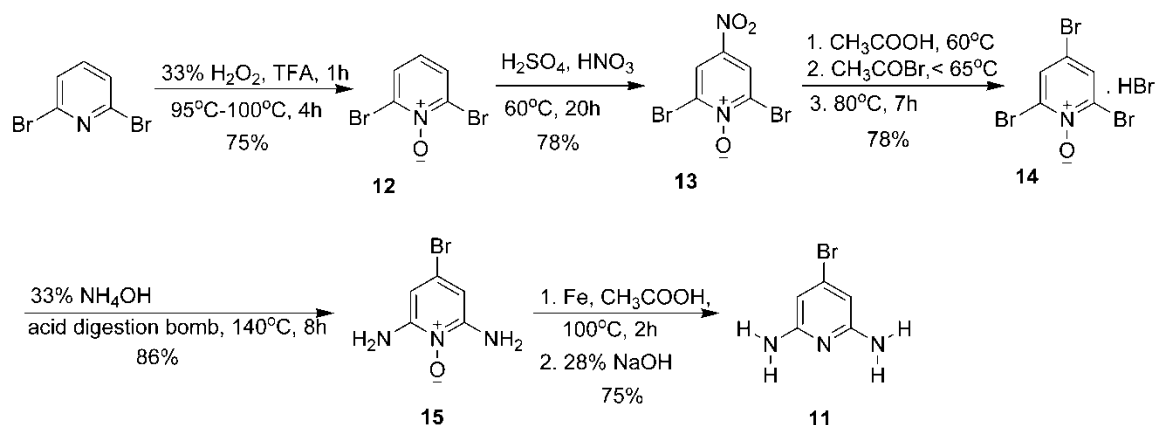


Figure 3-7 Synthesis of compound **11**

In re-evaluation of the approach to form **14** from **13**, it was suspected that acetyl bromide was evaporating during the addition, even though the temperature was kept below the boiling point of the acetyl bromide. Thus, the improved method involved addition of acetyl bromide twice during the course of reaction, which ultimately increased the yield to 78%. Compound **14** was always isolated as the hydrobromide adduct of pyridine **14** that was carried into the next step without further purification, because in the next step the hydrobromide would be neutralized by aqueous ammonia.

Efforts to synthesize pyridine **15** in a custom made sealed tube using the Nettikovan approach⁶⁴ and in a pressure vessel (ChemGlass) were ineffective due to their inability to withstand the ammonia pressure at high temperature. To overcome this problem an acid digestion bomb (Parr Instrument Company) was used, but the amount of starting material in each use was limited. As a result, this step was repeated numerous times.

After obtaining reasonable amounts of compound **15**, it was subjected to reduction with iron and acetic acid to afford compound **11** with a yield of 75%. Again, the product of this step also gave an acetic acid adduct as evidenced by the X-ray crystal structure.⁶²

The acetic acid adduct **15** was purified by washing with 28% NaOH. The next step was to protect the diamine functionalities of the pyridine **11** with acetyl groups as shown in **Figure 3-8**. Unlike the smooth transformation of amine to amide reported in the literature,^{60,55} in our hands the yield suffered. This unsatisfactory yield was corrected by screening different reaction conditions as shown in **Table 2**.

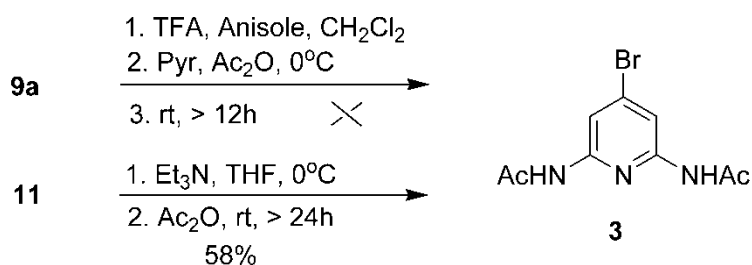


Figure 3-8 Synthesis of 2,6-Di-acetylamino-4-bromo-pyridine (**3**)

Table 2 Optimization of yield of 2,6-Di-acetylamino-4-bromo-pyridine (**3**) from pyridine **11**.

Entry	Reagents	Conditions	Solvent	% Yield
1	CH ₃ COCl, Et ₃ N	rt, > 12h	CH ₂ Cl ₂	0
2	Ac ₂ O, Pyridine	rt, > 12h	CH ₂ Cl ₂	0
3	Ac ₂ O, Pyridine, CsCO ₃	rt, > 12h	CH ₂ Cl ₂	17
4	Ac ₂ O, Et ₃ N	rt, > 24h	CH ₂ Cl ₂	36
5	Ac ₂ O, Et ₃ N	rt, > 24h	THF	58
6	Ac ₂ O, Et ₃ N	reflux, > 12h	THF	0

legends: rt-room temperature

Although conversion of pyridine **9a** to pyridine **3** was unsuccessful, pyridine **11** to pyridine **3** was successful. It was found that entry 5 in **Table 2** produced the best conditions for this conversion.

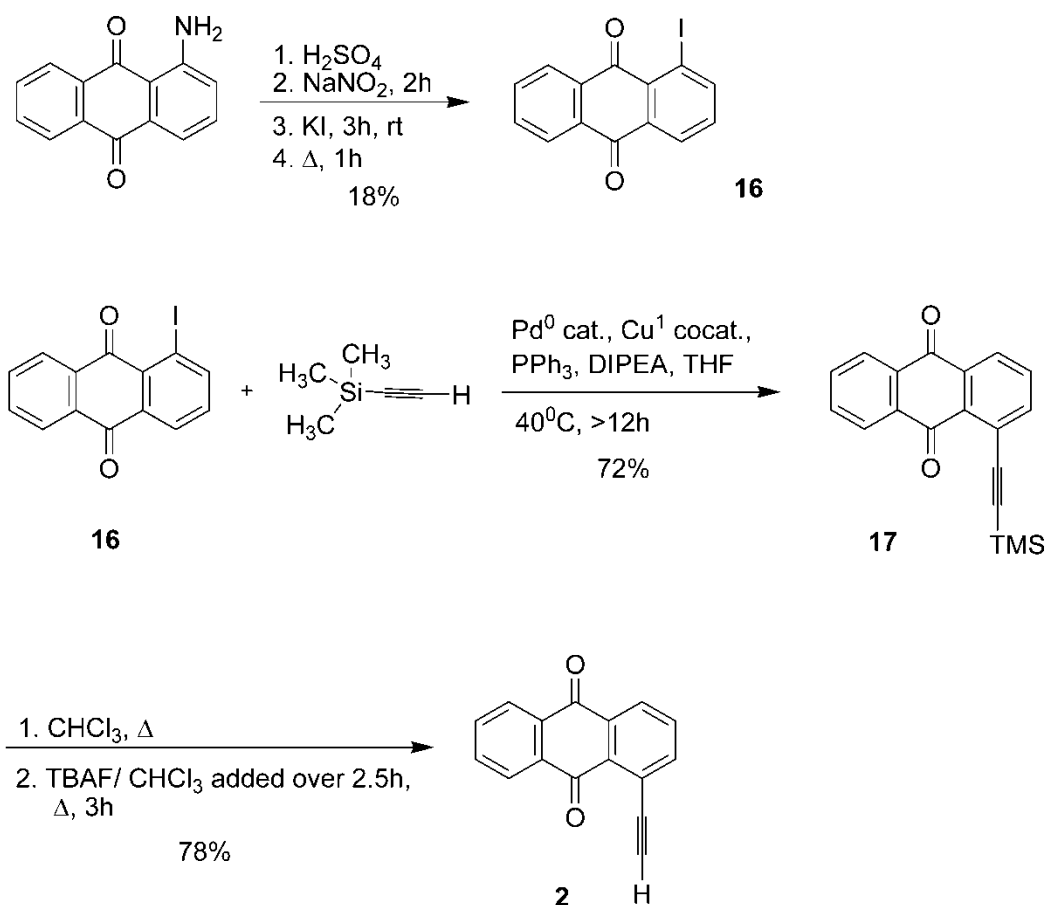


Figure 3-9 Synthesis of compound **2**

The work on the anthraquinone moiety, or **2**, began with preparation of 1-iodoanthraquinone from 1-aminoanthraquinone (**Figure 3-9**). Goldstein's method⁶⁵, shown in **Figure 3-9** (18% yield) was found to be better than Ma's method⁶⁶ (10% yield)

in terms of yield of **16**. The next step was to generate **17** by forming a new C-C σ bond between sp^2 and sp hybridized carbon atoms, using Sonogashira palladium mediated coupling reaction.

The Sonogashira reaction, which is named in honour of one of its discoverers, is a palladium catalyzed coupling reaction between terminal alkyne and aryl or heteroaryl halide in the presence of a copper co-catalyst and a base. The sequence of steps that is proposed to be involved in this reaction is summarized in **Figure 3-10**.⁸⁰⁻⁸² A coordinatively unsaturated 14-electron bis(triphenylphosphine)palladium(0) complex (**III**) is the putative active catalyst, could be formed *in situ* by dissociation of two PPh_3 ligands from $Pd^0(PPh_3)_4$ (**IV**) or through sequential transmetallation and reductive elimination from $Pd^{II}(PPh_3)_2Cl_2$ (**I**). Once formed, complex **III** participates in oxidative addition of the aryl or heteroaryl halide to provide the 16- electron palladium(II) complex **V**. The next step in the catalytic cycle is transmetallation with copper acetylide to furnish complex **VI**, which then affords cross-coupled final product and active catalyst by *cis/trans* isomerisation and reductive elimination.

The transformation of 1-iodoanthraquinone (**16**) to acetylenated AQ derivative (**17**) started with the union of **16** and trimethylsilyl (TMS) protected acetylene (TMSA) catalyzed by $Pd^{II}(PPh_3)_2Cl_2$, CuI, and a base. Having an activated and more reactive aryl halide (**16**) as a starting material, the Sonogashira reaction went smoothly with decent yield of 72%. This catalytic reaction is more efficient when an activated or electron deficient organohalide, such as **16**, is used. Furthermore, the general reactivity of organic electrophiles with respect to leaving group is aryl iodide > aryl triflate \geq aryl bromide. Although the base mediated (K_2CO_3 in MeOH) deprotection of TMS group worked well

on a small scale (10mmol; 52% yield), the large-scale (500mmol) reaction suffered low yield (23% yield) due to low solubility of **17** in MeOH. Despite the addition of co-solvent THF to the reaction mixture, the yield issue could not be rectified. The problem was conveniently fixed by using tetrabutylammonium fluoride in THF as the deprotecting agent, and the product was obtained without any purification step.

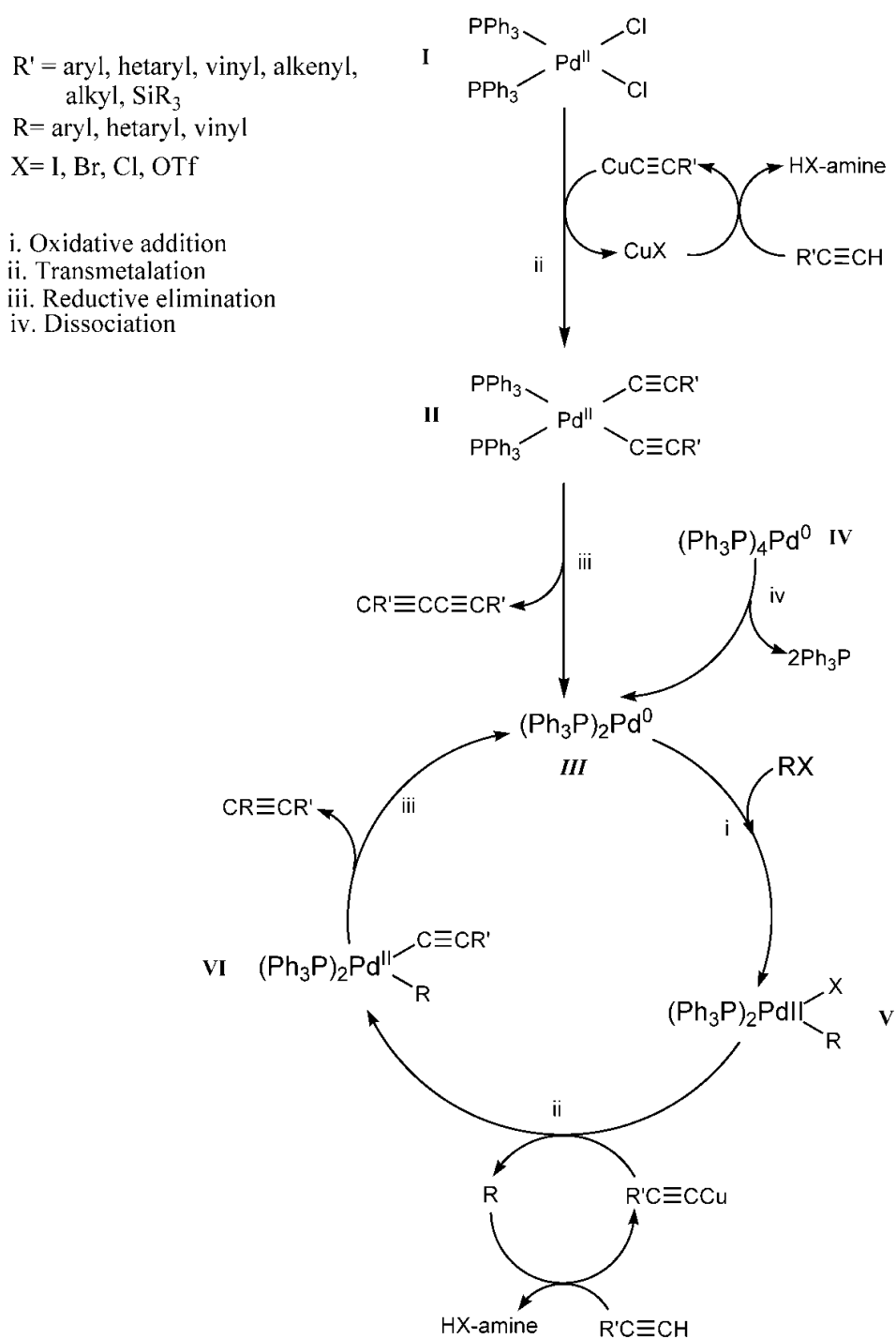


Figure 3-10 Catalytic cycle for Sonogashira reaction

The next task of the synthesis was to couple **2** with **3** using the Sonogashira reaction (**Figure 3-11**). Unfortunately, substrate **2** and **3** failed to participate in the initial trials of the Sonogashira reaction, suggesting that careful re-evaluation was needed on several variables that dictate the reaction namely, catalyst, amine base, additives, and reaction condition.

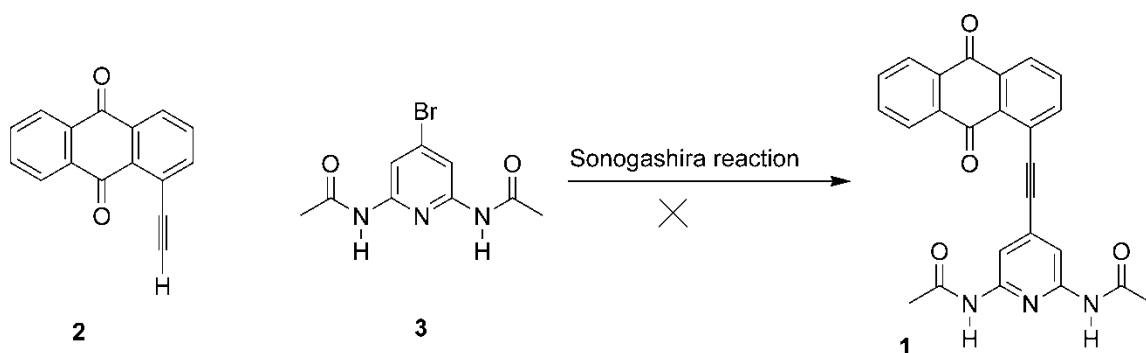


Figure 3-11 Attempted Sonogashira coupling of compounds **2** and **3**

The screening of several variables will be discussed here. **Table 3** summarizes the attempts of this unsuccessful step. Two standard Pd catalysts, $\text{Pd}^{\text{II}}(\text{PPh}_3)_2\text{Cl}_2$ and $\text{Pd}^0(\text{PPh}_3)_4$, were used, as both are known to produce the active catalytic species $\text{Pd}(0)^{80,81}$ during the course of the reaction as outlined in the **Figure 3-10**. $\text{Pd}^0(\text{PPh}_3)_4$ was preferred over the $\text{Pd}^{\text{II}}(\text{PPh}_3)_2\text{Cl}_2$, because the latter produces homocoupled alkyne, which is a deleterious side reaction. The stability of the $\text{Pd}^0(\text{PPh}_3)_2$ is crucial in the catalytic cycle, so that an additional 2-5% PPh_3 was added to stabilize it. The reactions were done in an inert-environment, to reduce the self-coupling of acetylene by copper (Glaser coupling) upon exposure to air.⁸² One type of copper salt, CuI, was used, except in one attempt the Zn salt (ZnOTf) was used, which is a variation of Sonogashira coupling.⁵⁵

When zinc triflate is used^{55,83} instead of a copper salt, a zinc acetylide would be formed *in situ* instead of copper acetylide. Negishi⁸³ showed that this would happen when excess or stoichiometric zinc salt are used, whereas in a typical Sonogashira coupling the copper acetylide will be formed *in situ* when catalytic amount of copper salt is used. Furthermore, the alkynylzinc protocol of palladium coupling would be beneficial where electron deficient alkynes⁸¹ are used as in the case of **2**.

Table 3 Attempted synthesis of **1** using **2** and **3**.

Attempt	2 /mol	3 /mol	Pd(PPh ₃) ₂ Cl ₂ / %mol	Pd(PPh ₃) ₄ / %mol	CuI / %mol	Zn(OTf) ₂ /mol	Base			PPh ₃ / %mol	Solvent	Temp /°C	Time /h
							Et ₃ N	Piperidine	DIPA				
1	1.2	1	20	NA	NA	1.2	√	NA	NA	2	DMF	80	24
2	1	1.2	5	NA	5	NA	NA	NA	√	2	DMF	80	24
3	1	1.2	NA	30	30	NA	NA	√	NA	5	DMF	110	8
4	1	1.8	NA	5	5	NA	NA	NA	√	NA	DMF	80	48

Note **2**= 1-Acetylenylantraquinone

3= 2,6-di-N-acetylamino-4-bromo-pyridine

Although the choice is highly substrate- dependant, the literature precedence shows that stronger bases, result in higher reaction rates. In our synthesis, three common bases - triethyl amine, diisopropyl amine, and piperidine - were employed, and none of these amines is strong enough to deprotonate acetylenic proton in **2**. The existence of copper-alkyne complex is well known with evidence for some of these complexes,⁸⁴ and

postulations for others.⁸⁴ Possibly, a copper-alkyne complex could form during the course of the catalytic cycle of Sonogashira reaction making the acetylenic proton acidic enough to be abstracted by amines.^{80,84}

The facile coupling was observed by others when the temperature of the reaction mixture was kept high,^{85,55,66,81,82} because oxidative addition is sluggish with heteroaryl bromides. Therefore, in all attempts the mixtures were heated.

When the above screenings failed to unite **2** and **3**, efforts were directed toward making the alkynyl substrate viable for coupling or re-examining the initial disconnection. The major issue responsible for the failed Sonogashira reaction was the electron withdrawing nature of the alkynyl-anthraquinone, which was unable to participate in the coupling reaction. It was postulated that removal of this obstruction by reducing the carbonyl group of the anthraquinone would enable successful coupling. Despite the large amount of precedence in the literature to reduce anthraquinones, in our hands it was not possible to isolate the reduced quinone compounds. Consequently, a second disconnection pattern was needed.

The pathway defined in **Figure 3-12** indicates that the new disconnection would provide suitable electronic character to the alkynyl substrate (**3'**) for the coupling. With routes already established in literature for the synthesis of **3'**,^{56,57,86} its coupling with **2'** would be a workable approach. It was envisioned to perform oxidation of the coupled product at the final stage of the synthesis to complete the transformation of anthracene to AQ.

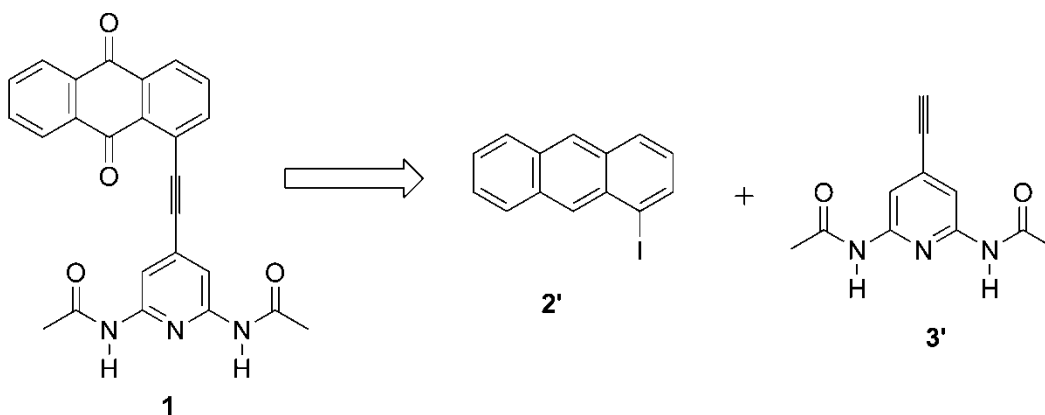


Figure 3-12 Revised retrosynthetic approach of compound **1**

Based on the plan shown in **Figure 3-12**, the synthesis began with appending the trimethylsilylacetylene group on 4th position of the **3** (**Figure 3-13**) by the Sonogashira reaction. The organic electrophile **3** that was used in the synthesis contains a bromide leaving group and two electron donating amides, thus probably making oxidative addition in the catalytic cycle as a rate-determining step, even though it is an electron deficient heteroaryl (pyridine). The reaction was carried out at high temperature. Once the reaction mixture was degassed thoroughly three times by freeze-pump-thaw method, the yield of **3'** improved from 6% to 64% (**Table 4**). Obtaining pure **3'** was a difficult task as it was contaminated with triphenylphosphine oxide. Several attempts of chromatographic separation by changing column width, length, and solvent systems could not produce an effective solution. As a result, it was decided to press forward with the $P(O)Ph_3$ contaminated **3'** for the desilylation (removal of TMS group). Desilylation of compound **18** was attempted but pure compound was not obtained. However, the crude product shows the presence of compound **3'**.

Synthesis of **2'** commenced with diazotization of 1-aminoanthracene, followed by the Sandmeyer reaction to afford 1-iodoanthracene (**Figure 3-13**). Although the crude product contains the desired product, it could not be isolated after making efforts, and the final target molecule **1** was not synthesized.

Table 4 Yield optimization of **3'**

Attempt	3 /mol	TMSA /mol	Pd(PPh ₃) ₂ Cl ₂ /%mol	Pd(PPh ₃) ₄ /%mol	CuI /%mol	Base		PPh ₃ /%mol	Solvent	Temp /°C	Time /h	% Yield of B'
						Et ₃ N	DIPA					
1	1	1.2	NA	30	30	NA	√	NA	DMF	80	24h	0
2	1	3	4	NA	4	√	NA	4	DMF	80	8h	6
3	1	20	4	NA	4	√	NA	4	DMF	rt to 80	8h	10
4	1	3	NA	15	30	√	NA	NA	DMF	80	8h	40
5	1	10	NA	10	20	√	NA	NA	DMF/ THF	80	12h	64

Note: **3**= 2,6-di-N-acetylamino-4-bromo-pyridine

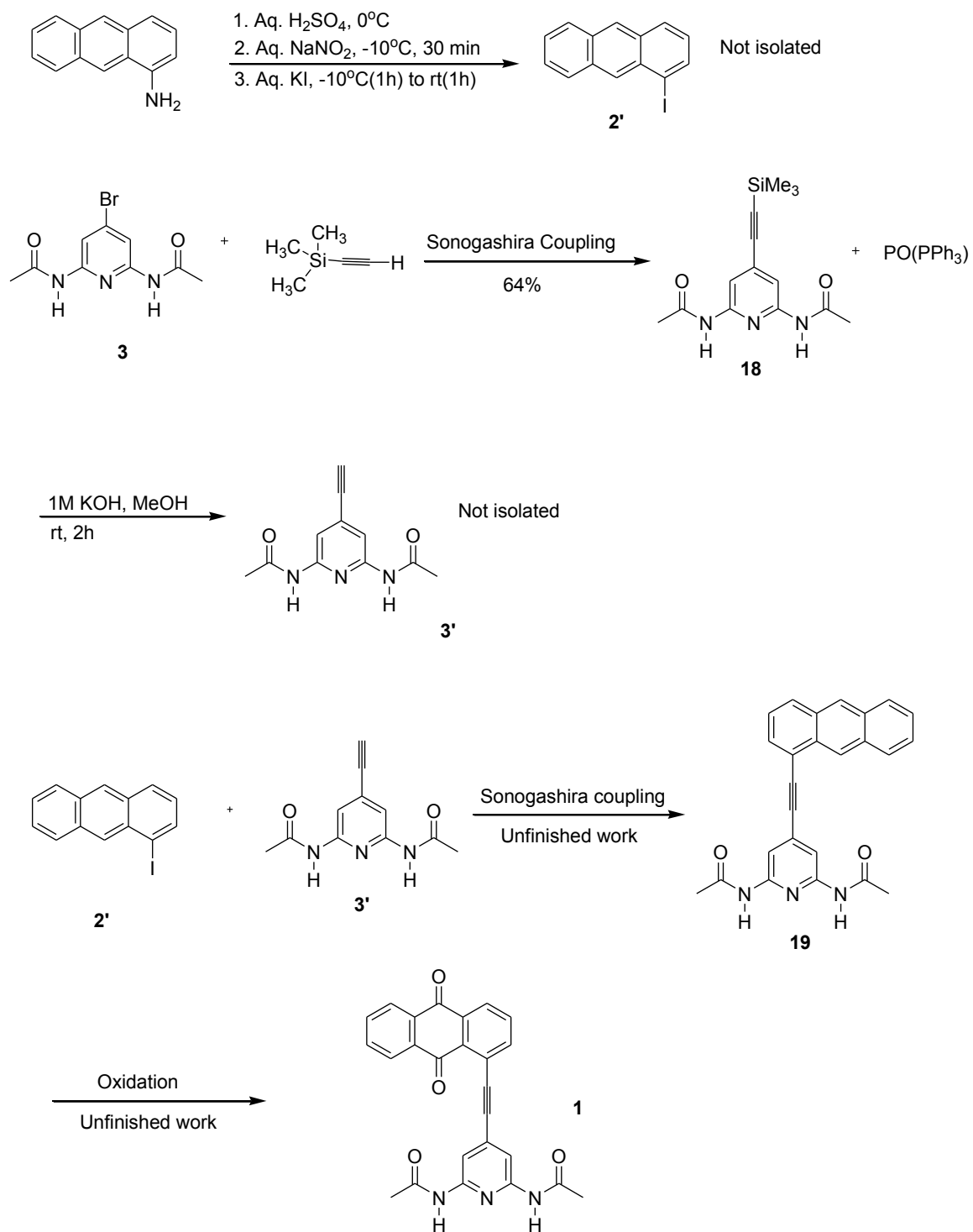


Figure 3-13 Synthesis of compound **2'**, **3'** and unfinished work

3.1.2 Solution electrochemical studies

It is essential to know the solution electrochemistry of essential anthraquinones synthesized. Therefore, the redox properties of the **2** were determined by cyclic voltammetry (CV) and electrochemical impedance spectroscopy (EIS). All electrochemical data of the studies are summarized in **Table 5**. A representative cyclic voltammogram and Nyquist/ bode plots of **2** are given in **Figures 3-14** and **3-15**, respectively.

Table 5 The summary of electrochemical parameters for compounds **2**. First and second $E^{0'}$ for first and second redox wave were obtained from CV and rest of the EIS parameters were obtained by curve-fitting the Randle's equivalent circuit for first redox wave.^a

$E^{0'} (1)$ V	$E^{0'} (2)$ V	R_s $\Omega \cdot \text{cm}^2$	R_{CT} $\Omega \cdot \text{cm}^2$	C_{dl}		W^c $\Omega \cdot \text{s}^{-1/2}$	χ^2 ^d
				C $\mu\text{F} \cdot \text{cm}^{-2}$	n^b		
-0.820	-0.144	31.12 (2.4)	62.4 (6.1)	7.7 (35.7)	0.8104 (4.4)	8.46 (2.0)	0.104

^a Numbers in parenthesis are standard deviations from curve-fitting errors.

^b n is an exponential modifier in the CPE circuit element described by:

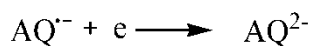
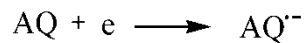
$$Z_{CPE} = 1 / [Q^0 \cdot (j\omega)^n]$$

^c Warburg diffusion element Z_w , which is given by: $Z_w = W \cdot j\omega^{-1/2}$

^d χ^2 (chi-squared) is a measure of the goodness of fit to the data using equivalent circuit model shown in **Figure 3-15c**.

Potentials are referenced against Ag|AgCl|KCl_{3M}

Literature precedence shows quinones (benzoquinones, naphthaquinones, anthraquinones),^{12,87,88} electrochemically behave in non-aqueous, aprotic organic solvents according to the following scheme.



Where AQ is the anthraquinone, $\text{AQ}^{\cdot-}$ is the semianthraquinone radical anion, and AQ^{2-} is the anthraquinone dianion. Consequently, these two one e transfer steps produce two consecutive waves in a cyclic voltammogram. The shape of the waves depends on the compound studied, type of electrode, and the solvent used.

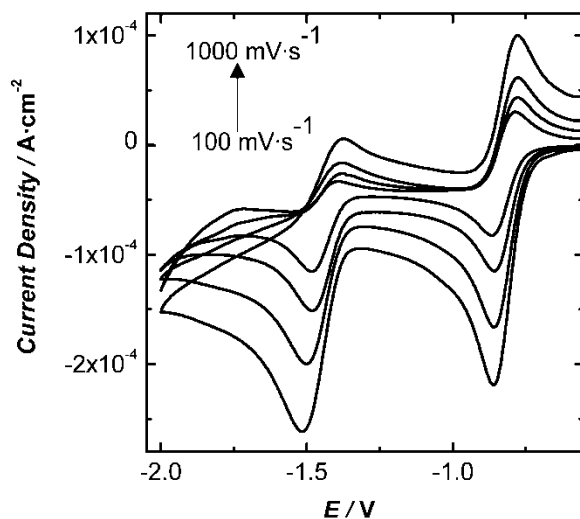
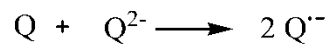


Figure 3-14 Cyclic voltammogram of **2** (1mM) in acetonitrile with tetrabutylammonium hexafluorophosphate (0.1 M) as supporting electrolyte at 25⁰C; sweep rate 0.1 to 1V·s⁻¹. Experiments were performed in a three electrode electrochemical cell using Pt wire, Pt mesh and Ag | AgCl | KCl_{3M} electrodes as working, counter, and reference electrode, respectively.

The cyclic voltammograms of the studied anthraquinone **2** in acetonitrile showed two typical redox waves corresponding to two sequential, quasi-reversible redox processes. The first wave is attributed to the redox couple anthraquinone (AQ) / semianthraquinone (AQ^{•-}) radical anion and the second wave is due to semianthraquinone radical anion / anthraquinone dianion (AQ²⁻).^{12,87,88} The apparent equilibrium potential ($E^{0'}$) of **2** shows a substituent effect on changing the $E^{0'}$ value with respect to non-substituted anthraquinone with $E^{0'}$ values -0.911V and -1.410V vs. Ag | AgCl | KCl_{sat.d.}⁸⁹ Zuman²⁴ and others claimed⁹⁰⁻⁹² that electron withdrawing substituents induce more positive $E^{0'}$ values, whereas electron donating substituents induce negative $E^{0'}$ values. The peak separation ΔE_p ($E_{pa} - E_{pc}$) of the first wave and second wave of anthraquinones **2** is observed to increase with increasing scan rate, a phenomenon characteristic of quasi-reversibility. However, the separation between first anodic and cathodic peak of **2** is close to the expected value of 59 mV for a reversible one electron process.⁴⁰ A similar response was observed for the second wave of **2** as the scan rate was lowered to 50mV·s⁻¹.

As expected for a diffusion controlled process, the anodic vs. cathodic peak current ratios (i_{pa}/i_{pc}) for the first wave of **2** are near unity at slow scan rates, but the ratio decreases with increasing scan rates.⁴⁰ These observations suggest that non-ideal behaviour, such as adsorption at the electrode could exist. However, the adsorption could not be very strong; otherwise, post or pre wave features would be seen on the voltammograms. The second wave is always shorter and broader than the first wave at all scan rates, and the i_{pa}/i_{pc} ratio is less than unity. The i_{pa}/i_{pc} ratio less than unity was earlier observed in quinone electrochemistry^{23,90} and it was attributed to a comproportionation reaction of the dianion

Q^{2-} leading to two semiquinone ($Q^{\cdot-}$) anion radicals, which are thermodynamically stable, according to following chemical equation.



Furthermore, a plot of square root of scan rate against peak current (i_{peak}) gave a linear relationship (**Figure 3-16**) for compounds **2**, supporting the notion that the redox processes are diffusion controlled according to Randle- Sevcik equation (**Equation 5**).

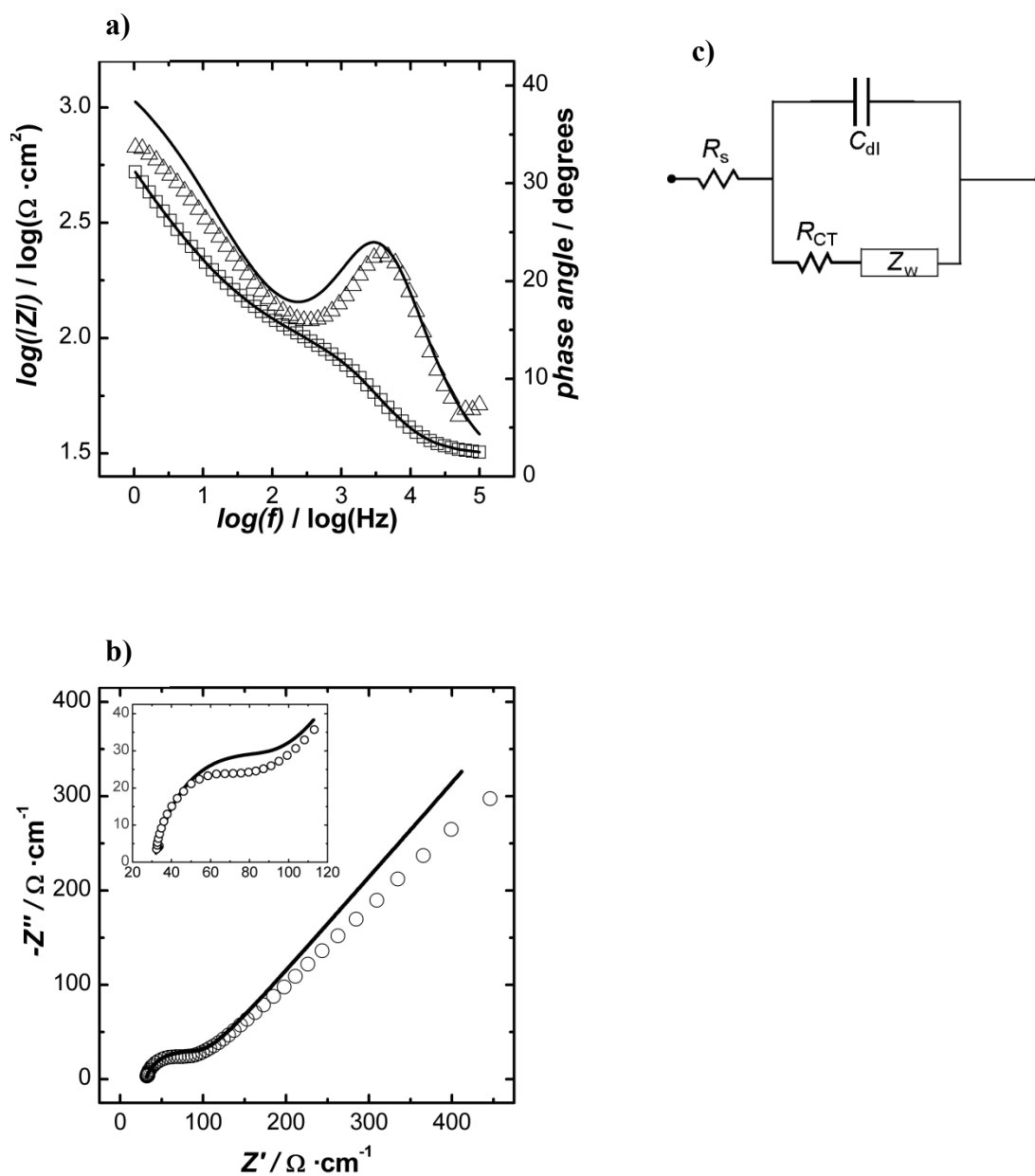


Figure 3-15 a) and b) are Bode and Nyquist plots of **2** (1 mM) corresponding to first redox wave, respectively with tetrabutylammonium hexafluorophosphate (0.1 M) as supporting electrolyte at 25⁰C. Applied potential was -0.820 V vs. Ag | AgCl | KCl₃M with 10 mV excitation signal and frequency range from 100 kHz to 1 Hz. All experimental data shown as symbol and line represents the best-fit data. Inset in **b** is the expansion of high frequency region. **c**) Randle equivalent circuit used to fit the spectra, consisting of an electrolyte resistance R_s , a double layer CPE C_{dl} , a charge transfer resistance R_{CT} , and a Warburg diffusion element Z_w .

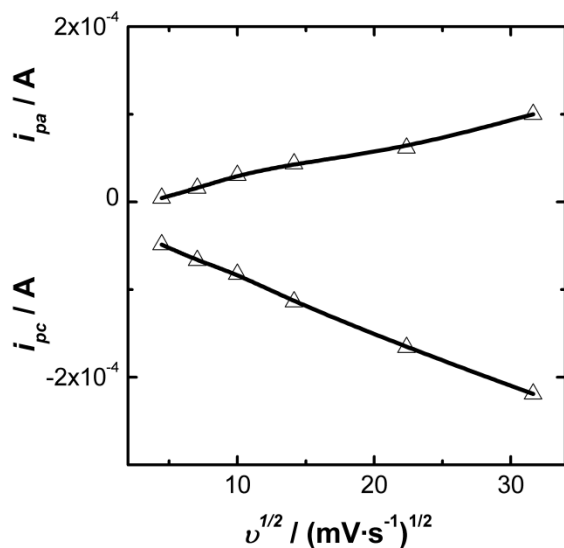


Figure 3-16 A plot of variation of anodic and cathodic peak current of first redox wave for **2** vs. square root of scan rates ($v^{1/2}$)

The impedance data of compound **2** was evaluated according to the Randle circuit (**Figure 3-15c**) for single electron transfer.³⁹ The Randle's circuit shown in **Figure 3-15c** is composed of a resistor (R_s) representing the solution resistance, double layer constant phase element (C_{dl}) representing the total interfacial capacitance, charge transfer resistor R_{CT} representing the resistance of the heterogeneous electron transfer, and Warburg impedance (Z_w) representing the diffusion process. The EIS spectrum was acquired at the first $E^{0'}$ (-0.820V) of the redox process of **2** and an AC excitation signal of 10 mV was applied. Since the second $E^{0'}$ (-1.440V) is much greater than the total AC (10mV) and DC (-0.820V) peak signal, the second ET is unlikely to happen at the first $E^{0'}$. Therefore, only a single electron transfers at first $E^{0'}$ DC potential is considered.

The Bode and Nyquist plots (**Figure 3-15a and b**) of **2** show that the electrochemistry is under both kinetic and diffusion controls. At high frequencies, the phase angle is near zero with low resistive impedance ($\sim 30\Omega$), which represents the solution resistance. Note that the analyte to supporting electrolyte concentration ratio (1:100) is kept high to control the migration current and to eliminate the frequency dependency of the solution resistance. Also, at high frequencies the impedance of the C_{dl} is near zero. As the frequency decreases ($\sim \log 5 \rightarrow 4$), impedance of the C_{dl} contributes more resulting an increase in the phase angle reaching closer to 25° degrees. The power exponent ($n \sim 0.8$) shows that the CPE element C_{dl} does not behave as an ideal capacitor and large error associated with the values of C indicate that it should be considered with care. However, chi squared (χ^2) values are below unity indicating that the goodness of the fits are acceptable. A further decrease of the frequency ($\sim \log 3.5 \rightarrow 2.5$) enables a significant ratio of the total current to flow through the R_{CT} and Z_w . This current flow makes the real component of the total impedance higher; hence lowers the phase angle to 15° . At this frequency (~ 316 Hz), the total impedance of the system as shown in the Bode plot has a value $\sim 100\Omega$. Also, the diameter of the extrapolated semicircle in the Nyquist plot has the value $\sim 100\Omega$ from the origin of the x axis. Only one semicircle was observed in the Nyquist plot suggesting that there is only one type of charge transfer process involved. As explained in the introduction, this R_{CT} value can be used to calculate the apparent rate constant of the electron transfer (k_{app}) using **Equation 14** for quasi reversible one electron/multi electron transfer process. As the frequency is decreased further ($\sim \log 0$), both the total impedance of the circuit and phase angle increased. The Nyquist plot also

shows linear behaviour at lower frequency having a slope of ~ 0.67 . These results reveal that at low frequency, the electron transfer process is faster than the diffusion of ions to the electrode- solution interface and the impedance is dominated by the Warburg circuit element. The ideal Warburg response for a reversible redox reaction should result in a slope of unity, and a phase angle of 45° . Since the faradaic and non-faradaic processes can explain the components shown in the Randle circuit, the circuit considered here is a true representation of the electrochemical cell.

3.2 Electron transfer studies at a Au surface

3.2.1 Material Synthesis

The objective is to synthesize target compounds (**22** and **27**) shown in **Figure 3-17** and use them for electron transfer studies at an Au interface. The target compounds must fulfil two requirements, one is they should be able to attach to a surface and the second is they should bear electron accepting / donating capability or redox centres. Having considered these requirements, two 1-substituted anthraquinone (AQ) derivatives, namely 1-aminoanthraquinone derivative (**22/22'**) and 1-hydroxyanthraquinone derivative (**27/27'**), were designed and synthesized (**Figure 3-17**).

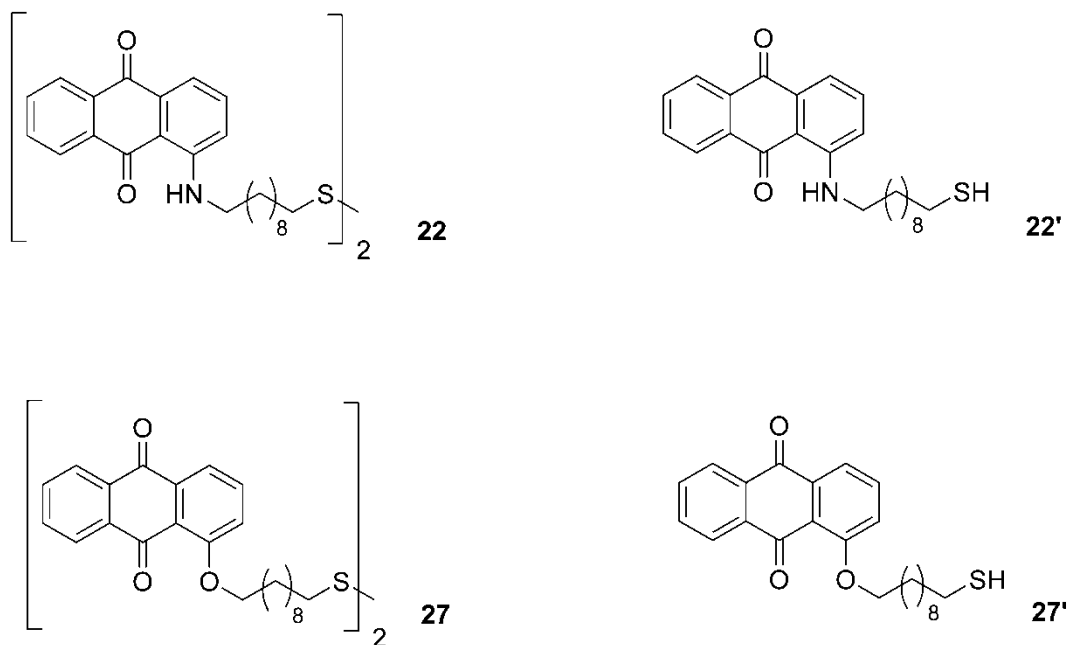


Figure 3-17 Structures of anthraquinone derivatives **22/22'** and **27/27'** for Self-assembled monolayer.

The synthetic approach used to prepare 1-substituted **22/ 22'** and **27/ 27'** began with commercially available 1-aminoanthraquinone. **Figure 3-18** illustrates the complete synthetic route of **22/ 22'**. Refluxing a solution of 1- aminoanthraquinone and 1,10-diododecane in acetonitrile yielded **20** via S_N2 type reaction with 24 % yield.⁶⁷ Note that 1,10-dibromodecane was also attempted instead of 1,10-diododecane using the same procedure, but the reaction was unsuccessful reproducing only starting materials. It is well known that iodide is a better leaving group than bromide in S_N2 type reactions. Since 1,10-diododecane is not commercially available, a trans-halogenation reaction was necessary to substitute bromides in 1,10-dibromodecane with iodide by reacting with NaI in a refluxing solution of acetone.⁹³ Also, 1,10-diododecane was one of the contributing factors that increased the amount of elimination side product seen in the ¹H NMR spectrum of **20** (appendix). An alternate route was sought because of the inefficiency of the above. Although Hida *et al.*⁹⁴ claimed they obtained much higher yields of the N-monoalkylated 1-aminoAQ in KOH/ DMSO system, in our hands it produced starting material with little amount of desired product. Therefore, it was elected to keep the previous method for synthesis of **20** while correcting the insolubility issue by adding THF as a co-solvent. However, high yields were not achieved and attention was turned to change the base. Initially, it was thought that additional base was not necessary, because excess 1-aminoanthraquinone would act as a base to neutralize the HI side product. An inorganic base caesium carbonate was chosen, since simple purification could be employed. In spite of these modifications, the yield was not increased. Probably, steric crowding around the substitution position caused by the carbonyl group, leaving group and incoming group of long alkyl chain might have played a role in the inefficiency of

the reaction. The treatment of **20** with potassium thioacetate in refluxing acetonitrile afforded **21** in 77% yield. The hydrolysis of thioester to afford **22/22'** was not a trivial task as illustrated in **Table 6**. Acid hydrolysis was tried as an initial step according to Caruso *et al.*⁶⁷ procedure, but the desired product was not obtained. However, an encouraging result (48% yield) was obtained under base hydrolysis conditions.⁶⁸ Subsequent attempts under base hydrolysis conditions did not produce the desired product. As a result, different bases, solvents, and temperatures were screened as per **Table 6**. Finally, the product was obtained following the initial procedure with the addition of 2% phase transfer catalyst, tetrabutylammonium bromide. Even though the reaction mixture was deoxygenated at 0°C for 20 minutes, disulfide **22** was obtained as the major product. The product was purified by column chromatography followed by methanol wash to remove the phase transfer catalyst.

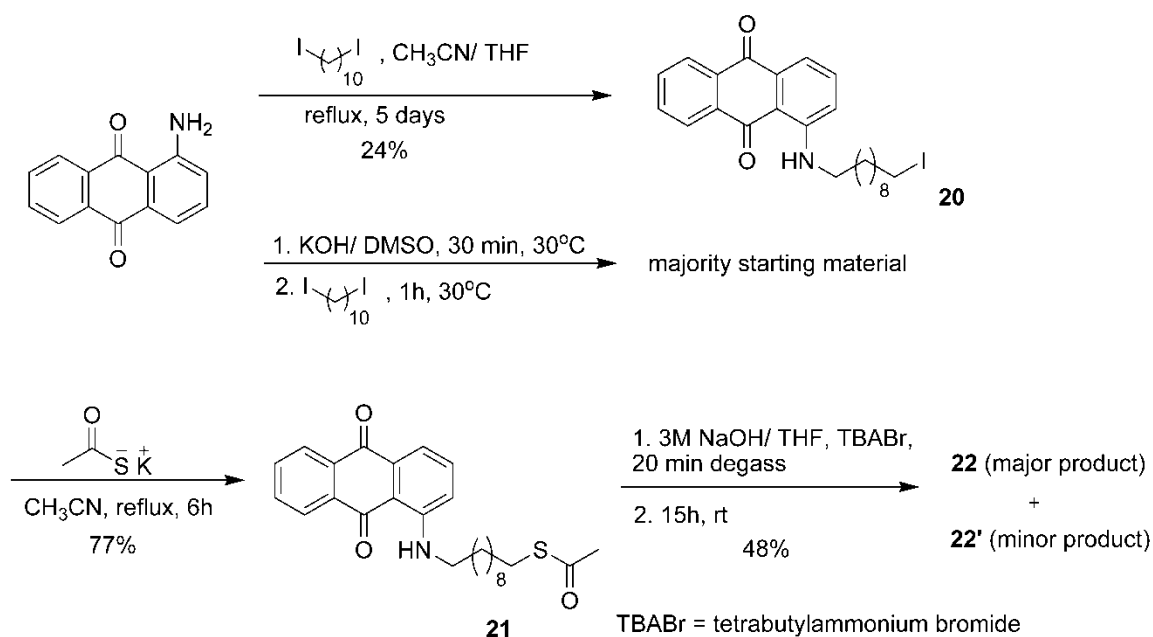


Figure 3-18 Synthesis scheme of compound **22** and **22'**

Table 6 The hydrolysis of **21** at various reaction conditions.

Entry	Reagents	Conditions	Solvent	% Yield
1	CH ₃ COCl	1. -78°C, 15 min 2. rt, 1h	CH ₃ OH	0
2	3M NaOH	0°C to rt, 5 days	(CH ₃) ₂ CO/ THF	48%
3	2M LiOH	0°C to rt, 3 days	THF	0
4	3M NaOH	0°C to rt, 5 days	(CH ₃) ₂ CO/ THF	0%
5	3M KOH	0°C to rt, 5 days	(CH ₃) ₂ CO/ THF	0%
6	3M KOH	0°C to reflux, 12h	(CH ₃) ₂ CO/ THF	< 1%
7	3M NaOH	0°C to rt, 5 days	THF	0%
8	3M NaOH, TBABr (2%)	0°C to rt, 15h	THF	39%

legends: rt- room temperature, TBABr- tetrabutylammonium bromide

As shown in **Figure 3-19**, the synthesis effort towards **27/27'** commenced with conversion of 1-aminoanthraquinone to 1-hydroxyanthraquinone (**23**). It was forecasted that the synthesis of **25** from **23** would be somewhat straightforward using method 1 of **Figure 3-19**. The objective was met, but, once again, with disappointingly low yields (17%). Therefore, an alternate and improved route was found as shown in method 2 of **Figure 3-19**. Method 2 involves the deprotonation of **23** by potassium *tert*-butoxide followed by etherification with 1,10-diiododecane in the presence of 18-crown-6 ether to afford **25** in 76% yield. The potassium cation of the 1-anthroxide (**24**) is stripped by the 18-crown-6 ether to separate the tight ion pair of the 1-anthroxide anion,⁷¹ thus facilitating the formation of the anthraquinone derivative **25**. Thioester **26** was formed

according to the previous procedure resulting in 64% yield. Finally, the synthesis of **27/27'** was completed upon hydrolysis of the thioester by aqueous NaOH.

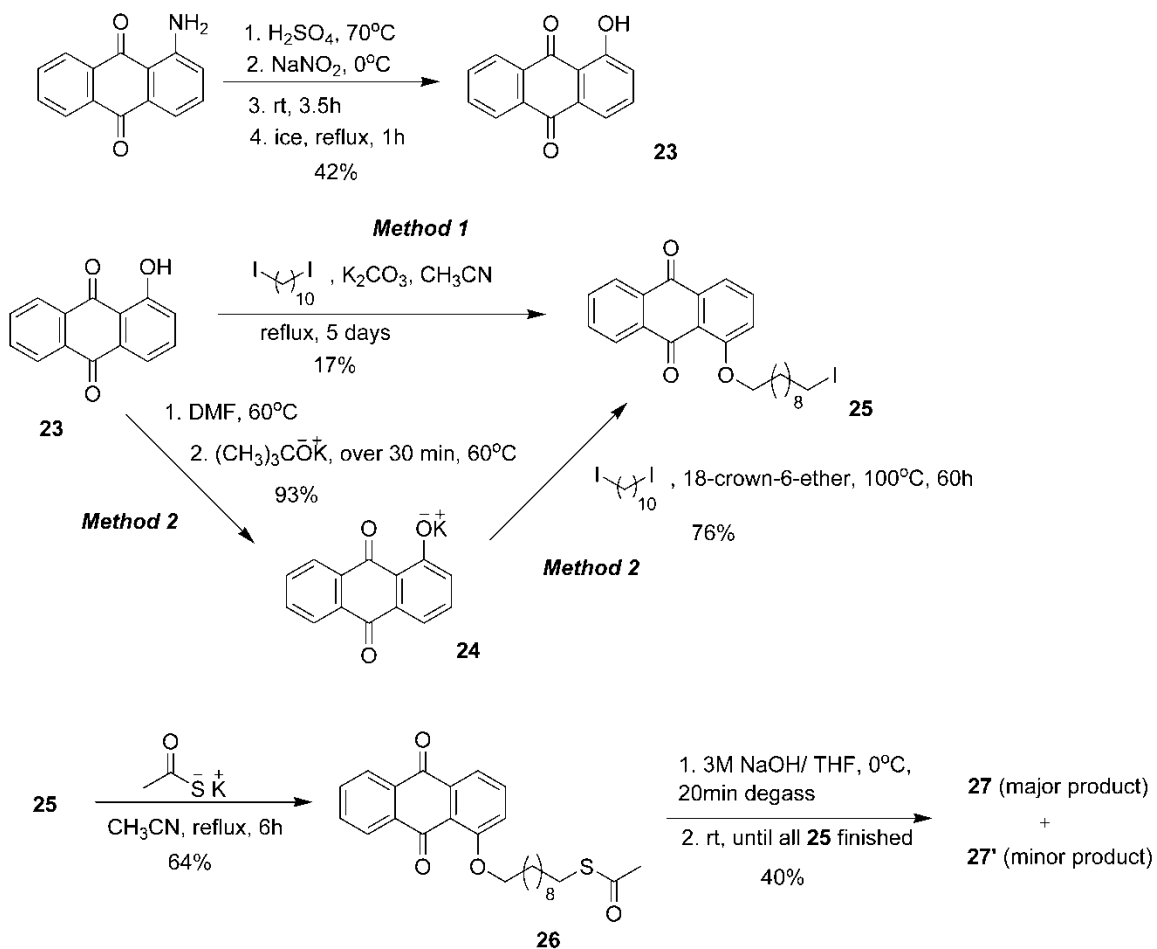


Figure 3-19 Synthesis scheme of **27/27'**

3.2.2 Monolayer preparation and SAM Characterization

In order to obtain good quality self assembled monolayers (SAMs) on polycrystalline gold surfaces a substantial effort was made to obtain contaminant free surfaces.⁷⁴ The formation of gold oxide then stripping the formed oxide is the most frequently employed method to clean gold surfaces.³⁰ Typically, ethanol is the preferred solvent for solution deposition of monolayers, but it can also be prepared from other solvents such as THF or ethyl acetate. The reason for the preference of EtOH is that the ethanol can chemically strip the gold oxides making the gold surface available for adsorption of organosulfur compound alkanethiol.^{74,95,96} Normally, 0.01-1mM solutions of alkanethiol / alkane disulfide is used as a deposition solution, and the incubation time to prepare SAMs varies with the organosulfur compound. A good quality SAM can generally be obtained when the incubation time is > 24h. The ultimate quality of the SAM structure is governed by factors such as the quality of the gold surface, the nature of the solvent and alkanethiol adsorbate, incubation time, and concentration of the alkanethiol. Therefore, no universal method can be employed to deposit alkanethiols on gold surface.

For the preparation of SAMs of **22**, gold beads were chemically oxidized in aqua regia (HCl; HNO₃ = 3:1) then they were dipped in 1mM solution of compound **22** in THF for 24h. But, the gold disk electrodes, which were used for the preparation of SAM of **27** underwent the whole procedure of cleaning as described by Tkac *et al.*⁷⁴ The full details of the Au preparation procedure are given in the experimental section. After cleaning of the electrode, it was dipped in 1mM solution of compound **27** in THF/ EtOH (v/v = 5:1) binary solvent for 24h.

In order to observe the structure of the SAM of **22**, a flat gold SAM was prepared following all steps that were used for preparing gold bead electrode. Using the PEMIRRAS method, the monolayer structure was analyzed. **Figure 3-20** shows PEMIRRAS spectrum of SAM of **22**. The important characteristics in the spectrum that need to be considered are the absorption peaks at ~ 2850 and ~ 2919 cm^{-1} , which are assigned to symmetric (d^+) and asymmetric (d^-) C-H stretching modes of CH_2 for an all-trans conformational sequence in a well organized, densely packed alkyl chains.⁵⁰⁻⁵² However, C-H stretching frequency of CH_2 of SAM of **22** is higher (2859 and 2928 cm^{-1}) than the ideal values of 2850 and 2919 cm^{-1} , which implies the presence of gauche defects in the alkyl chain resulting in lower packing densities. No carbonyl stretching peaks were observed in the low frequency region (~ 1700 cm^{-1}) probably, due to weak surface absorption of these transitions.

The monolayer structure of SAM of **27** is given in **Figure 3-21**. Relatively close-packed coverage structure was obtained for SAM of **27** compared to that of SAM of **22**, as indicated by the stretching frequencies of the methylene, but not ideal packing. The value for the symmetric stretching was 2848 cm^{-1} and 2924 cm^{-1} for the asymmetric methylene stretching. Even for SAM of **27** the carbonyl stretching could not be observed, probably for the same reason that could not be observed for SAM of **22**.

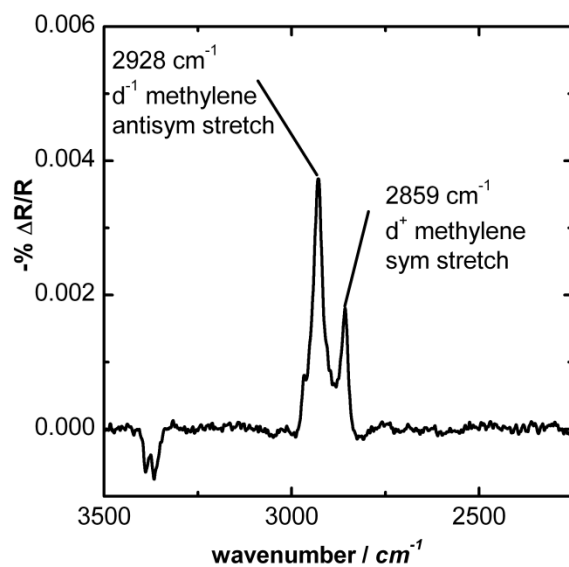


Figure 3-20 PEM-IRRAS spectrum of SAM of **22**. The spectrum shows the C-H stretching region of the C_{10} alkyl linker to the Au surface. The assigned stretches are indicated at the peak positions.

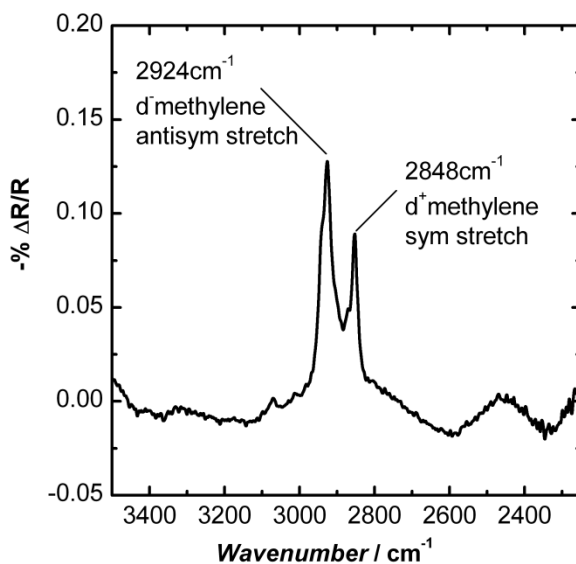


Figure 3-21 PEM-IRRAS spectrum of SAM of **27**. The spectrum shows the C-H stretching region of the C_{10} alkyl linker to the Au surface. The assigned stretches are indicated at the peak positions.

3.2.3 Surface Electrochemical Studies

Upon formation of SAMs of **22/22'** (hereafter these compounds will be named as **22** or 1-aminoAQdisulfide) and **27/27'** (hereafter these compounds will be named as **27** or 1-hydroxyAQdisulfide) on Au electrodes, the electrodes were subjected to electrochemical studies by CV and EIS techniques at different pHs and temperatures.

A limited electron transfer (ET) study for compound **22** was conducted in an unbuffered solution of pH 1 for nominal temperatures 5°C, 15°C, 25°C, 35°C and in unbuffered solutions of pHs 1.5, 5.5, 7.5, 11.5 at 25°C. On the contrary, compound **27** was subjected to comprehensive ET studies at different buffered solutions of pHs 1.5, 3.5, 5.5, 7.5, 9.5, 11.5, and 13.5 for 5°C, 15°C, 25°C, and 35°C each.

3.2.3.1 Electron Transfer studies of SAM of **22**

Figure 3-22 shows a typical CV of **22** in 0.1M H₂SO₄ as a function of scan rate at 7.3°C. A quasi-reversible signal is observed with only one anodic and cathodic peak, which is attributed to the proton coupled electron transfer (2e, 2H) of the anthraquinone redox centre. The two redox waves for consecutive 2 electron transfer process of the quinone in aprotic solvent coalesces to one wave in proton donor solvents as a result of proton coupled electron transfer. The formal potential ($E^{0'}/E_{1/2}$) is -137mV vs. Ag|AgCl|KCl_{3M}, which is determined from the average value of the peak potentials. A comparable $E^{0'}$ value (-120mV vs. Ag|AgCl|KCl_{3M}) can be obtained for a similar anthraquinone SAM, when its $E^{0'}$ from basic condition (0.1M KOH) was extrapolated considering 59mV per pH.^{13,97} Unlike a reversible system, which shows a symmetrical *i-E* curve,³⁹ the studied system shows an unsymmetrical *i-E* curve typical for a quasi-reversible system. The peak

half width or full-width-at-half-maximum (FWHM) is used to compare width of the peaks (both anodic and cathodic) in i - E curves at various scan rates. For the oxidation peak, FWHM ranges from 81mV to 184mV and for the reduction peak, the range was from 63mV to 154mV. However, a system under thermodynamic control should have FWHM value $91\text{mV}/n$ at 25°C . The cause of the deviation could be attributed to thermodynamic heterogeneity and/ or double layer effects.⁹⁸ Ideally, a Nernstian system should show zero peak splitting (ΔE_p), but SAMs of **22** did not fulfill this criterion even at a sufficiently slow scan rate of $2\text{mV}\cdot\text{s}^{-1}$ ($\Delta E_p = 38\text{mV}$; **Figure 3-23**). The nonzero peak splitting is largely the manifestation of several factors such as defects, non-ideal packing, rough surfaces, and/or changes in SAM as a function of oxidation state of the monolayer redox molecule. The last factor was minimized by keeping the electrolyte concentration (0.1M) sufficiently high.⁹⁹ A reversible system has equal energy for electron transfer of both reductant and oxidant, which results in the peak potential equal to the formal potential of the redox couple. As the kinetics become sluggish, peak separation begins to occur, and the separation will increase when the scan rate is increased. The SAM of **22** showed this behaviour and it is said that the system is under kinetic control.¹³

Verification of surface attachment of the redox centre is given in the form of a plot of i_p vs. scan rate (v), as shown in the **Figure 3-24**. Peak current is linearly proportional to scan rate indicating that the redox centres were indeed surface bound and behave as a thin film, according to Bard *et al.*³⁹ The integration of the area under the Faradaic peak of the background corrected voltammogram provides surface concentration of the redox centres and it can be readily obtained by substituting the total charges to Faraday's law **Equation 7**. It was found that the surface concentration per unit area is $1.7 \times 10^{-10} \text{ mol}\cdot\text{cm}^{-2}$, which

was calculated assuming two electrons uptake per molecule. This value is consistent with many reports,^{35,97,100,101} particularly with Zhang *et al.* paper,⁹⁷ which reported 2.9×10^{-10} mol·cm⁻² for a similar anthraquinone derivative at pH 13. Furthermore, the coverage is consistent with the theoretical coverage of 4.2×10^{-10} mol·cm⁻² calculated assuming that the **22** possesses a $12 \text{ \AA} \times 3.35 \text{ \AA}$ cross sectional area. Densely packed monolayer coverage was not obtained because of the gauche defects of the alkyl chain, as supported by the PEMIRRAS experiment results.

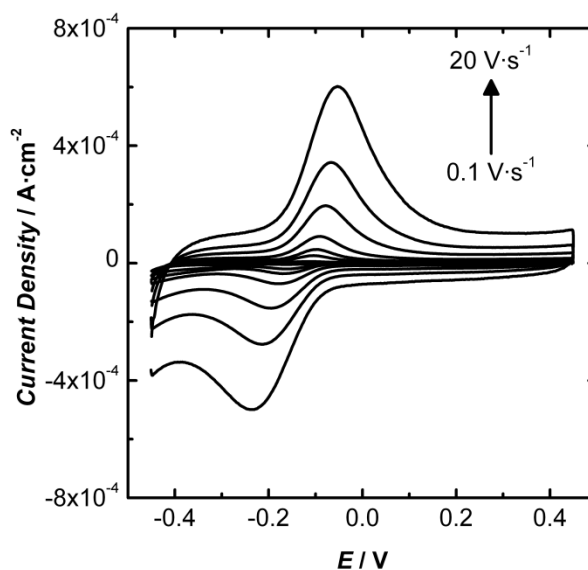


Figure 3-22 Example cyclic voltammograms of **22** at scan rates from $100 \text{ mV} \cdot \text{s}^{-1}$ to $10 \text{ V} \cdot \text{s}^{-1}$ in $0.1 \text{ M H}_2\text{SO}_4$ at $7.3 \text{ }^\circ\text{C}$ Potentials are referenced to $\text{Ag} | \text{AgCl} | \text{KCl}_{3\text{M}}$.

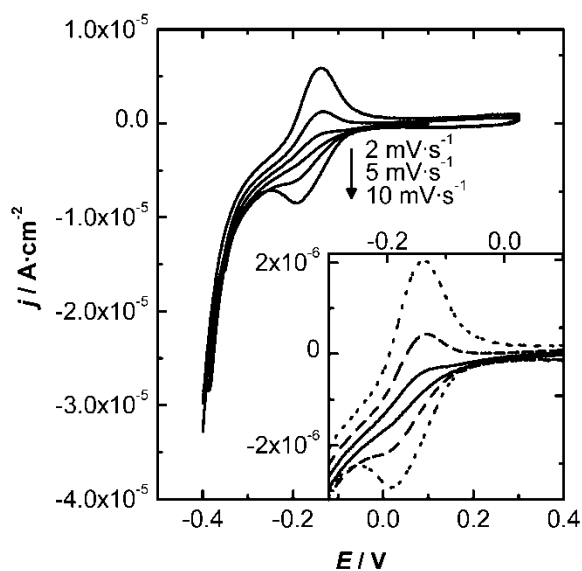


Figure 3-23 Slow scan rate CV of 22 in 0.1M H₂SO₄ at 24.8°C. Potentials are referenced to Ag | AgCl | KCl_{3M}.

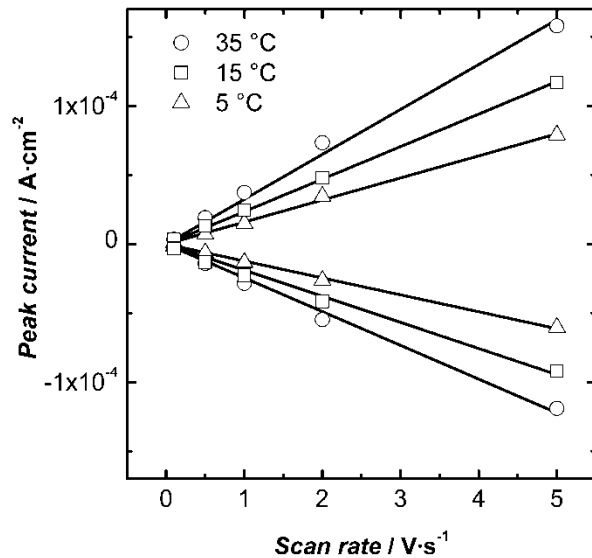


Figure 3-24 Background-subtracted peak current at various scan rates and temperatures

The Bultler- Volmer approach revised by Laviron⁴¹ for redox molecule tethered at electrode was used for calculating the macroscopic kinetic parameters such as the apparent electron transfer constant (k_{app}), and the transfer coefficient (α). **Equation 9** and **10** in the Laviron's formalism was used to calculate the k_{app} and α . In **Figure 3-25**, $E_p - E^0$ is plotted against natural logarithm of scan rate, for various temperatures.

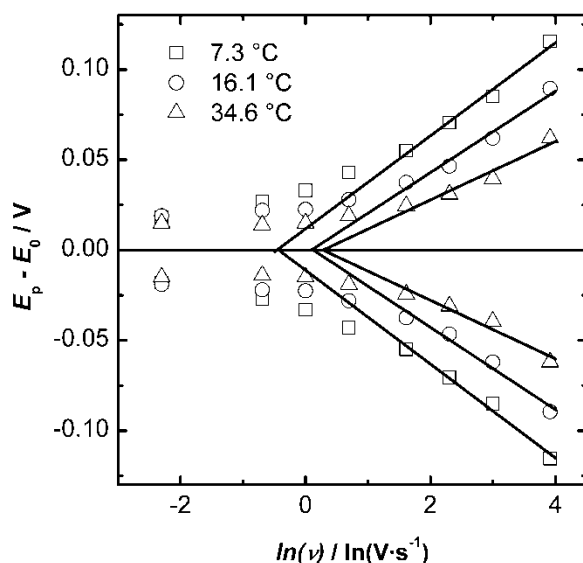


Figure 3-25 Charge transfer analysis of a SAM of **22** using Laviron formalism

As introduced in the chapter 1, the usage of Laviron formalism requires $\Delta E_p > 200/n$ mV. The experimental peak-to-peak separations considered for the calculations have to be greater than 100mV, because quinone reduction is a 2-electron process. The linear portion of the each curve in **Figure 3-25** was used to obtain the α (calculated value 0.5) and critical scan rates of cathodic and anodic processes. Using **Equation 11**, $k_{app}(s)$ were

calculated, and the values are 25, 44, and 49 s⁻¹ for temperatures of 7.3, 24.8, and 34.6°C, respectively.

EIS is another voltammetric method to measure the ET rate of an electro active monolayer. In EIS, the DC potential was set at the formal potential of the **22**, which forces the system to be at equilibrium, and a small 10 mV AC voltage signal was applied. The impedance of the cell was measured as a function of frequency (5 mHz to 100 kHz). The impedance data- namely, Nyquist and Bode plots, for **22** appear in **Figures 3-26** and **3-27**, respectively. Since EIS is recorded over many orders of magnitude of frequency, the monolayer integrity assessment was essential, and it was done by comparing initial CVs to the CVs recorded after each EIS experiment. All data shown in this work fulfilled the thermal stability criterion of less than 5% difference in integrated charge between the CVs recorded before and after EIS.

The complex plane analysis of impedance data was done by fitting them to equivalent circuits using the complex nonlinear least square method, which is included in the GPES 4.9 software. The best equivalent circuits that could explain the electrochemistry of the electrode with attached redox centres **22** are given in **Figure 3-28**.

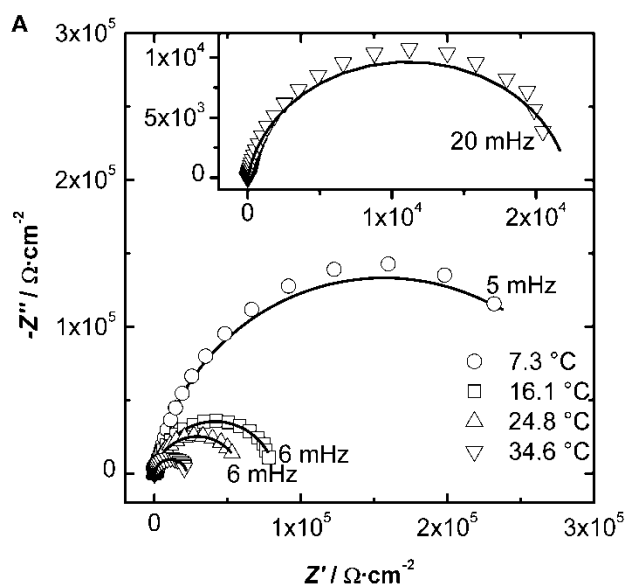


Figure 3-26 EIS Nyquist plots for SAMs of **22** in pH 1 H₂SO₄ solution at various temperatures; inset 34.6 °C data expanded. The EIS data was taken at applied potential of -0.14 V vs. Ag|AgCl|KCl_{3M} with 10 mV excitation signal and frequency range from 100 kHz to 5 mHz. All experimental data are shown as symbols and lines represent the best-fit data. Equivalent circuit **C** from **Figure 3-28** was used to fit data. Experiments were performed in a three electrode electrochemical cell using Au bead modified with SAM of **22**, Pt mesh and Ag | AgCl | KCl_{3M} electrodes as working, counter, and reference electrode, respectively.

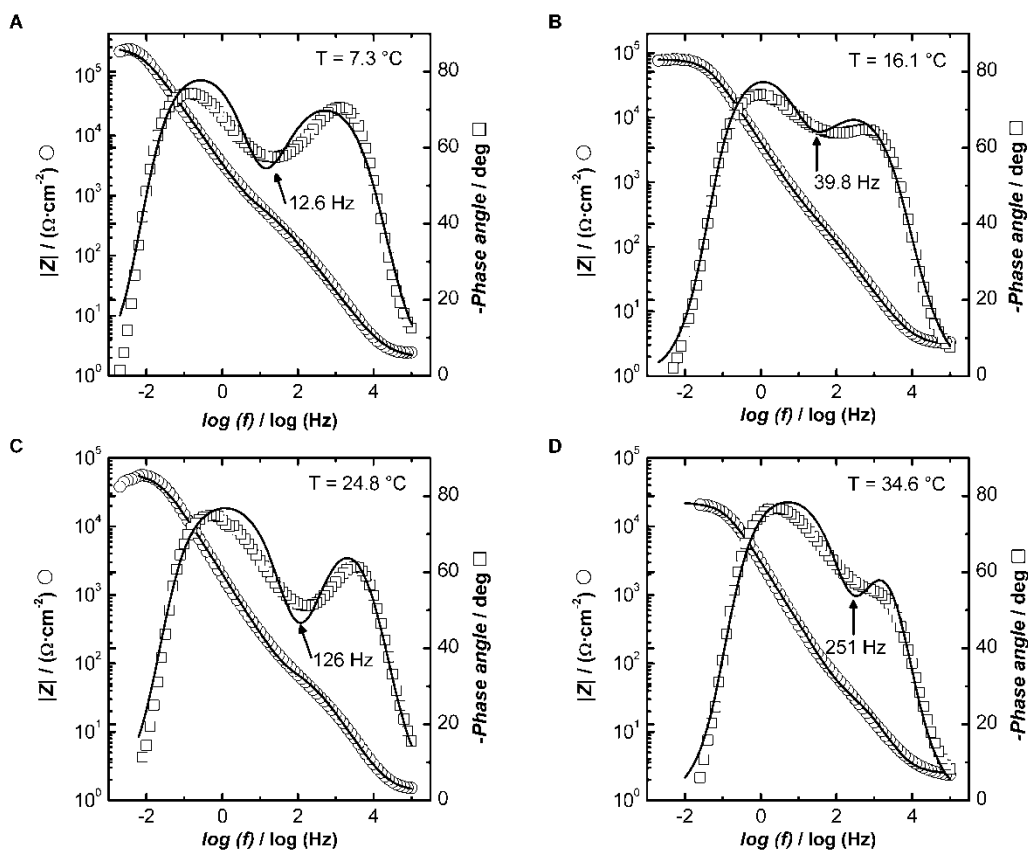


Figure 3-27 EIS Bode plots for SAMs of **22** in pH 1 H_2SO_4 solution at applied potential of -0.14 V vs. $\text{Ag}|\text{AgCl}|\text{KCl}_{3\text{M}}$ with 10 mV excitation signal and frequency range from 100 kHz to 5 mHz. All experimental data are shown as symbols and lines represent the best-fit data. Equivalent circuit **C** from **Figure 3-28** was used to fit data. Experiments were performed in a three electrode electrochemical cell using Au bead modified with SAM of **22**, Pt mesh and $\text{Ag}|\text{AgCl}|\text{KCl}_{3\text{M}}$ electrodes as working, counter, and reference electrode, respectively. **A)** 7.3 °C, **B)** 16.1 °C, **C)** 24.8 °C and **D)** 34.6 °C.

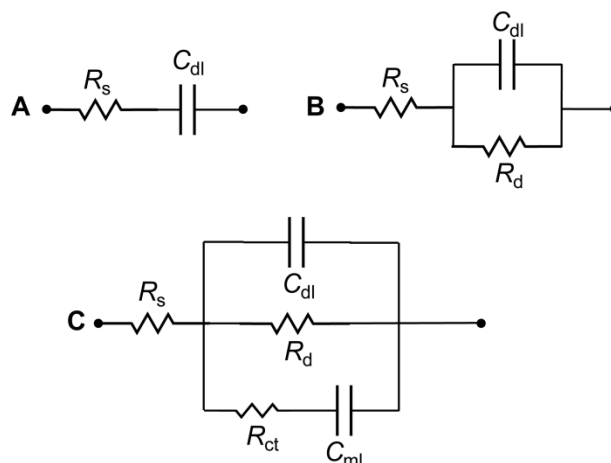


Figure 3-28 Three equivalent circuits used to fit impedance data of **22** (Figures 3-26, 3-27, 3-31, 3-32).

Table 7 Fitting analysis results of SAMs of **22** using the model presented in **Figure 3-28C** at selected temperatures. ^a

Temp °C	R_s $\Omega \cdot \text{cm}^2$	C_{dl}		R_{CT} $\Omega \cdot \text{cm}^2$	C_{m1}		R_d $\text{k}\Omega \cdot \text{cm}^2$	χ^2	k_{app} s^{-1}
		C $\mu\text{F} \cdot \text{cm}^{-2}$	n^b		C $\mu\text{F} \cdot \text{cm}^{-2}$	n^b			
7.3	2.1	21.8 (2)	0.9	696 (83)	34.0 (1)	0.9	326 (21)	0.7	1.1
16.1	3.1	27.3 (12)	0.9	382 (72)	18.0 (3)	0.9	84.7 (2)	0.3	1.9
24.8	1.3	34.9 (7)	0.8	98.4 (12)	60.9 (7)	0.9	61.0 (3)	0.7	7.4
34.6	2.4	30.4 (10)	0.9	58.1 (14)	30.5 (9)	0.9	22.3 (1)	0.5	12.6

^a Numbers in parenthesis are standard deviations from curve-fitting errors.

^b n is an exponential modifier in the CPE circuit element described by:

$$\text{CPE} = 1 / [|Z| \cdot (j\omega)^n]$$

^c χ^2 (chi-squared) is a measure of the goodness of fit to the data using equivalent circuit model shown in **Figure 3-28C**.

The **Figures 3-26** and **3-27** are best represented by equivalent circuit **3-28C**, and **Table 7** contains the fitting parameters. At high frequency, the phase angle (**Fig 3-27**) is near zero for all temperatures with low resistive impedance ($2.5 \Omega \cdot \text{cm}^2$), which represents the R_s and the value is reasonable considering the high electrolyte concentration. Also, the high frequency limiting behaviour of the double layer capacitance C_{dl} is visible in Bode plots with a peak having phase angle ranges from 60 to 70 degrees. As mentioned in the introduction, this is a constant phase element (CPE), and the power modifiers for the CPE for all temperatures are ~ 0.86 , which indicates that the double layer does not behave as a pure capacitor. The value of the C_{dl} is in the range of $22\text{-}35 \mu\text{F} \cdot \text{cm}^2$, which slightly increases with the temperature except for 35°C , suggesting temperature dependent changes in the diffuse layer are occurring. As the frequency decreases, the impedance of the charge transfer resistor (R_{CT}) is comparable to the C_{dl} resulting in a significant ratio of the total current passing through the Faradaic impedance elements R_{CT} and monolayer capacitance (C_{ml}). Now, the total impedance of the system become more resistive because the two parallel capacitors C_{dl} and C_{ml} give total capacitive impedance lower than the resistive-impedance. Consequently, phase angles decrease from the peak values. Further decreases in frequency, increases the capacitive impedance resulting in another peak with the phase angle $\sim 80^\circ$ degrees for all temperatures. As shown in **Figure 3-27** the valley frequency (valley is the region between two peaks) decreases with lowering temperature indicating that the significance of the frequency and temperature dependent charge transfer resistance. Moreover, a marked drop (from 696 to $98 \Omega \cdot \text{cm}^2$) in the charge transfer resistance can be observed with increasing temperature follows the common relationship between temperature (T) and ET rate constant (k_{app}). k_{app} was calculated

using **Equation 14**. Even though the interfacial monolayer CPE C_{ml} values are scattered at different temperatures, giving little information about structure of the electro active monolayer, the power exponents ($n \sim 0.9$) values are consistent for all temperatures indicating low surface roughness and reasonable surface blocking. At the low frequency region, the impedance of the cell tends to be resistive as marked by the zero phase angle. This resistive impedance is mainly caused by the ion penetration into the hydrophobic monolayer due to defect sites in the blocking layer, and the resistance is called defect resistance or ion penetration resistance R_d .¹⁰² No attempt was made to detect the cause of the defects, but, as evidenced by the PEMIRRAS data, the structural perturbation or gauche effect might have caused these low frequency dependant defects. Like all other elements, R_d is also temperature dependent, i.e. R_d is linearly proportional to $1/T$ having values $326\text{k}\Omega\cdot\text{cm}^2$ at 7.3°C and $22\text{k}\Omega\cdot\text{cm}^2$ at 34.6°C . The total impedance of the system continuously increases while lowering the frequency, with at least two gradients in the respective peak regions indicating that two CPEs are in the circuit.³⁹

The Nyquist plot (**Figure 3-26**) of the total in-phase (Z') and out-of-phase (Z'') impedances by theory should have two semicircles, whose diameter represents two resistive elements R_{CT} and R_d . However, in the **Figure 3-26**, these two appear as a one semicircle, because the value of the R_d is much larger than that of the R_{CT} . Moreover, the temperature dependence of resistive element (R_d) can also be seen in the graph with the largest diameter for the semicircle at 7.3°C .

Table 8 ET rate constant (k_{app}) for **22** as function of temperature and calculation method

Temperature °C	k_{app} / s^{-1}		
	CV	EIS	PSEIS
5	25	1.1	-
15	-	1.9	-
25	44	7.4	9
35	49	12.6	-

EIS- Complex plane analysis

PSEIS- Brevnov *et.al.* protocol

Table 8 summarizes the k_{app} values obtained by CV and EIS, which are not in good agreement. The reasons for the disagreement are unknown; possible explanations are experimental and calculation uncertainties, thermodynamic and kinetic heterogeneity. Using the Brevnov *et al.* protocol, based on potential scan EIS (PSEIS)⁴⁴ offers a solution to experimental and calculation uncertainties of the EIS method. As explained in the introduction, this protocol is derived from Laviron's faradaic admittance theory.^{45,103,104} **Figure 3-29** demonstrates the stepwise procedure, which is given in the introduction chapter, to extract faradaic admittance from the cell admittance. Using Microsoft Excel's goal seek function, the resulted faradaic admittance was fitted to Laviron's equations (**Equation 15-20**) obtaining the following values, $k_{app} = 9s^{-1}$, $\alpha = 0.5$, and $\Gamma = 4 \times 10^{-11} \text{ mol}\cdot\text{cm}^{-2}$. PSEIS and EIS both provide better agreement in k_{app} values. Although a common series RC circuit (**Figure 3-30a**) is considered in Brevnov's protocol to extract the faradaic admittance, the system for compound **22** contains the additional parallel element R_d . However, the effect of admittance of the R_d can be neglected considering its high resistivity.

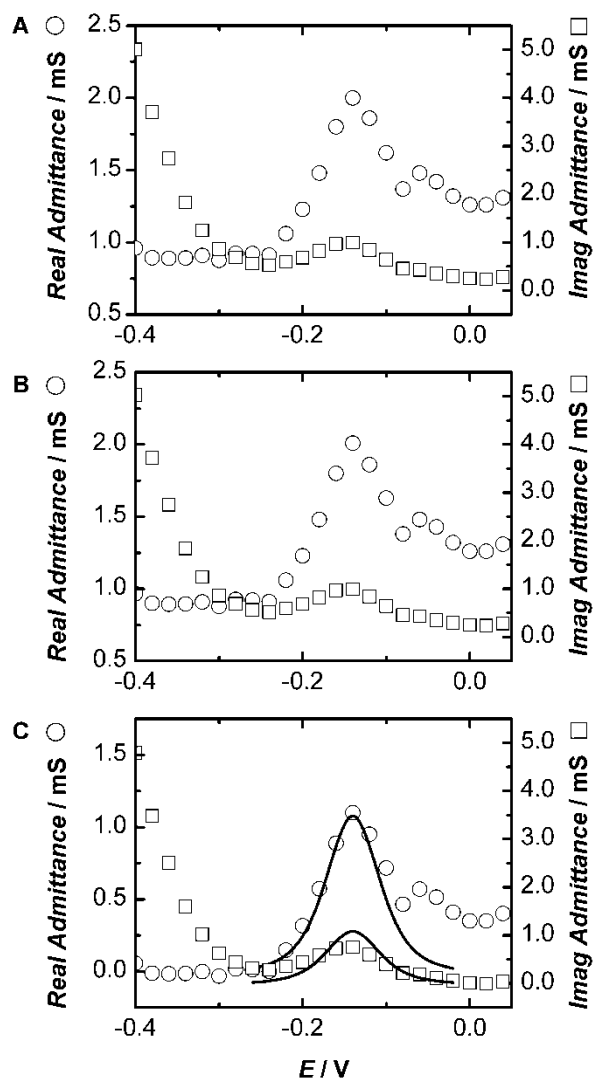


Figure 3-29 Admittance for SAM of **22** at 3.2 Hz and 24.8 °C. **A)** Total cell admittance. **B)** Interfacial admittance. **C)** Faradaic admittance.

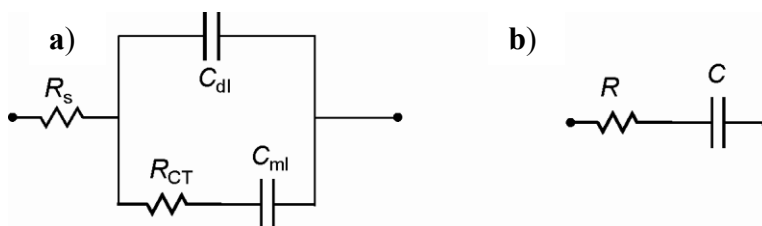


Figure 3-30 Equivalent circuits of **a)** common electrolytic cell with electro active monolayer and **b)** a simple RC circuit.

Further analysis of the potential scan EIS (PSEIS) data provides a better understanding of the ET transfer across the SAM of **22**. As explained in the introduction chapter, in PSEIS the DC potential is stepped (stepping potential was 25 mV) over a sufficiently wide range of potentials (usually $E^{0'} \pm 0.25$ V, but in our case it was -0.4 V to +0.3 V) while 10 mV of AC potential was applied as function of frequency (10 mHz - 100kHz). Three regions were identified to understand the nature of the electrochemistry of **22**; $E_{app} > E^{0'}$, $E_{app} = E^{0'}$, $E_{app} < E^{0'}$. The Bode and Nyquist plots corresponding to the three potential regions are shown in **Figures 3-31** and **3-32**.

When the applied DC potential is more anodic than equilibrium potential, the Bode plot (phase angle vs. $\log f$) adopts a sigmoid shape and the Nyquist plot has an almost vertical line parallel to the imaginary axis with the real axis intercept. This impedance spectrum can be represented by a series RC circuit (**Figure 3-30b**). At high frequency, the total impedance is resistive with zero phase angle and capacitive impedance dominates the low frequency region with higher value for phase angle ($\sim 70^\circ$ degree). In the Nyquist plot (Δ of **Figure 3-31A**), the real axis intercept is the value of R or resistance and the slight angle observed for the vertical line is because of the frequency dependent nature of the CPE.

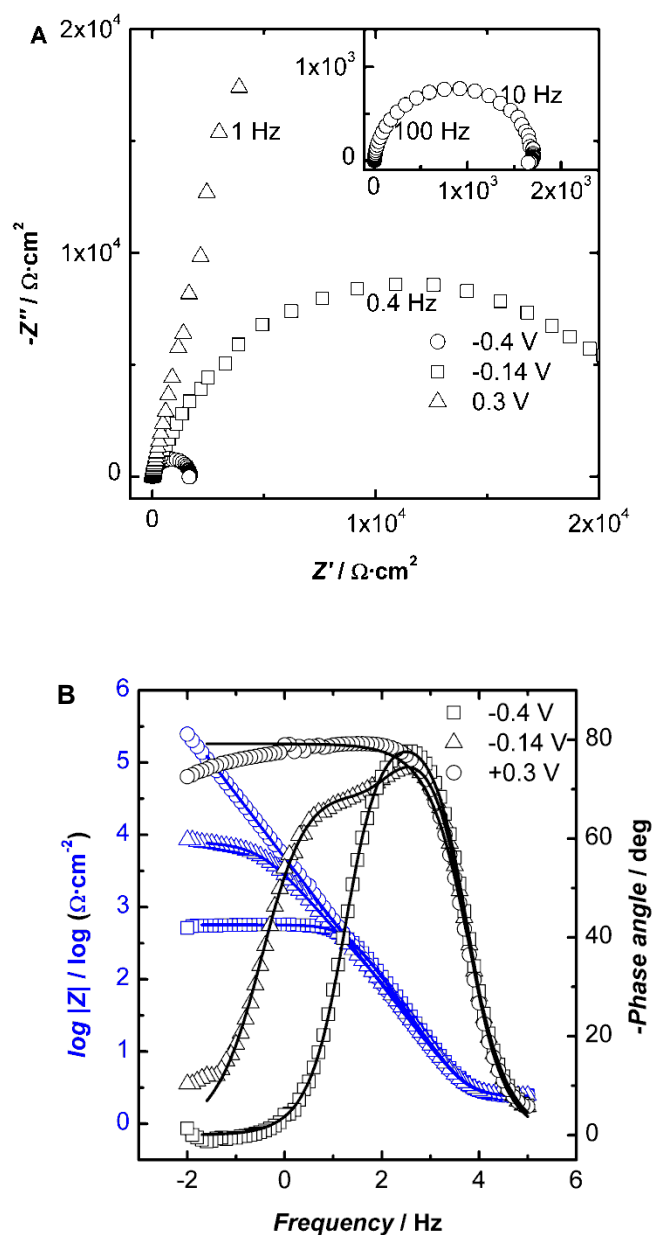


Figure 3-31 Impedance spectra of SAMs of **22** in pH 1 H_2SO_4 solution at 24.2 °C using frequencies of 100 kHz to 10 mHz and applied d.c. potentials of -0.4 V, -0.14 V and 0.3 V vs. $\text{Ag}|\text{AgCl}|\text{KCl}_{3\text{M}}$. All experimental data shown as symbols and lines represent the best-fit data. **A)** A Nyquist representation; Inset is the expansion of the -0.4 V applied potential. **B)** Bode plots of the same data at the same three applied potentials and frequency range.

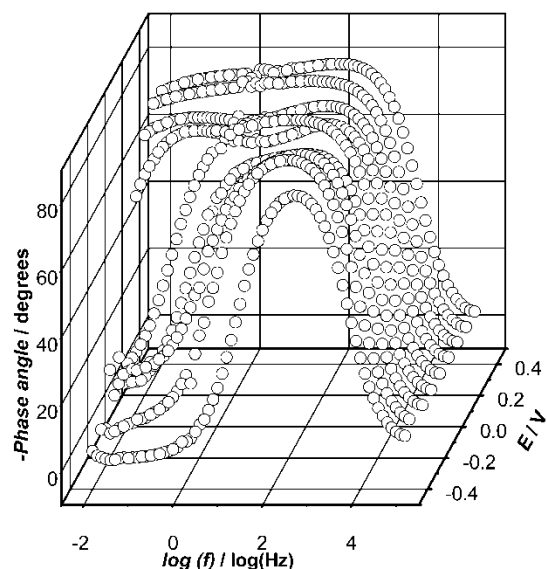


Figure 3-32 Bode plots of SAMs of **22** in pH 1 H₂SO₄ solution at 24.2 °C using excitation frequencies of 100 kHz to 10 mHz and applied DC potentials from -0.4 V to 0.3 V vs. Ag|AgCl|KCl_{3M} in 100 mV steps.

This evidence suggests that under anodic potentials, the SAM of **22** also behaves as a series RC circuit (**Figure 3-28A**). At this anodic potential, the monolayer of **22** is completely oxidized and no ET equilibrium would take place as in the case of $E_{app} = E^{0'}$. It renders the elimination of the faradaic RC elements from the circuit **3-28C** leaving behind the parallel element R_d in addition to the R_s and C_{dl} . However, it is suspected that only small H₃O⁺ ions have penetrated into the monolayer even though nitrogen of the aryl amine may also be protonated (ammonium species) in this highly acidic medium, hence would attract the oppositely charged HSO₄⁻ ions. The interaction of the positively charged electrode repels the positively charged proton / hydronium ion penetration, and hence eliminating the R_d from the circuit resulting in circuit **3-28A**. Circuit **3-28A** suggests that the SAM of **22** is an uncharged blocking electrode and the CNLS fitting

results show that R_s is $2.4\Omega\cdot\text{cm}^{-2}$ and C_{dl} is $41\mu\text{F}\cdot\text{cm}^{-2}$. Even though the interfacial capacitance is named as C_{dl} , it is, in reality, composed of two capacitances (C_{dl} and C_{ml}) in series. In general, for most alkanethiol SAMs with 10 or more carbon alkyl chain has an interfacial capacitance between $1\text{-}5\mu\text{F}\cdot\text{cm}^{-2}$.³⁹ Nevertheless, the high value for this SAM of **22** is acceptable since it is an electro active SAM. Unlike nonelectroactive SAMs, the electro active SAM would have a different solvation environment resulting in higher capacitance. Furthermore, the uncharged monolayer is a result of positive charges on the nitrogen (ammonium) removed by the applied anodic potential. Protonation of an aryl amine is a function of surface pK_a , the bulk pH, and the applied electric field. Electric field driven protonation / deprotonation reactions are non-faradaic process that have been described by Smith and White¹⁰⁵, Fawcett *et al.*^{106,107}, and others.¹⁰⁸

In the $E_{app} = E^{0'}$ region, the CNLS fitting results shows that the system is better represented by circuit **3-28C** yielding values for each element consistent (see appendix for values) with the values that are shown in **Table 7** at 24.8°C . Moreover, when the potential is set to $E^{0'}$ both the protonated and neutral surface confined aryl amines could populate the monolayer. Comparisons of rate constants of similar quinone redox reactions measured by Hong *et al.* shows charge transfer kinetics with a rate of 0.003s^{-1} of a C_{10} -thiol quinone SAM redox reaction in acidic media.³³ Clearly, the measured charge transfer rates are not consistent with Hong's charge transfer rates. The three orders of magnitude difference (0.003 s^{-1} vs. 7.4 s^{-1}) is a clear indication that the surface anthraquinone redox species is not the neutral anthraquinone and suggests the amino group is fully protonated to the ammoniumAQ. In addition, under equilibrium conditions

there is less of a driving force for ion penetration compared to $E_{app} < E^{0'}$ region, resulting in a larger R_d term.

Once the applied potential is scanned to -0.4V, the electrochemistry of the system is changed to a single peak for the phase angle and a sigmoid shape for the total impedance in the Bode plot; a semicircle in the Nyquist plot with the smallest diameter of all semicircles. The qualitative features of the system's impedance agree with the circuit model RC parallel elements in series with R_s , as in figure **3-28B**. The fitting values for each elements are $565\Omega\cdot\text{cm}^2$, $21\mu\text{F}\cdot\text{cm}^{-2}$, and $2.5\Omega\cdot\text{cm}^2$ for R_d , C_{dl} and R_s , respectively. The peak in Bode plot shifted toward the high frequency region because of low value for the R_d . When the applied potential is 260mV more negative than the equilibrium potential of the **22**, it is assumed all the redox centres are fully reduced, thus increasing the faradaic R_{CT} element value to infinity. This situation makes the electro active monolayer behave as a charged blocking layer for the electrode and the monolayer capacitance replaces the Helmholtz or double layer capacitance. The remaining resistance in **3-28B** is represented by ion penetration resistance or R_d , because this element is only visible or active at more cathodic potentials than the $E^{0'}$. It is suggested that the R_d is caused by ion penetration or defects but not by pinholes, because pinholes would have been observed under more anodic potentials. In addition, at -0.4V applied potential the value for the R_d is smallest of all the applied potentials indicating that low resistance for positively charged protons to pull towards negatively charged electrode. Furthermore, it is reasonable to assume that all the aryl amines are protonated in this region due to cathodic applied potential and pH (**Figure 3-33**). The solution resistance remains constant for all regions.

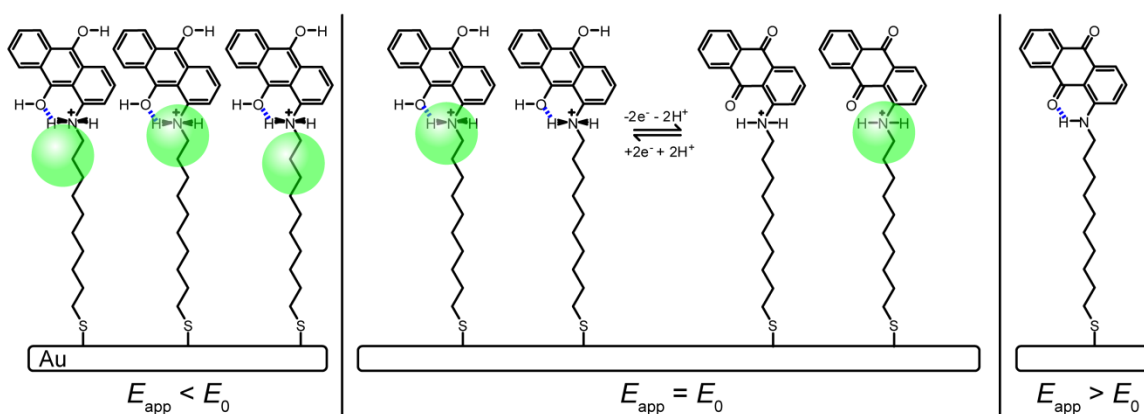


Figure 3-33 Proposed reactions occurring on SAMs of **22** on Au surface under 3 applied potential regions.

Typical aryl aminiums have pK_a s of ~ 5 and our results clearly show the surface pK_a is substantially different from solution pK_a . A report from Crooks¹⁰⁸ has measured the surface pK_a of a 4-aminothiophenol SAM to be 6.9 using a differential capacitance method, which is 2 orders of magnitude different compared to the bulk pK_a value of 4.3 determined by titration experiments. The results of **22** cannot assign a surface pK_a value, but do indicate the protonated aminoAQ can be deprotonated by applied dc potential even in 0.1 M H_2SO_4 solution. Additional investigations into pH were undertaken and the resulting CVs are included in **Figure 3-34**. The CVs in acidic media show fast quasireversible behavior and more basic solutions exhibited the typical quinone redox response of a cathodic shift (**Figure 3-34**). Because quinone redox processes are strongly dependent on proton concentration, the effect of increasing the pH of the bulk solution necessitates larger negative potentials to undergo the anthraquinone redox reactions.

Previous results of quinone redox chemistry have shown the rate of the PCET reaction increases in more basic solutions³² and our findings also support a faster redox reaction (as assessed by the small peak separation in CV) at pH 11.5.

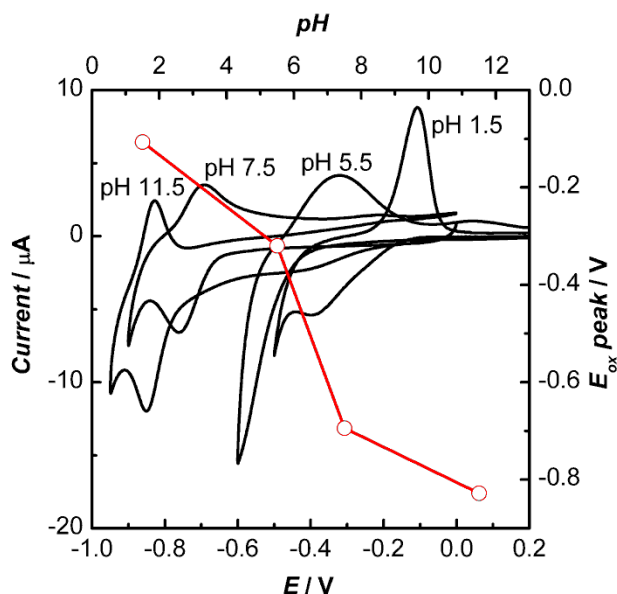


Figure 3-34 Cyclic voltammograms of SAMs of **22** at different pHs and scan rates of $100 \text{ mV}\cdot\text{s}^{-1}$. The left and bottom axis are for the CVs and the top and right axis show the relationship between pH and oxidation peak potential. Note the pH solutions were adjusted with 3 M NaOH and 3M HCl solutions and are unbuffered. No attempts were made to have uniform ionic strength solutions.

An Eyring and Arrhenius plots of the kinetic data of SAMs of **22** from **Table 7** is shown in **Figure 3-35**. From the linear plot, E_{act} , ΔH^\ddagger and ΔS^\ddagger of the charge transfer reaction (k_{ct}) were found to be $69 \text{ kJ}\cdot\text{mol}^{-1}$, $67 \text{ kJ}\cdot\text{mol}^{-1}$ and $-5 \text{ J}\cdot\text{mol}^{-1}$, respectively. The activation energy of the ammonium-anthraquinone redox reaction is high at $69 \text{ kJ}\cdot\text{mol}^{-1}$, especially when compared to a similar C_{10} -thiol derivatized benzoquinone SAM ($34 \text{ kJ}\cdot\text{mol}^{-1}$).¹⁰⁹ The energetics are consistent with the notion that an intramolecular hydrogen-bond to the

nearest carbonyl group, forming a favourable six-member ring, is broken upon reduction. The presence of an intramolecular hydrogen-bond in the oxidized aminoanthraquinone was confirmed by dilution $^1\text{H-NMR}$ experiments (**Figure 3-36**) of **22**. The energetic contribution attributed to the intramolecular hydrogen-bond of **22** was quantified at $30 \text{ kJ}\cdot\text{mol}^{-1}$ following Reuben's ¹¹⁰ work using the chemical shift of the amine proton at 9.75 ppm compared to *N*-methylaniline (3.69 ppm). Synthesis of the reduced dihydroxy-aminoAQ was unsuccessful, so DFT calculations of the protonated, dihydroxy-aminoAQ were undertaken to probe whether intramolecular hydrogen bonding plays a role.

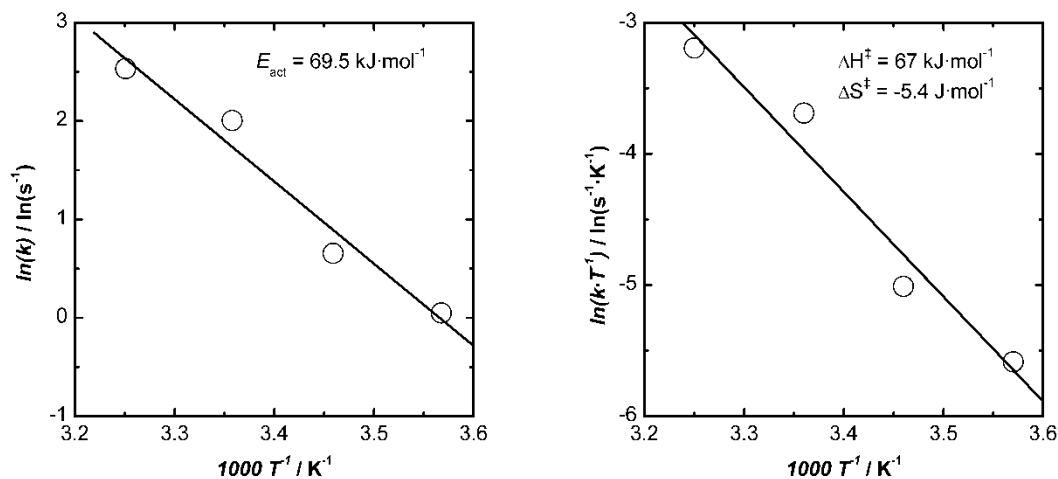


Figure 3-35 Eyring and Arrhenius plots of charge transfer reaction for **22**.

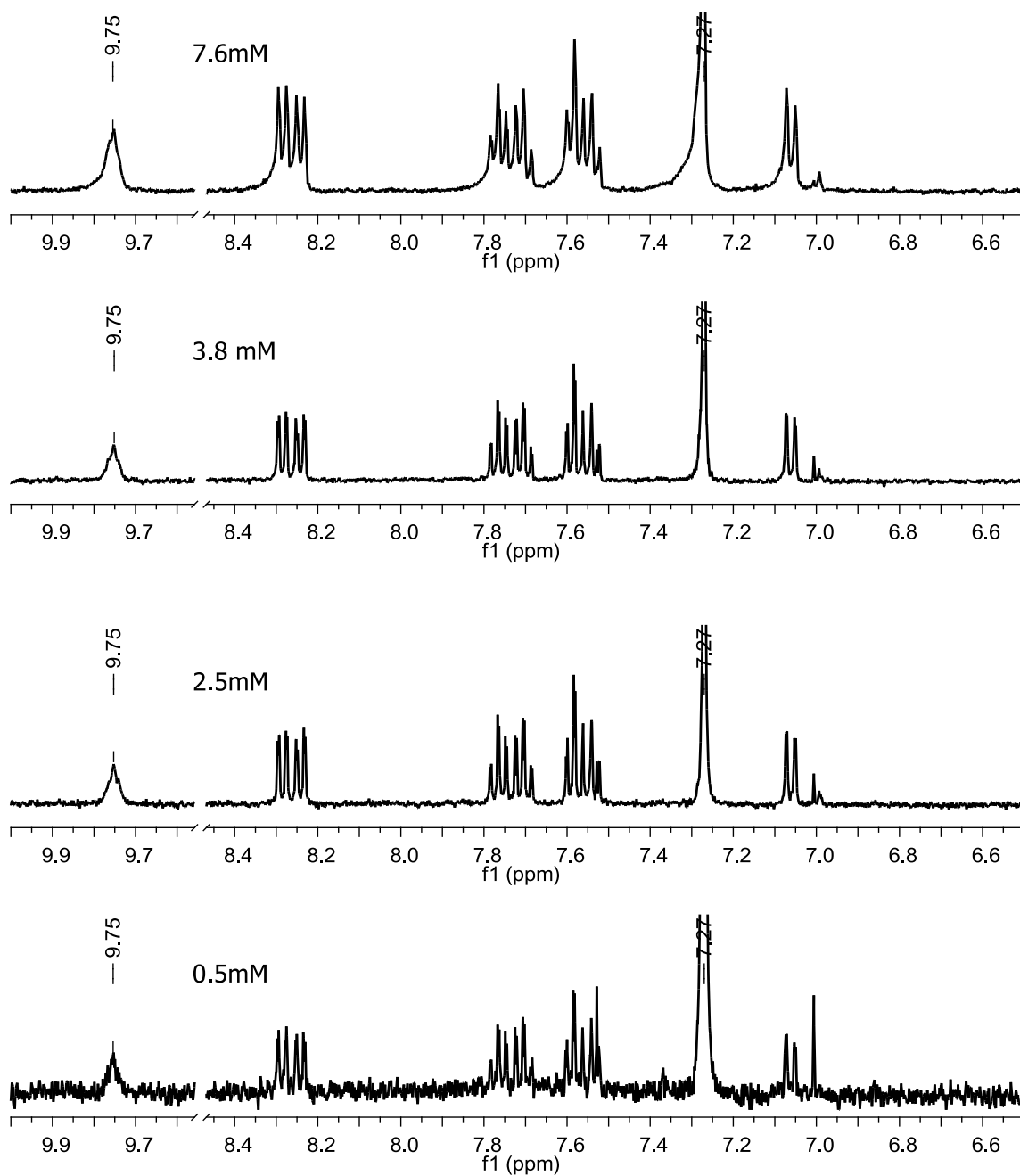


Figure 3-36 $^1\text{H-NMR}$ of **22** in CDCl_3 of the amine and aromatic regions at various concentrations indicating that the amine proton is only involved in intramolecular hydrogen bonding.

3.2.3.2 Electron Transfer studies of **27**

Working electrodes modified with SAMs of **27** were subjected to electrochemical studies by using CV and EIS techniques as functions of pH and temperature. Each experiment was performed with freshly prepared working electrode. Electrochemical parameters extracted from each technique will be discussed separately. However, the ET kinetic properties such as electron transfer coefficient (α), apparent ET rate constant (k_{app}), cathodic ET rate constant (k_c), and anodic ET rate constant (k_a) obtained are discussed as a single section.

CVs of all pHs show a quasi reversible single redox wave attributed to proton coupled electron transfer (PCET) of anthraquinone redox centre. A typical background subtracted cyclic voltammogram is seen in **Figure 3-37** for pH 3.34 at $25\pm 0.5^\circ\text{C}$ (CVs for other temperatures are included in the appendix).

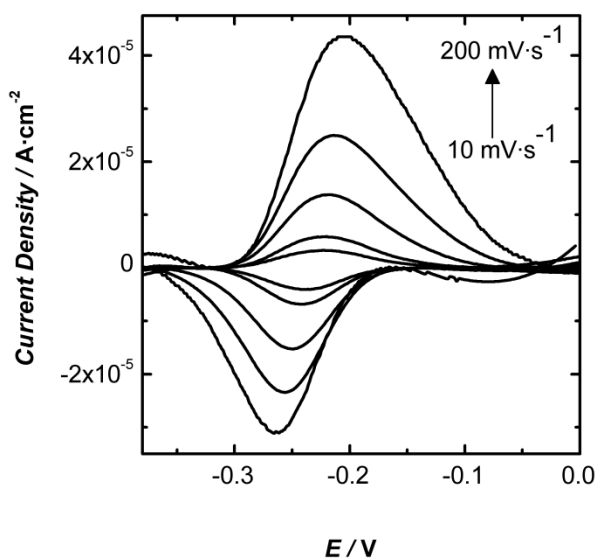


Figure 3-37 Example cyclic voltammograms of **27** at scan rates from $10 \text{ mV}\cdot\text{s}^{-1}$ to $200 \text{ mV}\cdot\text{s}^{-1}$ in pH 3.34 solution at $25\pm 0.5^\circ\text{C}$; Potentials are referenced to $\text{Ag}|\text{AgCl}|\text{NaCl}_{3\text{M}}$.

Under the conditions that thermodynamics rather than kinetics prevail, the current response of the electro active SAM of **27** provided reversible electrochemical information such as, formal potential ($E^{\theta'}$), full width at half maximum (FWHM), peak splitting (ΔE_p), and surface coverage (Γ).

Usually, CVs were acquired between $10 \text{ mV}\cdot\text{s}^{-1}$ and $1 \text{ V}\cdot\text{s}^{-1}$ scan rates. However, the solvent potential window and monolayer stability determined the actual scan range in some instances. Monolayers were stable for the usual scan rates, and stability was always checked by comparing the initial CV of a selected scan rate with the CV of the same scan rate after acquiring all CVs. Background subtracted CVs of complete pH range at $50\text{mV}\cdot\text{s}^{-1}$ scan rate is shown in **Figure 3-38**.

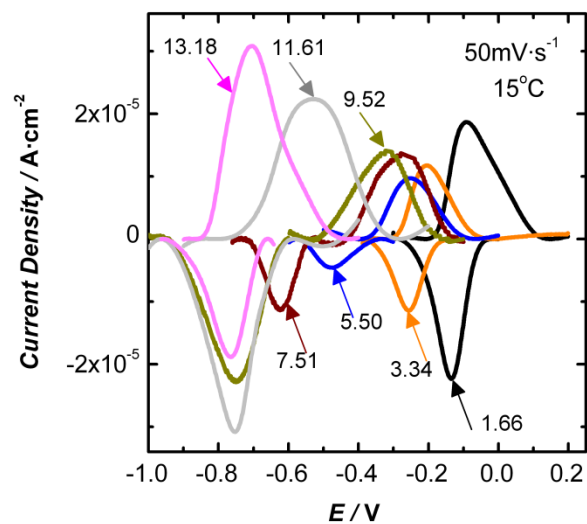


Figure 3-38 Cyclic voltammograms of **27** at scan rate $50 \text{ mV}\cdot\text{s}^{-1}$ as a function of pH at $15\pm 0.8^\circ\text{C}$; Potentials are referenced to $\text{Ag}|\text{AgCl}|\text{NaCl}_{3\text{M}}$. Various pHs are indicated by arrows and colours.

A flat region away from the either side of the faradaic peak in an i - E curve indicates a constant charging current. Almost all of the CVs have shown the mentioned characteristics in the anodic region, i.e. the potential region more positive to the anodic peak, but not in the cathodic zone. The possible reason for not observing the flat region in the cathodic region was that the switching potential in the cathodic side could not be extended to potentials that are more negative because the SAM can desorb.¹¹¹ The PEMIRRAS results also support that the SAM of **27** is not an ideal blocking layer (discussed in the appropriate sections).

The following discussion deals with the thermodynamic parameters extracted from CV as a function of pH at constant temperature then these data will be compared with the other temperatures.

Table 9 summarizes the extracted thermodynamic parameters from CV at 25°C as a function of pH. $E^{0'}$ values of the surface redox couple anthraquinone **27** is pH dependant as can be seen from **Figure 3-39**, which shows the expected Nernstian behaviour for a proton coupled electron transfer redox reaction. The formal potential of the anthraquinone **27** became more negative as the pH of the solution was increased. This shift in $E^{0'}$ with pH is in accordance with Laviron's theory based on the nine member square scheme.²⁷ In the pH range between 1.5 and 9.5 the slope of the $E^{0'}$ vs. pH graph is ~60mV/ pH consistent with the 2e, 2H⁺ mechanism, but pHs above 9.5 the slope is ~40mV/pH, which may correspond to 2e, 1H⁺ mechanism (actual value for 2e, 1H⁺ process is 30mV/pH unit).^{26,37} The data are consistent with the anthraquinone **27** undergoing the following mechanisms at different pHs.¹¹²

Furthermore, other temperatures also follow the same trend as can be seen from the **Tables 10, 11, and 12.**

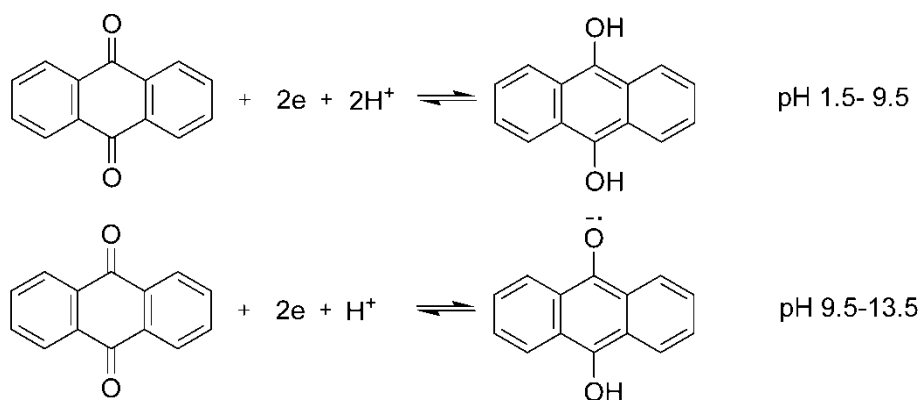


Table 9 Extracted thermodynamic parameters from CV for **27** at 50 mV·s⁻¹ at 25^o±0.5C as a function of pHs.

pH	E ^{0'} mV	ΔE _p mV	Γ × 10 ¹⁰ mol·cm ⁻²	FWHM / mV	
				Anodic	Cathodic
1.66	-80	75	2.3	171	107
3.34	-235	29	1.5	121	77
5.50	-345	283	1.7	127	46
7.51	-460	287	1.3	193	72
9.52	-580	54	1.5	270	65
11.61	-648	206	6.6	289	99
13.18	-739	84	10.4	273	140

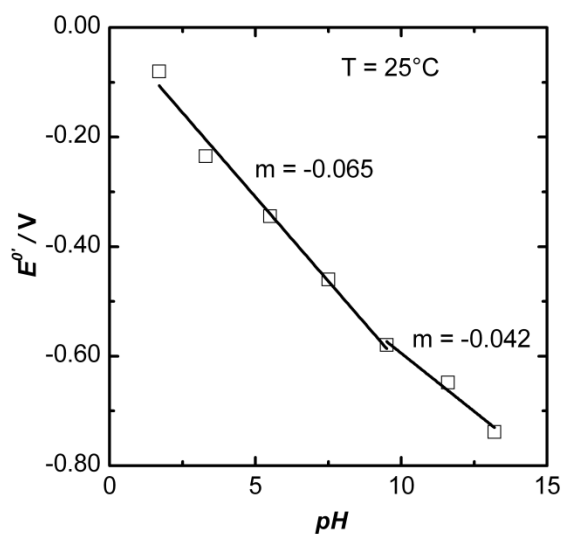


Figure 3-39 Formal potential of SAM of **27** vs. $\text{Ag}|\text{AgCl}|\text{NaCl}_{3\text{M}}$ as a function of pH at $25^\circ \pm 0.5^\circ\text{C}$

Table 10 Extracted thermodynamic parameters from CV for **27** at $50 \text{ mV}\cdot\text{s}^{-1}$ at $15 \pm 0.8^\circ\text{C}$ as a function of pHs.

pH	$E^{0'}$ mV	ΔE_p mV	$\Gamma \times 10^{10}$ $\text{mol}\cdot\text{cm}^{-2}$	FWHM / mV	
				Anodic	Cathodic
1.66	-107	42	2.6	174	91
3.34	-230	49	1.4	135	88
5.50	-361	219	1.1	191	98
7.51	-451	338	2.6	193	79
9.52	-552	426	3.8	275	79
11.61	-641	229	5.8	314	115
13.18	-734	60	4.3	248	120

The formal potential value changes slightly with temperature within a pH, and for pHs 3.34, 7.51, 11.61, and 13.18, the most negative $E^{0'}$ value was obtained for 35°C. The maximum change observed was ~31 mV (for pHs 1.5, 5.5, and 9.5) and minimum change was ~15 mV (for pH 3.5) respectively, which is reasonable considering experimental uncertainties such as drift in the reference electrode.

The temperature at 15°C is selected for the explanation of peak splitting (ΔE_p). As can be seen from the **Table 10**, the peak splitting (ΔE_p) values deviate from the ideal value of zero. However, a trend can be seen for temperatures 5°C (**Table 11**), 15°C, and 35°C (**Table 12**). The ΔE_p increases from low pH (1.5-3.5) to mid pH (5.5-9.5), then, it decreases at high pH (11.5-13.2). A nonzero peak splitting could arise from several factors. Apart from factors such as defects, non-ideal packing, and rough surfaces already mentioned, different electrolytes that were used to obtain the different pHs may have contributed to nonzero peak splitting. Furthermore, changing the oxidation state of the redox centre may change the solvation of the redox centres by ion pairing, hydrophobicity / hydrophilicity of the redox centre or the structure of the SAM, such as phase changes in the monolayer.⁹⁹ Also, the solution resistance can cause nonzero ΔE_p . However, the effect of the solution resistance was minimized by having electrolyte concentrations above 0.1 M.⁹⁹ The reasons for the scattering of ΔE_p with pH are not obvious, and a systematic study is needed. Moreover, no trend of ΔE_p with temperature was observed.

The other important parameter that can be extracted from the peak shape of the CV is FWHM, which provides information about the thermodynamic heterogeneity of the SAM

of **27**. The CVs obtained for SAM of **27** did not show the FWHM value close to the 45mV expected for a 2 electron process, except for certain cathodic peaks (**Table 9,11**).

Generally, anodic peaks are broader than the cathodic peaks.

Table 11 Extracted thermodynamic parameters from CV for **27** at $50\text{mV}\cdot\text{s}^{-1}$ at $5\pm 1^\circ\text{C}$ as functions of pHs.

pH	$E^{0'}$ mV	ΔE_p mV	$\Gamma \times 10^{10}$ $\text{mol}\cdot\text{cm}^{-2}$	FWHM / mV	
				Anodic	Cathodic
1.66	-111	30	1.6	97	74
3.34	-225	59	1.3	151	90
5.50	-330	261	0.9	288	44
7.51	-452	312	2.1	194	102
9.52	-548	453	3.6	225	133
11.61	-643	240	5.4	312	155
13.18	-713	20	3.1	171	135

Table 12 Extracted thermodynamic parameters from CV for **27** at $50\text{mV}\cdot\text{s}^{-1}$ at $35\pm 0.5^\circ\text{C}$ as functions of pHs.

pH	$E^{0'}$ mV	ΔE_p mV	$\Gamma \times 10^{10}$ $\text{mol}\cdot\text{cm}^{-2}$	FWHM / mV	
				Anodic	Cathodic
1.66	-110	8	2.2	96	73
3.34	-240	20	1.3	151	64
5.50	-343	131	1.0	250	108
7.51	-478	388	1.7	186	90
9.52	-555	345	3.9	129	137
11.61	-660	145	6.3	254	129

This evidence shows that there could be existence of multiple formal potentials or double layer effect, high surface concentration of redox centres.^{30,98} Basically, multiple formal potentials are mainly a result of different micro environments around the redox group such as those buried inside the monolayer, or those exposed to the external surface. The SAM under investigation has 100% anthraquinone redox pendants (pure SAM) and it is reasonable to assume that there may be interactions between adjacent anthraquinones affecting the shape of the CV. Zhang *et al.*⁹⁷ and Hickman *et al.*¹¹³ showed that high concentration of redox centres in a monolayer increases the interaction between them, which results in broadening of the CV peaks deviating from the FWHM $91/n$ mV formula. Furthermore, Chidsey *et al.*¹¹⁴ reported that ferrocene SAMs show ideal criteria of FWHM = $91/n$ when the surface coverage of redox centre is 30% or less, which can be achieved by diluting the electro active SAM with the same length alkanethiols (mixed SAM). SAMs consisting of more than one type of alkanethiol are called mixed SAMs. The electrolyte concentration was always maintained above 0.1 M, which is far greater than the redox centre concentration on the surface to reduce the double layer effect. Otherwise, double layer effects can make the CV peaks broader than the ideal 45mV (assuming 2e process). Besides, no correlation was found between FWHM and temperature or pH.

The area under the baseline corrected faradaic peak of the *i-E* curve corresponds to the approximate coverage (Γ) of the redox group on the electrode surface. **Table 10** shows the coverage of the SAM of **27** at 15°C. The coverage decreases as the pH is increased to the lowest value at pH 5.5, then it increases with further increasing of pH. Although similar trends can be seen for temperatures of 5°C (**Table 11**) and 35°C (**Table 12**), the

coverage at 25°C (**Table 9**) with various pHs is scattered. The pH effect on monolayer coverage is unexplainable at this point.

The temperature effect on coverage of SAM of **27** could not be ascertained due to scattered coverage data. Initially, it was predicted that the potential scan might destroy the monolayer at high temperature of 35°C, but this is not occurring as verified by the monolayer integrity experiments. Note, for pH 13.18 the monolayer was destroyed during CV measurements.

A close packed monolayer of SAM of **27** with $12 \text{ \AA} \times 3.35 \text{ \AA}$ cross sectional area should give $4.2 \times 10^{-10} \text{ mol}\cdot\text{cm}^{-2}$ of maximum coverage. At this point, the higher measured values at high pH (pH 11.5-13.2; **Table 9, 10, 11, 12**) could not be explained. SAMs of AQ derivatives reported by others have coverage ranging from $(1.7 \times 10^{-10} \text{ mol}\cdot\text{cm}^{-2})^{13}$ to $(2.9 \times 10^{-10} \text{ mol}\cdot\text{cm}^{-2})$.⁹⁷

The surface attachment of the AQ redox centre is verified by plotting i_p vs. scan rate (v) as seen in **Figure 3-40** for pH 1.66 buffer solution (other graphs are included in the appendix). The linear relationship between i_p and scan rate is an indication of surface confinement of redox centres, according to the equation $i_p = (n^2 F^2 / RT) \nu A \Gamma$, where A is area of the electrode; other symbols have their usual meanings.³⁹

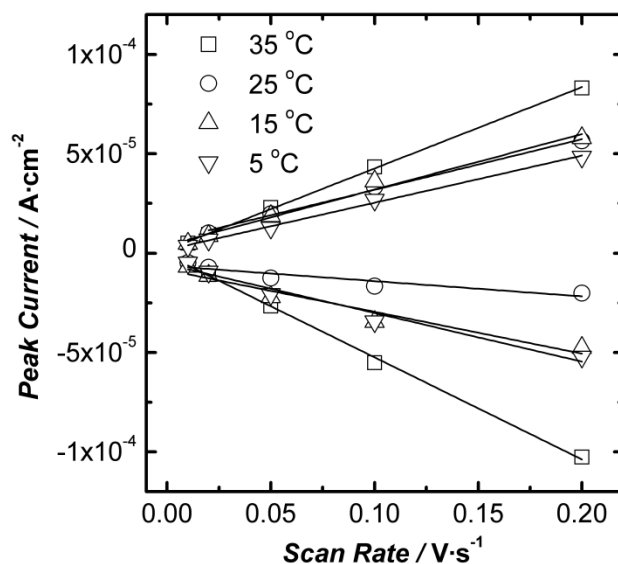


Figure 3-40 Background-subtracted peak current at various scan rates and temperatures in pH 1.66 buffer solution for SAM of **27**

The EIS measurements were generally obtained in a frequency range between 5 mHz and 100kHz with an AC perturbation signal of 10mV at the formal potential of SAM of **27** in different pH buffer solutions as a function of temperature. At the formal potential, the concentration of oxidized and reduced species of the redox groups is equal. Since EIS is recorded over many orders of magnitude of frequency, the monolayer integrity assessment was essential, and it was done by comparing initial CVs to the CVs recorded after each EIS experiment. All data shown in this work fulfilled the thermal stability criterion of less than 5% difference in integrated charge between the CVs recorded before and after EIS.

Bode and Nyquist plots of the electro active monolayer are in **Figures 3-41 to 3-47**. Complex plane analysis of these spectra was done by fitting the data to equivalent circuits (**Figure 3-48A and Figure 3-48B**) involving solution resistance (R_s), interfacial CPEs

(C_{dl} and C_{ml}), charge transfer resistance (R_{CT}), and ion penetration resistance (R_d). Impedance plots and fitting data provide information about quality of the SAM of **27** and ET kinetics. This part of the discussion will deal with the general electrochemical behaviour of the system extracted from impedance data, and it will be discussed for each pH, then general trends as a function of pH will be covered.

At pH 1.66 buffer solution, the SAM of **27** behaves in the same manner that the SAM of **22** in 0.1M H₂SO₄ solution. As a result, the analysis of the impedance of the SAM of **22** holds valid for SAM of **27**. At high frequency ($\sim \log 5$ Hz), the phase angle (**Figure 3-41** and circuit diagram **3-48A**) is near zero for all temperatures with low resistive impedance ($\sim 2.5 \Omega \cdot \text{cm}^{-2}$), which represents the R_s and the value is reasonable considering the high electrolyte concentration. Also, the high frequency ($\sim \log 3$ Hz) limiting behaviour of the double layer capacitance C_{dl} is visible in Bode plots with a peak having phase angle range of 60-70 degrees except for 35°C, which has phase angle close to 40 degree. As mentioned in the introduction, this is a constant phase element (CPE), and the power modifiers for the CPE for all temperatures are ~ 0.82 , which indicates that the double layer does not behave as a pure capacitor. The value of C_{dl} is in the range of 28-95 $\mu\text{F} \cdot \text{cm}^{-2}$, which does not correlate with temperature. The C_{dl} value for 35°C should be considered with care because it is associated with high error in fitting. However, these values suggest there are temperature dependent changes in the C_{dl} . As the frequency decreases, the impedance of the charge transfer resistance (R_{CT}) becomes comparable to that of C_{dl} resulting in a significant ratio of the total current passing through the Faradaic impedance elements R_{CT} and monolayer capacitance (C_{ml}). Now, the total impedance of the system becomes more resistive because the two parallel capacitors C_{dl} and C_{ml} give

total capacitive impedance lower than the resistive-impedance. Consequently, the phase angles decrease from the peak values at 1000 Hz to 10 Hz, at 25°C. Further decreases of the frequency (< 10 Hz), increases the capacitive impedance according to $Z = 1/j\omega C$ resulting in another peak with the phase angle $\sim 80^\circ$ degrees for all temperatures. Moreover, a marked drop [from 393 to 25 $\Omega \cdot \text{cm}^{-2}$; at 15°C, the value 412 $\Omega \cdot \text{cm}^{-2}$ is a outlier (**Table 13**)] in the charge transfer resistance is observed with increasing temperature, which follows the common relationship between temperature (T) and ET rate constant (k_{app}). The k_{app} was calculated using **Equation 14**. The interfacial monolayer CPE C_{ml} values increase with temperatures, indicating systematic structural changes with temperature, and the power exponents ($n \sim 0.8$) values are consistent for all temperatures indicating low surface roughness, and reasonable surface blocking. Probably, ion permeability into the monolayer has caused the C_{ml} value to increase with temperature as can be seen from the decrease of R_d at high temperature. In the low frequency region of < 1 mHz, the impedance of the cell tends to be resistive as marked by the zero phase angle. This resistive impedance is mainly caused by the ion penetration into the hydrophobic monolayer due to defect sites in the blocking layer.¹⁰² Since R_d is detected in the low frequency region, it supports the hypothesis that ion permeation is a kinetically slow process.^{13,102} The circuit elements, R_d is indeed temperature dependant, i.e. R_d is linearly proportional with $1/T$ having values 342 $\text{k}\Omega \cdot \text{cm}^2$ at $5 \pm 1^\circ\text{C}$ and 82 $\text{k}\Omega \cdot \text{cm}^2$ at $34 \pm 0.5^\circ\text{C}$.

The Nyquist plot (**Figure 3-49**) of the total in-phase (Z') and out-of-phase (Z'') impedances by theory should have two semicircles, whose diameters represent two

resistive elements R_{CT} and R_d . However, in **Figure 3-49** these two appear as one semicircle, because the value of the R_d is much larger than that of the R_{CT} . The temperature dependence of R_d can also be seen in the graph by having the largest diameter of the semicircle at $5 \pm 1.0^\circ\text{C}$.

At pH 3.34 (**Figure 3-42**) buffer solutions, the system has electrochemistry similar to pH 1.66, and circuit **A** (**Figure 3-48**) was used for CNLS curve fitting. Two peaks are clearly distinguishable for pH 3.5. R_s values are larger than that of in pH 1.66, which could be attributed to activity of the organic electrolyte phthalate. However, R_s decreases with increasing temperature as was shown with pH 1.66. The highest values for C_{dl} were obtained at 35°C , which is similar to the value at pH 1.66. The n values (~ 0.9) indicate close to capacitive behaviour and the linear relationship between R_{CT} and $1/T$ is also established.

Nyquist plots for pH 3.34 shows a single semicircle for the same reason that was explained for pH 1.66, and the diameter of the semicircle increases as the temperature decreased indicating temperature dependent R_{CT} .

At pH 5.5, Bode peaks appear as one peak or a broad peak with a shoulder. Data was adequately fit to **Figure 3-46A** circuit. A remarkable difference is noticed for C_{ml} at pH 5.5 compared to pH 1.66 and 3.5, which could be attributed to the high concentration of phthalate anion. As usual, R_d decreased with increasing temperature, but it was strikingly lower in pH 5.5 (**Table 13**). This gives an indication that anionic phthalates could penetrate into the monolayer easily with, probably, structural changes in monolayer as shown by the power exponent value ($n \sim 0.5$) of the CPE. Furthermore, the very low value

of the R_d in pH 5.5 shifts the second peak of the Bode plot towards high frequency region yielding the peak with a shoulder.

Nyquist plots for both pHs (3.34 and 5.50) show a single semicircle for the same reason that was explained for pH 1.66, and the diameter of the semicircle increases as the temperature decreased indicating temperature dependent R_{CT} .

The electrochemistry of the SAM of **27** changed in pH 7.5 buffer solution; The Bode plots (**Figure 3-44**) show a single peak and the total impedance of the system shows a sigmoidal shape. The circuit **3-28A** was used initially to fit the experimental data, but it was not successful. The RC parallel circuit better describes the shape of the Bode plot. However, the monolayer was intact as assessed by CV after EIS experiments, which mean the data at pH 7.5, should fit to circuit **B** in **Figure 3-48**. The inclusion of the monolayer capacitance C_{ml} in the circuit for CNLS fitting provided unfavourable fitted results, especially for the power exponent value of the C_{ml} because too few data points were available in the low frequency region. A simulation test was carried out with the pH 1.66 data to prove the assumption. With a full range of frequencies (100 kHz to 0.1 mHz) CNLS curve fitting was carried out with circuit **3-28A** and resulted in reasonable values for all the circuit components. After removing the low frequency data points (1 Hz to 0.1 mHz), the CNLS curve fit was repeated using circuit **3-28A**, which resulted in different values for circuit components, especially $n \sim 0.5$ for C_{ml} . Curve fitting with circuit **3-28B** also gave similar values. This control experiment suggests the C_{ml} values with $n \sim 0.5$ are unreliable.

Besides the movement of the Bode peak (**Figure 3-44**) with frequency, visually, the Bode plots do not show significant temperature effects. At high frequency, the resistive

impedance is dominated by R_s having values ranging from 10.3 to 6.6 $\Omega\cdot\text{cm}^2$. R_s decreases as the temperature is increased, a universal phenomenon seen throughout this pH study. Also, the high frequency limiting behaviour of the double layer capacitance C_{dl} is visible in Bode plots with a peak having phase angle ~ 80 degrees, and the value of C_{dl} increases with lower temperatures. Power modifiers for the CPE for all temperatures are ~ 0.89 , which indicates that the double layer does not behave as a pure capacitor. As the frequency decreases, the impedance of the charge transfer resistor (R_{CT}) is comparable to the C_{dl} resulting in a significant ratio of total current passing through the Faradaic impedance elements R_{CT} and monolayer capacitance (C_{ml}). Now (~ 100 Hz to ~ 1 mHz), the total impedance of the system becomes more resistive because, the two parallel capacitors C_{dl} and C_{ml} give a total capacitive impedance lower than the resistive impedance. Consequently, phase angles decrease from the peak values. R_{CT} values decrease as the temperature is increased (**Table 13**) except for 5°C and 15°C, which have identical values. Further decreases in frequency (~ 100 mHz) lowers the phase angle to almost zero, indicating capacitance of the monolayer is quite high, in other words, the impedance is more resistive. Even though the low frequency (< 1 mHz) data is not as reliable because of inherent error in its measurement, the Bode plots around 10 mHz show that the phase angle starts to increase suggesting the addition of impedance of C_{ml} to the total impedance. This effect can also be seen on the total impedance curve. Moreover, in pH 1.66 the second peak appeared because of the additional impedance caused by the R_d element. Nevertheless, at pH 7.5, the Bode plot shows the R_d should have a very large value. Accordingly, the second peak might appear at very low frequency, which is only discerned by the impedance plots not by the CNLS fitted results.

No attempt was made to acquire data lower than 1 mHz. The data suggest that unlike hydronium ions, the alkaline metal cations hardly penetrate into the monolayer.

The Nyquist plots (**Figure 3-49 to 3-50**) also show that there is a second semicircle starting to form, but it is not completed because not enough low frequency data points were obtained. Further, the diameter of the visible semicircle shrinks when the temperature is increased indicating that R_{CT} is inversely proportional to temperature.

The electrochemistry of SAM of **27** between pH 9.51 and 13.18 shows very similar responses to pH 7.51 (**Figure 3-45 to 3-47**). CNLS fitting could not be done for data acquired at 25°C and 35°C at pH 9.51 buffer solution because the fitting resulted in negative values for R_{CT} . However, for 15°C and 5°C, the CNLS fitting of the impedance data was performed. Solution resistance was noticeably high (**Table 13**) compared to other pHs, which is $30.1\Omega\cdot\text{cm}^{-2}$ and $17.5\Omega\cdot\text{cm}^{-2}$ for 5°C and 35°C, respectively, which could be attributed to the borax buffer. Likewise, at 5°C, the highest R_{CT} was obtained compared to all measured pHs. The Bode plot near 10 mHz shows that the phase angle slowly raising to a higher value from near zero denoting that the kinetically slow ion penetration process is contaminating the impedance of the system. Nyquist plots (**Figure 3-49**) show a poorly resolved single semicircle, whose diameter narrows with increasing temperature.

The extension of the electrochemistry of SAM of **27** at pH 7.51 can be seen at pH 11.61 (**Figure 3-46**). R_s decreases with lowering the temperature; R_{CT} has reciprocal relationship with temperature except for 25°C whose value is higher than 15°C. Clearly, the Bode and Nyquist plots show that the resistance for ion penetration is decreasing as indicated by the increasing phase angle value in the low frequency region (10 mHz).

At pH 13.18, the EIS data (**Figure 3-47**) are fitted to circuit **B** in **Figure 3-48**, but the Bode plot provides shapes that are different from other pHs. The Nyquist plots do not show semicircles and the Bode plots show indistinguishable peaks. CV analysis of monolayer integrity before and after EIS experiments assures that the monolayer is intact. Nevertheless, the CNLS fitted results show normal behaviour of the elements. R_s value is constant around $2.5\Omega\cdot\text{cm}^{-2}$ for all temperatures suggesting that when simple $z+$ and $z-$ salts (KCl, NaOH, HCl) were used, the solution resistance can be maintained low. R_{CT} at this pH are the lowest among all pHs; hence ET are the fastest, except pH 1.66 at 35°C .

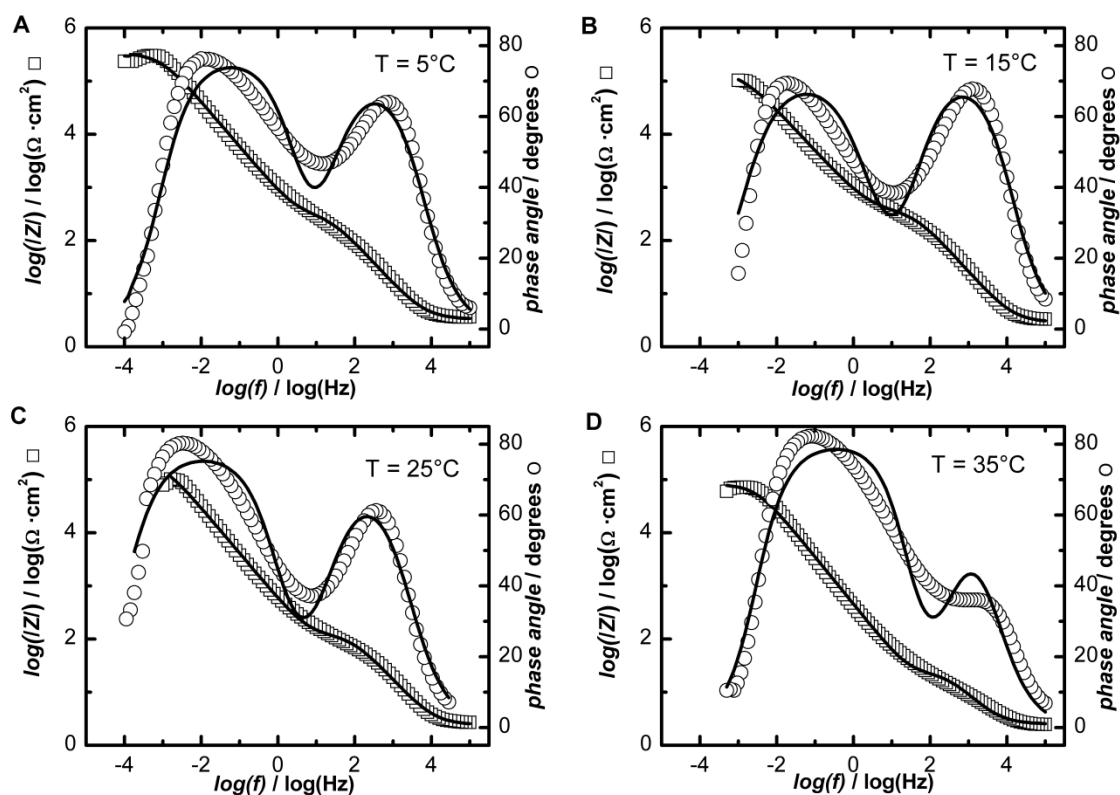


Figure 3-41 EIS Bode plots for SAMs of **27** in pH 1.66 buffer solution at applied potential of -0.11 V vs. Ag|AgCl|NaCl_{3M} with 10 mV excitation signal and frequency range from 100 kHz to the values shown in the plots. All experimental data are shown as symbols and lines represent the best-fit data. Equivalent circuit **A** from **Figure 3-48** was used to fit data. Experiments were performed in a three electrode electrochemical cell using Au disk modified with SAM of **27**, Pt mesh and Ag | AgCl | KCl_{3M} electrodes as working, counter, and reference electrode, respectively. **A**) 5 ± 1.0 °C, **B**) 15 ± 0.8 °C, **C**) 25 ± 0.5 °C and **D**) 35 ± 0.5 °C.

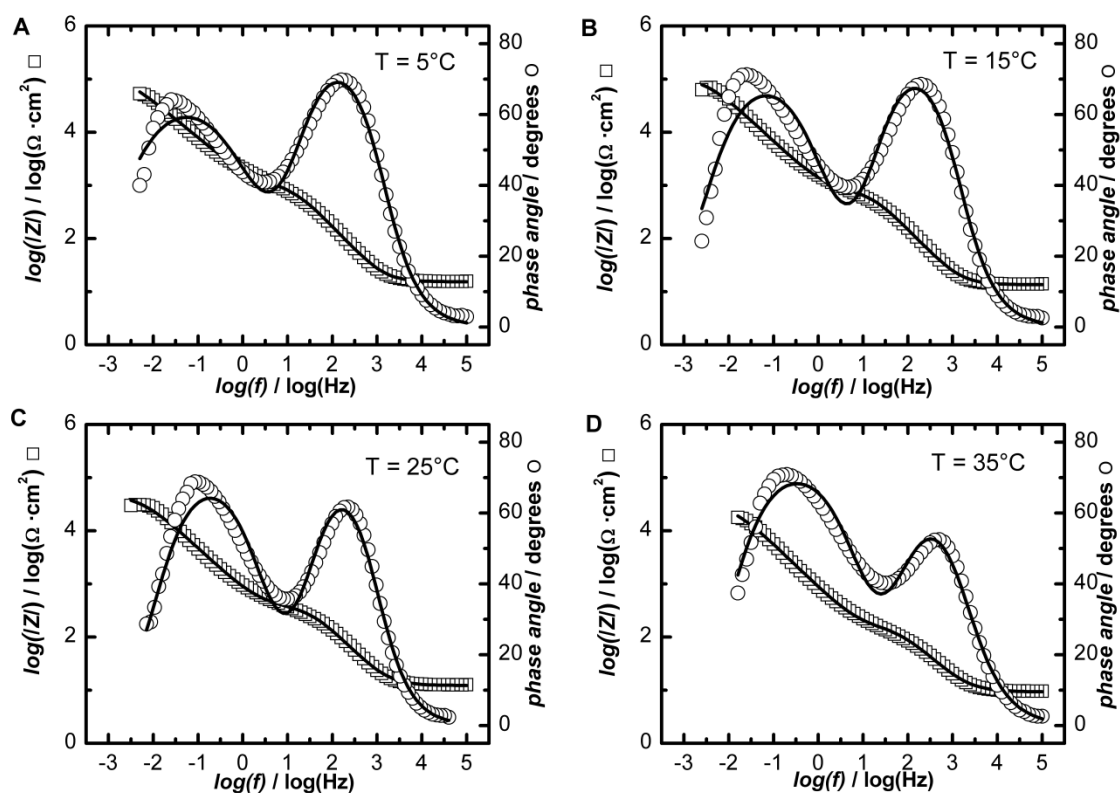


Figure 3-42 EIS Bode plots for SAMs of **27** in pH 3.34 buffer solution at applied potential of -0.24 V vs. Ag|AgCl|NaCl_{3M} with 10 mV excitation signal and frequency range from 100 kHz to the values shown in the plots. All experimental data are shown as symbols and lines represent the best-fit data. Equivalent circuit **A** from **Figure 3-48** was used to fit data. Experiments were performed in a three electrode electrochemical cell using Au disk modified with SAM of **27**, Pt mesh and Ag | AgCl | KCl_{3M} electrodes as working, counter, and reference electrode, respectively. **A**) 5 ± 1.0 °C, **B**) 15 ± 0.8 °C, **C**) 25 ± 0.5 °C and **D**) 35 ± 0.5 °C.

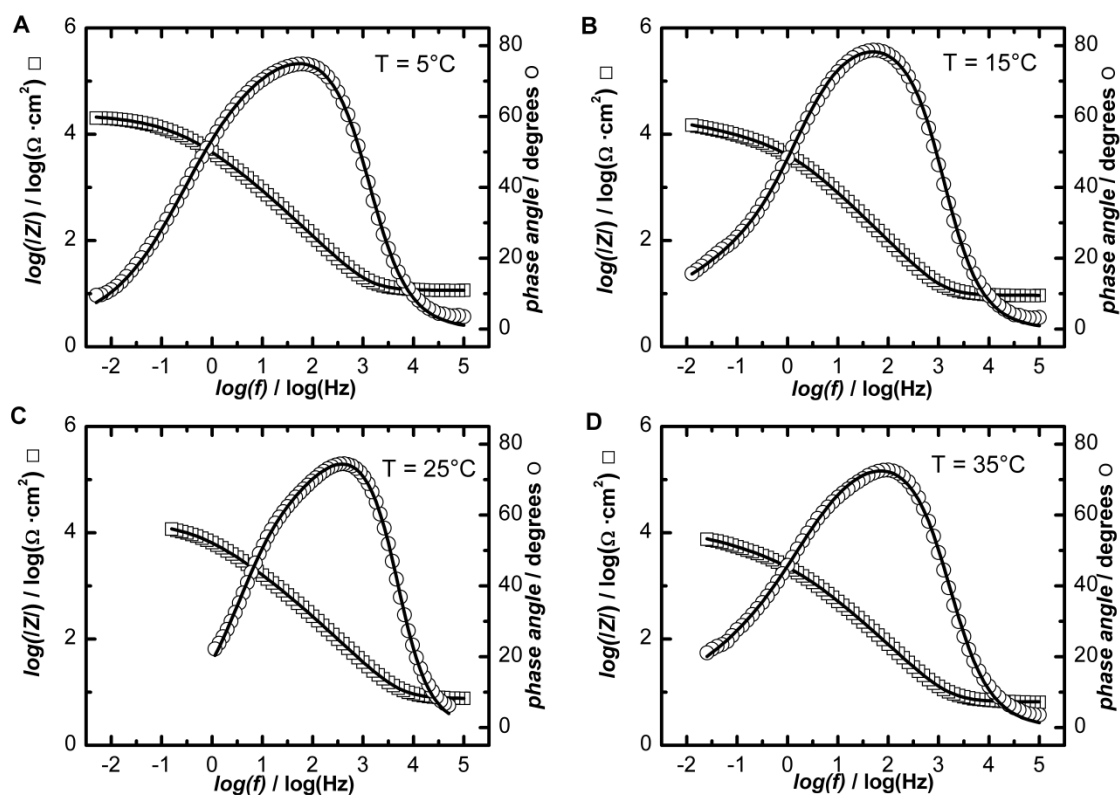


Figure 3-43 EIS Bode plots for SAMs of **27** in pH 5.50 buffer solution at applied potential of -0.35 V vs. Ag|AgCl|NaCl_{3M} with 10 mV excitation signal and frequency range from 100 kHz to the values shown in the plots. All experimental data are shown as symbols and lines represent the best-fit data. Equivalent circuit **A** from **Figure 3-48** was used to fit data. Experiments were performed in a three electrode electrochemical cell using Au disk modified with SAM of **27**, Pt mesh and Ag | AgCl | KCl_{3M} electrodes as working, counter, and reference electrode, respectively. **A**) 5 ± 1.0 °C, **B**) 15 ± 0.8 °C, **C**) 25 ± 0.5 °C and **D**) 35 ± 0.5 °C.

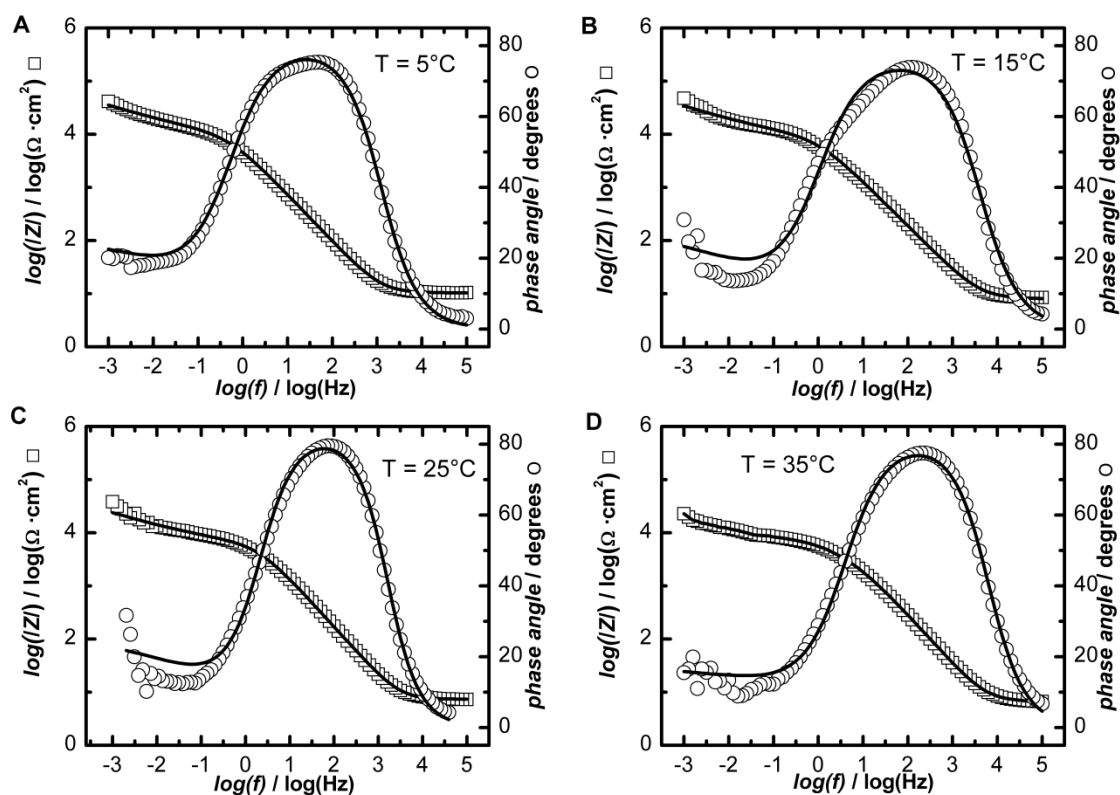


Figure 3-44 EIS Bode plots for SAMs of **27** in pH 7.51 buffer solution at applied potential of -0.46 V vs. Ag|AgCl|NaCl_{3M} with 10 mV excitation signal and frequency range from 100 kHz to the values shown in the plots. All experimental data are shown as symbols and lines represent the best-fit data. Equivalent circuit **B** from **Figure 3-48** was used to fit data. Experiments were performed in a three electrode electrochemical cell using Au disk modified with SAM of **27**, Pt mesh and Ag | AgCl | KCl_{3M} electrodes as working, counter, and reference electrode, respectively. **A**) 5 ± 1.0 °C, **B**) 15 ± 0.8 °C, **C**) 25 ± 0.5 °C and **D**) 35 ± 0.5 °C.

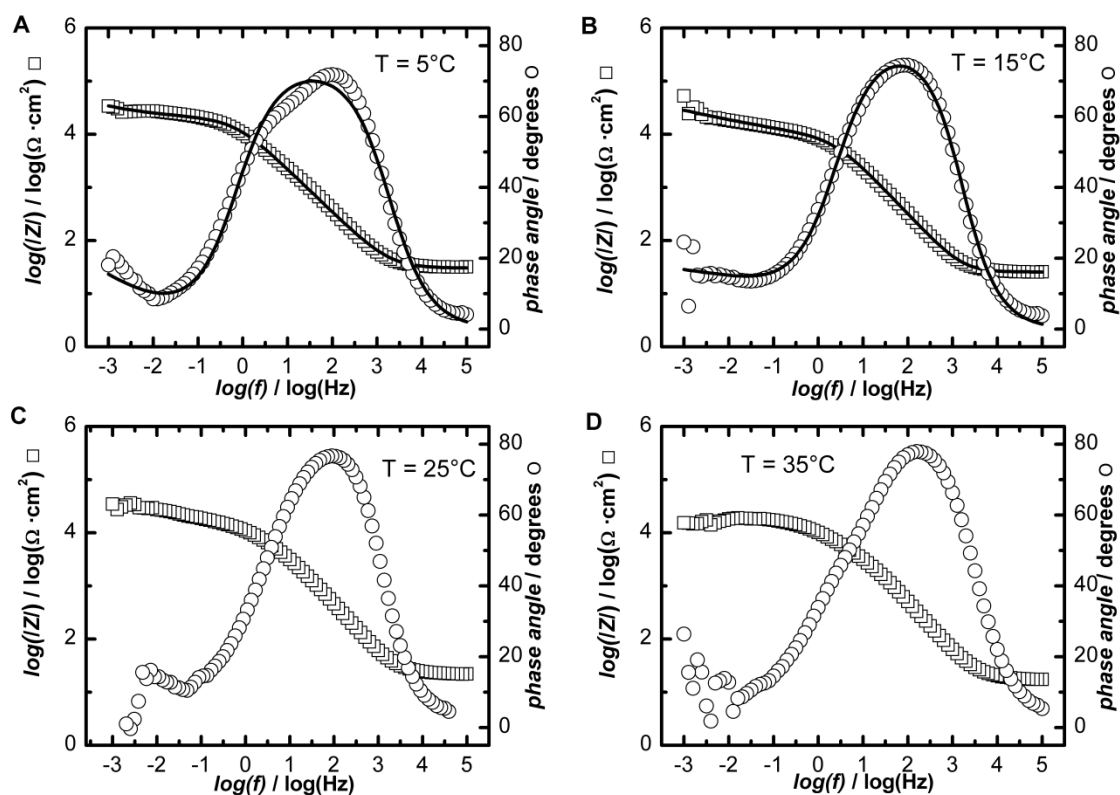


Figure 3-45 EIS Bode plots for SAMs of **27** in pH 9.52 buffer solution at applied potential of -0.58 V vs. Ag|AgCl|NaCl_{3M} with 10 mV excitation signal and frequency range from 100 kHz to the values shown in the plots. All experimental data are shown as symbols and lines represent the best-fit data. Equivalent circuit **B** from **Figure 3-48** was used to fit data. Experiments were performed in a three electrode electrochemical cell using Au disk modified with SAM of **27**, Pt mesh and Ag | AgCl | KCl_{3M} electrodes as working, counter, and reference electrode, respectively. **A**) 5 ± 1.0 °C, **B**) 15 ± 0.8 °C, **C**) 25 ± 0.5 °C and **D**) 35 ± 0.5 °C.

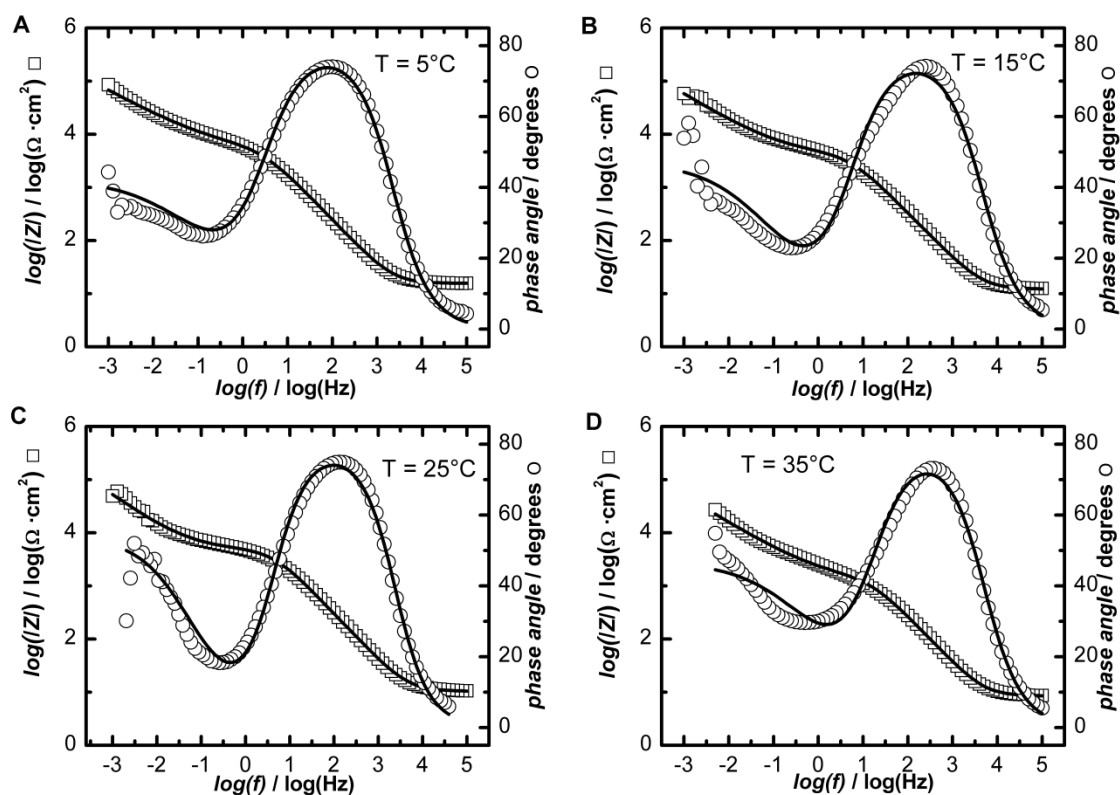


Figure 3-46 EIS Bode plots for SAMs of **27** in pH 11.61 buffer solution at applied potential of -0.65 V vs. Ag|AgCl|NaCl_{3M} with 10 mV excitation signal and frequency range from 100 kHz to the values shown in the plots. All experimental data are shown as symbols and lines represent the best-fit data. Equivalent circuit **B** from **Figure 3-48** was used to fit data. Experiments were performed in a three electrode electrochemical cell using Au disk modified with SAM of **27**, Pt mesh and Ag | AgCl | KCl_{3M} electrodes as working, counter, and reference electrode, respectively. **A**) 5 ± 1.0 °C, **B**) 15 ± 0.8 °C, **C**) 25 ± 0.5 °C and **D**) 35 ± 0.5 °C.

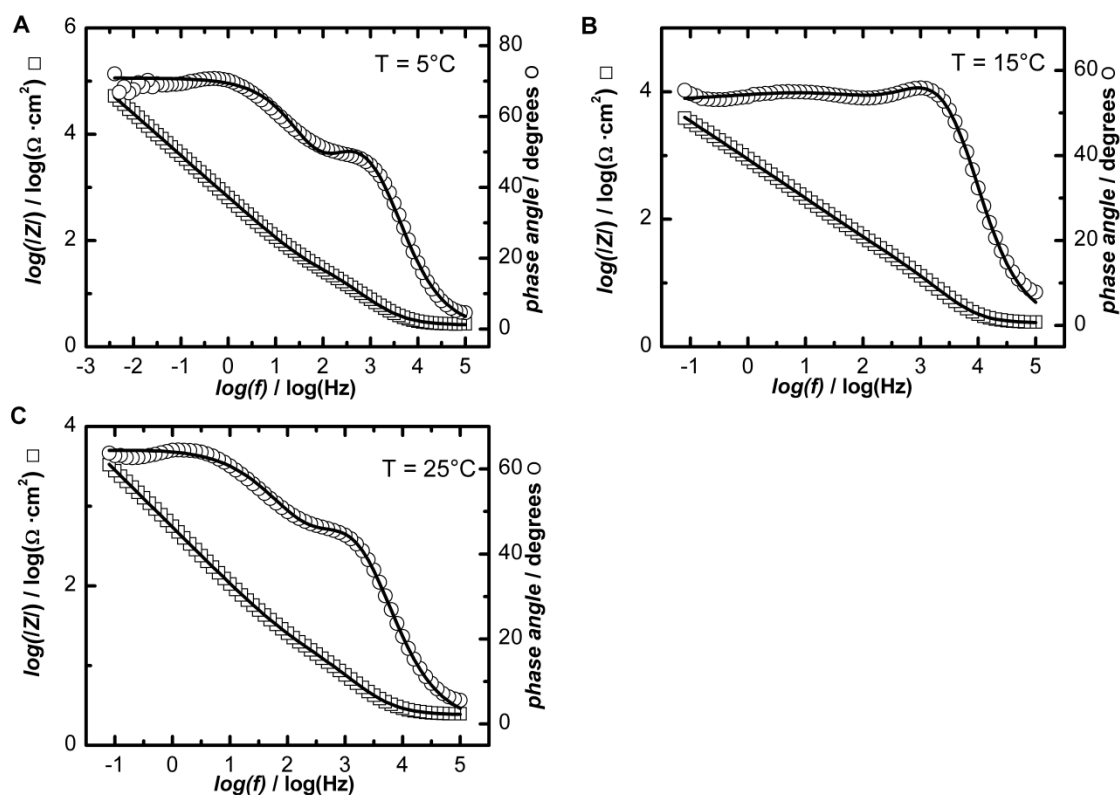


Figure 3-47 EIS Bode plots for SAMs of **27** in pH 13.18 buffer solution at applied potential of -0.74 V vs. Ag|AgCl|NaCl_{3M} with 10 mV excitation signal and frequency range from 100 kHz to the values shown in the plots. All experimental data are shown as symbols and lines represent the best-fit data. Equivalent circuit **B** from **Figure 3-48** was used to fit data. Experiments were performed in a three electrode electrochemical cell using Au disk modified with SAM of **27**, Pt mesh and Ag | AgCl | KCl_{3M} electrodes as working, counter, and reference electrode, respectively. **A)** 5 ± 1.0 °C, **B)** 15 ± 0.8 °C, and **C)** 25 ± 0.5 °C

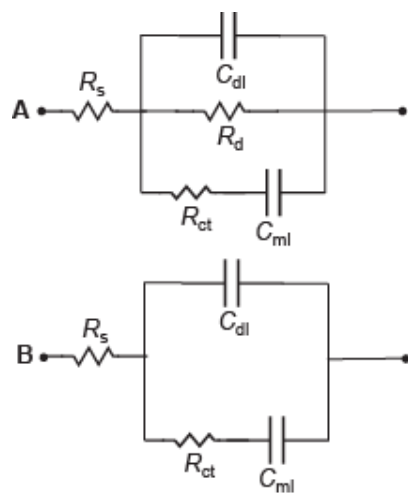


Figure 3-48 Two equivalent circuits used to fit impedance data of SAM of 27.

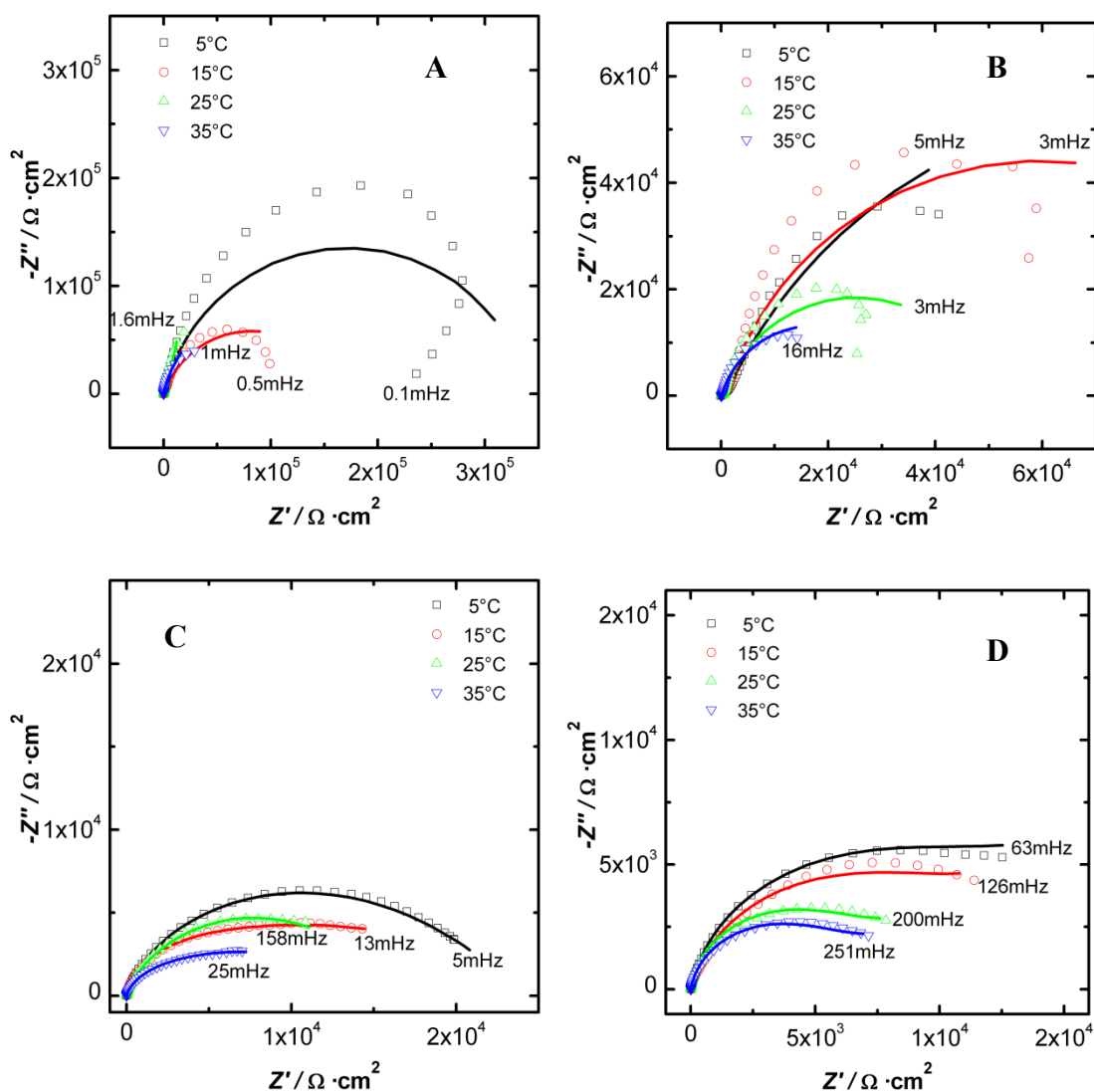


Figure 3-49 Nyquist plots for **27** at different temperatures. The EIS data was taken at $E^{0'}$ vs. Ag|AgCl|NaCl_{3M} DC potential with 10 mV AC voltage signal and frequency range was 100 kHz to the value indicated in plots. All experimental data are shown as symbols and lines represent the best-fit data. Equivalent circuit **A** (pH 1.66, 3.34, and 5.50) and **B** (pH 7.51) from **Figure 3-48** was used to fit data. Experiments were performed in a three electrode electrochemical cell using Au disk modified with SAM of **27**, Pt mesh and Ag | AgCl | KCl_{3M} electrodes as working, counter, and reference electrode, respectively. **A**) pH 1.66, **B**) pH 3.34, **C**) pH 5.50, and **D**) pH 7.51.

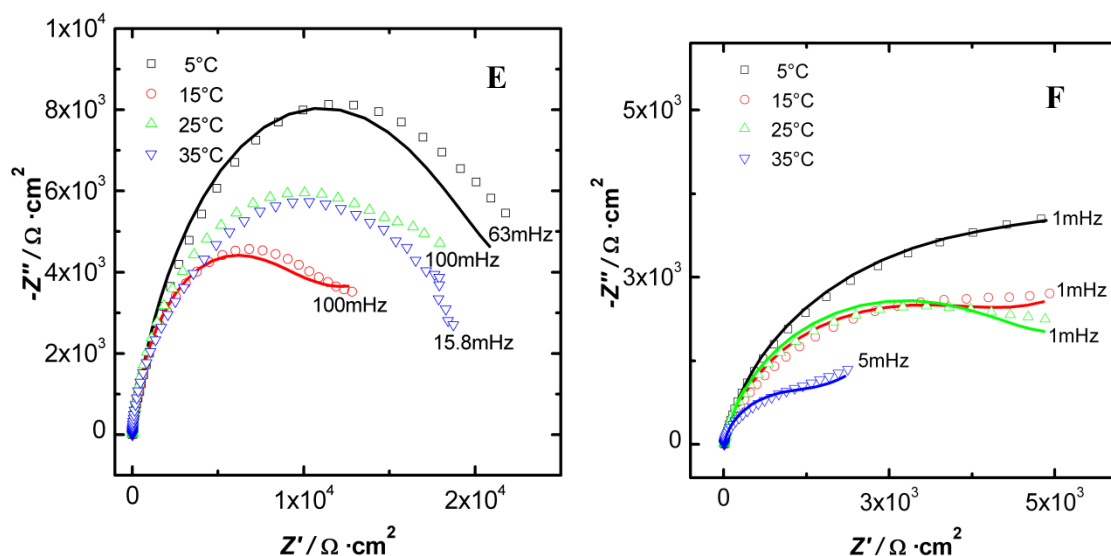


Figure 3-50 Nyquist plots for **27** at different temperatures. The EIS data was taken at $E^{0'}$ vs. $\text{Ag}|\text{AgCl}|\text{NaCl}_{3\text{M}}$ DC potential with 10 mV AC voltage signal and frequency range was 100 kHz to the value indicated in plots. All experimental data are shown as symbols and lines represent the best-fit data. Equivalent circuit **B** from **Figure 3-48** was used to fit data. Experiments were performed in a three electrode electrochemical cell using Au disk modified with SAM of **27**, Pt mesh and $\text{Ag}|\text{AgCl}|\text{KCl}_{3\text{M}}$ electrodes as working, counter, and reference electrode, respectively. **E)** pH 9.52, **F)** pH 11.61.

Table 13 Fitting analysis results of SAMs of **27** from data presented in **Figures 3-41 to 3-50** using the models presented in **Figure 3-48 A and B** at selected temperatures. ^a

<i>pH</i>	<i>Temp</i> °C	<i>R_s</i> Ω·cm ²	<i>C_{dl}</i>		<i>R_{ct}</i> Ω·cm ²	<i>C_{mt}</i>		<i>R_d</i> kΩ·cm ²	χ^2 ^c	<i>k_{app}</i> s ⁻¹
			<i>C</i> μFcm ⁻²	<i>n</i> ^b		<i>C</i> μFcm ⁻²	<i>n</i> ^b			
1.66	5 ± 1.0	3.3	198 (5)	0.86 (2)	393 (11)	54.2 (15)	0.81 (2)	342 (5)	1.52	0.43
1.66	15 ± 0.8	2.9	267 (3)	0.79 (2)	412 (7)	28.0 (13)	0.83 (2)	163 (11)	1.14	0.26
1.66	25 ± 0.5	2.4	315 (4)	0.87 (1)	134 (7)	46.1 (17)	0.82 (2)	241 (15)	1.07	0.88
1.66	35 ± 0.5	2.5	334 (13)	0.91 (3)	24.6 (14)	95.0 (42)	0.81 (6)	82.4 (6)	1.85	5.92
3.34	5 ± 1.0	15.3	168 (2)	0.73 (1)	1115 (4)	16.6 (6)	0.91 (1)	168 (12)	0.21	0.16
3.34	15 ± 0.8	13.5	197 (3)	0.81 (2)	873 (6)	20.1 (10)	0.90 (1)	119 (8)	0.61	0.23
3.34	25 ± 0.5	12.2	281 (2)	0.81 (1)	401 (5)	23.8 (11)	0.88 (2)	50.1 (5)	0.45	0.50
3.34	35 ± 0.5	9.2	212 (3)	0.83 (1)	175 (6)	40.5 (12)	0.84 (2)	34.4 (7)	0.20	1.32
5.50	5 ± 1.0	11.5	41.9 (2)	0.49 (3)	1811 (31)	22.9 (4)	0.91 (.5)	24.1 (2)	0.02	0.09
5.50	15 ± 0.8	9.3	84.3 (3)	0.39 (8)	2813 (24)	24.4 (2)	0.93 (3)	25.3 (8)	0.02	0.07
5.50	25 ± 0.5	7.6	27.2 (5)	0.54 (3)	1256 (20)	10.1 (4)	0.91 (4)	16.6 (2)	0.01	0.18
5.50	35 ± 0.5	6.5	143 (3)	0.37 (9)	483 (92)	38.7 (7)	0.90 (1)	16.3 (12)	0.03	0.31
7.51	5 ± 1.0	10.3	170 (10)	0.31 (5)	8020 (9)	34.2 (2)	0.89 (.4)		0.12	0.02
7.51	15 ± 0.8	8.0	192 (18)	0.33 (10)	8030 (14)	22.4 (5)	0.85 (1)		0.61	0.01
7.51	25 ± 0.5	7.3	232 (16)	0.30 (10)	4870 (15)	15.6 (6)	0.92 (1)		0.63	0.03
7.51	35 ± 0.5	6.6	193 (11)	0.21 (8)	3005 (19)	10.7 (4)	0.90 (1)		0.21	0.05
9.52	5 ± 1.0	30.1	421 (32)	0.38 (15)	19820 (6)	14.6 (4)	0.82 (1)		0.42	0.01
9.52	15 ± 0.8	25.5	147 (17)	0.24 (12)	6210 (20)	9.8 (6)	0.90 (1)		0.42	0.02
11.61	5 ± 1.0	15.6	171 (4)	0.47 (2)	5720 (5)	13.7 (3)	0.88 (1)		0.21	0.03
11.61	15 ± 0.8	12.1	257 (5)	0.53 (2)	4420 (5)	11.3 (5)	0.87 (1)		0.50	0.03
11.61	25 ± 0.5	10.4	424 (6)	0.60 (3)	4910 (4)	11.5 (5)	0.88 (1)		0.56	0.03
11.61	35 ± 0.5	8.4	280 (3)	0.52 (2)	1471 (5)	12.0 (6)	0.89 (1)		0.33	0.10
13.18	5 ± 1.0	2.5	207 (9)	0.79 (1)	48.5 (11)	156 (12)	0.79 (2)		0.06	3.12
13.18	15 ± 0.8	2.4	359 (1)	0.58 (.4)	25.0 (9)	26.7 (11)	0.90 (1)		0.02	6.06
13.18	25 ± 0.5	2.4	397 (3)	0.69 (.3)	19 (6)	96.8 (11)	0.83 (1)		0.02	7.97

^a Numbers in parentheses are standard deviations from curve-fitting errors.

^b *n* is a power-law modifier in the CPE circuit element described by: $Z_{CPE} = 1/[Q^{\circ} \cdot (j\omega)^n]$.

^c χ^2 (chi-squared) is a measure of the goodness of fit to the data using equivalent circuit model shown in **Figure 3-48 A and B**.

The following section discusses the kinetics of the SAM of **27** obtained by CV and EIS. First, general trends seen in both methods will be covered then kinetic data of 25°C will be discussed extensively.

The analysis of CV data of SAM of **27** to obtain kinetic information was done in the same manner as it was done for SAM of **22**. The widely cited Laviron's theoretical treatment was used⁴¹ to determine the apparent electron transfer rate constant (k_{app}) and transfer coefficient (α) as a function of pH and temperature; **Equations 9, 10 and 11** were used for calculations. Necessary unknowns α , v_a and v_c were extracted from the irreversible CVs ($\Delta E_p > 200/n$ mV). **Figure 3-51** shows a representative $\Delta E_p - E^{0'}$ vs. $\ln v$ graph for pH 3.34.

The transfer coefficient (α) is a measure of activation energy barrier,^{39,42} and when the transition state is approximately halfway between the reactant and product, the value of α tends to be 0.5. Most often, symmetrical cathodic and anodic peaks gives an indication that the transfer coefficient is 0.5. Here, α was determined from the graph of $\Delta E_p - E^{0'}$ vs. $\ln v$, according to **Equations 9 and 10**. The value of α is scattered as can be seen from the **Figure 3-54**, which shows α as a function of temperature and pH. Also, it is manifested from the graphs in **Figure 3-51** that α changes with temperature and pH. These α values are acceptable considering that the CV peaks are unsymmetrical (see **Figure 3-37** and **Figure 3-38**; other CV Figures in appendix).

From **Figure 3-52** and **Table 14**, it can be seen that there are vast differences between the anodic and cathodic rate constants calculated from CV data. The average k_{app} values follow a systematic trend for 5°, 15°, 25°C as a function of pH except for pH 3.34 at

25°C; fast kinetics are observed in the acidic pH, slow kinetics in the neutral region of the pH, then the rate slowly becomes faster at basic pHs. At pH 3.34 and 25°C, the rate is unusually faster and the reason for this fast kinetics is unknown.

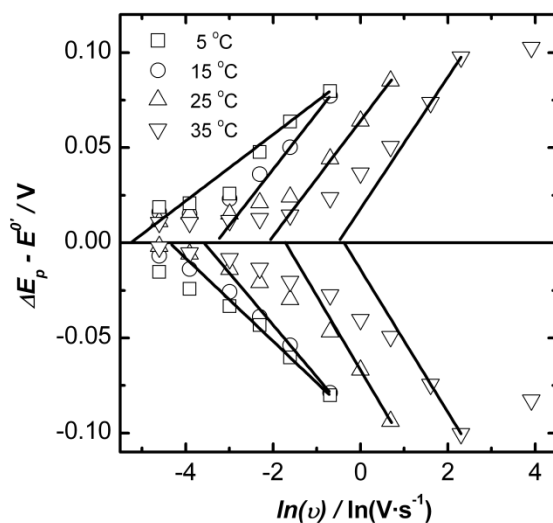


Figure 3-51 ET rate analysis of a SAM of **27** using Laviron's formalism in pH 3.34 buffer solution. Data from **Tables 9, 10, 11, and 12** were used.

The kinetic information from EIS for SAM of **27** was derived in the same manner as it was done for the SAM of **22**; **Equation 14** was used to calculate the k_{app} . **Figure 3-53** shows the k_{app} as a function of pH at various temperatures, and **Table 14** summarizes the calculated rate constants. The kinetics of the SAM of **27** follows a similar trend at 5°, 15°, and 25°C. Fast kinetics were observed in acidic pH 1.66 then slow kinetics were observed until pH 9.51, and very fast kinetics was observed for basic pH 13.18. In contrast, at 35°C, very fast kinetics was observed for SAM of **27** in pH 1.66 compared to other

temperatures. As mentioned earlier, at 25° and 35°C, k_{app} values could not be obtained for pH 9.51 since CNLS fitting failed to produce R_{CT} values.

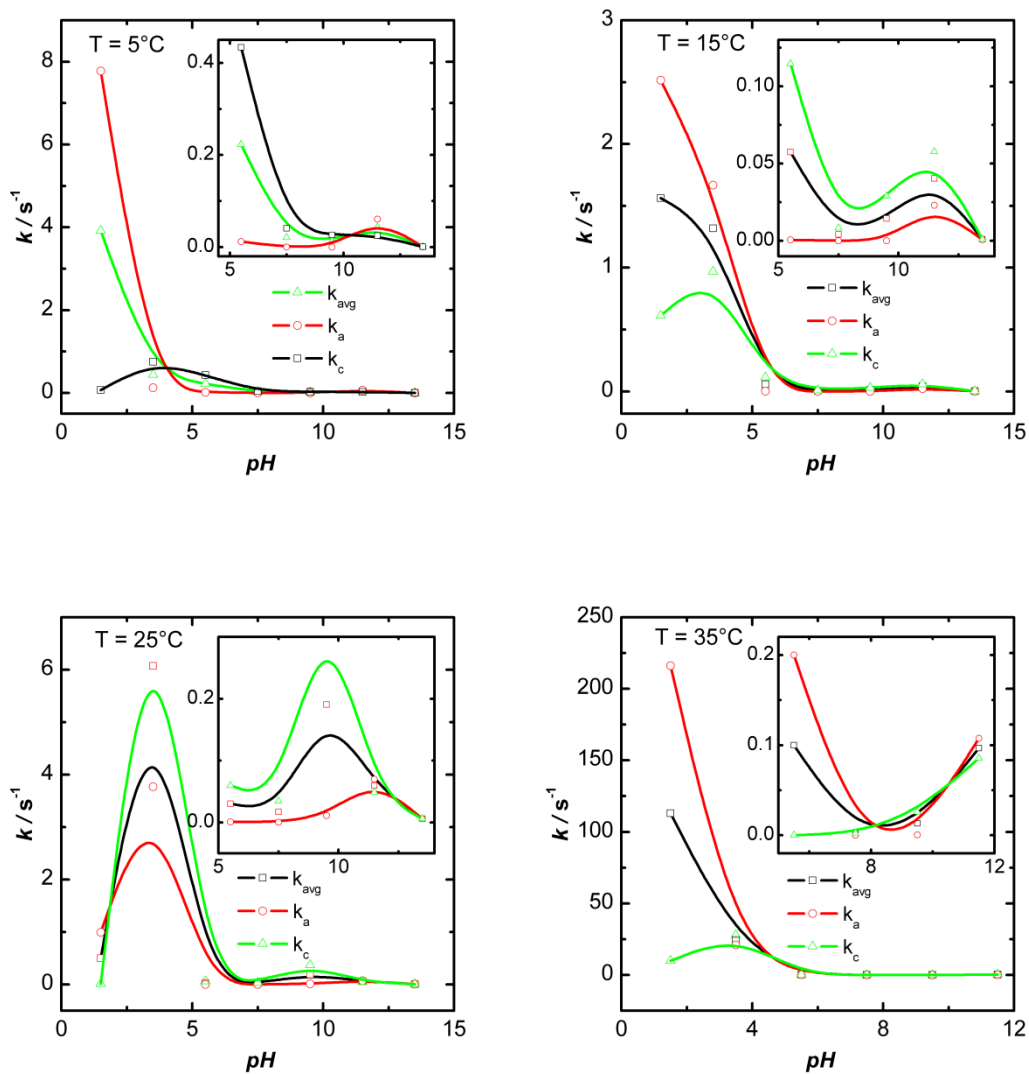


Figure 3-52 ET rate constant obtained by CV at various temperature and pH for SAM of 27. Data from Table 14 were used.

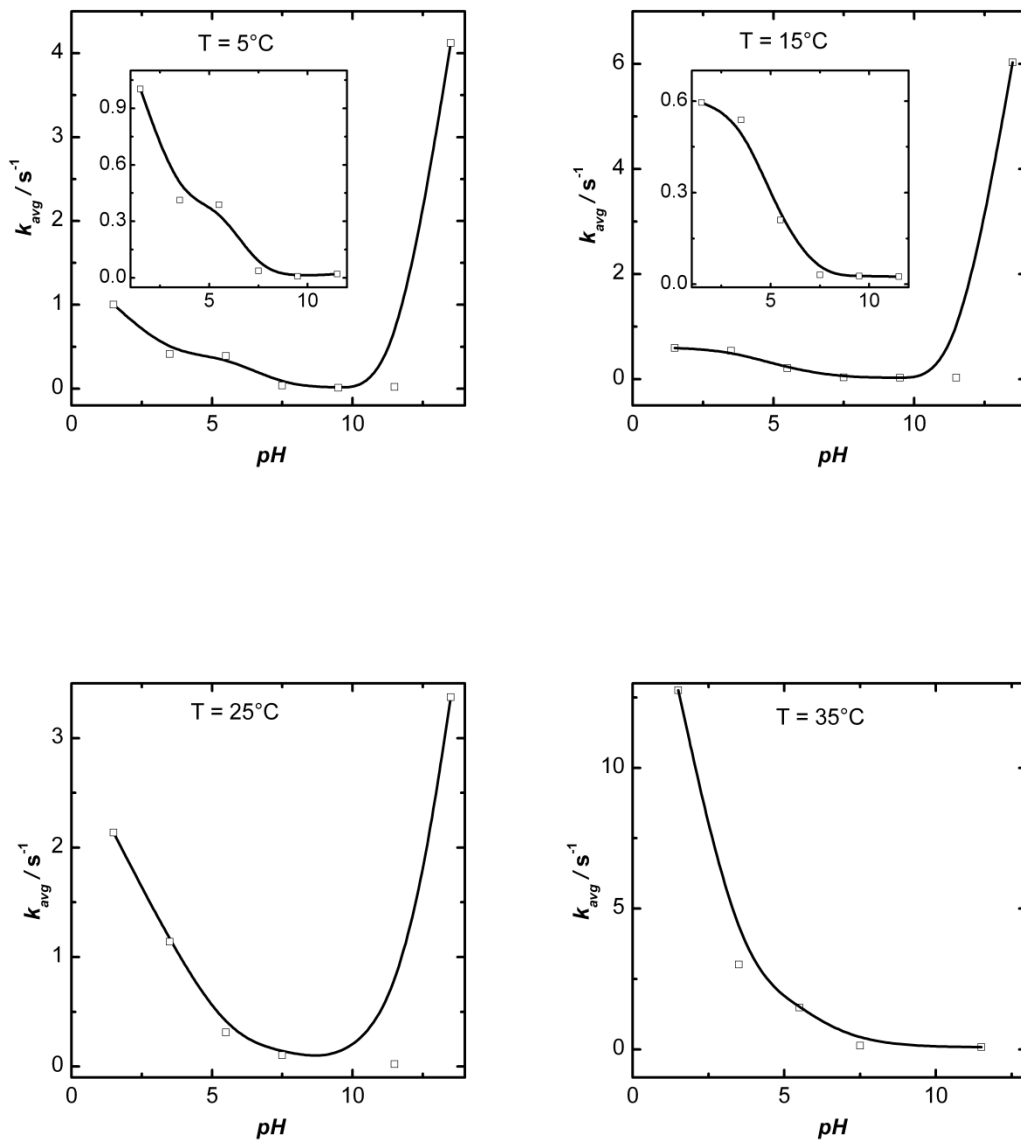


Figure 3-53 ET rate constants obtained by EIS as function of temperature and pH. Data from **Table 14** were used.

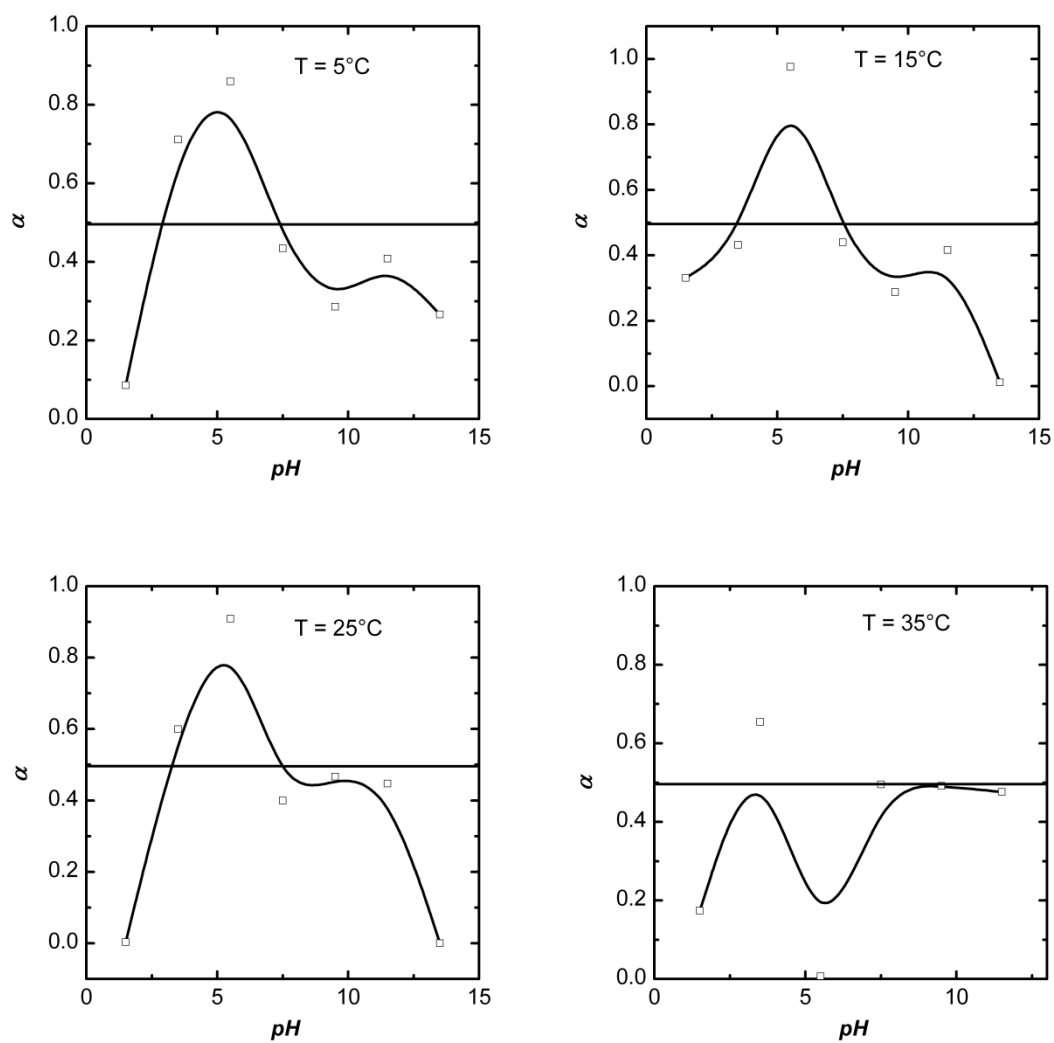


Figure 3-54 α vs. pH at various temperatures; Data from **Table 14** were used.

Table 14 k_{app} obtained by CV and EIS as function of temperature and pH

Temp / °C	pH	k_{app} / s^{-1}		CV	
		CV	EIS	k_c / s^{-1}	k_a / s^{-1}
35±0.5	1.66	1.13E+02	1.28E+01	9.88E+00	2.16E+02
	3.34	2.43E+01	3.01E+00	2.78E+01	2.09E+01
	5.50	1.00E-01	1.48E+00	8.88E-06	2.00E-01
	7.51	1.31E-03	1.33E-01	2.45E-03	1.60E-04
	9.52	1.31E-02	na	2.58E-02	4.57E-04
	11.61	9.66E-02	7.41E-02	8.56E-02	1.07E-01
25±0.5	1.66	5.02E-01	2.14E+00	9.41E-03	9.94E-01
	3.34	6.07E+00	1.14E+00	8.37E+00	3.77E+00
	5.50	3.01E-02	3.12E-01	5.97E-02	5.95E-04
	7.51	1.73E-02	1.03E-01	3.42E-02	3.70E-04
	9.52	1.91E-01	na	3.70E-01	1.09E-02
	11.61	5.94E-02	2.04E-02	4.90E-02	6.98E-02
15±0.8	13.18	5.90E-03	3.37E+00	5.72E-03	6.09E-03
	1.66	1.56E+00	5.95E-01	6.13E-01	2.51E+00
	3.34	1.32E+00	5.39E-01	9.68E-01	1.67E+00
	5.50	5.76E-02	2.11E-01	1.15E-01	5.87E-04
	7.51	4.13E-03	3.11E-02	8.19E-03	7.72E-05
	9.52	1.44E-02	2.70E-02	2.88E-02	2.95E-09
5±1.0	11.61	4.03E-02	2.51E-02	5.76E-02	2.31E-02
	13.18	5.90E-03	6.03E+00	9.73E-04	8.92E-04
	1.66	1.56E+00	1.00E+00	7.16E-02	7.77E+00
	3.34	4.38E-01	4.13E-01	7.50E-01	1.26E-01
	5.50	2.23E-01	3.88E-01	4.33E-01	1.21E-02
	7.51	2.04E-02	3.75E-02	4.08E-02	1.12E-08
	9.52	1.32E-02	8.64E-03	2.64E-02	5.82E-12
	11.61	4.29E-02	2.02E-02	2.51E-02	6.07E-02
	13.18	6.03E-04	4.12E+00	7.10E-04	4.95E-04

Arrhenius plots ($\ln k_{app}$ vs. $1/T$) and Eyring plots ($\ln k_{app}/T$ vs. $1/T$) are shown in **Figure 3-55**. The calculated thermodynamic parameters (ΔH^\ddagger , ΔS^\ddagger , ΔG^\ddagger , E_a) are summarized in **Table 15**. SAMs of **27** show linear plots of Arrhenius and Eyring only at pHs 3.34 and 13.18. In contrast, other pHs (1.66, 5.50, and 11.61) adopt nonlinear (here, it is called two linear regions) Arrhenius and Eyring plots resulting in concave plots. In pH 7.5 and 9.5, it is not clear what direction the plots would adopt. Nonlinearity in Arrhenius and Eyring plots is common¹¹⁵ and literature precedence interpreted concave nonlinearity feature as either involvement of at least two different rate determining reaction steps or involvement of tunnelling for the rate of the reaction for gaseous state.¹¹⁵

Linear and concave features, in Arrhenius and Eyring plots, were also observed in EIS kinetics data. While pH 3.34 shows linear Arrhenius and Eyring plots, pHs 1.66, 5.50, and 7.51 show nonlinear concave Arrhenius and Eyring plots.

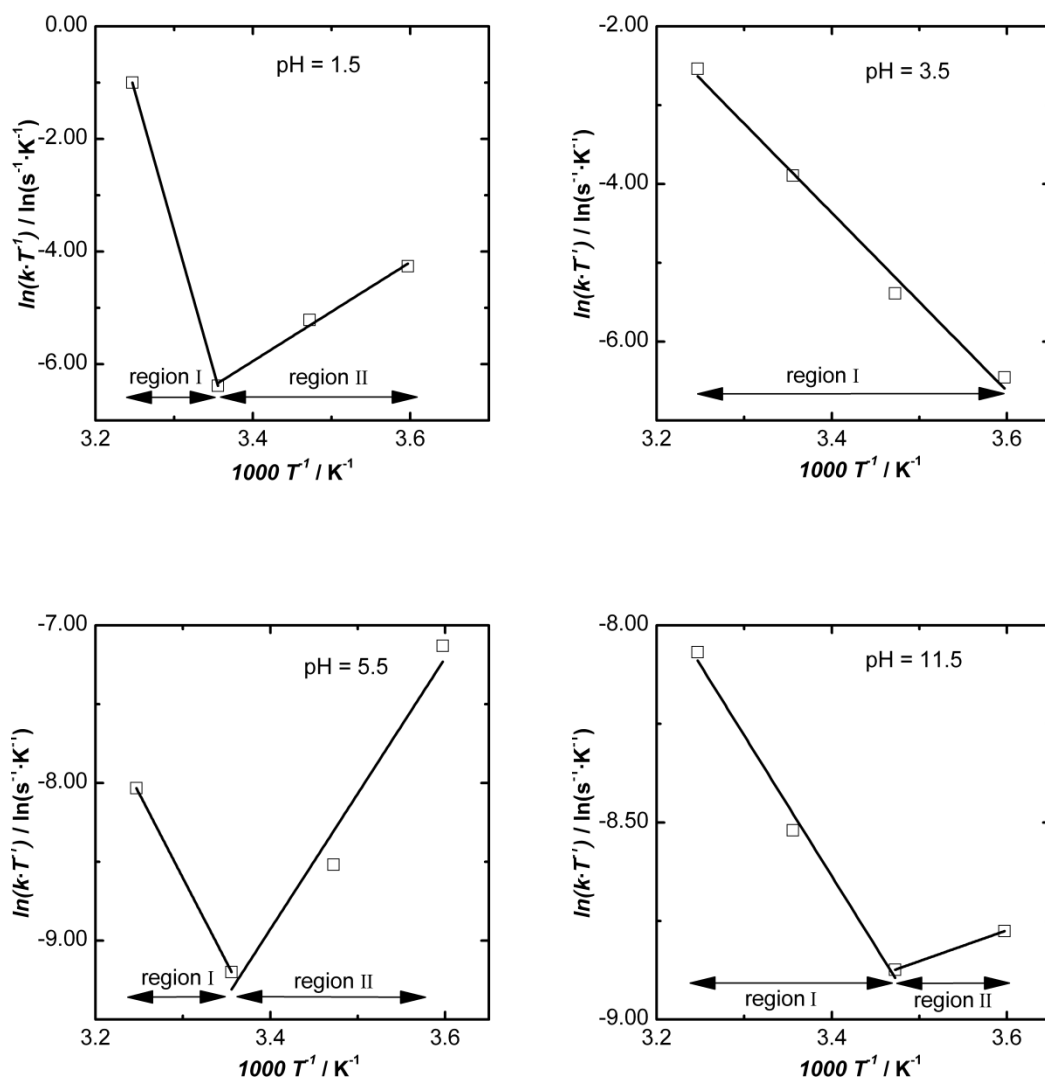


Figure 3-55 Eyring plots of SAM of **27** at selected pHs and temperatures; Data from **Table 15** were used.

Table 15 Thermodynamic parameters extracted from Eyring plots.

pH	ΔH^\ddagger kJ·mol ⁻¹	ΔS^\ddagger kJ·mol ⁻¹	ΔG^\ddagger kJ·mol ⁻¹	E_a kJ·mol ⁻¹
1.66 (region I)	411	1.13	63.4	413
1.66 (region II)	-73.1	-0.50	74.6	-70.6
3.34 (region I)	94.0	0.09	69.3	96.4
5.50 (region I)	89.0	0.02	82.2	91.3
5.50 (region II)	-71.5	-0.52	69.1	-69.3
11.61 (region I)	29.7	-0.17	81.6	32.2
11.61 (region II)	-6.51	-0.29	81.1	-4.03
13.18 (region I)	75.6	-0.04	86.0	78.0

In the following paragraphs, comparison of EIS and CV kinetics data will be covered, followed by a detailed discussion of the 25°C data.

Even though the numbers for k_{app} are different for EIS and CV, both follow a similar trend (except for pH 13.18) in k_{app} vs. pH graph at various temperatures (**Figure 3-52** to **3-53**). Although Arrhenius and Eyring plots of SAM of **27** show the same temperature effects in pHs 1.66, 3.34, and 5.50 by both methods, other pHs show discrepancies.

Since the majority of the pH studies of quinone electrochemistry in the literature were done at 25°C, it is reasonable to compare the experimental trend at 25°C with literature. Although k_{app} values from both methods show similar trends, the CV data shows subtle changes. Moreover, as explained in the EIS general electrochemistry discussion, CNLS fitting resulted in uncertainties in monolayer CPE element, especially the value of power exponent, which caused uncertainties in R_{CT} . Therefore, k_{app} data as a function of pH obtained by CV will be analysed here (**Figure 3-52**).

At the most acidic pH 1.66, the rate of the ET of anthraquinone **27** is $5.02 \times 10^{-1} \text{ s}^{-1}$. At pH 3.34, the k_{app} is 6.07 s^{-1} , which is typically smaller than the k_{app} at pH 1.66.^{26,29,116} A further decrease in the ET rate ($3.01 \times 10^{-2} \text{ s}^{-1}$) is seen at pH 5.50. k_{app} slowly increased to $1.91 \times 10^{-1} \text{ s}^{-1}$ ($1.73 \times 10^{-2} \text{ s}^{-1}$ and $1.91 \times 10^{-1} \text{ s}^{-1}$ for pH 7.51 and pH 9.52, respectively). At pH 11.61, the rate slows to $5.94 \times 10^{-2} \text{ s}^{-1}$ and to $5.90 \times 10^{-3} \text{ s}^{-1}$ at pH 13.18. These subtle changes show a distorted ‘W’ shaped curve in k_{app} vs. pH plot. Literature precedence shows that at pH 13.18 k_{app} is highest. However, in the present study the k_{app} from CV shows that the k_{app} at pH 13.18 decreased from pH 11.61. Even though the k_{app} value from EIS is not reliable for higher pHs, it supports the literature trend.

Laviron’s theory based on the nine member square scheme for stepwise PCET proposes a ‘W’ shaped curve of k_{app} vs. pH.²⁷, subsequently the theory was supported by model studies and a few experimental results.²⁶ All possible combinations of 2 electron and the two proton transfer between fully oxidized and reduced quinone are present in the nine member square scheme (**Figure 3-56**). $E^{0'}$ denotes transfer of one electron and pK_a describes the transfer of a proton.

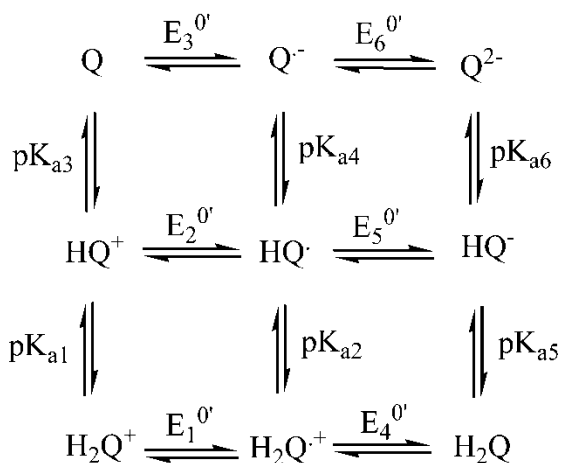


Figure 3-56 Laviron's proposed 9-member square scheme

Although the results of the SAM of **27** shows a distorted 'W' curve, the mechanistic pathway of reduction and oxidation of anthraquinone redox centres could not be ascertained by the existing results. Nevertheless, the electrochemistry of the anthraquinone is indeed proton coupled ET as can be verified by the $E^{0'}$ value at different pHs. Furthermore, the Nernstian slope of 60mV pH^{-1} in $E^{0'}$ value suggests that between pH 1.66 and pH 9.52, the ET mechanism is via two electrons and two protons ($2\text{e}, 2\text{H}^+$). In the region of 9.52 to 13.18 pHs, ET could happen via 2e and 1H^+ because the slope of the $E^{0'}$ vs. pH graph is 40mV pH^{-1} . The 2e and 1H^+ transfer reduces the nine member square scheme to six member square scheme (**Figure 3-57**).

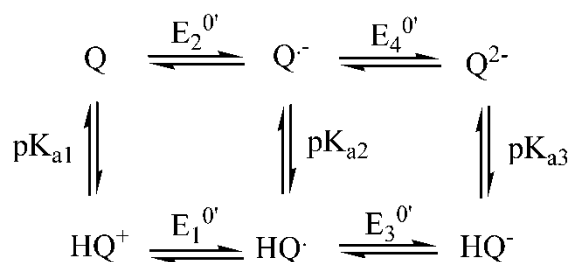


Figure 3-57 Laviron's proposed 6-member square scheme

It is important to know the pK_a and $E^{0'}$ values of the each individual intermediate to understand why k_{app} changes with pH for the complete oxidation / reduction of AQ. However, instabilities of the intermediate species make it an arduous task to experimentally determine the values of pK_a and $E^{0'}$. Usually, a simulation is made to fit the experimental data with the model data calculated from the theory to extract these values. Attempts to do such a simulation did not produce favourable results. As a result Laviron's^{26,27,116} condition are chosen to explain the results of k_{app} .

For benzoquinones, Laviron claimed that near the formal potential and in acidic or low pH, reduction of quinone follows protonation of one of the carbonyl carbon first followed by electron transfer, then protonation of the second carbonyl carbon and finally second electron transfer, which is simply denoted as the HeHe path. The opposite is true for the oxidation. In the mid or neutral pH the reduction path is eHHe, and for high or basic pH, the eHeH pathway is operating.²⁶

The results obtained for the anthraquinone **27** SAM could be explained by the paths described in the above mechanism. At acidic pH 1.66, the proton concentration is high. Therefore, the kinetics follows the HeHe process. As the pH is increased, the proton

concentration is decreased, consequently, the eHHe path dominates and the HeHe pathway is limited. Probably, the changes in the rate constant are observed as a result of new eHHe pathway. When the system reaches the basic pHs, extremely low proton concentrations are available, resulting in an eHe mechanism.

3.2.4 DFT Calculations

Experimental research can be further strengthened by incorporating electronic structure theory. *N*-ethyl-aminoanthraquinone and 1-ethoxyanthraquinone were subjected to DFT calculation, and the resultant of electronic nature of reduced and oxidized species of individual compound will be discussed.

DFT calculations using Gaussian 03 software¹¹⁷ with B3LYP/6-31G+(d,p) basis set was used to optimize the structure of an *N*-ethyl-aminoanthraquinone (Et-aminoAQ) derivative. The energy-minimized structures offer much insight into the reactions occurring on the surface. **Figure 3-58** shows the minimized structures of the oxidized (**3-58A**) and reduced (**3-58B**) forms of Et-aminoAQ in addition to the oxidized and reduced form of the amine protonated Et-ammoniumAQ (**3-58C** and **3-58D**). Both oxidized molecules, **3-58A** and **3-58C**, adopt a planar geometry with the dihedral angle between the pendant ethyl group and the AQ ring systems approaching 180°. Molecule **3-58A** exhibits a strong intramolecular hydrogen bond to the neighbouring carbonyl group with a N-H...O distance of 1.82 Å, which is consistent with the ¹H-NMR experimental data. The hydrogen-bonded structure gives *sp*² hybridization to the N atom, which allows the N lone pair to participate in aromaticity. Aromaticity is inferred from the HOMO orbital

being delocalized over the AQ ring(s) and the nitrogen atom. The sp^2 -hybridized N atom is consistent with other reports of aniline derivatives^{110,118} that show similar N-H...O distances of 1.81 Å and 1.86 Å for 2'(methylamino)acetophenone and 2'-aminoacetophenone, respectively.¹¹⁸ Note that both acetophenone structures are optimized structures calculated at a similar level, namely B3LYP/6-31G(d,p), to this work. The HOMO orbital of Et-aminoAQ is confined to the N atom and half of the AQ ring system whereas the LUMO orbital of Et-aminoAQ is delocalized over the entire AQ ring system. Conversely, the protonated amine **3-58C** does not show a hydrogen bond but rather a planar structure with N-H...O bond distances of 2.26 and 2.28 Å. A consequence of protonation is a lowering of the HOMO energy level such that HOMO, HOMO-1 and HOMO-2 are very close in energy and little change in the LUMO energy is observed because the N-atom orbitals do not play a role in the LUMO. In addition, the protonated amine shows a dramatic effect on the HOMO orbital of **3-58C** because the N-substituent changed from an electron donating group (**3-58A**) to an electron withdrawing group (**3-58C**) and the HOMO orbital is confined to the other half of the AQ ring system.

Interestingly, reduction ($2e^-$, $2H^+$) to the dihydroxyAQ of both the neutral (**3-58B**) and protonated amine (**3-58D**) result in structures that are not planar. The dihedral angles of the ethyl pendant to the AQ ring systems are 66.1° and 101.2° for **3-58B** and **3-58D**, respectively. Planar geometries of **3-58B** and **3-58D** were calculated and they did result in local energy minima; however, the perpendicular ethyl structures were energetically preferred. Unlike **3-58A**, **3-58B** does not exhibit an intramolecular hydrogen bond. If geometry around the N atom of **3-58A** and **3-58B** did not change during reduction, then the LUMO of **3-58A** should mirror the HOMO of **3-58B** and clearly, this is not the case

here because bond rotation has occurred to in the reduction of **3-58A** to **3-58B**, which allows the N-atom to participate in aromaticity. Additionally, the reduced AQ, **3-58B**, shows an increase in its HOMO orbital energy compared to the HOMO orbital energy of **3-58A**, which is typical behavior of redox couples. Interestingly, structure **3-58D** does show a very strong intramolecular hydrogen bond with a N-H \cdots O distance of 1.73 Å. More importantly, the energy of the HOMO orbital of **3-58D** is below the energy of the HOMO of **3-58C**, which is not typical for a reduction. The small differences in HOMO orbital energy levels between **3-58C** and **3-58D** could explain the fast rate observed in CV and EIS.

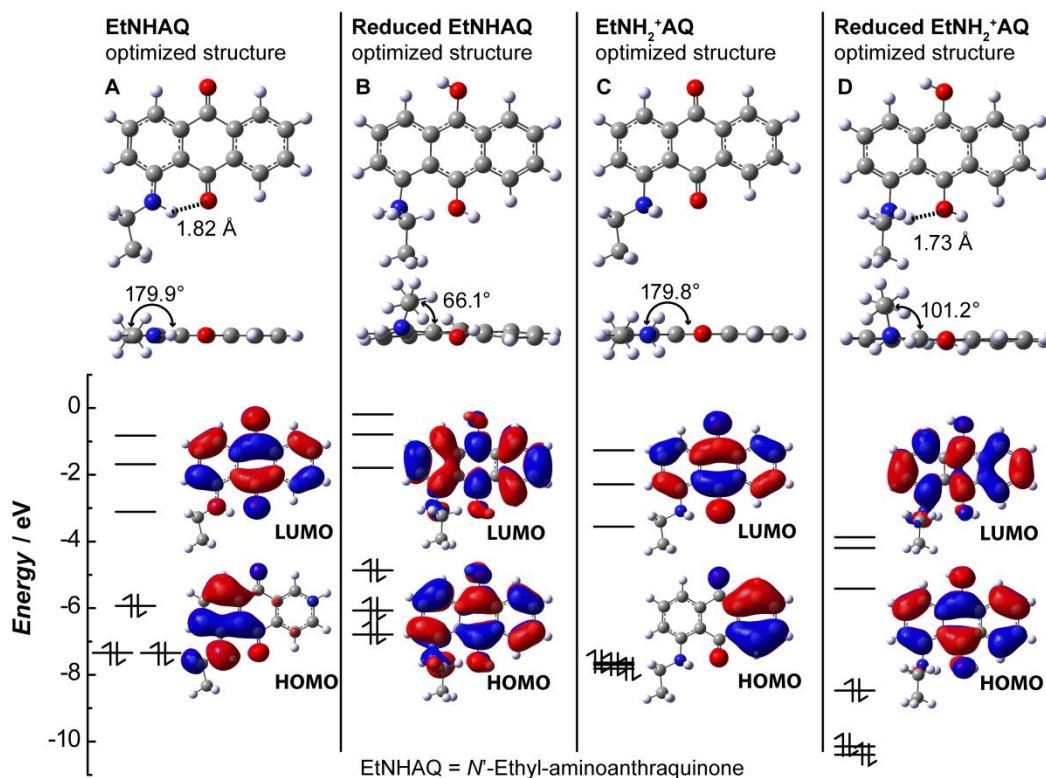


Figure 3-58 Optimized ground-state geometries of N-Ethyl-aminoAQ in its oxidized, reduced and amine protonated forms calculated with Gaussian 03 using DFT methods [B3LYP/6-31G+(d,p)] and solvent (water) was included using the Polarizable Continuum Model (PCM). From top to bottom, images correspond to top view, side view, molecular orbital energy level and HOMO and LUMO shapes. **A)** Oxidized *N*-ethyl-aminoAQ showing a planar conformation, short hydrogen-bond distance and electron delocalization over the N atom in the HOMO orbital. **B)** Reduced dihydroxyaminoAQ showing a bent optimized geometry and no intramolecular hydrogen bond. **C)** Oxidized *N*-ethyl-ammoniumAQ showing planar geometry and no intramolecular hydrogen bond. **D)** Reduced dihydroxyammoniumAQ showing bent geometry and a short, strong intramolecular hydrogen bond.

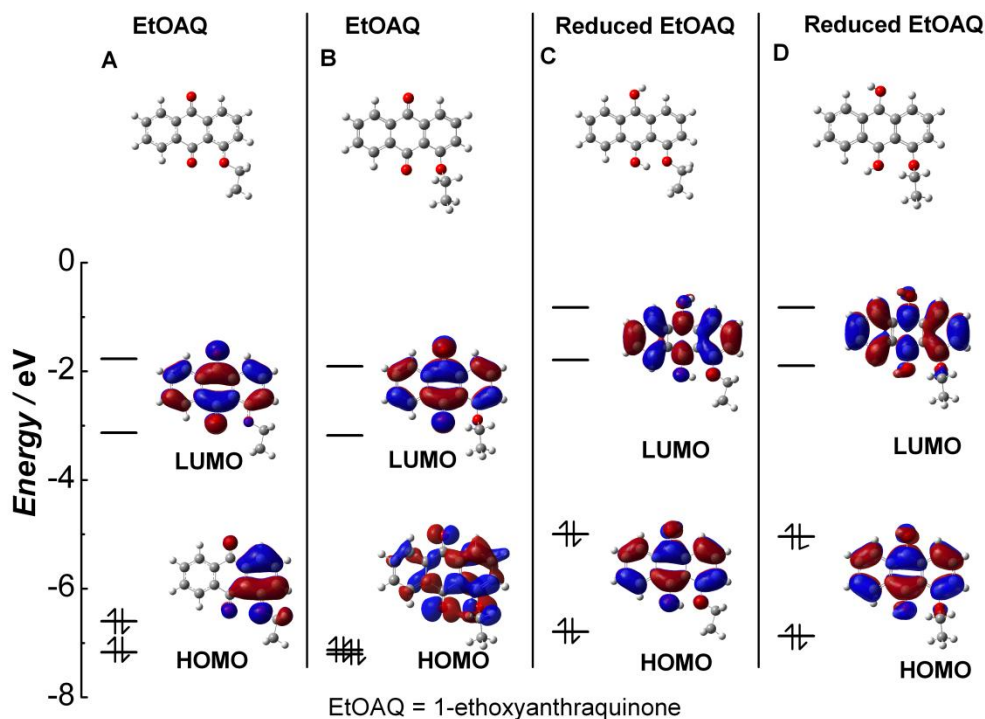


Figure 3-59 Optimized ground-state geometries of EtOAQ in its oxidized, and reduced forms calculated with Gaussian 03 using DFT methods [B3LYP/6-31G+(d,p)] and solvent (water) was included using the Polarizable Continuum Model (PCM). From top to bottom, images correspond to top view, side view, molecular orbital energy level and HOMO and LUMO shapes. **A)** Oxidized 1-ethoxy anthraquinone having a dihedral angle of zero degree. **B)** Oxidized 1-ethoxy anthraquinone having a dihedral angle of ninety degree. **C)** Reduced 1-ethoxy anthraquinone having a dihedral angle of zero degree. **D)** Reduced 1-ethoxy anthraquinone having a dihedral angle of zero degree.

DFT calculation for 1-ethoxyanthraquinone (EtOAQ) was done in the same manner as was done for N-ethyl-aminoanthraquinone; Gaussian 03 software¹¹⁷ with B3LYP/6-31G+(d,p) basis set was used to optimize the structures of reduced and oxidized states of EtOAQ as a function of dihedral angle between the pendant ethyl group and AQ moiety. Two dihedral angles were chosen, i.e. zero and ninety degrees. **Figure 3-59** shows energy minimized structures of the EtOAQ; **A**, **B**, **C**, and **D** in the **Figure 3-59** stand for zero and

ninety degree dihedral angle of oxidized and reduced compounds, respectively. Although the energies of LUMOs of the oxidized state of both dihedral angles resemble each other, the HOMOs have quite different energies. Energy of the HOMO **3-59B** is lower than the energy of HOMO (-1) of oxidized **3-59A** indicating a 90 degree dihedral angle of the ethyl substituent to AQ ring is favoured by the molecule. In **3-59A** position, the HOMO energy is confined to the ethoxy bearing ring.

LUMOs and HOMOs of the reduced molecules (**3-59C** and **3-59D**) have similar energies, but the energies are higher than the oxidized species, which is common for redox compounds. Furthermore, similar to oxidized structure **3-59B**, **3-59D** also has lower energy than their counterparts **3-59A** and **3-59C** indicating that the ninety degree dihedral angle is favoured by the molecule.

3.2.5 Spectroelectrochemistry

In spectroelectrochemistry, the electronic absorption properties of the different redox species can be investigated if those intermediates are stable during the experiment. **Figure 3-60** shows a UV-VIS-NIR spectrum of compound **27** that was obtained during *in-situ* reduction. The spectra was recorded while applying a DC potential progressively, (200mV step potential was applied starting from 200mV) and holding the potential for 1.5 minutes. The $E^{0'}$ of the compound **27** in THF was found to be -0.87 V vs. Ag|AgCl|KCl_{3M}. Three peaks seen in the **Figure 3-60** are assigned to π - π^* transition of quinonoid (286 nm) and benzenoid (326 nm) structure of the anthraquinone and n - π^* transition of the carbonyl (381 nm).¹¹⁹ The redox reversibility of the compound **27** was

not observed in THF solution and the spectroelectrochemical experiment results did not show reversibility when the anodic potentials were applied. Intensity of the peaks changed as the potential was stepped cathodically, but the peak position is unchanged with progressive reduction. The absorption difference spectrum (**Figure 3-61**) is obtained by subtracting the spectra at 200mV from the spectrum acquired at different potential.

From **Figure 3-61**, the growth (positive values) of two new peaks at 295nm and 340nm are attributed to two π - π^* transitions of the reduced anion anthraquinone **27**. A clear isosbestic point is observed at 354nm, suggesting conversion of the neutral anthraquinone to the radical anion / dianion of anthraquinone.

Importantly, intensity of the n - π^* transition peak of neutral anthraquinone **27** is decreasing with more cathodic potential, which is consistent with formation of reduced anthraquinone **27**.

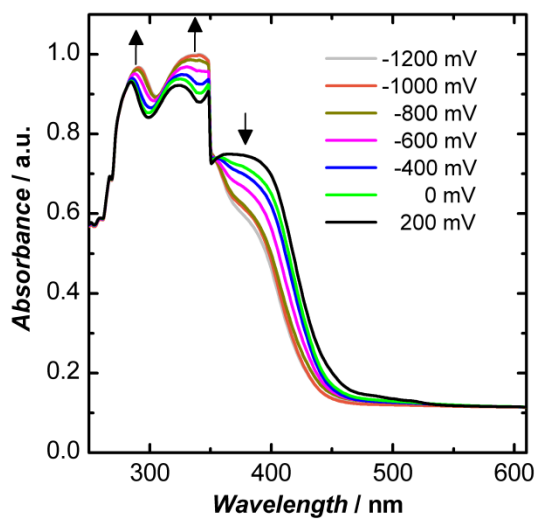


Figure 3-60 UV-VIS-NIR spectra obtained during in-situ reduction of compound **27** in an OTTLE cell at ambient temperature. $\text{NH}_4^+\text{PF}_6^-$ was used as supporting electrolyte and analyte to electrolyte concentration ratio is 1:100 (0.33mM: 33mM).

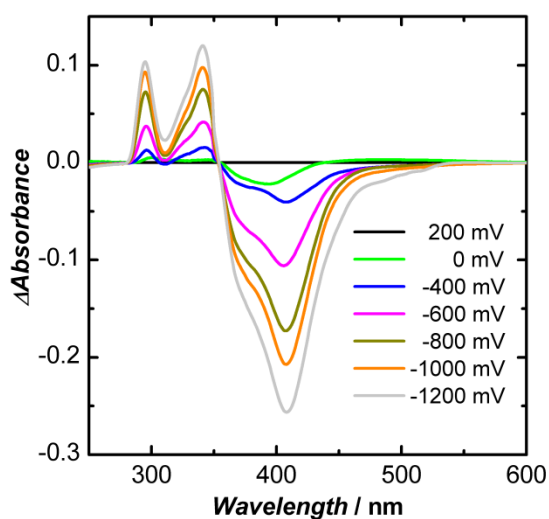


Figure 3-61 Absorption difference spectra obtained from UV-VIS-NIR spectra of compound **27** during in-situ reduction.

Chapter Four: Conclusion

The goal of this thesis was to investigate electron transfer reactions of anthraquinone, at a modified electrode interface and in solution mediated by hydrogen bonds. The major findings of these two studies are discussed here.

For studies of ET in solution, the target compound was anthraquinone diamidopyridine derivative **1**. Crucial intermediates of target compound **1**, 2,4,6-trisubstituted pyridine *N*-oxide derivatives **14** and **15**, and 2,4,6-trisubstituted pyridines **11** and **3** were synthesised using existing methodologies. However, some modifications to the existing methodologies had to be employed, for example, synthesis of 4-bromo,2,6-diaminopyridine (**11**) was not possible until pyridine *N*-oxide route with the acid digestion bomb used. Ultimately, target compound **1** synthesis was unsuccessful, however, the solution electrochemistry of anthraquinone intermediates 1-acetylenylanthraquinone (**2**) was performed and $E^{0'}$ in acetonitrile is -0.820V vs. Ag/AgCl/KCl_{3M}.

For studies of ET at a surface, the target compounds were 1-aminoantraquinone derivative **22** and 1-hydroxyantraquinone derivative **27**.

Compound **22** was successfully synthesized and used to form a SAM on gold surface as a model system to study electron transfer at a hydrophobic|hydrophilic interface in 0.1 M H₂SO₄. As evidenced by PEMIRRAS results, the SAM of **22** is sufficiently organized and CV results showed thermal stabilities up to 35°C. The proton-coupled-electron-transfer reaction of the SAM of **22** was investigated by CV and EIS. It's $E^{0'}$ value is -0.14 V and charge transfer reaction rate is 7.4s⁻¹. The redox reaction of the 1-

aminoanthraquinone derivative **22** was found to have a higher reorganizational energy (2.7eV) than that of the related SAMs of ferrocene (1.4eV) and quinone (0.9eV) and that is attributed to the intramolecular hydrogen bond being broken upon reduction.

Synthesis of 1-hydroxyanthraquinone derivative **27** was successful. Organized SAMs were obtained for compound **27**, as evidenced by the C-H stretching regions of IR results. A thorough interfacial electron transfer study of **27** as a function of pH (buffer) and temperature, using CV and EIS techniques, was undertaken. At pH 1.5 buffer solution the $E^{0'}$ value of the SAM of **27** is -0.11V. The conditions at which $E^{0'}$ values of **22** and **27** measured are different and therefore they are not comparable, although their values are similar. Furthermore, $E^{0'}$ values of the SAM of **27** shifted towards cathodic direction as pH increases indicating PCET mechanism and follows the Nernst equation. From pH 1.5 to 9.5, rate of change was 60mVpH⁻¹ and 40mVpH⁻¹ rate of change was observed from pH 9.5 to 13. The electron transfer rate constant (k_{app}) as a function of pH follows Laviron's stepwise theory of PCET for quinones. From pH 1.5 to 9.5 the PCET mechanism of the SAM of **27** attributed to 2e, 2H⁺, whereas from pH 9.5 to 13 the mechanism was 2e, 1H⁺. Eyring and Arrhenius plots from variable temperature studies of the SAM of **27** are linear only at pH 3.5 and at other pHs concave plots were obtained, which warrants further mechanistic study.

Chapter Five: Future Work

One of the long-term goals in our group is to make more efficient organic photovoltaic device for carbon neutral energy production. The exploration of polymers blended with *p* and *n* type materials to make bulk heterojunction photovoltaic cells is underway. After successful synthesis, anthraquinone diamidopyridine derivative **1** could be used as an *n* type material, which forms bulk heterojunctions through hydrogen bonds with a *p* type partner that bears complementary binding sites. In photovoltaic application, charge separation and its recombination is a major problem that reduces the efficiency of light conversion to electrical energy, making the understanding of charge transfer between components essential. Binding studies and electron transfer studies between *n*-type anthraquinone derivative **1** and its *p* type complementary partner will provide the information required to improve the cell efficiency.

A preliminary study of a process suitable for sensors, using anthraquinone derivative **1** as an analyte and flavin modified electrode as a recognition unit is proposed. In the application of electrode modified with SAMs for sensing biomolecule or chemicals, electrode will be the signal transducer and recognition unit will be the SAM bearing the redox unit. A specific recognition reaction should happen between the SAM and the analyte. Differences in current through the electrode, when the sample is introduced will be used to establish the presence or absence of the analyte. If the recognition reaction is not unique to the analyte, mixed samples of chemicals or biomolecules can cause false positives in the sensing process. Therefore, to ensure that only the analyte binds to the recognition unit and makes a difference in the current, non covalent interactions

involving hydrogen bonding between recognition units and analyte has to be designed. **Figure 5-1** shows an anthraquinone derivative **1** hydrogen bonded to a SAM modified electrode with flavin. Flavin can be used to recognize anthraquinone derivative **1** since it contains complimentary hydrogen bonding motifs (Acceptor-Donor-Acceptor). Change of redox current is an indication of the presence of the analyte anthraquinone. Ideal behaviour of flavin could be observed by forming a highly organized mixed monolayer. Synthesis of anthraquinone diamidopyridine derivative **1** is near completion and flavin derivative synthesis is in early the stages. Flavins and Quinones are ubiquitous in nature; biological respiratory chain uses reduced flavin mononucleotide (FMNH₂) to reduce ubiquinone, providing an added incentive to study electrochemical interaction mediated by hydrogen bonding between flavins and quinones.

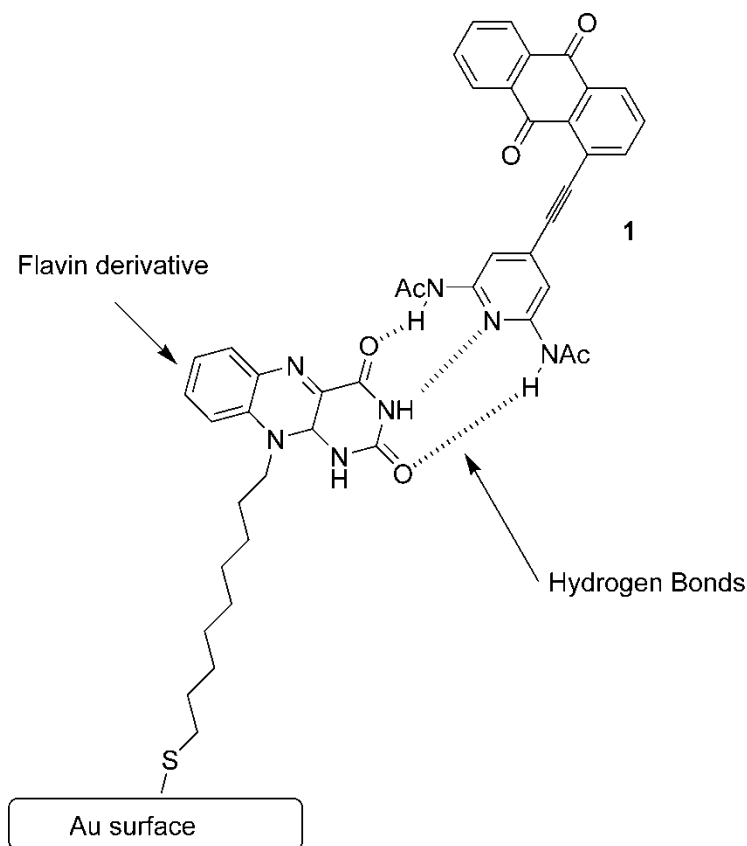


Figure 5-1 Compound **1** binds with self-assembled flavin derivative through hydrogen bonds.

In the thesis, electron transfer across electro active SAM was discussed. Here the monolayer consisted of 100% electro active (pure monolayer) anthraquinone derivatives **22** and **27**. Nonideal behaviour of the thermodynamic and kinetic parameters can be minimized when the electro active SAM is diluted with alkanethiols (mixed monolayers) with the same or different lengths. **Figure 5-2** shows mixed monolayers. Experimentations with mixed SAMs will provide details of a more ideal behaviour of anthraquinone derivatives at the interface.

The solution electrochemistry of quinone becomes more complex when it is bound to a biomembrane. The extent at which the quinone is buried inside the biomembrane will affect the electrochemistry. The diluent alkanethiol length can be varied to bury or expose the quinone moiety of the SAM. This model can be used as an analogue to study quinones in different depths of a biomembrane.

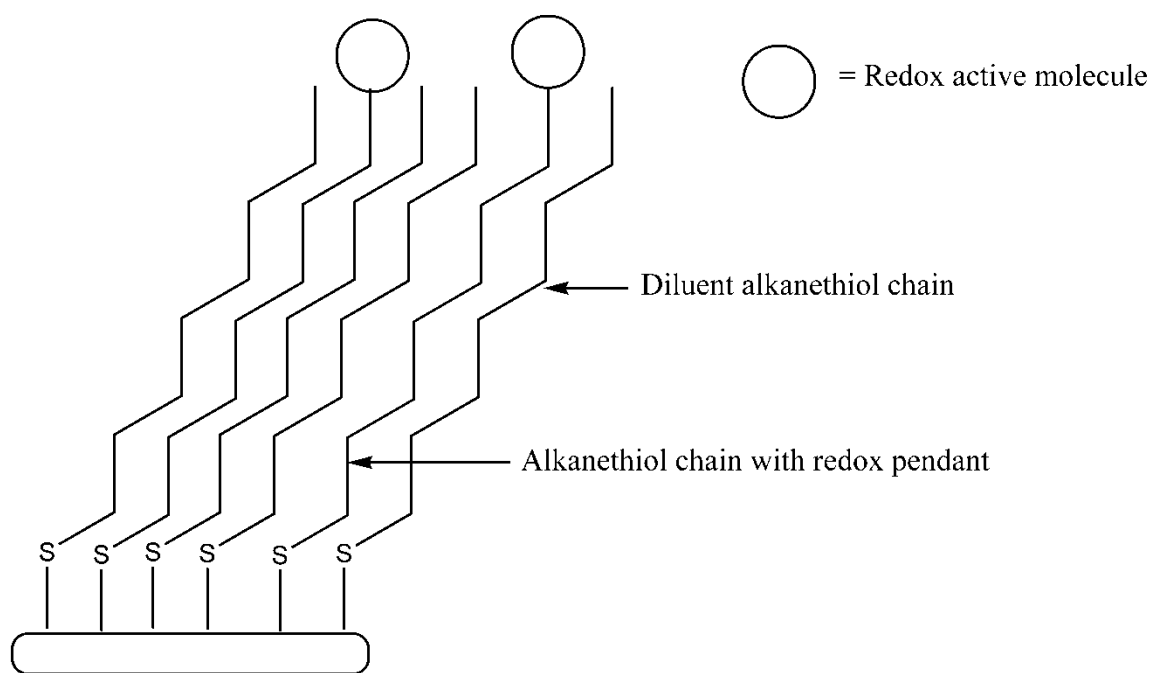


Figure 5-2 SAM mixed with diluents

Chapter Six: References

- (1) Gennis, R. B. *Biomembranes : molecular structure and function*; Springer: New York, 1989, xvii, 533.
- (2) Crane, F. L. *Annu. Rev. Biochem.* **1977**, *46*, 439-469.
- (3) Balzani, V. *Electron transfer in chemistry*; Wiley-VCH: Weinheim ; New York, 2001; Vol. 1,
- (4) Sun, H.; Steeb, J.; Kaifer, A. E. *J. Am. Chem. Soc.* **2006**, *128*, 2820-2821.
- (5) de Rege, P. J. F.; Williams, S. A.; Therien, M. J. *Science* **1995**, *269*, 1409-1413.
- (6) Sanchez, L.; Sierra, M.; Martin, N.; Myles, A. J.; Dale, T. J.; Rebek, J., Jr.; Seitz, W.; Guldi, D. M. *Angew. Chem., Int. Ed.* **2006**, *45*, 4637-4641.
- (7) Balzani, V. *Electron transfer in chemistry*; Wiley-VCH: Weinheim ; Chichester, 2001; Vol. 3,
- (8) Sanchez, L.; Martin, N.; Guldi, D. M. *Angew. Chem., Int. Ed.* **2005**, *44*, 5374-5382.
- (9) Quan, M.; Sanchez, D.; Wasylkiw, M. F.; Smith, D. K. *J. Am. Chem. Soc.* **2007**, *129*, 12847-12856.
- (10) Trammell, S. A.; Moore, M.; Lowy, D.; Lebedev, N. *J. Am. Chem. Soc.* **2008**, *130*, 5579-5585.
- (11) Prime, K. L.; Whitesides, G. M. *Science* **1991**, *252*, 1164-1167.
- (12) Dryhurst, G. *Biological electrochemistry*; Academic Press: New York, 1982,
- (13) Abhayawardhana, A. D.; Sutherland, T. C. *J. Phys. Chem. C* **2009**, *113*, 4915-4924.
- (14) Costentin, C. *Chem. Rev.* **2008**, *108*, 2145-2179.
- (15) Costentin, C.; Robert, M.; Saveant, J.-M. *J. Am. Chem. Soc.* **2006**, *128*, 8726-8727.
- (16) Costentin, C.; Robert, M.; Saveant, J.-M. *J. Am. Chem. Soc.* **2007**, *129*, 5870-5879.
- (17) Costentin, C.; Robert, M.; Saveant, J.-M. *J. Am. Chem. Soc.* **2007**, *129*, 9953-9963.
- (18) Chang, C. J.; Chang, M. C. Y.; Damrauer, N. H.; Nocera, D. G. *Biochim. Biophys. Acta, Bioenerg.* **2004**, *1655*, 13-28.
- (19) Stubbe, J.; Nocera Daniel, G.; Yee Cyril, S.; Chang Michelle, C. Y. *Chem Rev* **2003**, *103*, 2167-2201.
- (20) Miller, A.-F. *Curr. Opin. Chem. Biol.* **2004**, *8*, 162-168.
- (21) Zon, A.; Palys, M.; Stojek, Z.; Sulowska, H.; Ossowski, T. *Electroanalysis* **2003**, *15*, 579-585.
- (22) Mohran, H. S. *Am. J. Appl. Sci.* **2005**, *2*, 1629-1633.
- (23) Gupta, N.; Linschitz, H. *J. Am. Chem. Soc.* **1997**, *119*, 6384-6391.
- (24) Zuman, P. *Substituent effects in organic polarography*; Plenum Press: New York, 1967, xvi, 384 p.

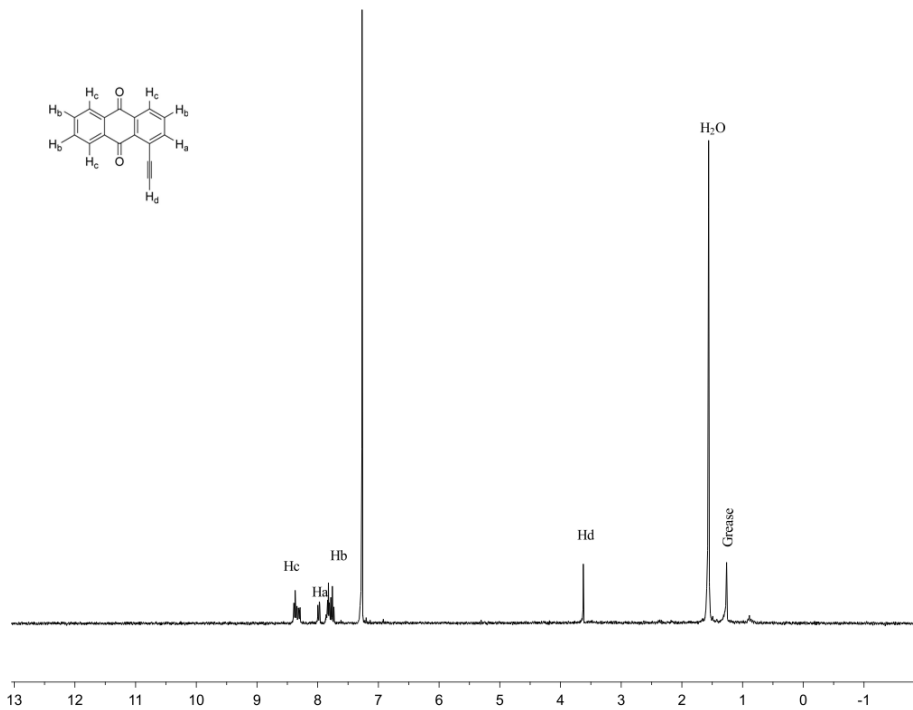
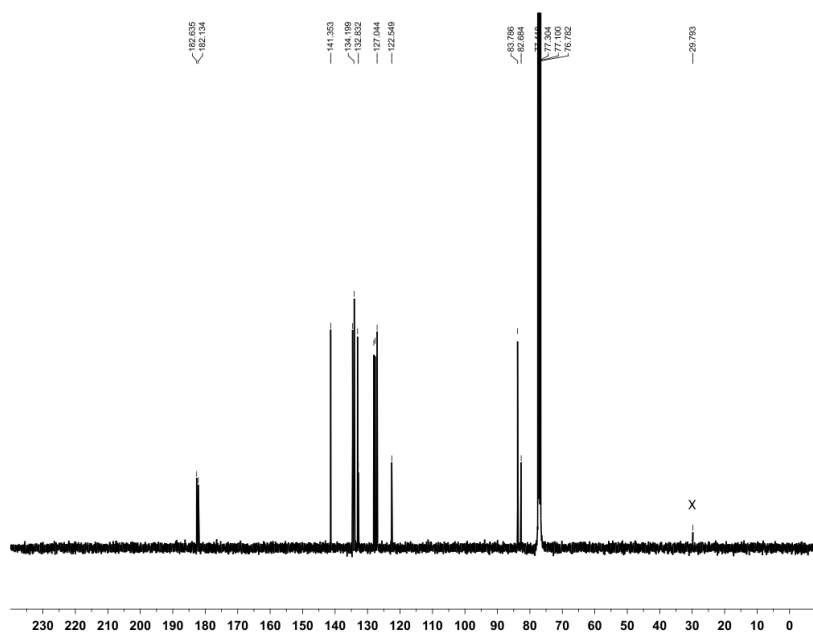
- (25) Given, P. H.; Peover, M. E. *J. Chem. Soc.* **1960**, 385-393.
- (26) Laviron, E. *J. Electroanal. Chem. Interfacial Electrochem.* **1984**, *164*, 213-227.
- (27) Laviron, E. *J. Electroanal. Chem. Interfacial Electrochem.* **1983**, *146*, 15-36.
- (28) March, G.; Reisberg, S.; Piro, B.; Pham, M. C.; Delamar, M.; Noel, V.; Odenthal, K.; Hibbert, D. B.; Gooding, J. J. *J. Electroanal. Chem.* **2008**, *622*, 37-43.
- (29) Trammell, S. A.; Lebedev, N. *J. Electroanal. Chem.* **2009**, *632*, 127-132.
- (30) Fujihira, M.; Rubinstein, I.; Rusling, J. F. *Modified electrodes*; Wiley-VCH: Weinheim, 2007; Vol. 10, xii, 838 p.
- (31) Trammell, S. A.; Moore, M.; Schull, T. L.; Lebedev, N. *J. Electroanal. Chem.* **2009**, *628*, 125-133.
- (32) Trammell, S. A.; Lowy, D. A.; Seferos, D. S.; Moore, M.; Bazan, G. C.; Lebedev, N. *J. Electroanal. Chem.* **2007**, *606*, 33-38.
- (33) Hong, H.-G.; Park, W. *Langmuir* **2001**, *17*, 2485-2492.
- (34) Park, W.; Ahmed, J.; Kim, S. *Colloids Surf B Biointerfaces* **2009**, *68*, 120-124.
- (35) Sato, Y.; Fujita, M.; Mizutani, F.; Uosaki, K. *J. Electroanal. Chem.* **1996**, *409*, 145-154.
- (36) Stine, K. J.; Andrauskas, D. M.; Khan, A. R.; Forgo, P.; D'Souza, V. T. *J. Electroanal. Chem.* **1999**, *465*, 209-218.
- (37) Nagata, M.; Kondo, M.; Suemori, Y.; Ochiai, T.; Dewa, T.; Ohtsuka, T.; Nango, M. *Colloids Surf., B* **2008**, *64*, 16-21.
- (38) Trammell, S. A.; Seferos, D. S.; Moore, M.; Lowy, D. A.; Bazan, G. C.; Kushmerick, J. G.; Lebedev, N. *Langmuir* **2007**, *23*, 942-948.
- (39) Bard, A. J.; Faulkner, L. R. *Electrochemical methods : fundamentals and applications*; Wiley: New York ; Chichester, 1980, xviii, 718 p.
- (40) Mabbott, G. A. *J. Chem. Educ.* **1983**, *60*, 697-702.
- (41) Laviron, E. *J. Electroanal. Chem. Interfacial Electrochem.* **1979**, *101*, 19-28.
- (42) Bockris, J. O. M.; Reddy, A. K. N.; Gamboa-Aldeco, M. *Modern electrochemistry*; 2nd ed.; Plenum Press: New York, 1998; Vol. 2A, 3 v. (liv, 2053 p.).
- (43) Barsoukov, E.; Macdonald, J. R. *Impedance spectroscopy : theory, experiment, and applications*; 2nd ed.; Wiley-Interscience: Hoboken, N.J., 2005, xvii, 595 p.
- (44) Brevnov, D. A.; Finklea, H. O.; Van Ryswyk, H. *J. Electroanal. Chem.* **2001**, *500*, 100-107.
- (45) Laviron, E. *J. Electroanal. Chem. Interfacial Electrochem.* **1979**, *97*, 135-149.
- (46) Love, J. C.; Estroff Lara, A.; Kriebel Jennah, K.; Nuzzo Ralph, G.; Whitesides George, M. *Chem Rev* **2005**, *105*, 1103-1169.
- (47) Nuzzo, R. G.; Allara, D. L. *J. Am. Chem. Soc.* **1983**, *105*, 4481-4483.
- (48) Green, M. J.; Barner, B. J.; Corn, R. M. *Rev. Sci. Instrum.* **1991**, *62*, 1426-1430.

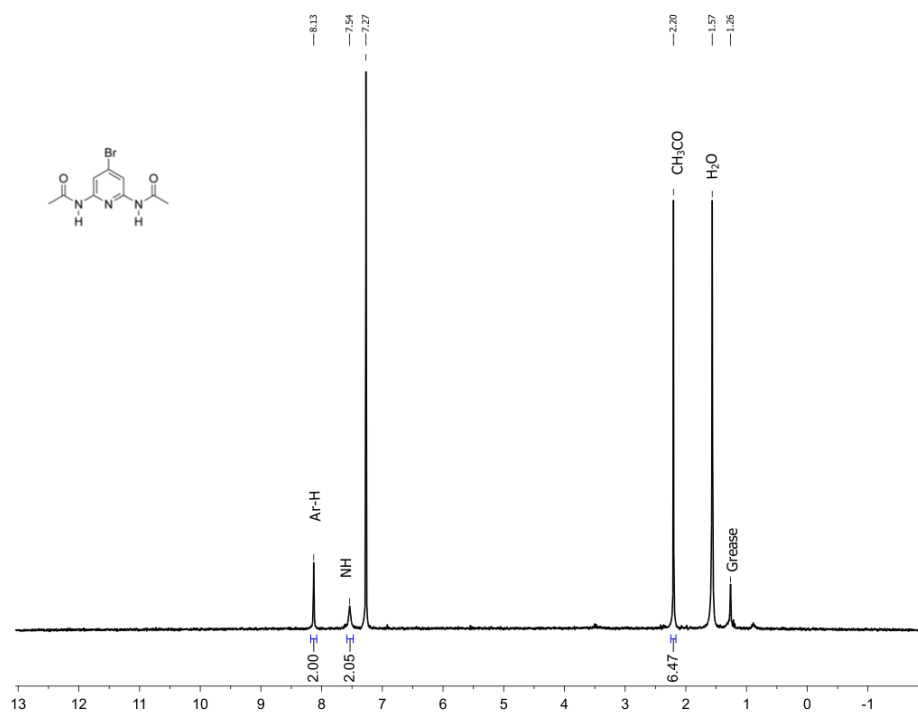
- (49) Golden, W. G.; Saperstein, D. D. *J. Electron Spectrosc. Relat. Phenom.* **1983**, *30*, 43-50.
- (50) Nuzzo, R. G.; Dubois, L. H.; Allara, D. L. *J. Am. Chem. Soc.* **1990**, *112*, 558-569.
- (51) Parikh, A. N.; Allara, D. L. *J. Chem. Phys.* **1992**, *96*, 927-945.
- (52) Bensebaa, F.; Ellis, T. H.; Badia, A.; Lennox, R. B. *Langmuir* **1998**, *14*, 2361-2367.
- (53) Perrin, D. D.; Armarego, W. L. F. *Purification of laboratory chemicals*; 3rd ed.; Pergamon Press: Oxford ; New York, 1988, xii, 391 p.
- (54) Gouloumis, A.; Gonzalez-Rodriguez, D.; Vazquez, P.; Torres, T.; Liu, S.; Echevoyen, L.; Ramey, J.; Hug, G. L.; Guldi, D. M. *J. Am. Chem. Soc.* **2006**, *128*, 12674-12684.
- (55) Pauvert, M.; Laine, P.; Jonas, M.; Wiest, O. *J. Org. Chem.* **2004**, *69*, 543-548.
- (56) Llanes-Pallas, A.; Palma, C.-A.; Piot, L.; Belbakra, A.; Listorti, A.; Prato, M.; Samori, P.; Armaroli, N.; Bonifazi, D. *J. Am. Chem. Soc.* **2009**, *131*, 509-520.
- (57) Inouye, M.; Hyodo, Y.; Nakazumi, H. *J. Org. Chem.* **1999**, *64*, 2704-2710.
- (58) Riegel, E. R.; Zwilgmeyer, F. *Org. Synth.* **1937**, *17*, 40-42.
- (59) Riegel, E. R.; Reinhard, M. C. *J. Am. Chem. Soc.* **1926**, *48*, 1334-1345.
- (60) Gray, M.; Goodman, A. J.; Carroll, J. B.; Bardon, K.; Markey, M.; Cooke, G.; Rotello, V. M. *Org. Lett.* **2004**, *6*, 385-388.
- (61) Pryor, K. E.; Shipps, W., Jr.; Skyler, D. A.; Rebek, J., Jr. *Tetrahedron* **1998**, *54*, 4107-4124.
- (62) Abhayawardhana, A. D.; Parvez, M.; Sutherland, T. C. *Acta Crystallogr., Sect. E: Struct. Rep. Online* **2007**, *E63*, o2963-o2965.
- (63) Chessa, G.; Canovese, L.; Visentin, F.; Santo, C.; Seraglia, R. *Tetrahedron* **2005**, *61*, 1755-1763.
- (64) Nettekoven, M.; Jenny, C. *Org. Process Res. Dev.* **2003**, *7*, 38-43.
- (65) Goldstein, A. E. *J. Am. Chem. Soc.* **1939**, *61*, 1600-1601.
- (66) Ma, H.; Kang, M.-S.; Xu, Q.-M.; Kim, K.-S.; Jen, A. K. Y. *Chem. Mater.* **2005**, *17*, 2896-2903.
- (67) Caruso, E. B.; Petralia, S.; Conoci, S.; Giuffrida, S.; Sortino, S. *J. Am. Chem. Soc.* **2007**, *129*, 480-481.
- (68) Gu, W.; Nusinzon, I.; Smith, R. D.; Horvath, C. M.; Silverman, R. B. *Bioorg. Med. Chem.* **2006**, *14*, 3320-3329.
- (69) Rochlin, E.; Rappoport, Z. *J. Org. Chem.* **2003**, *68*, 216-226.
- (70) Blankespoor, R. L.; Smart, R. P.; Batts, E. D.; Kiste, A. A.; Lew, R. E.; Van der Vliet, M. E. *J. Org. Chem.* **1995**, *60*, 6852-6859.
- (71) Gustowski, D. A.; Delgado, M.; Gatto, V. J.; Echevoyen, L.; Gokel, G. W. *J. Am. Chem. Soc.* **1986**, *108*, 7553-7560.
- (72) Susan, M. A. B. H.; Tani, K.; Watanabe, M. *Colloid Polym. Sci.* **1999**, *277*, 1125-1133.
- (73) Lide, D. R.; Weast, R. C.; Chemical Rubber Company. *CRC Handbook of chemistry and physics : a ready reference book of chemical and physical data*; 83rd ed.; CRC Press: Boca Raton, Fla. ;, 2002,

- (74) Tkac, J.; Davis, J. J. *J. Electroanal. Chem.* **2008**, *621*, 117-120.
- (75) Bag, S. P.; Quintus, F.; Freiser, H. *Inorg. Chem.* **1962**, *1*, 887-890.
- (76) Hall, A. K.; Harrowfield, J. M.; Skelton, B. W.; White, A. H. *Acta Crystallogr., Sect. C: Cryst. Struct. Commun.* **2000**, *C56*, 448-450.
- (77) Smith, M.; March, J. *March's advanced organic chemistry : reactions, mechanisms, and structure*; 5th ed.; Wiley: New York, 2001, xviii, 2083 p.
- (78) Sy, A. O.; Raksis, J. W. *Tetrahedron Lett.* **1980**, *21*, 2223-2226.
- (79) Rane, D. S.; Sharma, M. M. *J. Chem. Technol. Biotechnol.* **1994**, *59*, 271-277.
- (80) Sonogashira, K. *J. Organomet. Chem.* **2002**, *653*, 46-49.
- (81) Meijere, A. d.; Diederich, F. *Metal-catalyzed cross-coupling reactions*; 2nd, completely rev. and enl. ed.; Wiley-VCH: Weinheim, 2004; Vol. 2, 2 v. (xxii, 916 p.).
- (82) Chinchilla, R.; Najera, C. *Chem. Rev.* **2007**, *107*, 874-922.
- (83) Anastasia, L.; Negishi, E.-i. *Org. Lett.* **2001**, *3*, 3111-3113.
- (84) Bertus, P.; Fecourt, F.; Bauder, C.; Pale, P. *New J. Chem.* **2004**, *28*, 12-14.
- (85) Toyota, S.; Kurokawa, M.; Araki, M.; Nakamura, K.; Iwanaga, T. *Org. Lett.* **2007**, *9*, 3655-3658.
- (86) Llanes-Pallas, A.; Matena, M.; Jung, T.; Prato, M.; Stohr, M.; Bonifazi, D. *Angew Chem Int Ed Engl* **2008**, *47*, 7726-7730.
- (87) Mann, C. K.; Barnes, K. K. *Electrochemical reactions in nonaqueous systems*; M. Dekker: New York, 1970, viii, 560 p.
- (88) Patai, S. *The chemistry of the quinonoid compounds*; Interscience: London, New York, 1974, 2 v. (xiv, 1274, xiv p.).
- (89) Shamsipur, M.; Siroueinejad, A.; Hemmateenejad, B.; Abbaspour, A.; Sharghi, H.; Alizadeh, K.; Arshadi, S. *J. Electroanal. Chem.* **2007**, *600*, 345-358.
- (90) Li, C.-Y.; Caspar, L.; Dixon, D. W., Jr. *Electrochim. Acta* **1980**, *25*, 1135-1142.
- (91) Peover, M. E. *J. Chem. Soc.* **1962**, 4540-4549.
- (92) Frontana, C.; Vazquez-Mayagoitia, A.; Garza, J.; Vargas, R.; Gonzalez, I. *J. Phys. Chem. A* **2006**, *110*, 9411-9419.
- (93) Skulason, H.; Frisbie, C. D. *Langmuir* **1998**, *14*, 5834-5840.
- (94) Arai, S.; Kato, S.; Hida, M. *Bull. Chem. Soc. Jpn.* **1985**, *58*, 1458-1463.
- (95) Ron, H.; Rubinstein, I. *J. Am. Chem. Soc.* **1998**, *120*, 13444-13452.
- (96) Liu, X.; Xu, B.; Haubrich, J.; Madix, R. J.; Friend, C. M. *J. Am. Chem. Soc.* **2009**, *131*, 5757-5759.
- (97) Zhang, L.; Lu, T.; Gokel, G. W.; Kaifer, A. E. *Langmuir* **1993**, *9*, 786-791.
- (98) Smith, C. P.; White, H. S. *Anal. Chem.* **1992**, *64*, 2398-2405.
- (99) Feldberg, S. W.; Rubinstein, I. *J. Electroanal. Chem. Interfacial Electrochem.* **1988**, *240*, 1-15.
- (100) Mebrahtu, T.; Berry, G. M.; Bravo, B. G.; Michelhaugh, S. L.; Soriaga, M. P. *Langmuir* **1988**, *4*, 1147-1151.
- (101) Stern, D. A.; Wellner, E.; Salaita, G. N.; Laguren-Davidson, L.; Lu, F.; Batina, N.; Frank, D. G.; Zapien, D. C.; Walton, N.; Hubbard, A. T. *J. Am. Chem. Soc.* **1988**, *110*, 4885-4893.

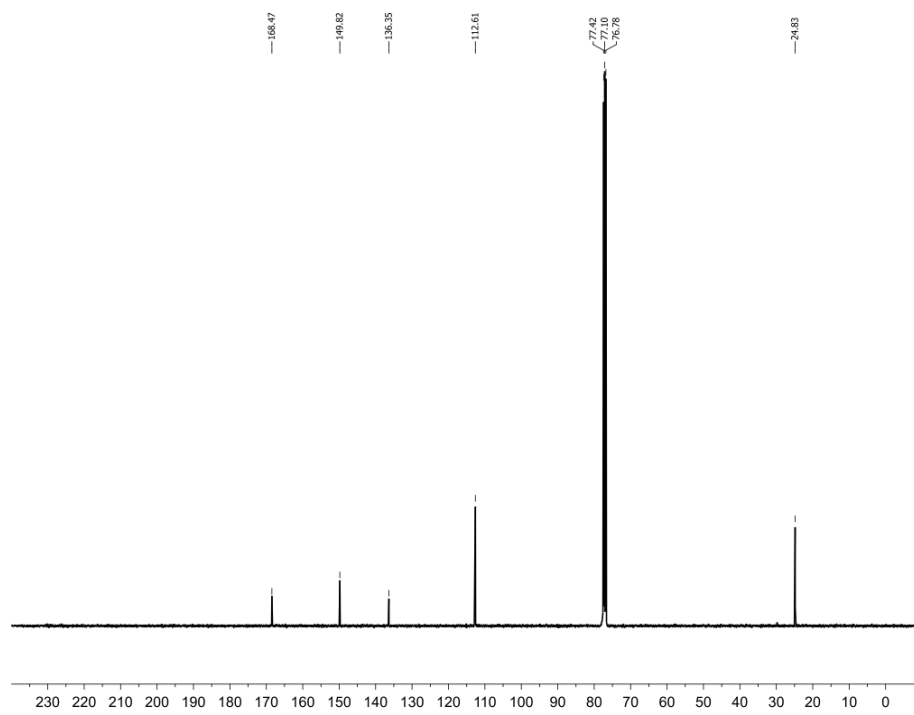
- (102) Boubour, E.; Lennox, R. B. *J. Phys. Chem. B* **2000**, *104*, 9004-9010.
- (103) Los, P.; Laviron, E. *J. Electroanal. Chem.* **1997**, *432*, 85-99.
- (104) Laviron, E. *J. Electroanal. Chem. Interfacial Electrochem.* **1979**, *105*, 35-42.
- (105) Smith, C. P.; White, H. S. *Langmuir* **1993**, *9*, 1-3.
- (106) Andreu, R.; Fawcett, W. R. *J. Phys. Chem.* **1994**, *98*, 12753-12758.
- (107) Fawcett, W. R.; Fedurco, M.; Kovacova, Z. *Langmuir* **1994**, *10*, 2403-2408.
- (108) Bryant, M. A.; Crooks, R. M. *Langmuir* **1993**, *9*, 385-387.
- (109) Park, W.; Hong, H.-G. *Bull. Korean Chem. Soc.* **2006**, *27*, 381-385.
- (110) Reuben, J. *J. Am. Chem. Soc.* **1987**, *109*, 316-321.
- (111) Lee, L. Y. S.; Lennox, R. B. *Langmuir* **2007**, *23*, 292-296.
- (112) Shamsipur, M.; Hemmateenejad, B.; Akhond, M.; Sharghi, H. *Talanta* **2001**, *54*, 1113-1120.
- (113) Hickman, J. J.; Ofer, D.; Laibinis, P. E.; Whitesides, G. M.; Wrighton, M. S. *Science* **1991**, *252*, 688-691.
- (114) Chidsey, C. E. D.; Bertozzi, C. R.; Putvinski, T. M.; Mujsee, A. M. *J. Am. Chem. Soc.* **1990**, *112*, 4301-4306.
- (115) Masgrau, L.; Gonzalez-Lafont, A.; Lluch, J. M. *Theor. Chem. Acc.* **2003**, *110*, 352-357.
- (116) Finklea, H. O. *J. Phys. Chem. B* **2001**, *105*, 8685-8693.
- (117) M. J. Frisch, G. W. T., H. B. Schlegel, G. E. Scuseria, M. A. Robb, J. R. Cheeseman, J. A. Montgomery, Jr., T. Vreven, K. N. Kudin, J. C. Burant, J. M. Millam, S. S. Iyengar, J. Tomasi, V. Barone, B. Mennucci, M. Cossi, G. Scalmani, N. Rega, G. A. Petersson, H. Nakatsuji, M. Hada, M. Ehara, K. Toyota, R. Fukuda, J. Hasegawa, M. Ishida, T. Nakajima, Y. Honda, O. Kitao, H. Nakai, M. Klene, X. Li, J. E. Knox, H. P. Hratchian, J. B. Cross, V. Bakken, C. Adamo, J. Jaramillo, R. Gomperts, R. E. Stratmann, O. Yazyev, A. J. Austin, R. Cammi, C. Pomelli, J. W. Ochterski, P. Y. Ayala, K. Morokuma, G. A. Voth, P. Salvador, J. J. Dannenberg, V. G. Zakrzewski, S. Dapprich, A. D. Daniels, M. C. Strain, O. Farkas, D. K. Malick, A. D. Rabuck, K. Raghavachari, J. B. Foresman, J. V. Ortiz, Q. Cui, A. G. Baboul, S. Clifford, J. Cioslowski, B. B. Stefanov, G. Liu, A. Liashenko, P. Piskorz, I. Komaromi, R. L. Martin, D. J. Fox, T. Keith, M. A. Al-Laham, C. Y. Peng, A. Nanayakkara, M. Challacombe, P. M. W. Gill, B. Johnson, W. Chen, M. W. Wong, C. Gonzalez, J. A. Pople In *Gaussian 03, Revision E.01* Wallingford CT, 2004.
- (118) Shimada, H.; Nakamura, A.; Yoshihara, T.; Tobita, S. *Photochem. Photobiol. Sci.* **2005**, *4*, 367-375.
- (119) Gautrot, J. E.; Hodge, P.; Cupertino, D.; Helliwell, M. *New J. Chem.* **2006**, *30*, 1801-1807.

Chapter Seven: Appendix

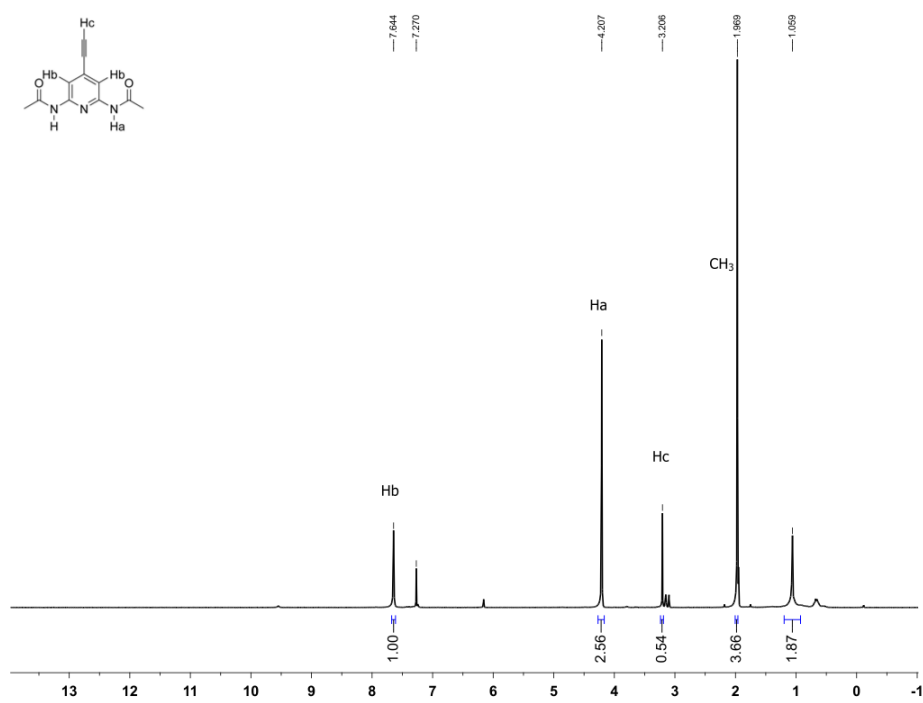
7.1 ^1H and ^{13}C NMR Spectra of Compounds ^1H NMR of compound 2 ^{13}C NMR of compound 2



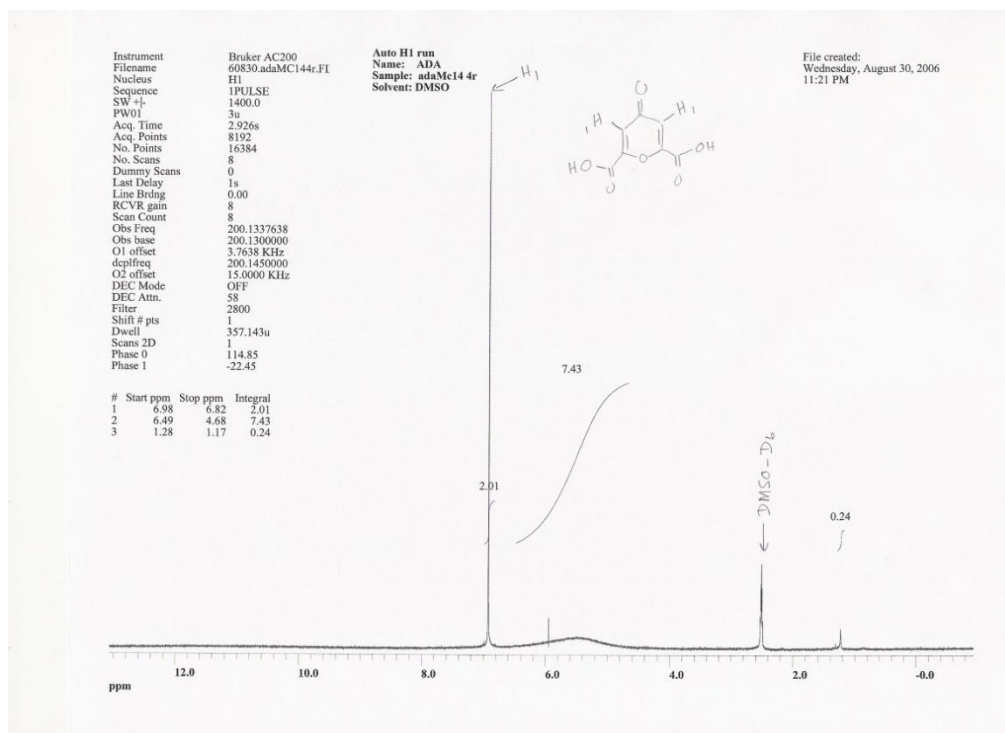
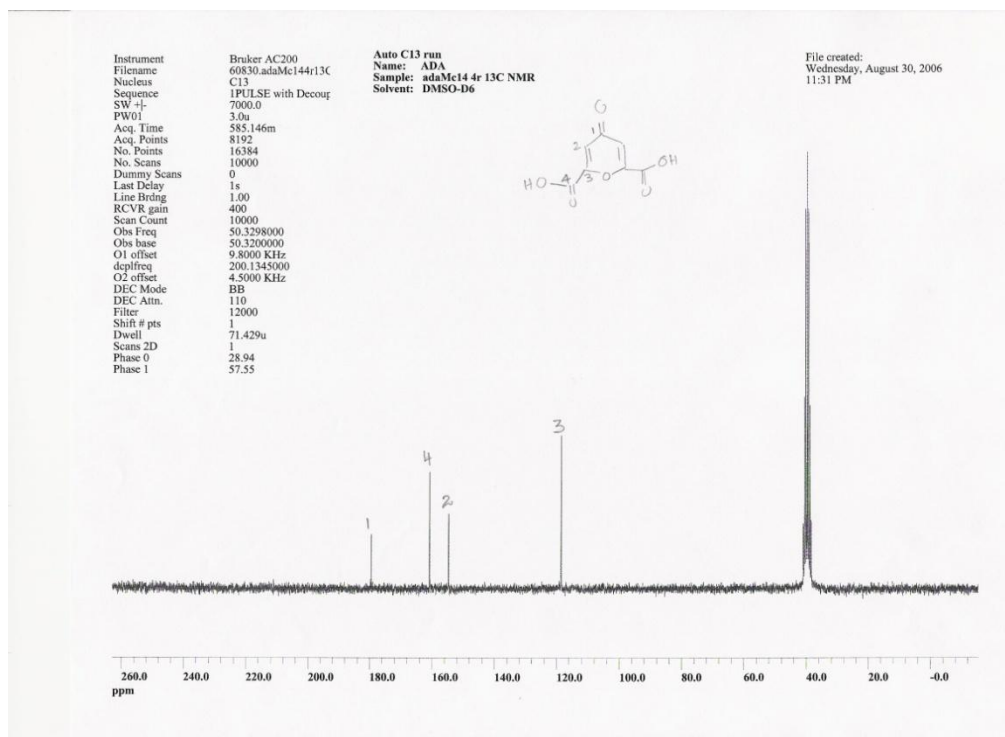
¹H NMR of compound **3**

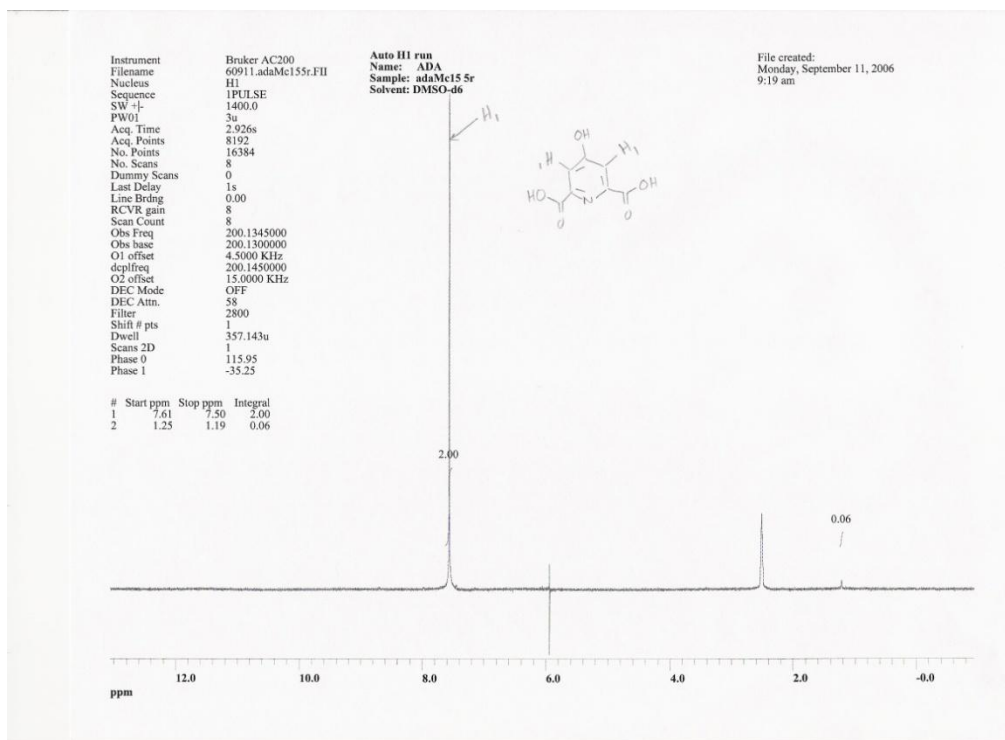
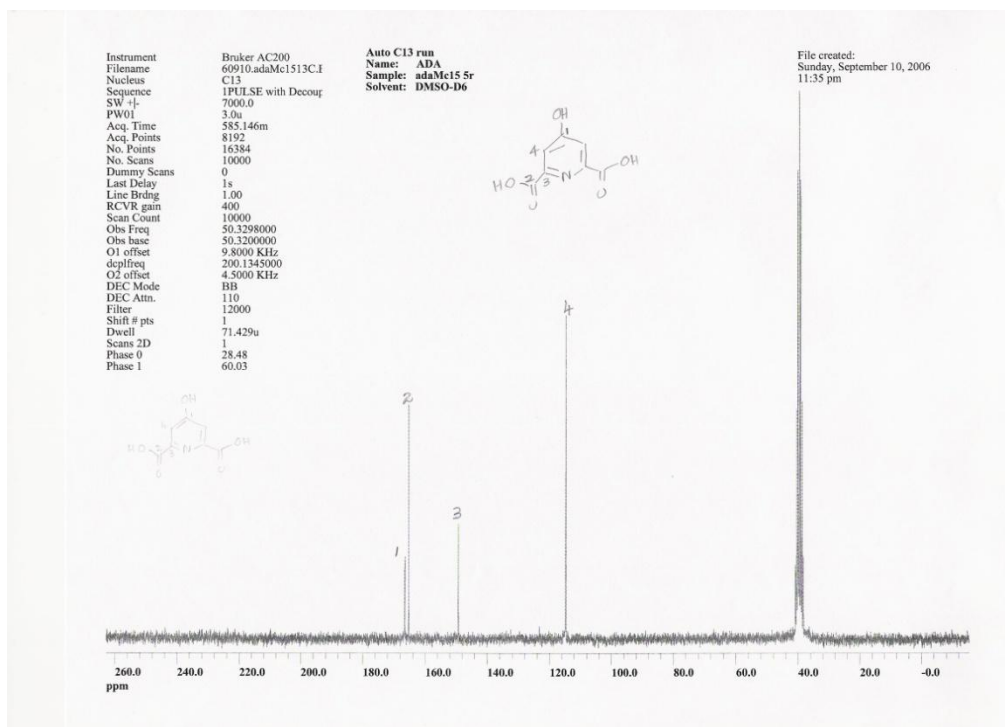


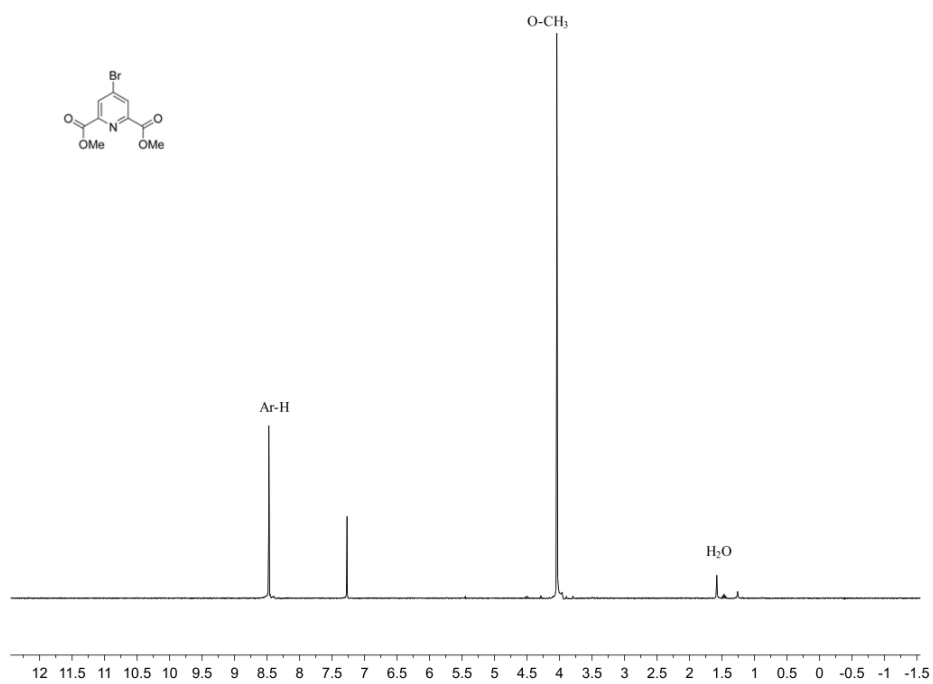
¹³C NMR of compound **3**



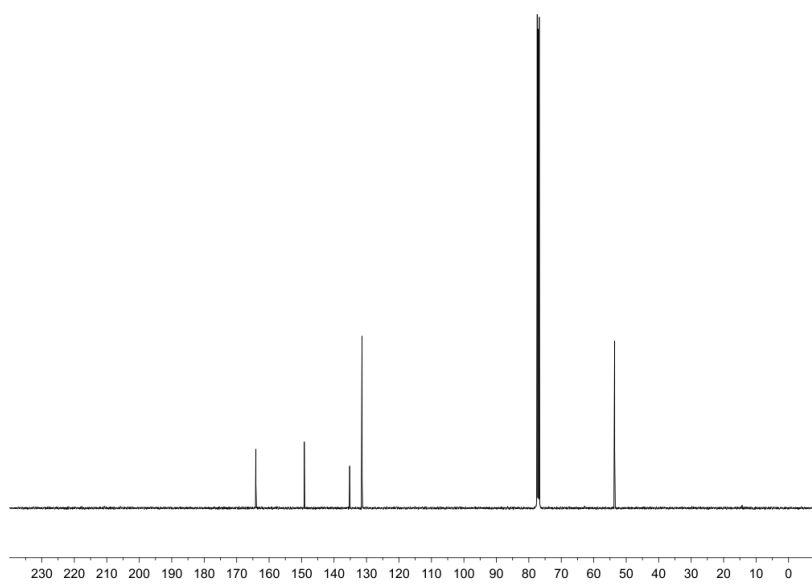
^1H NMR of compound **3'**

 ^1H NMR of compound 4 ^{13}C NMR of compound 4

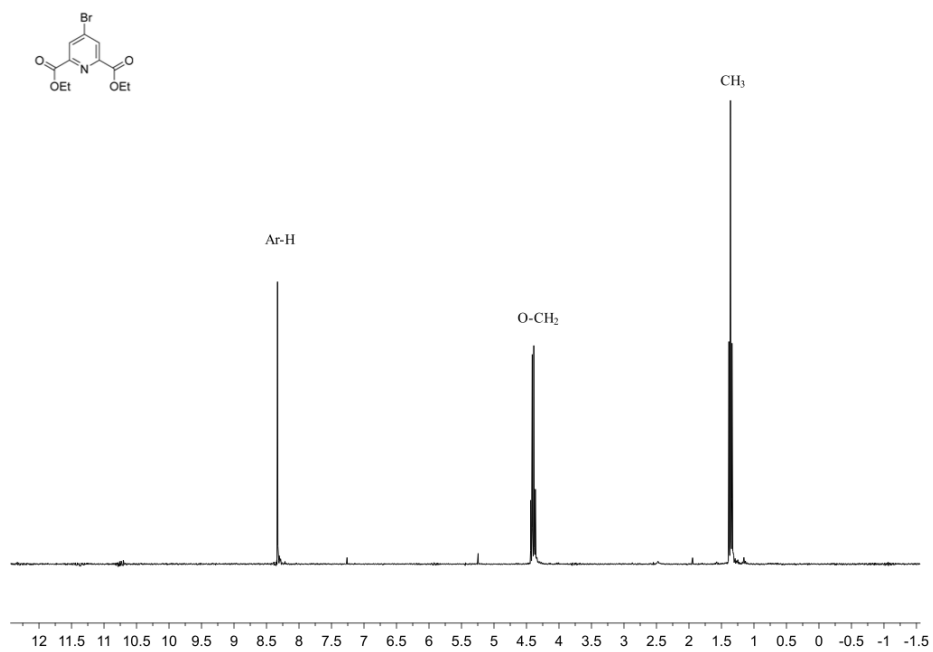
 ^1H NMR of compound 5 ^{13}C NMR of compound 5



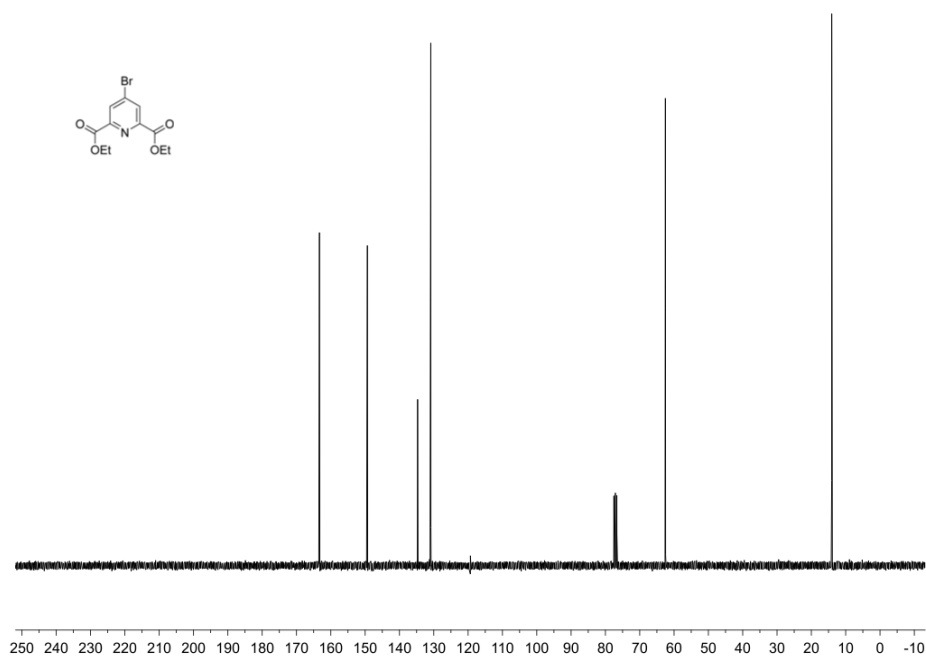
^1H NMR of compound **6a**



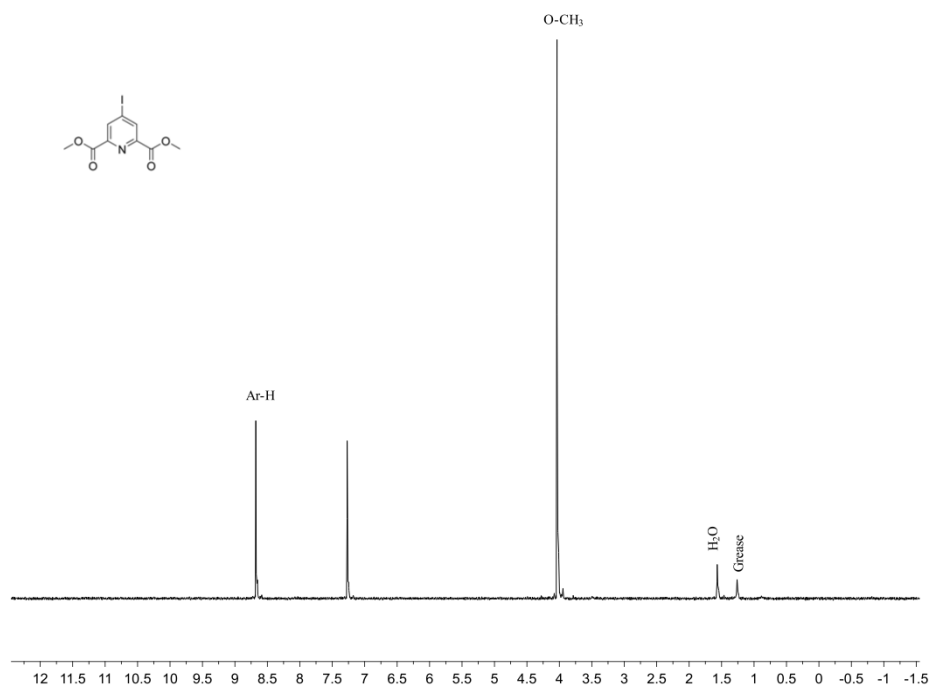
^{13}C NMR of compound **6a**



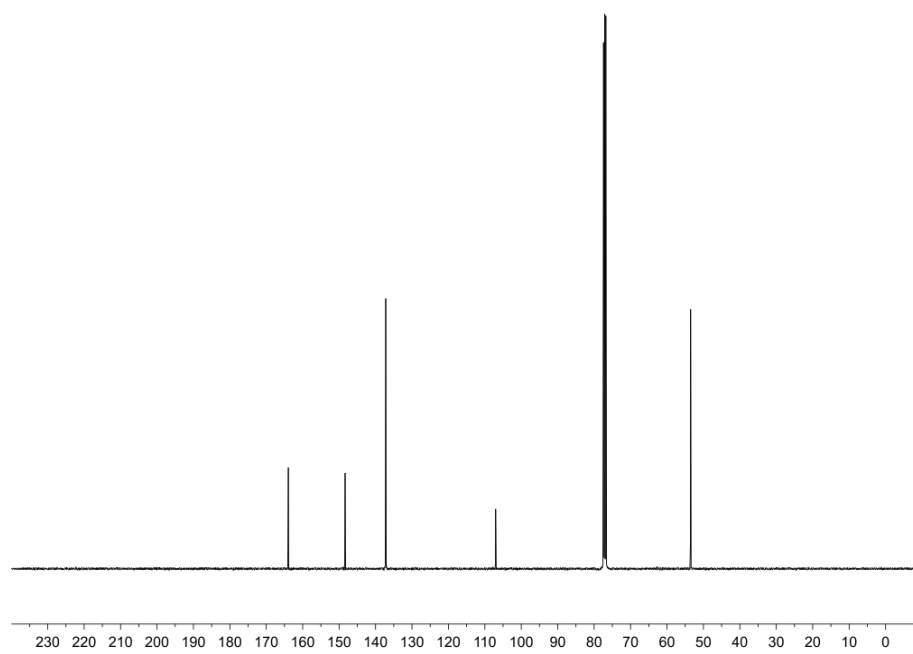
^1H NMR of compound **6b**



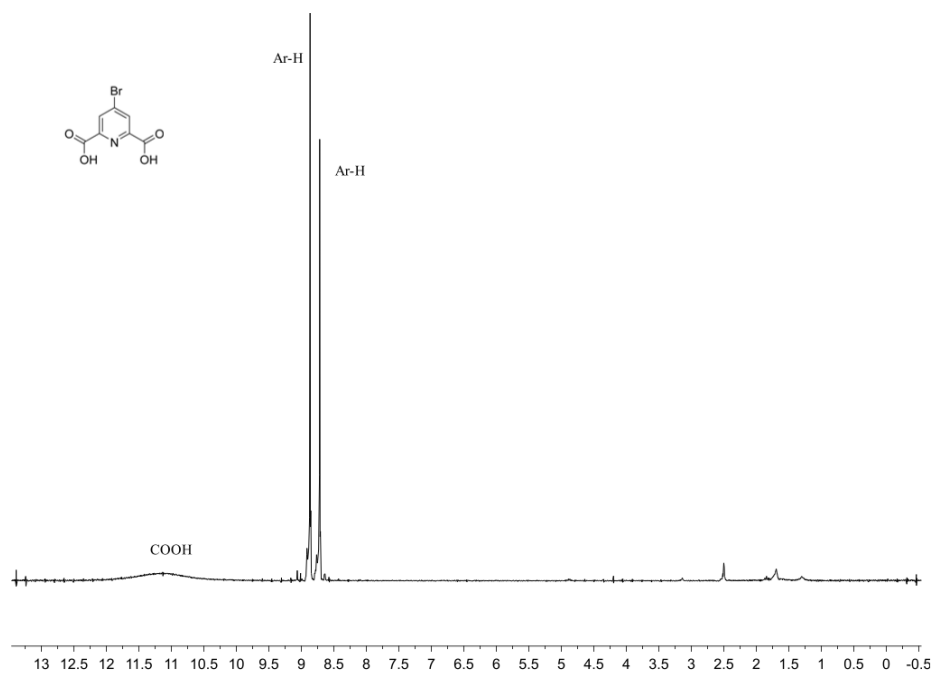
^{13}C NMR of compound **6b**



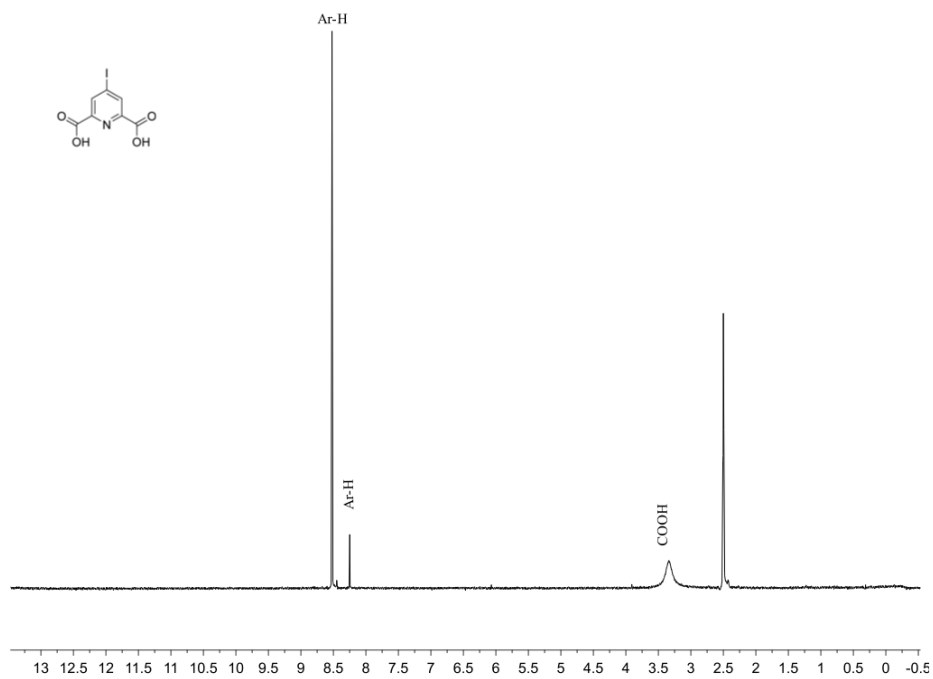
¹H NMR of compound 7



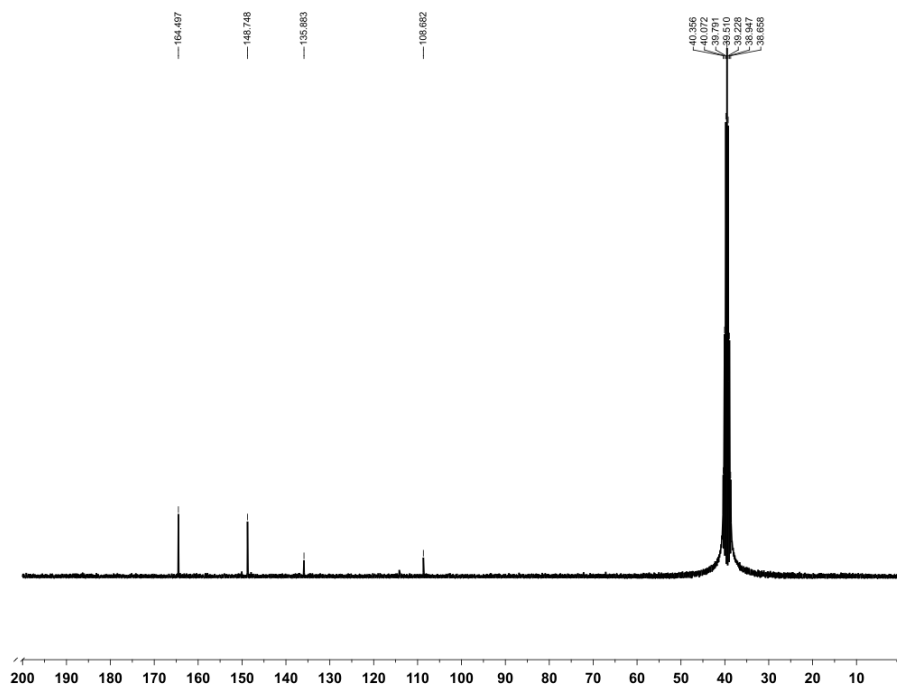
¹³C NMR of compound 7



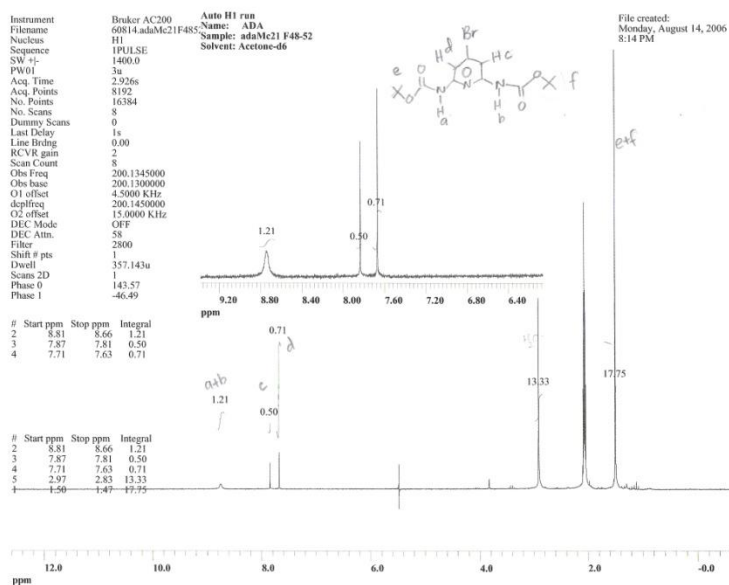
^1H NMR of compound **8a**

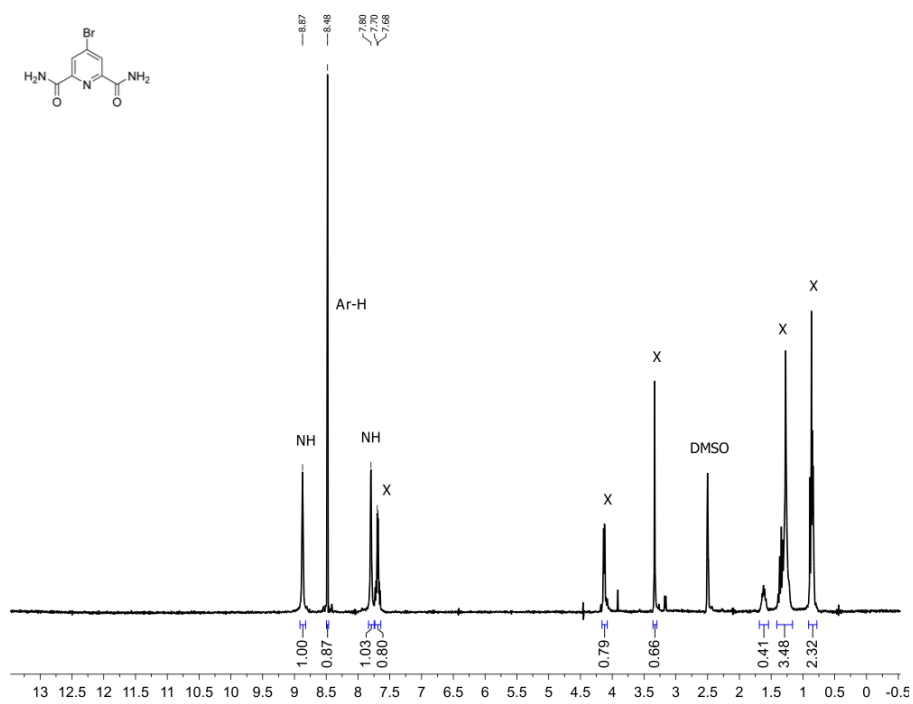


¹H NMR of compound **8b**

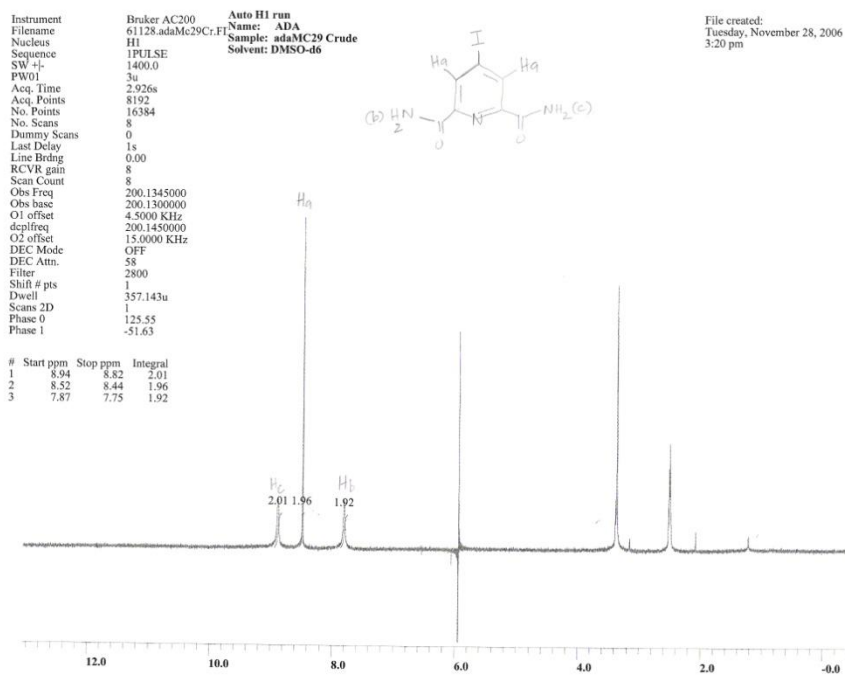
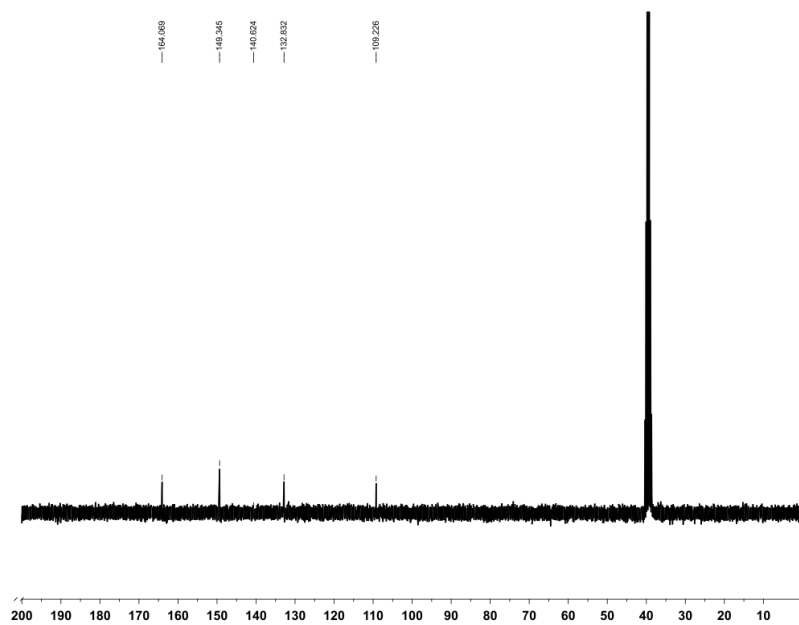


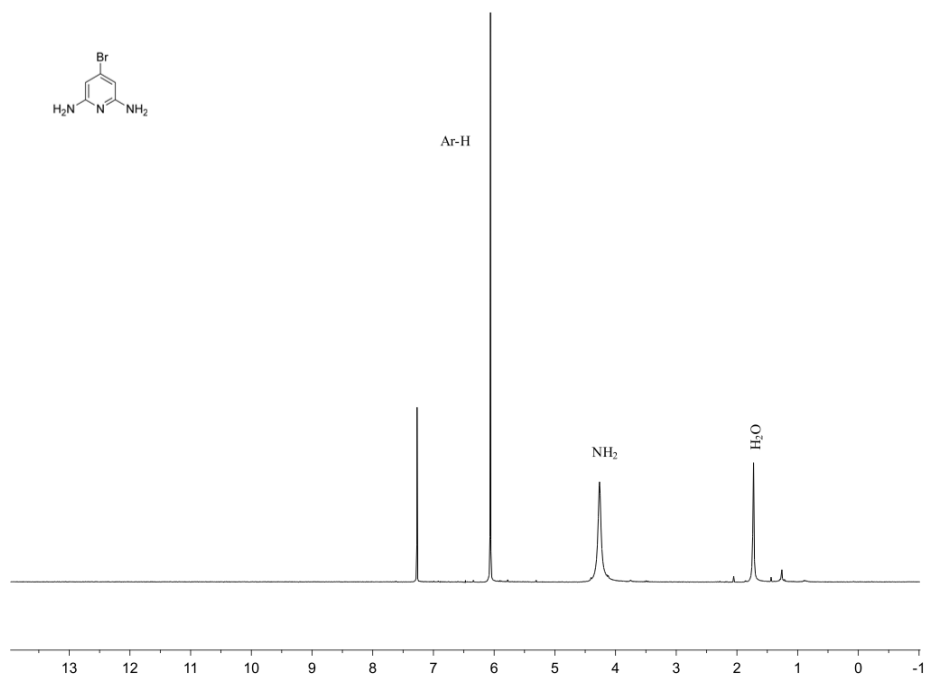
¹³C NMR of compound **8b**

¹H NMR of compound 9

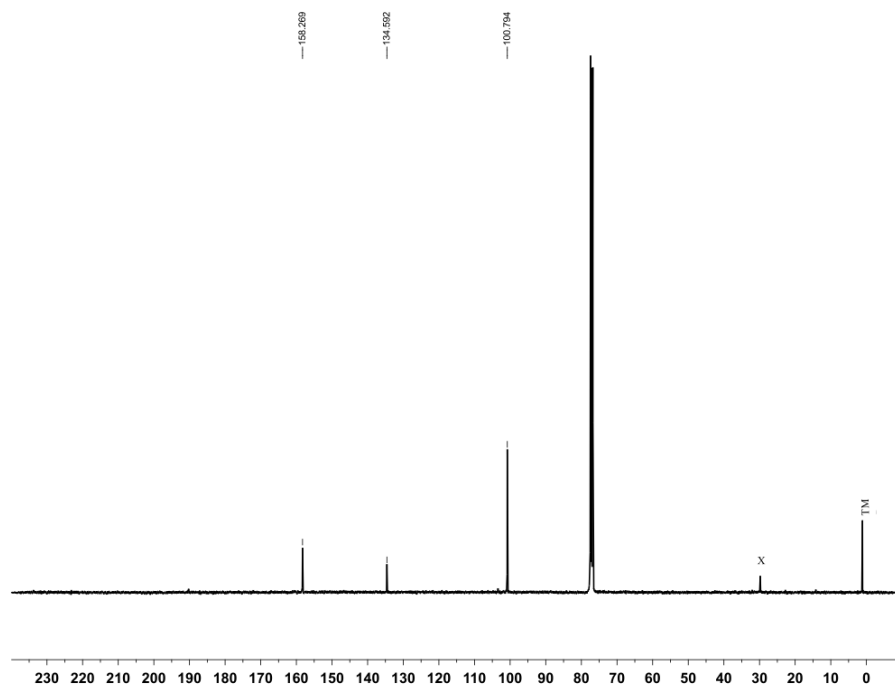


^1H NMR of compound **10a**

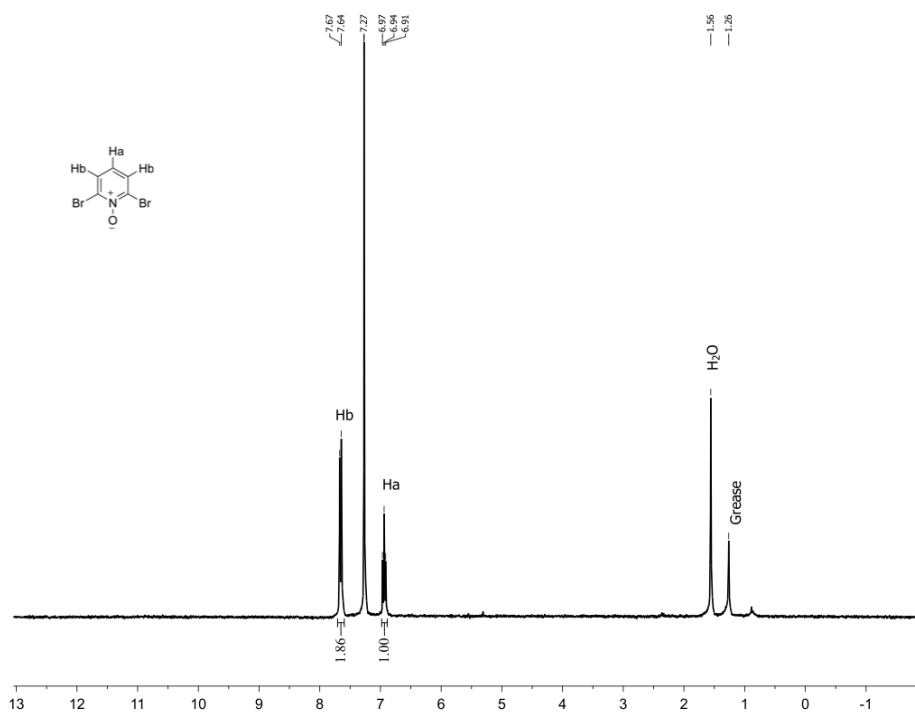
 ^1H NMR of compound **10b** ^{13}C NMR of compound **10b**



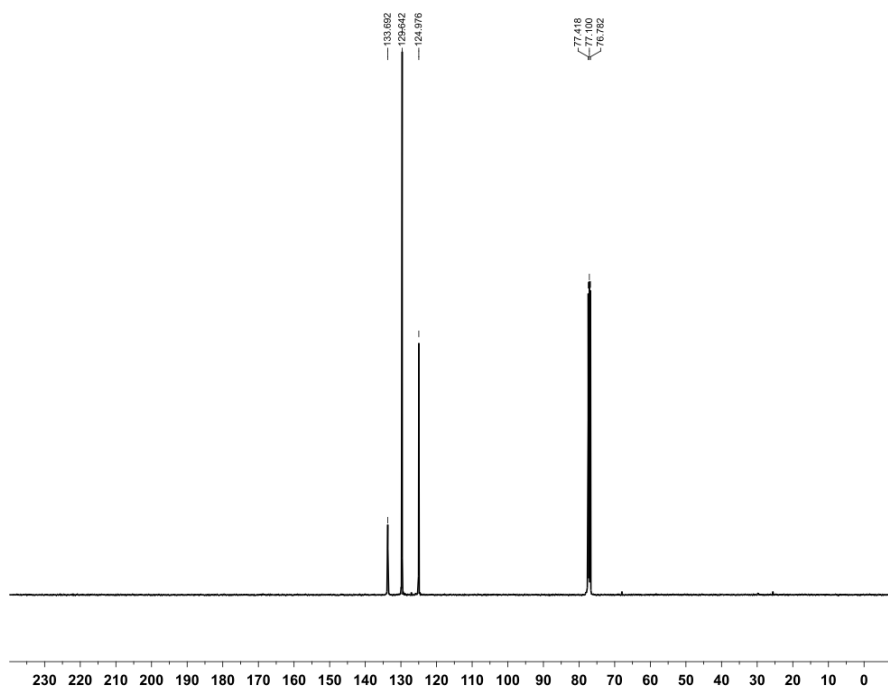
¹H NMR of compound **11**



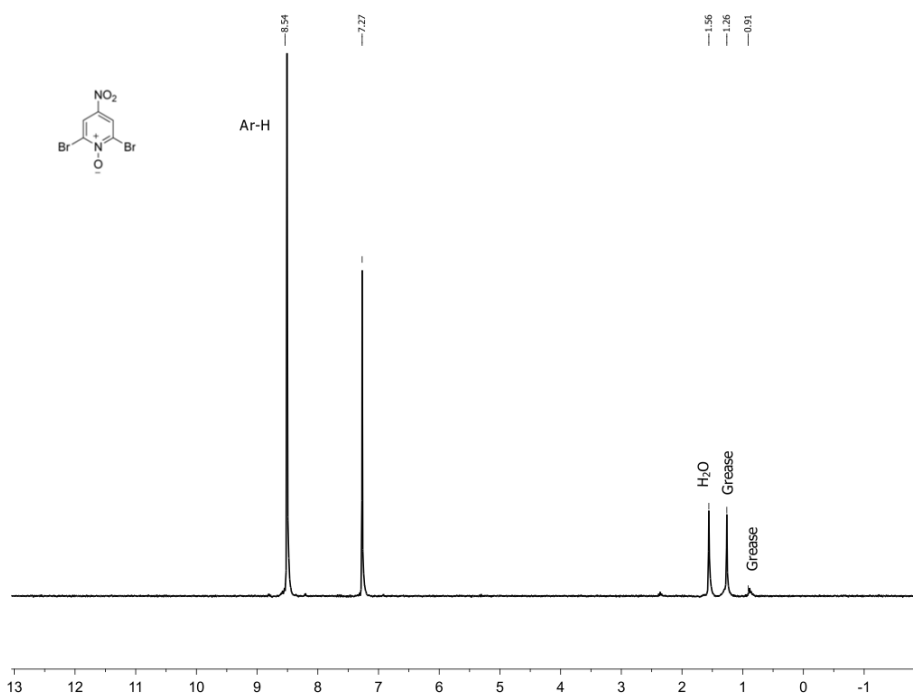
¹³C NMR of compound **11**



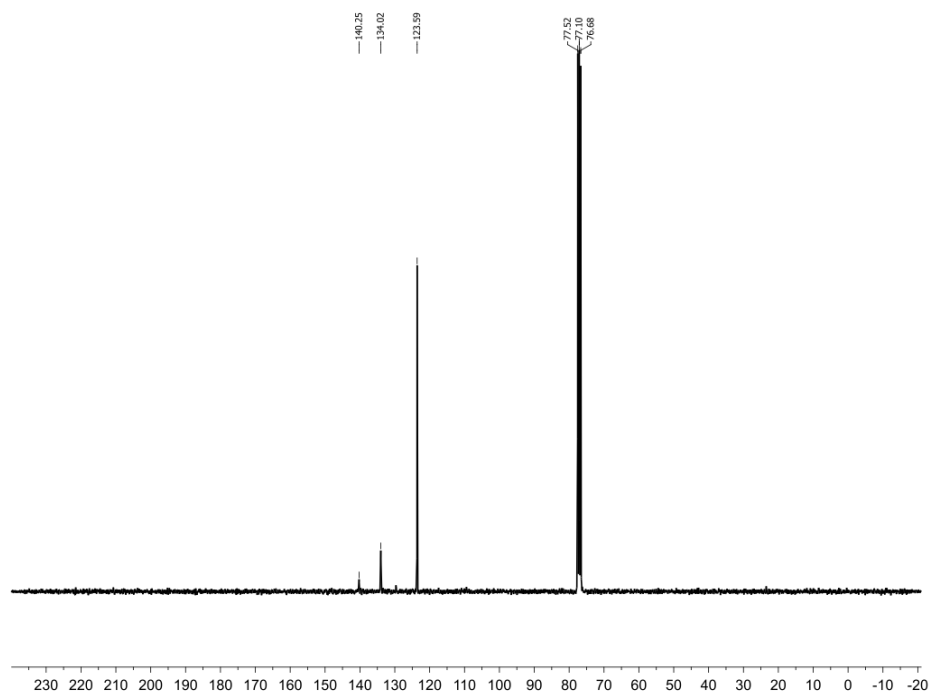
¹H NMR of compound **12**



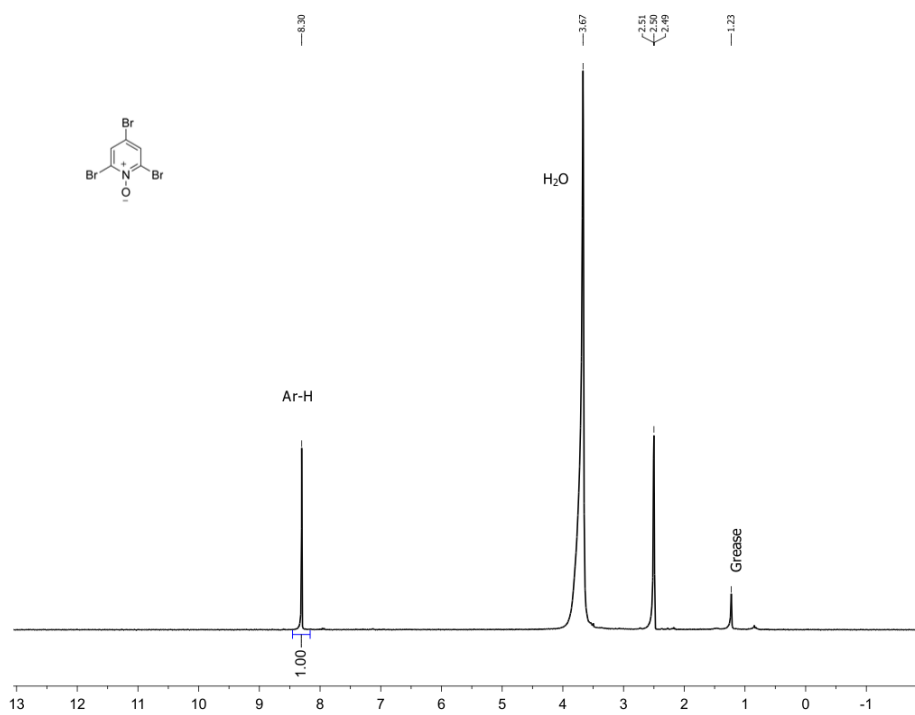
¹³C NMR of compound **12**



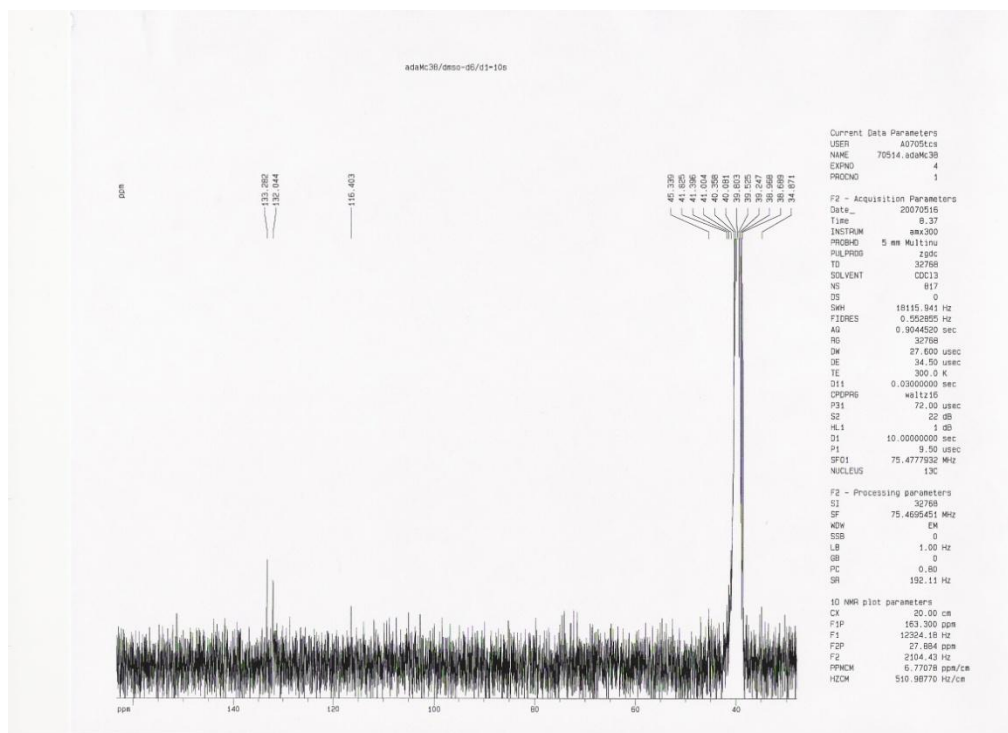
¹H NMR of compound **13**



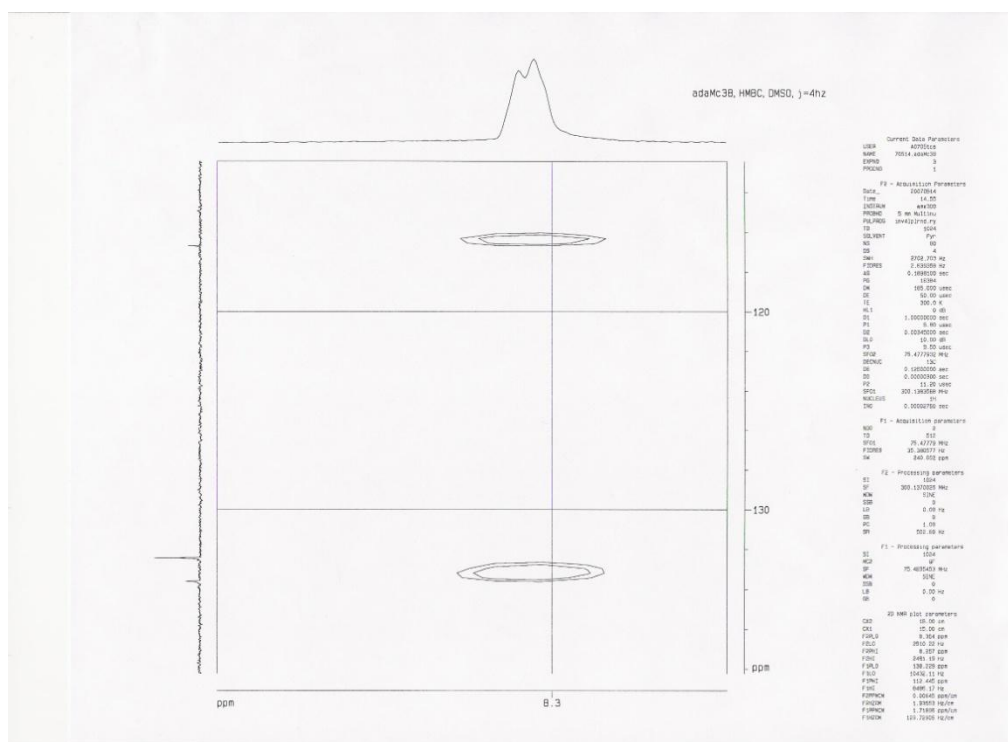
¹³C NMR of compound **13**



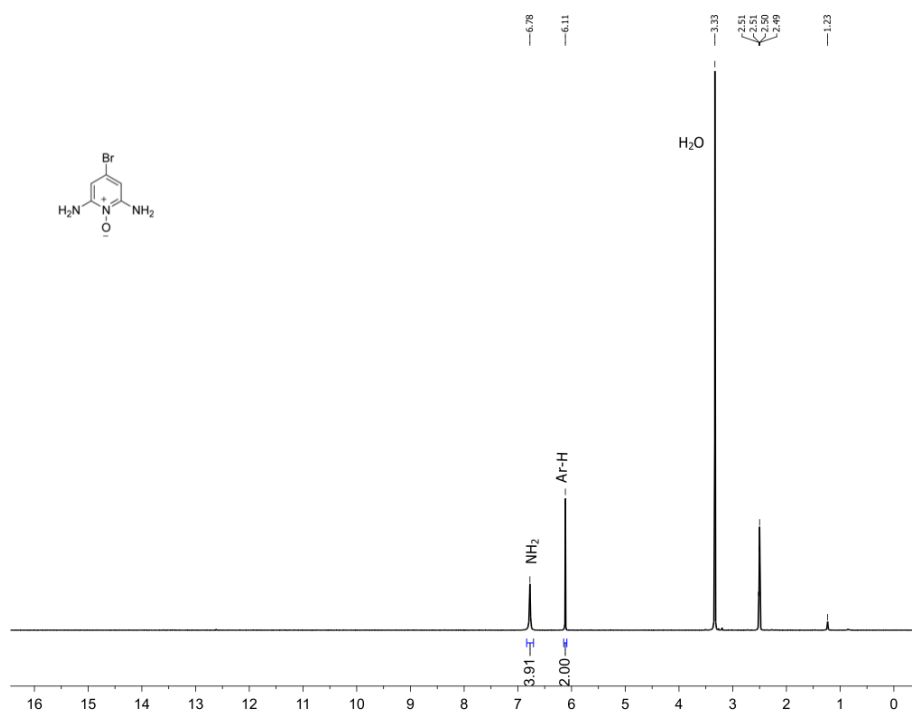
¹H NMR of compound 14



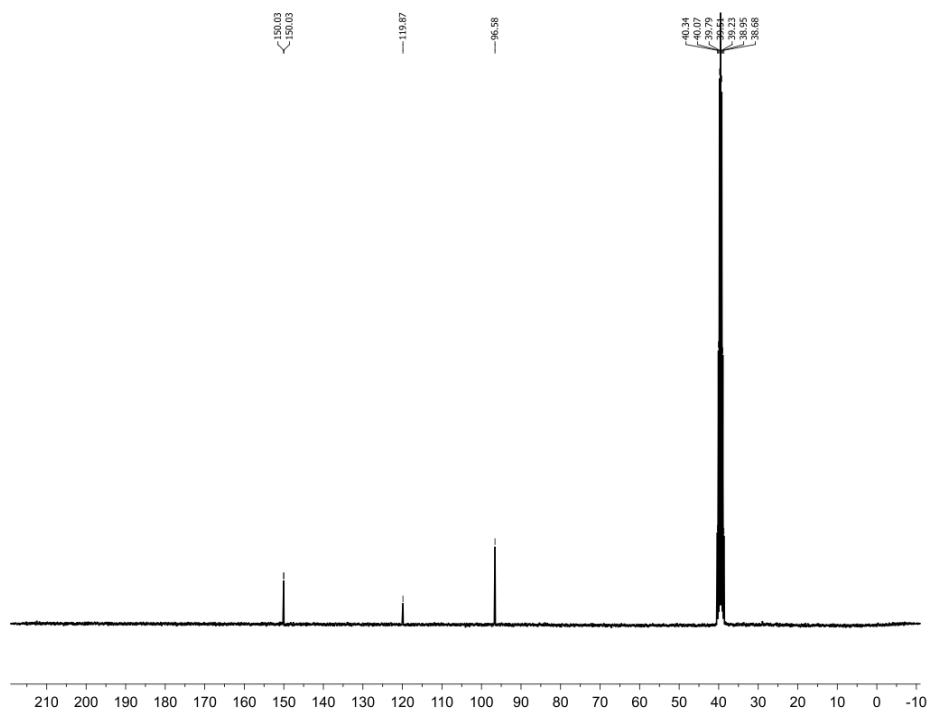
¹³C NMR of compound 14



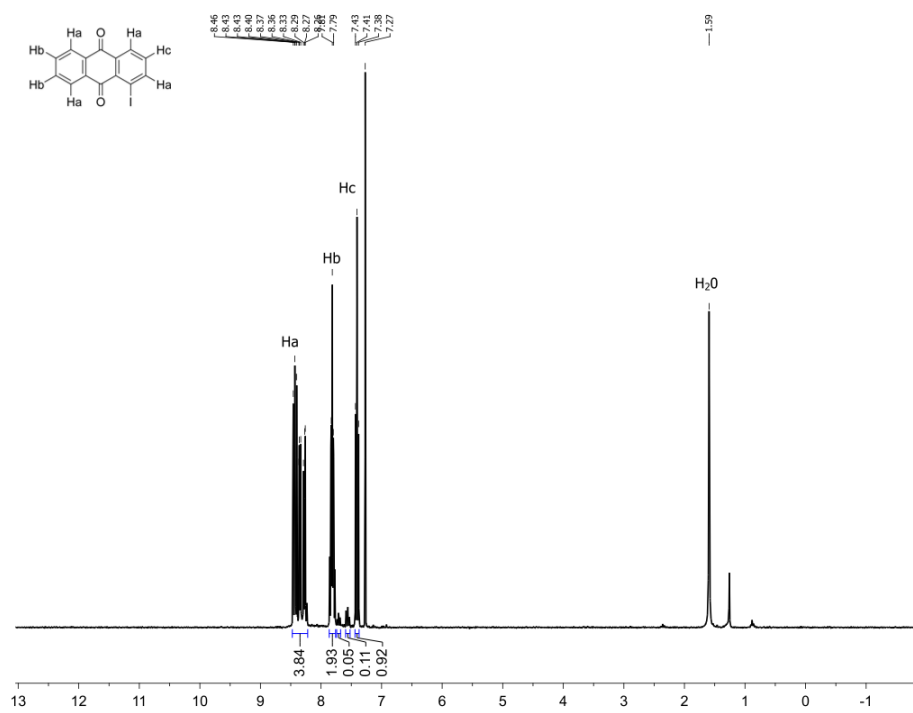
HMBC of compound 14



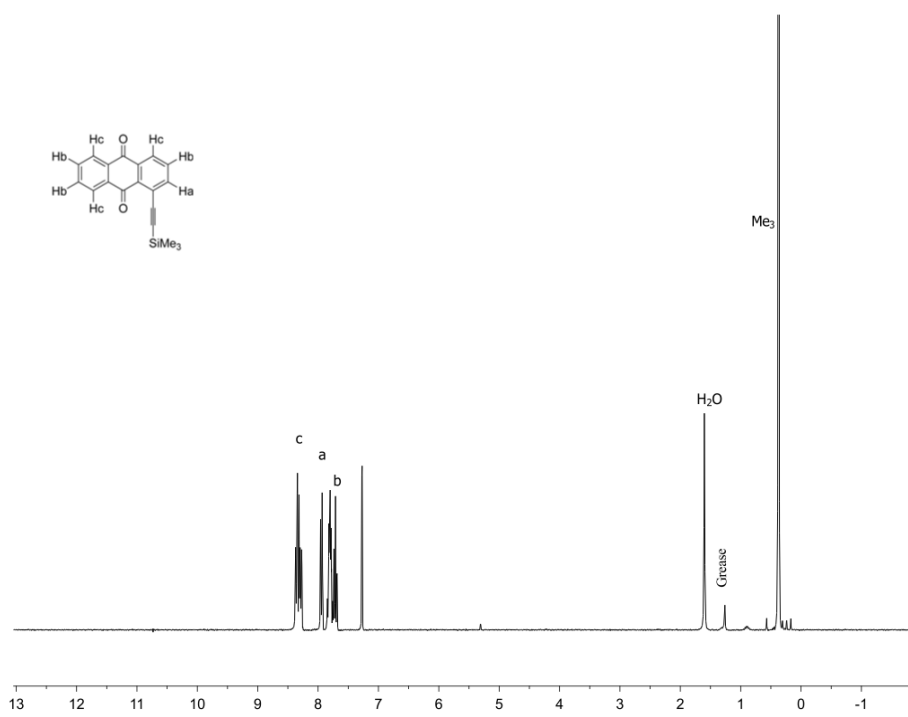
¹H NMR of compound **15**



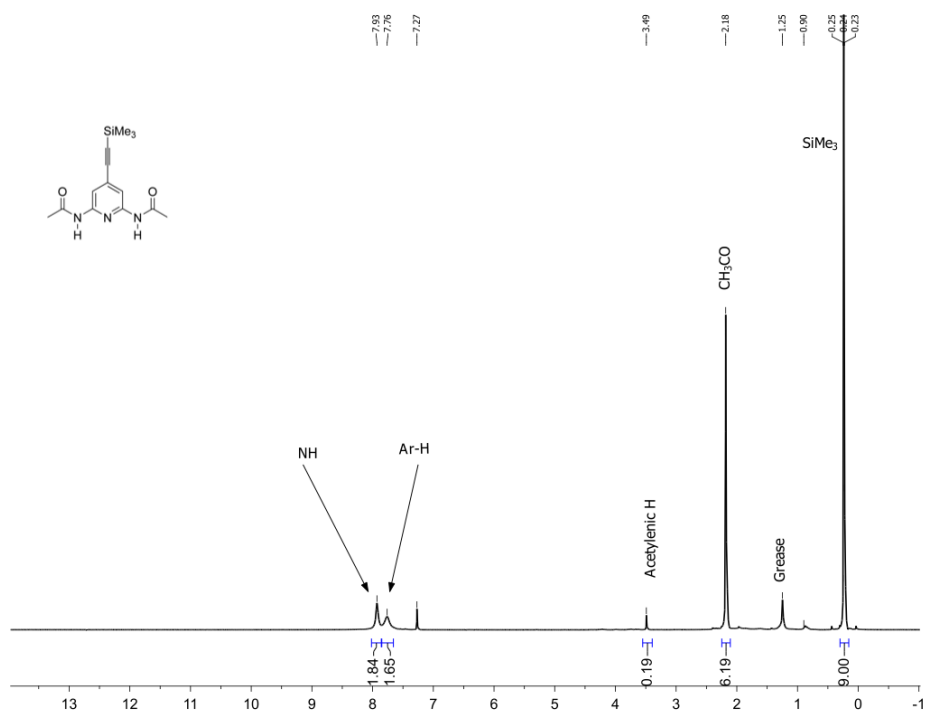
¹³C NMR of compound **15**



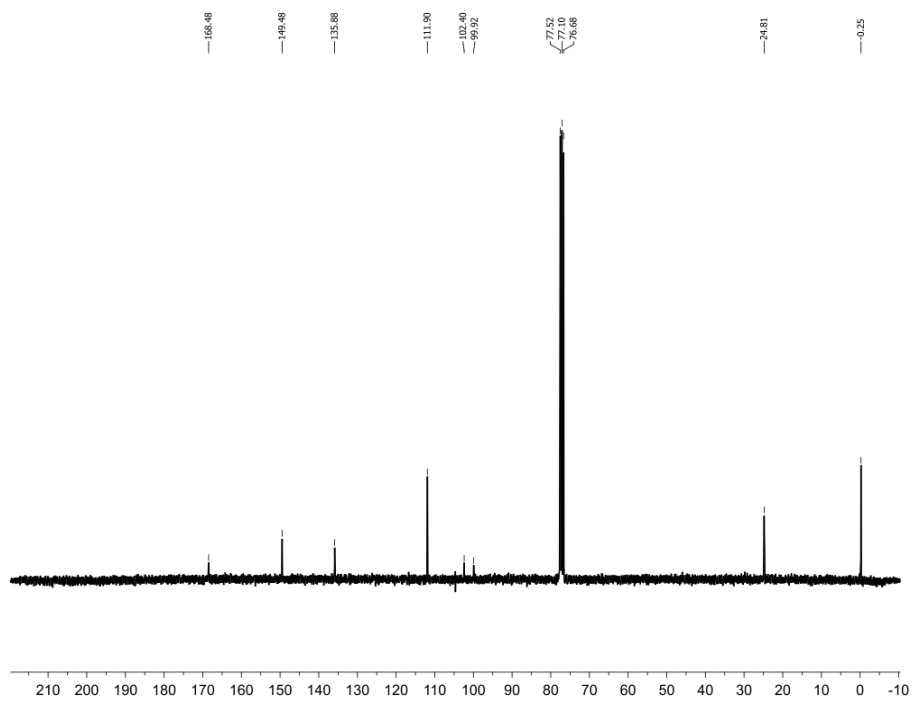
^1H NMR of compound **16**



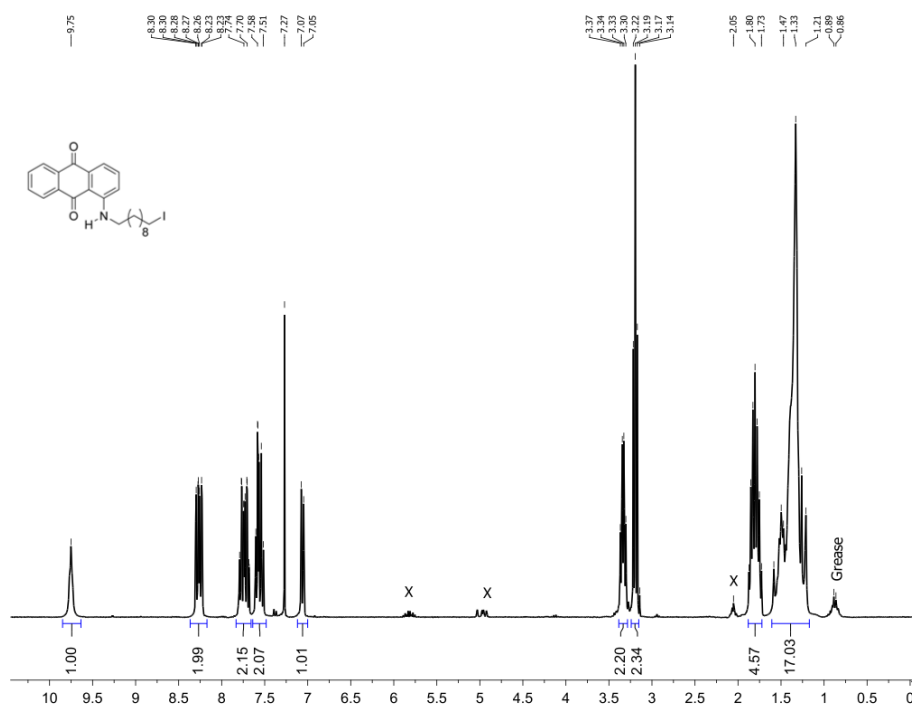
^1H NMR of compound 17



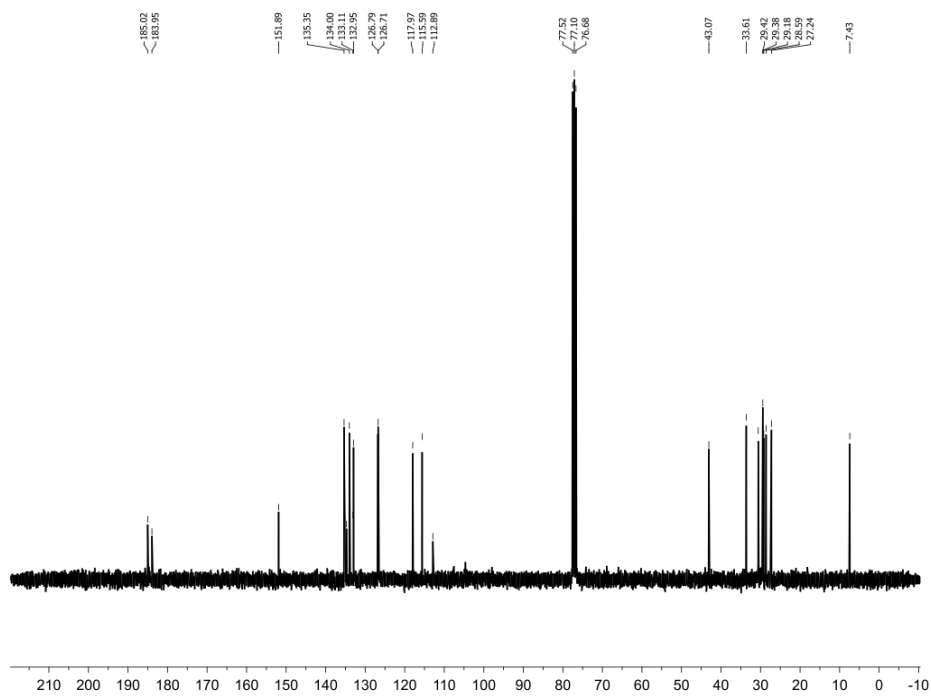
¹H NMR of compound 18



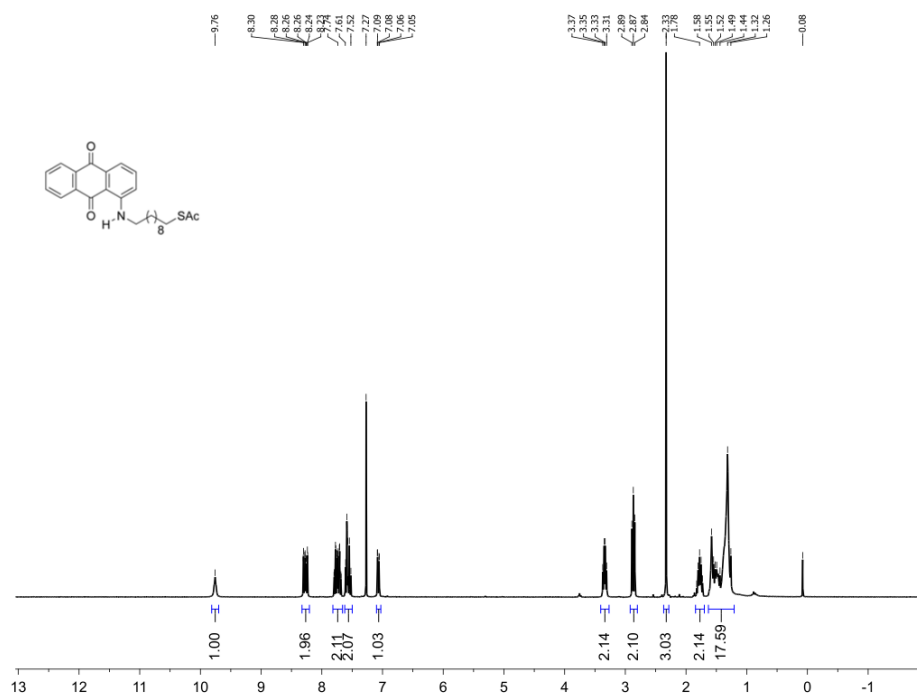
¹³C NMR of compound 18



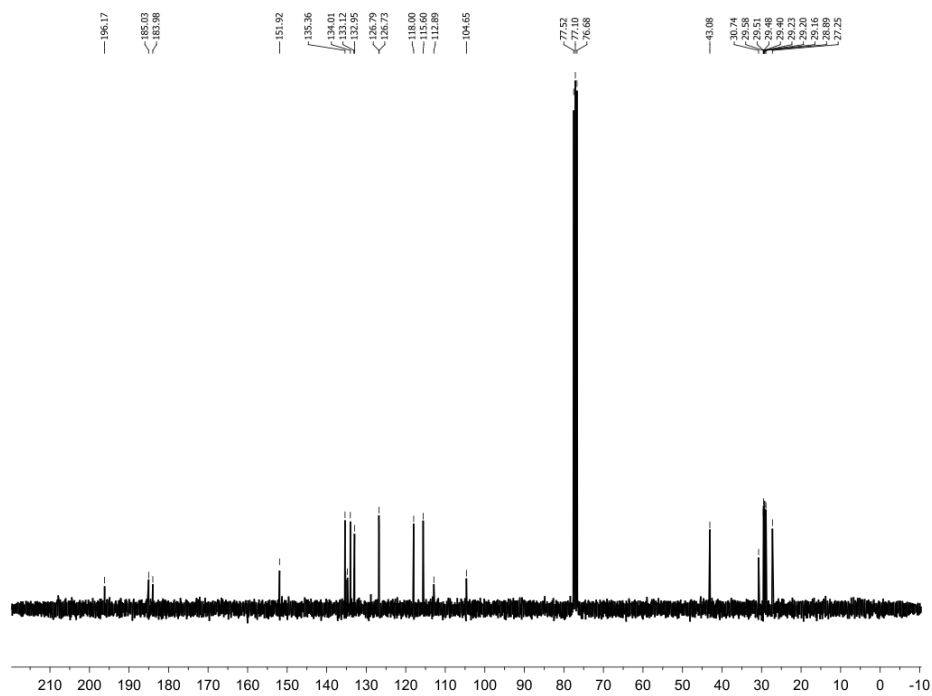
¹H NMR of compound 20



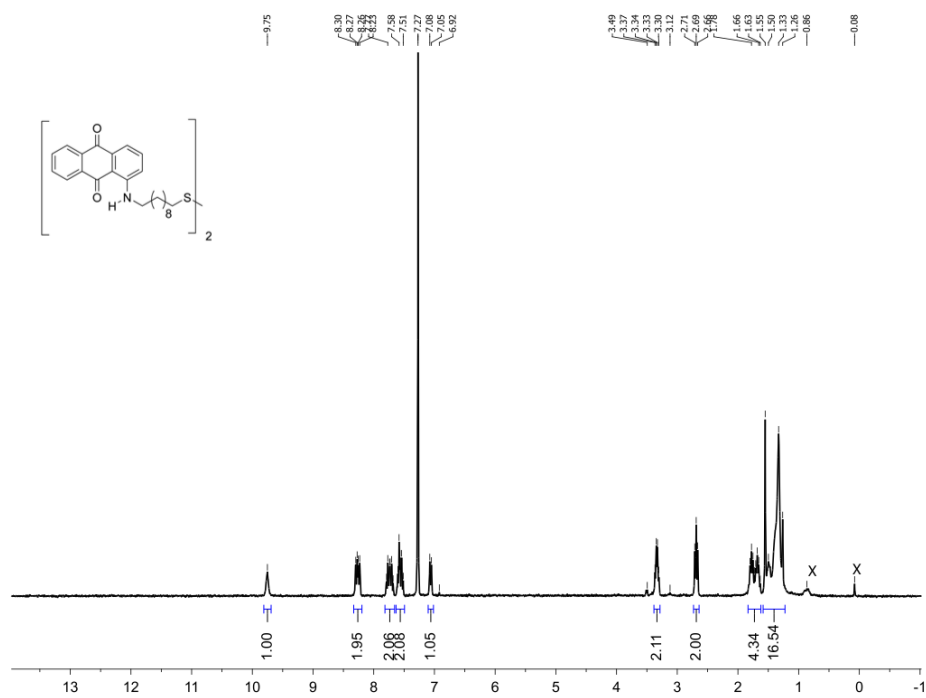
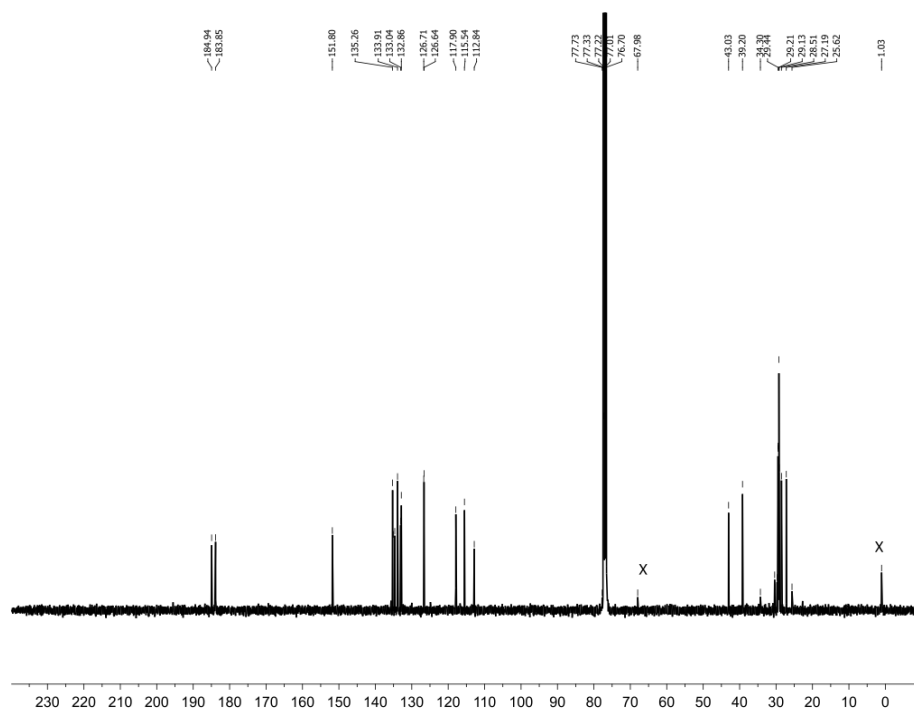
¹³C NMR of compound 20

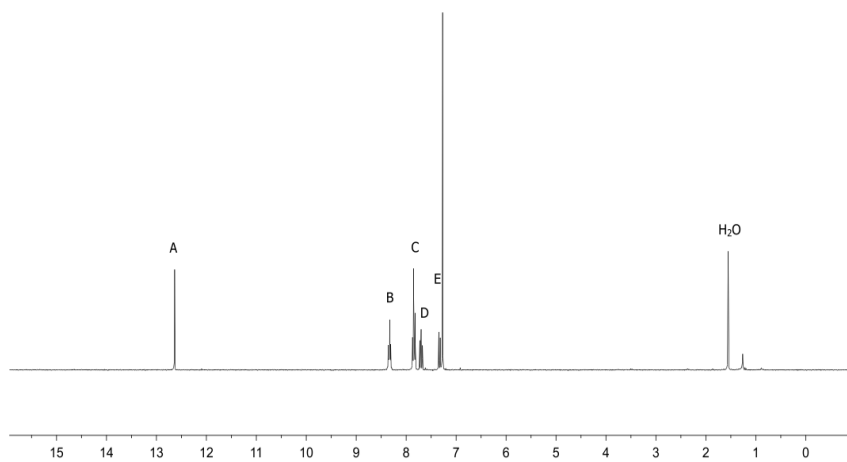
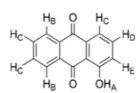


¹H NMR of compound **21**

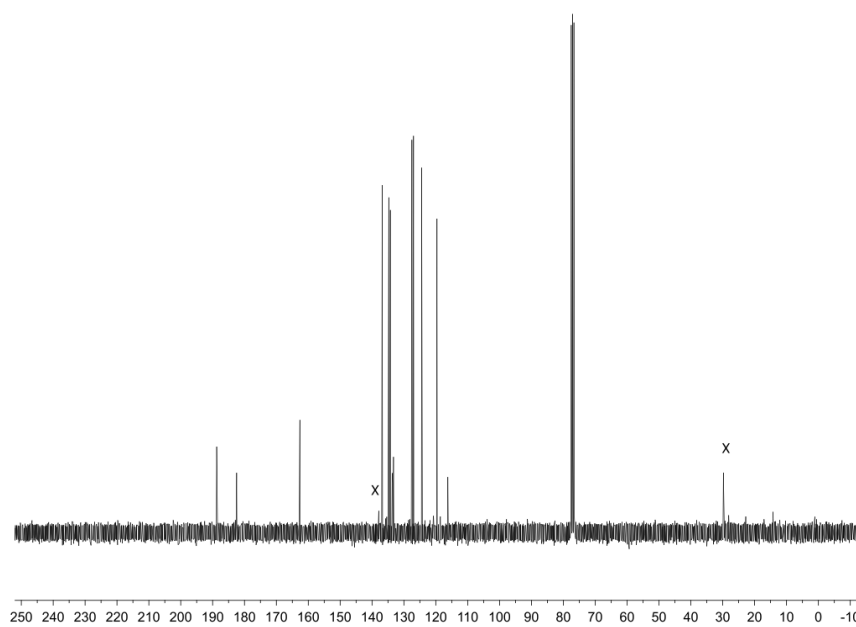


¹³C NMR of compound **21**

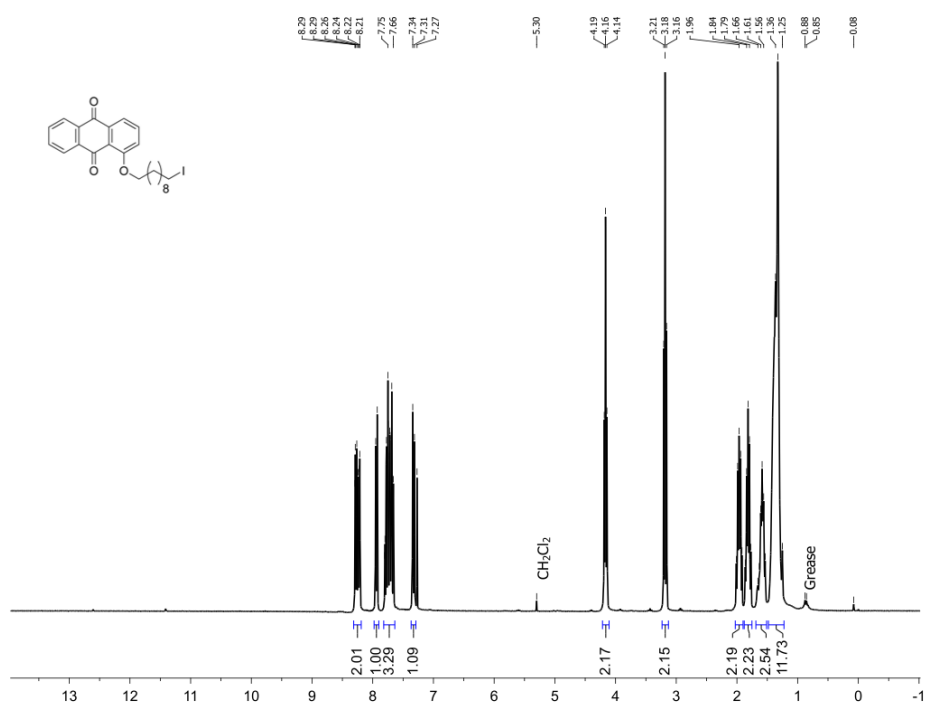
 ^1H NMR of compound 22 ^{13}C NMR of compound 22



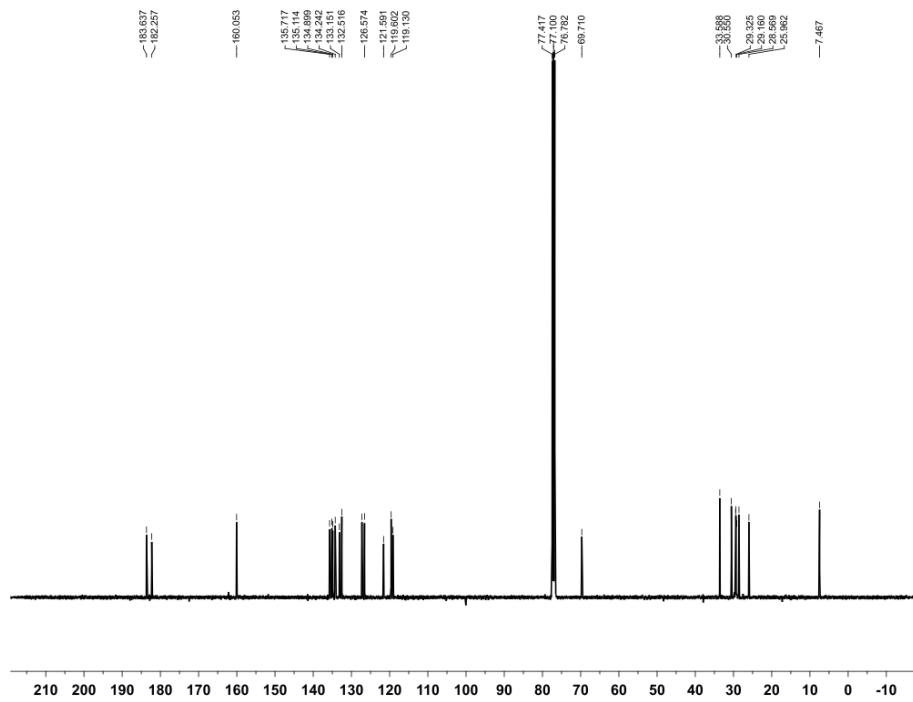
^1H NMR of compound **23**



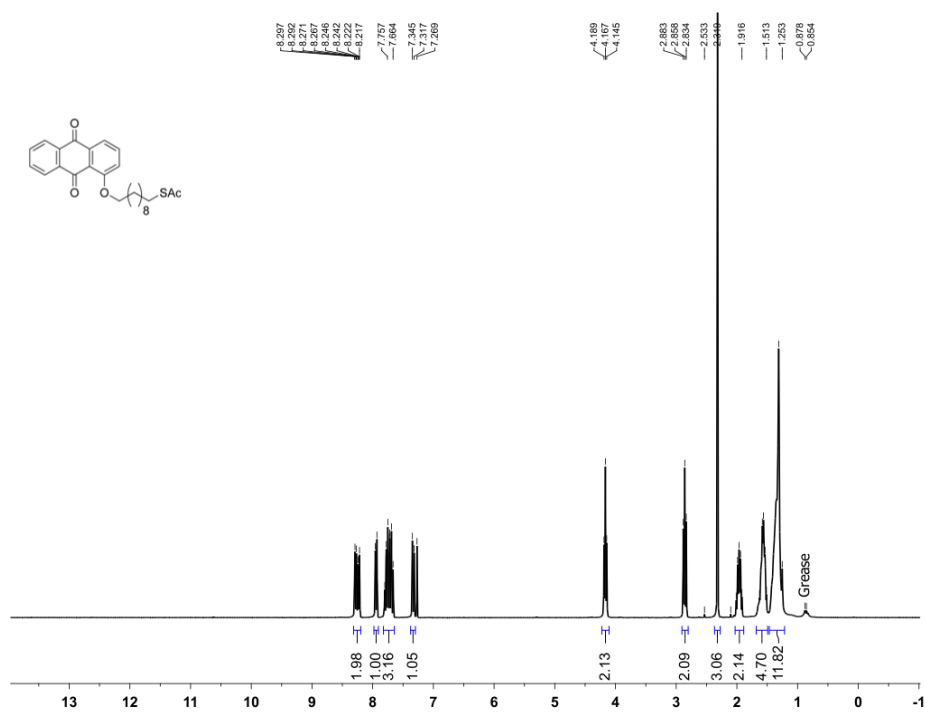
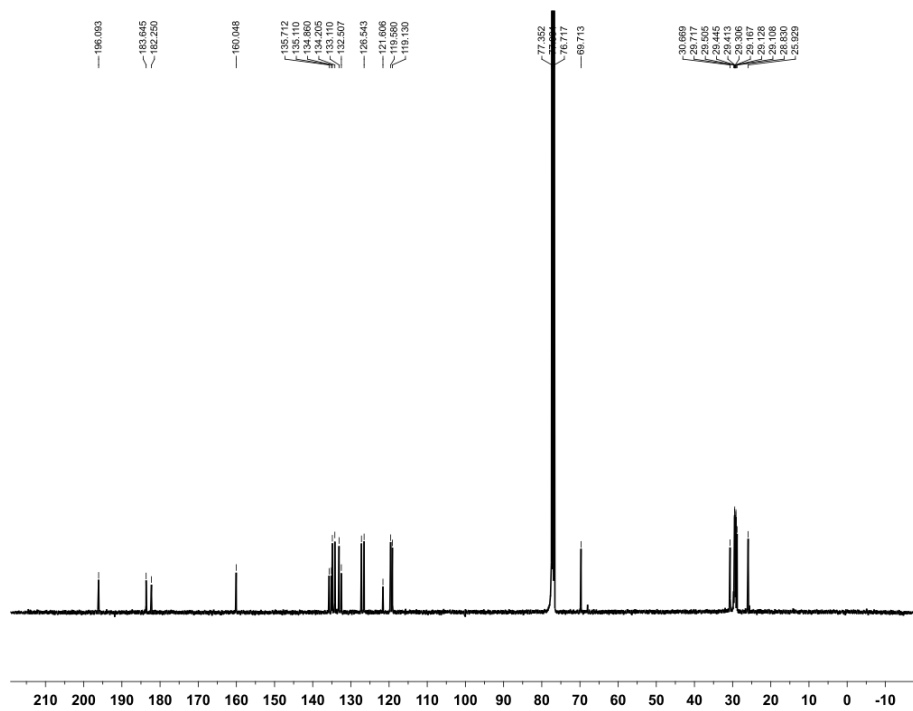
^{13}C NMR of compound **23**

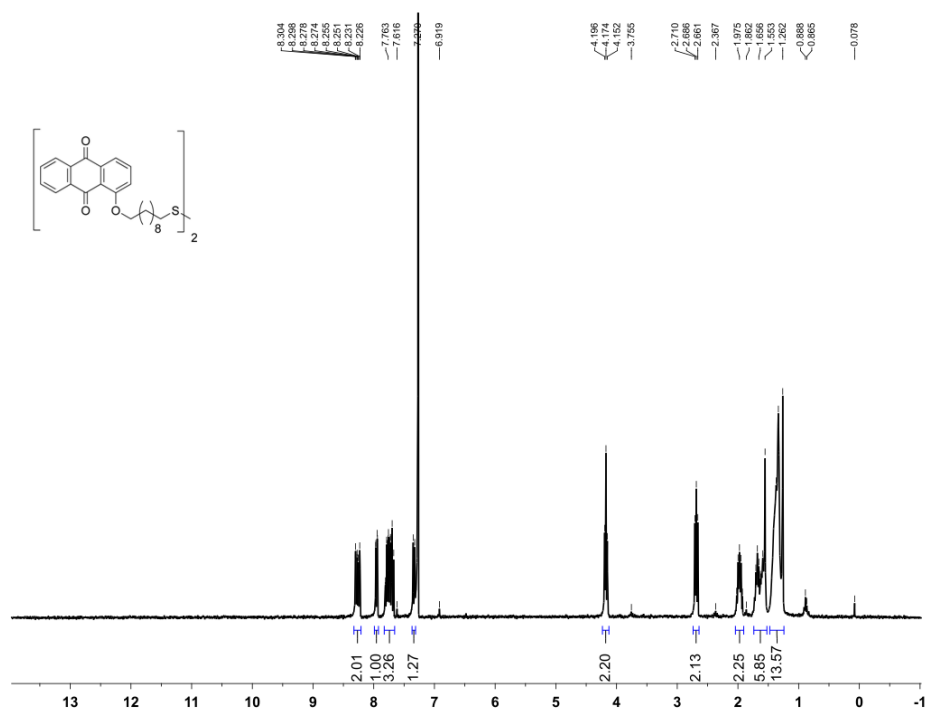


¹H NMR of compound 25

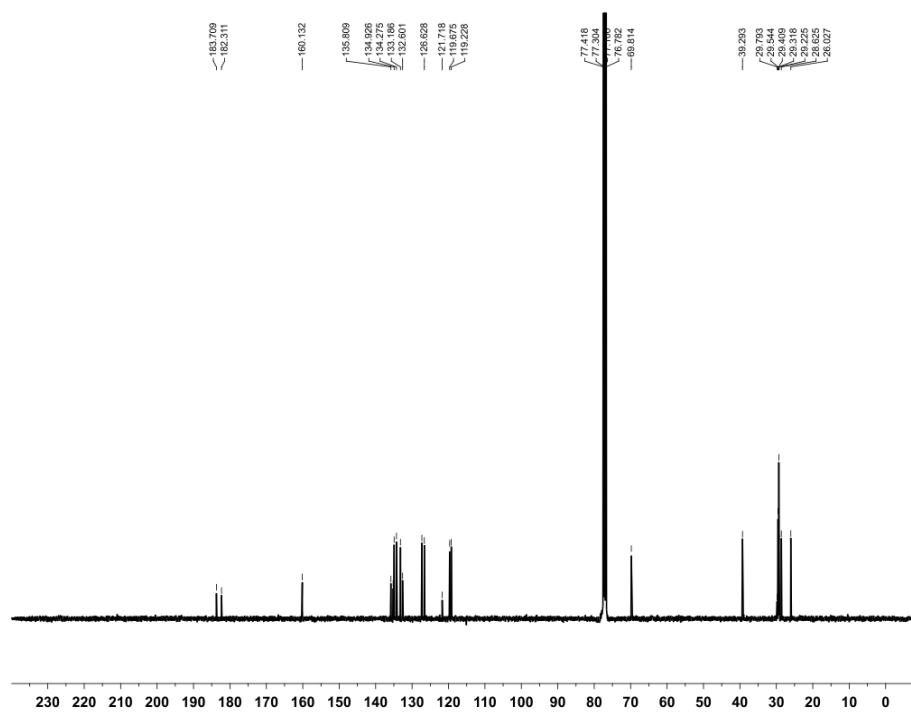


¹³C NMR of compound 25

 ^1H NMR of compound 26 ^{13}C NMR of compound 26

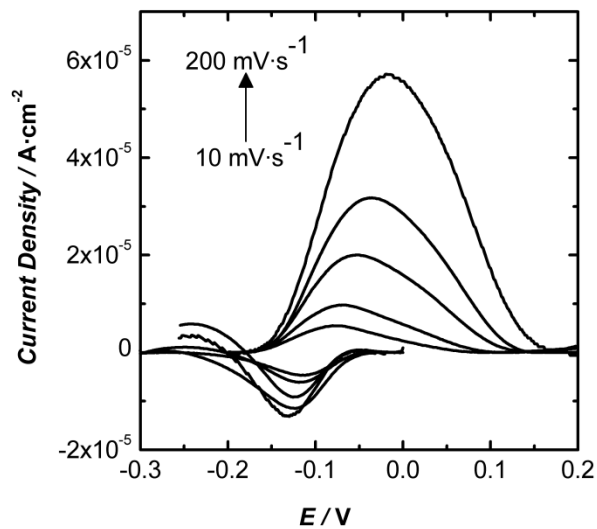


$^1\text{H NMR}$ of compound 27

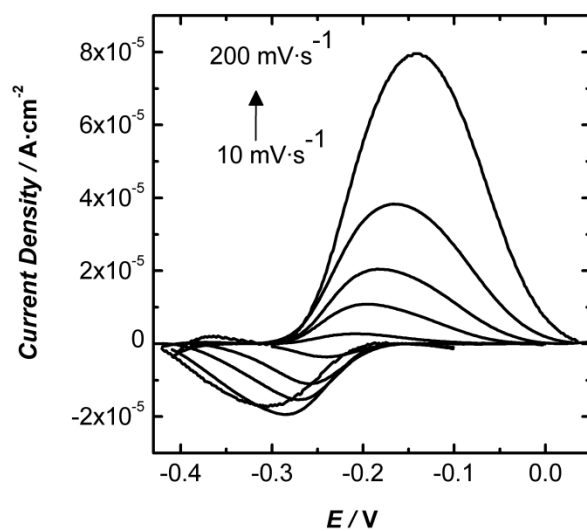


$^{13}\text{C NMR}$ of compound 27

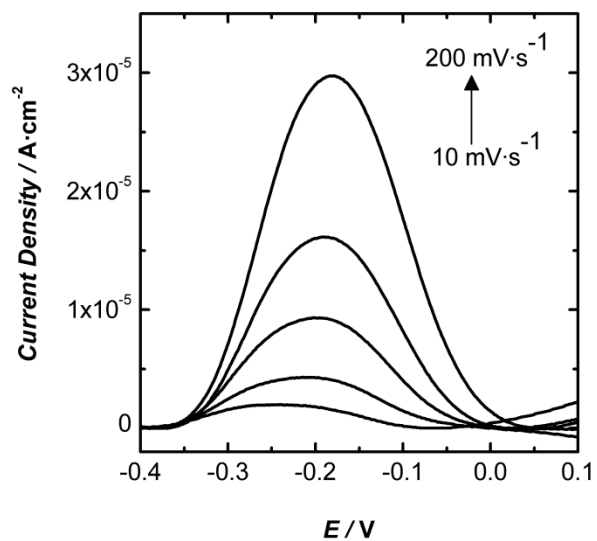
7.2 CV data of SAM of 27.



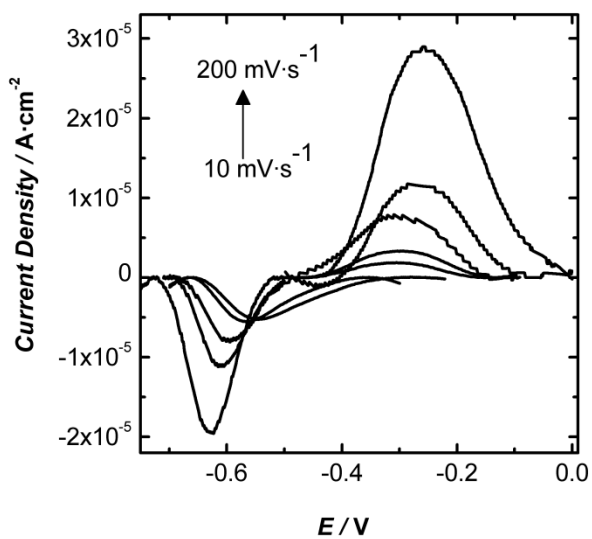
CV of SAM of 27 at pH 1.66 and $5 \pm 1.0^\circ\text{C}$.



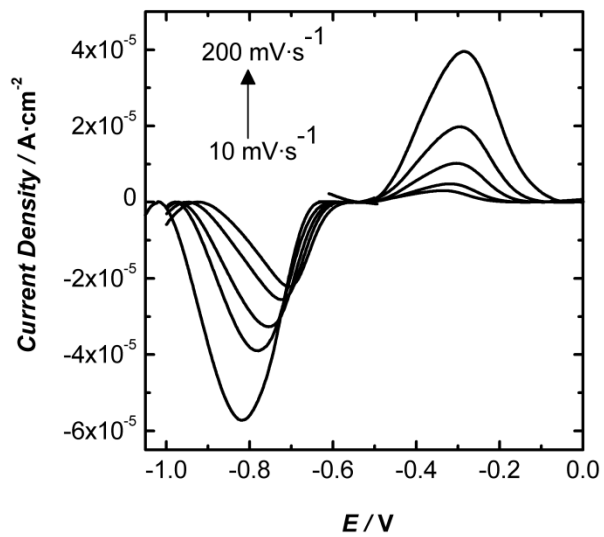
CV of SAM of 27 at pH 3.34 and $5 \pm 1.0^\circ\text{C}$.



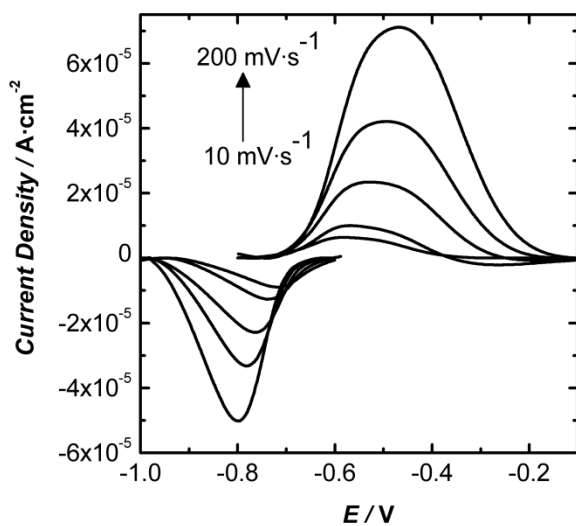
CV of SAM of **27** at pH 5.50 and 5±1.0°C.



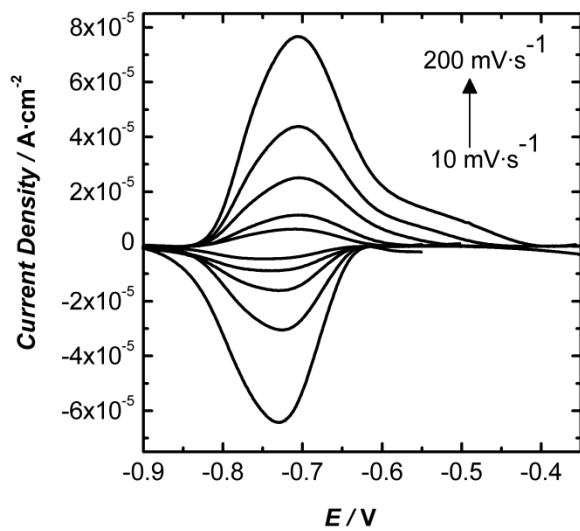
CV of SAM of **27** at pH 7.51 and 5±1.0°C.



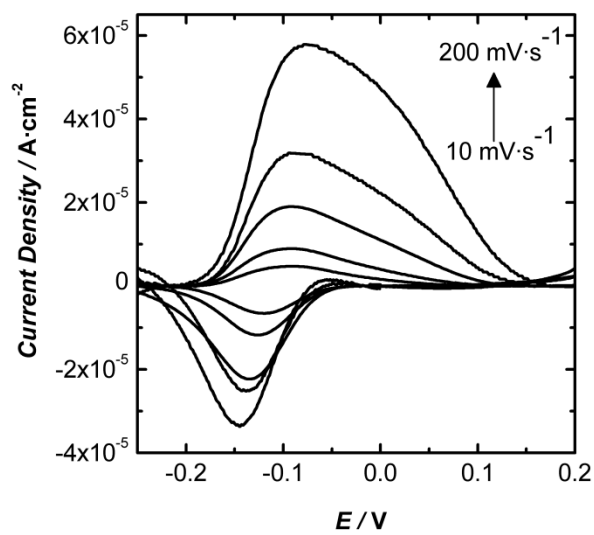
CV of SAM of **27** at pH 9.52 and 5 ± 1.0 °C.



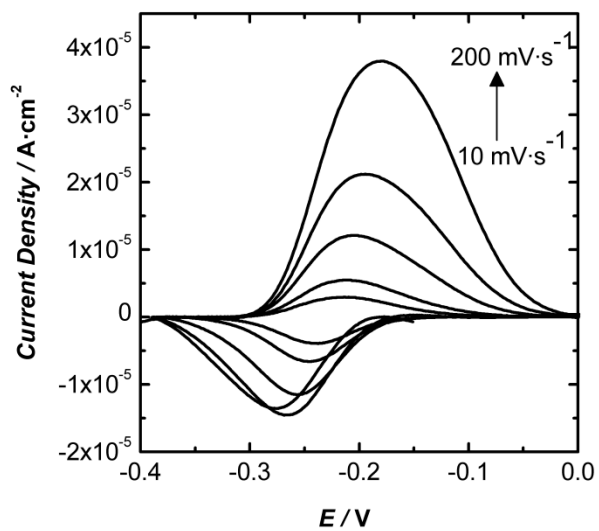
CV of SAM of **27** at pH 11.61 and 5 ± 1.0 °C.



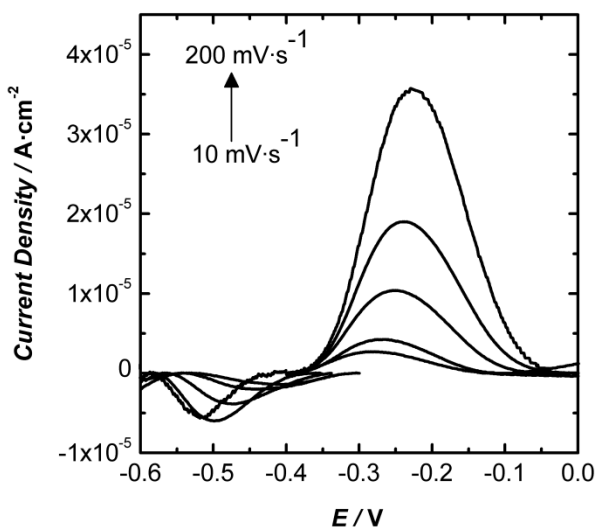
CV of SAM of **27** at pH 13.18 and 5 ± 1.0 °C.



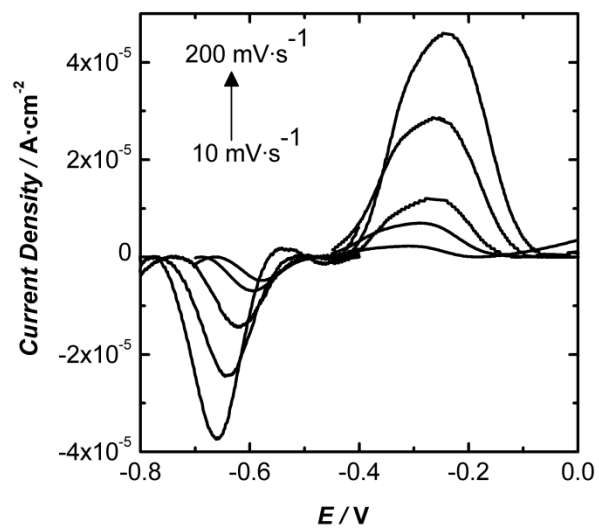
CV of SAM of **27** at pH 1.66 and 15 ± 0.8 °C.



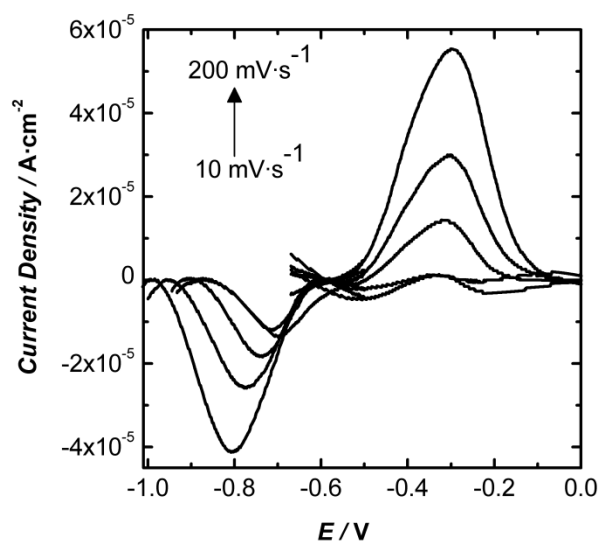
CV of SAM of **27** at pH 3.34 and $15 \pm 0.8^\circ\text{C}$.



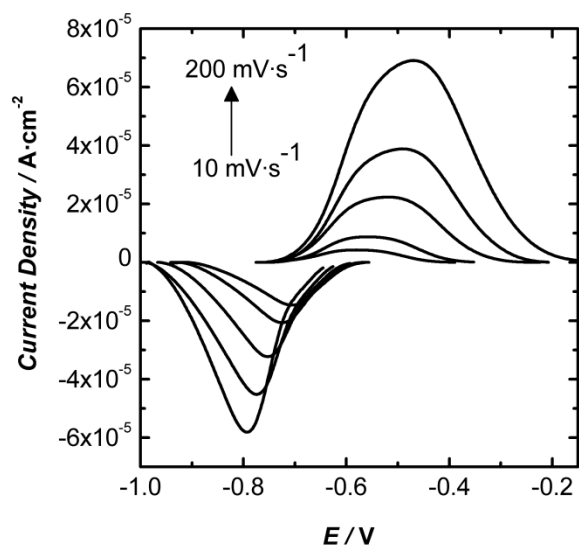
CV of SAM of **27** at pH 5.50 and $15 \pm 0.8^\circ\text{C}$.



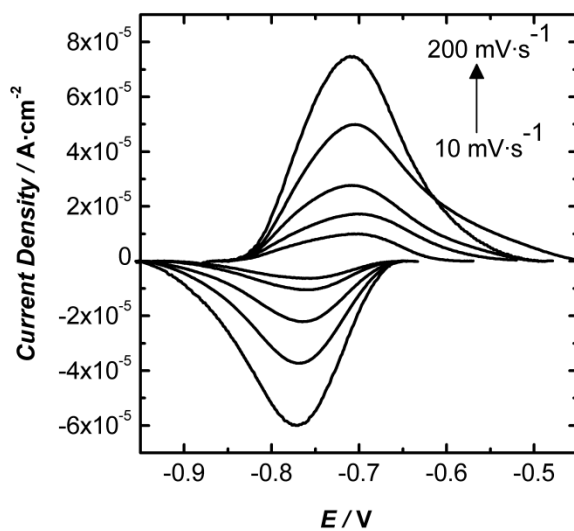
CV of SAM of **27** at pH 7.51 and $15 \pm 0.8^\circ\text{C}$.



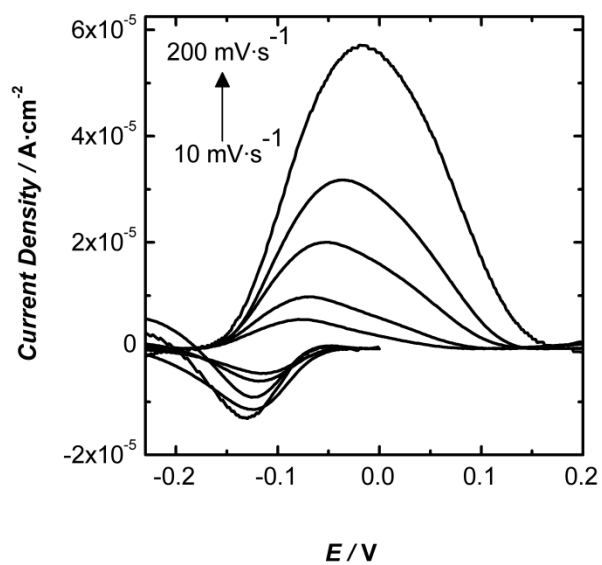
CV of SAM of **27** at pH 9.52 and $15 \pm 0.8^\circ\text{C}$.



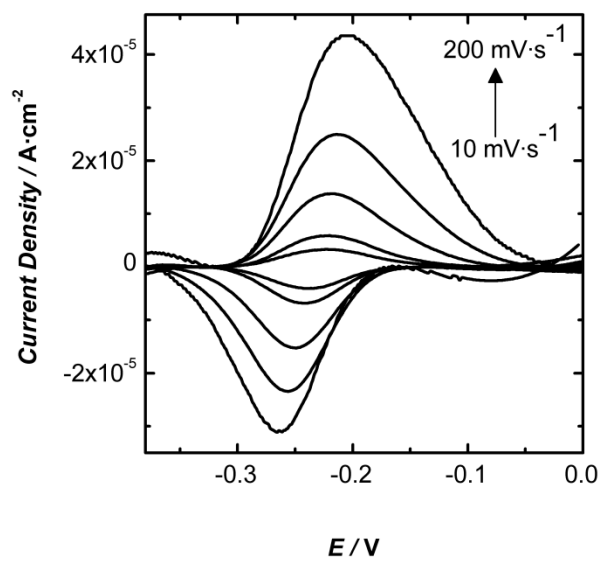
CV of SAM of **27** at pH 11.61 and $15 \pm 0.8^\circ\text{C}$.



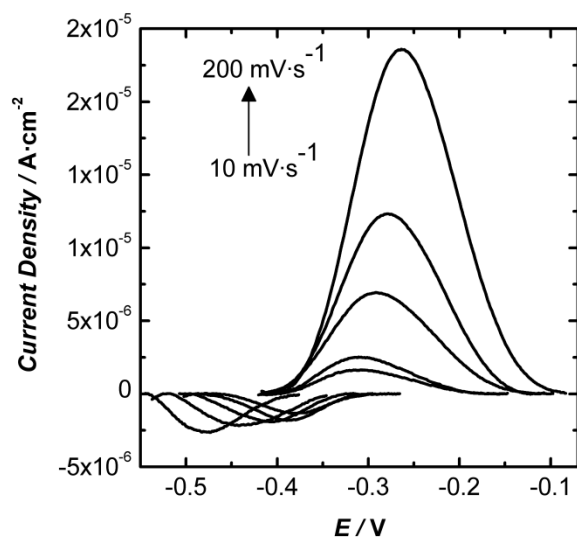
CV of SAM of **27** at pH 13.18 and $15 \pm 0.8^\circ\text{C}$.



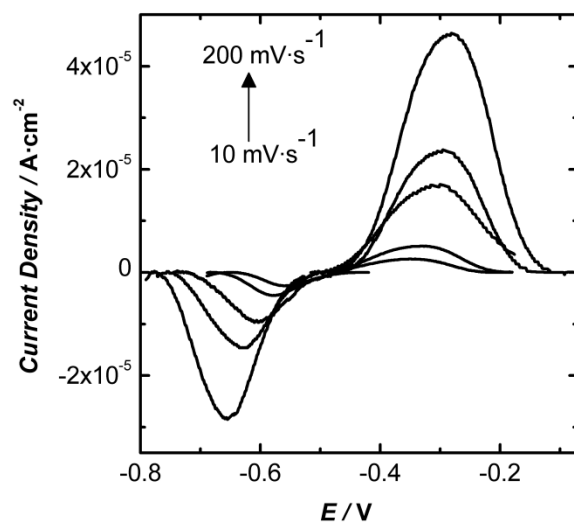
CV of SAM of **27** at pH 1.66 and 25±0.5°C.



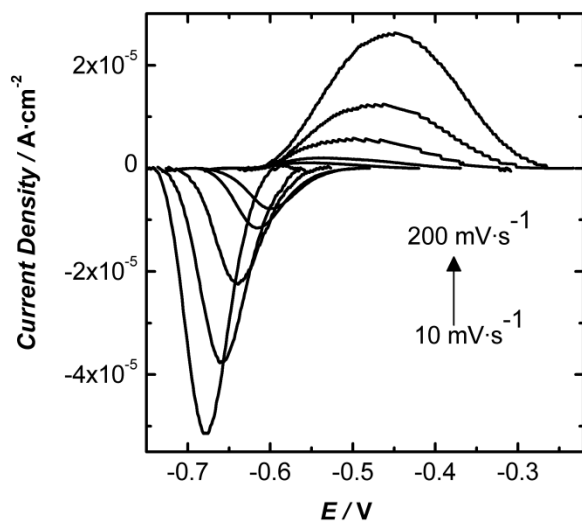
CV of SAM of **27** at pH 3.34 and 25±0.5°C.



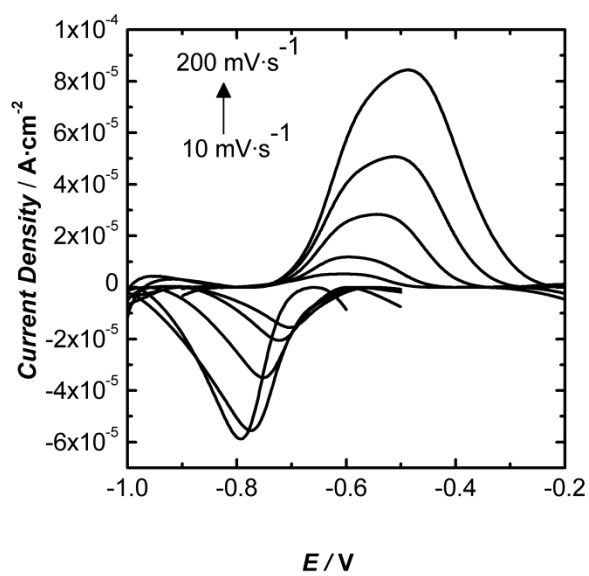
CV of SAM of **27** at pH 5.50 and $25 \pm 0.5^\circ\text{C}$.



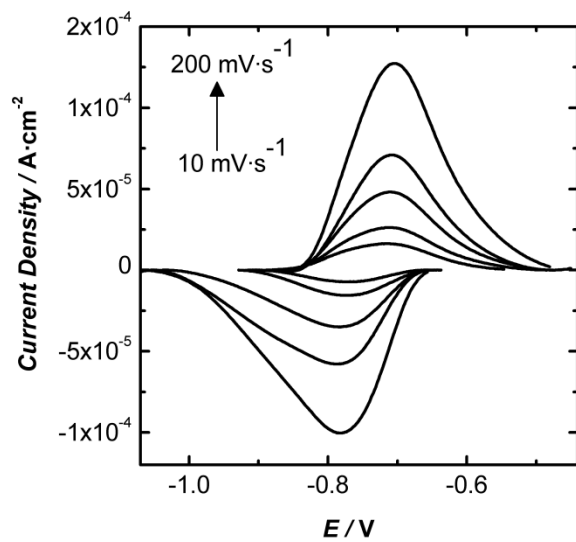
CV of SAM of **27** at pH 7.51 and $25 \pm 0.5^\circ\text{C}$.



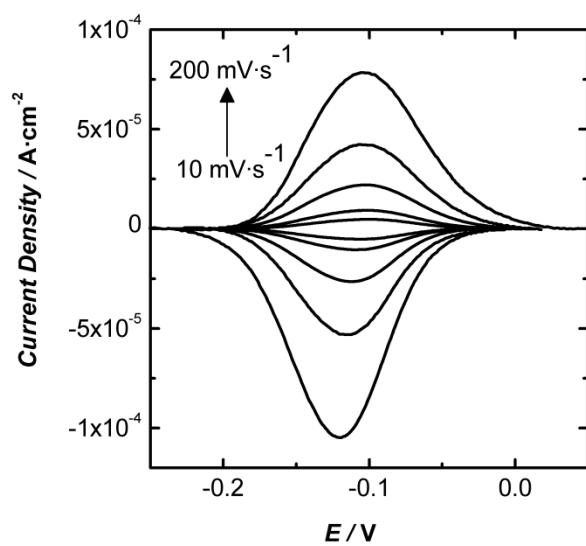
CV of SAM of **27** at pH 9.52 and $25\pm 0.5^\circ\text{C}$.



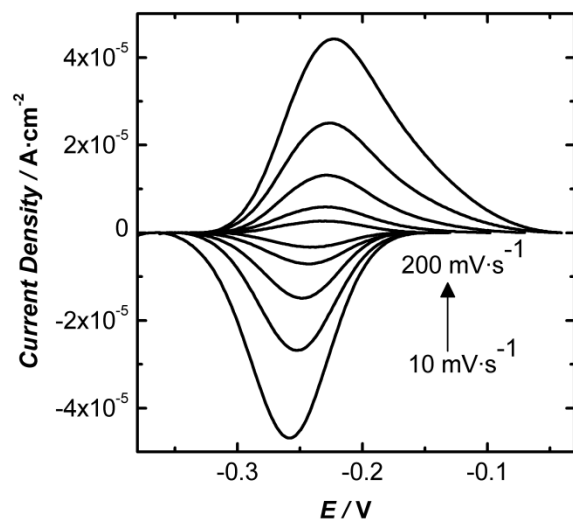
CV of SAM of **27** at pH 11.61 and $25\pm 0.5^\circ\text{C}$.



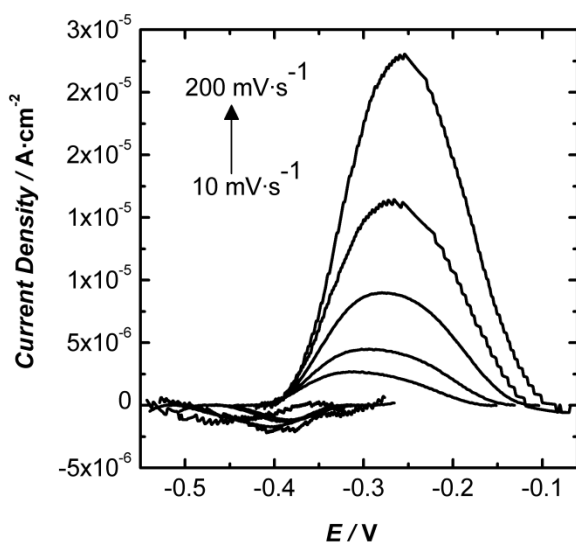
CV of SAM of **27** at pH 13.18 and $25 \pm 0.5^\circ\text{C}$.



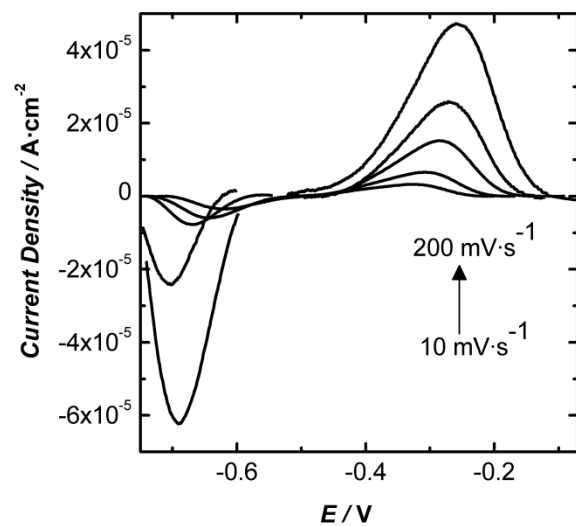
CV of SAM of **27** at pH 1.66 and $35 \pm 0.5^\circ\text{C}$.



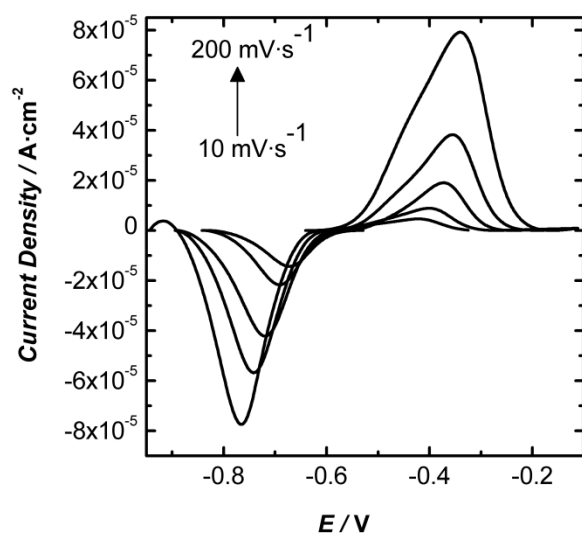
CV of SAM of **27** at pH 3.34 and $35 \pm 0.5^\circ\text{C}$.



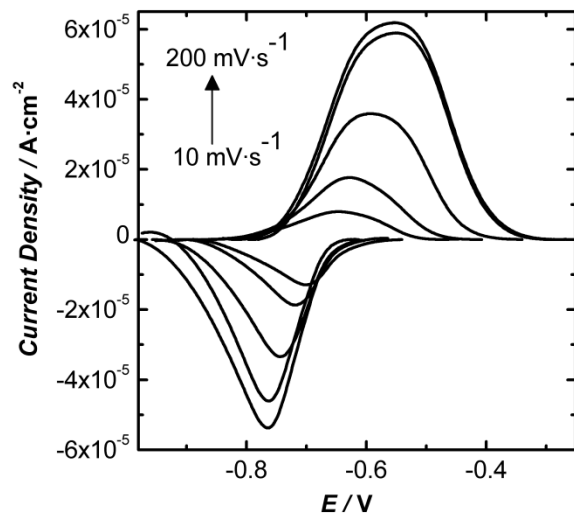
CV of SAM of **27** at pH 5.50 and $35 \pm 0.5^\circ\text{C}$.



CV of SAM of **27** at pH 7.51 and 35±0.5°C.

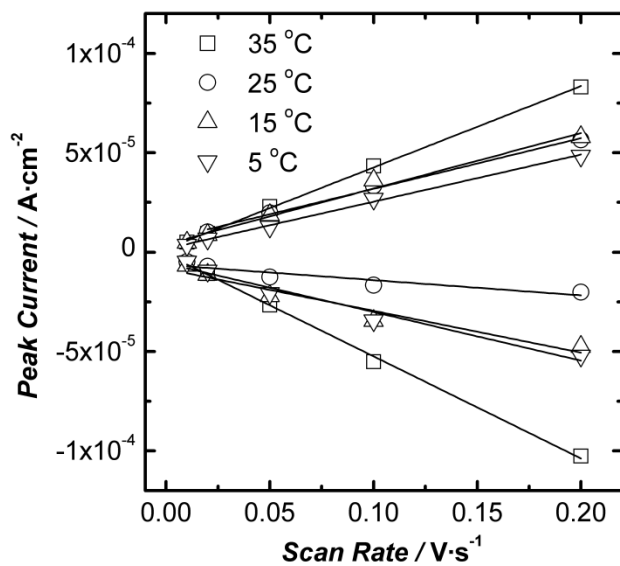


CV of SAM of **27** at pH 9.52 and 35±0.5°C.

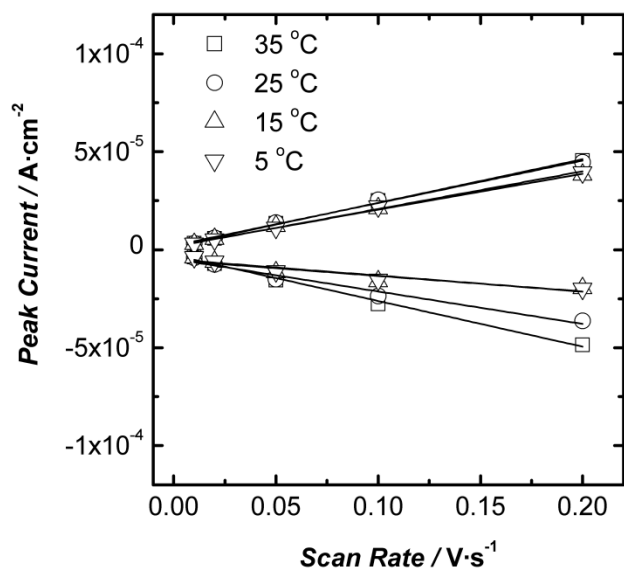


CV of SAM of **27** at pH 11.66 and $35 \pm 0.5^\circ\text{C}$.

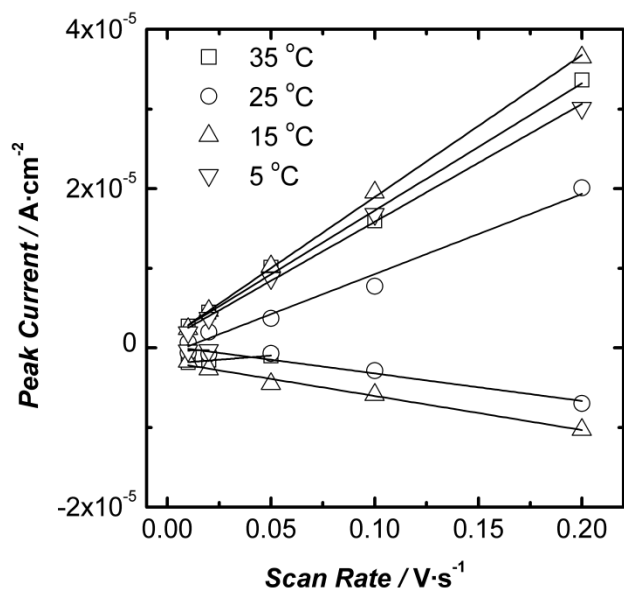
7.3 Plots of peak current as a function of scan rate – For SAM of **27**



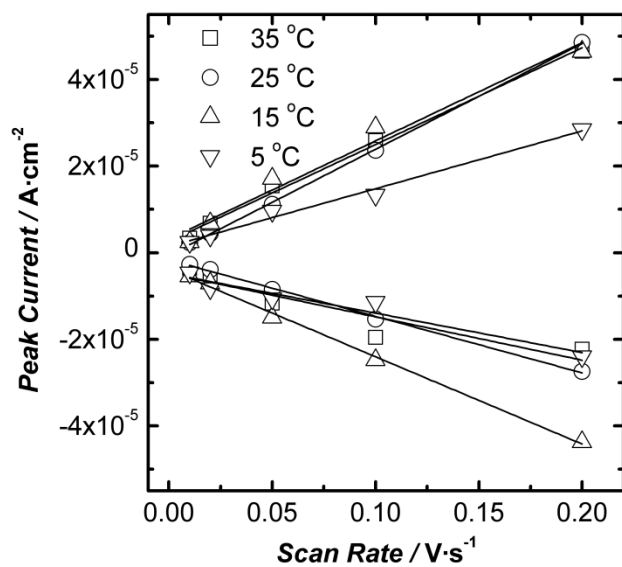
Peak current vs. scan rate at pH 1.66 at various temperatures



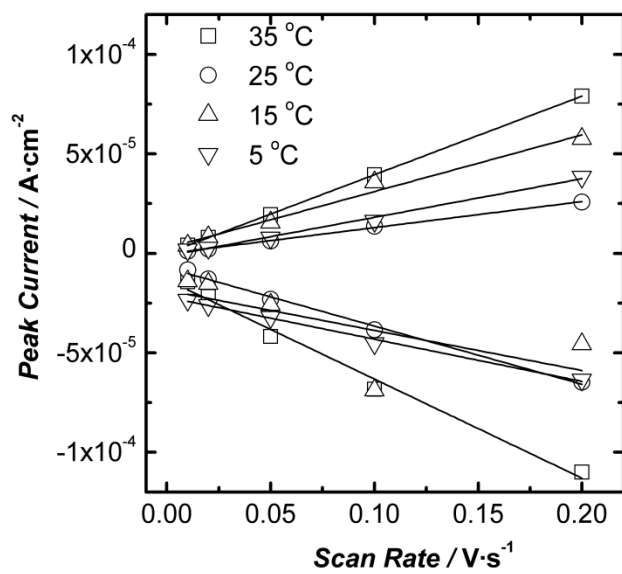
Peak current vs. scan rate at pH 3.34 at various temperatures



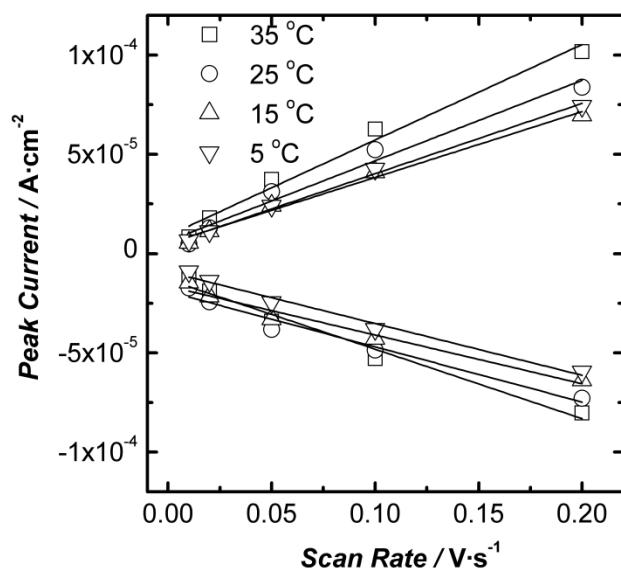
Peak current vs. scan rate at pH 5.50 at various temperatures



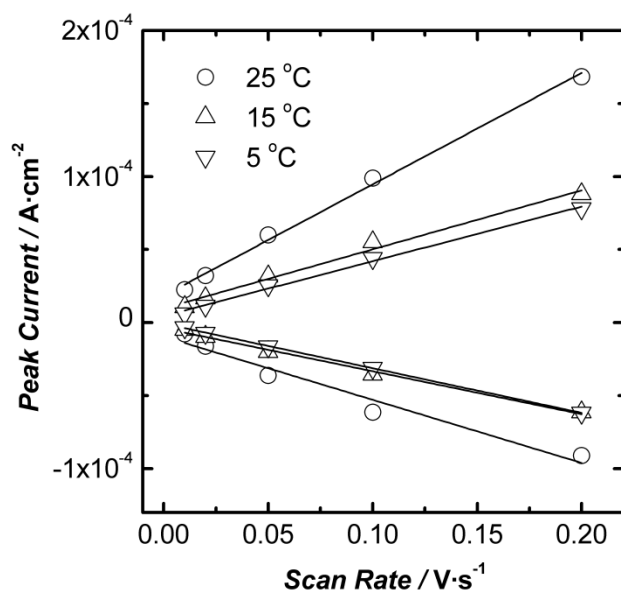
Peak current vs. scan rate at pH 7.51 at various temperatures



Peak current vs. scan rate at pH 9.52 at various temperatures

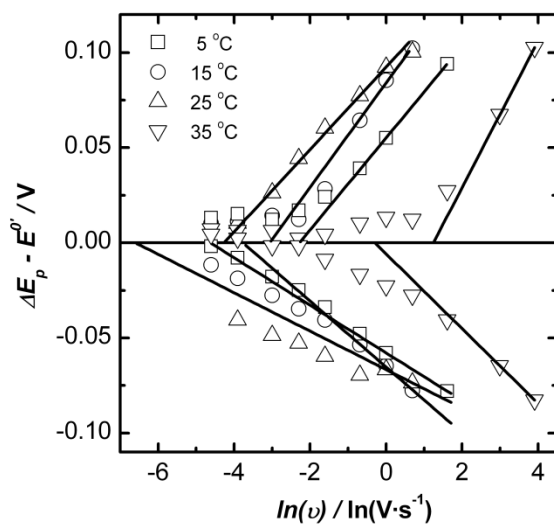


Peak current vs. scan rate at pH 11.66 at various temperatures

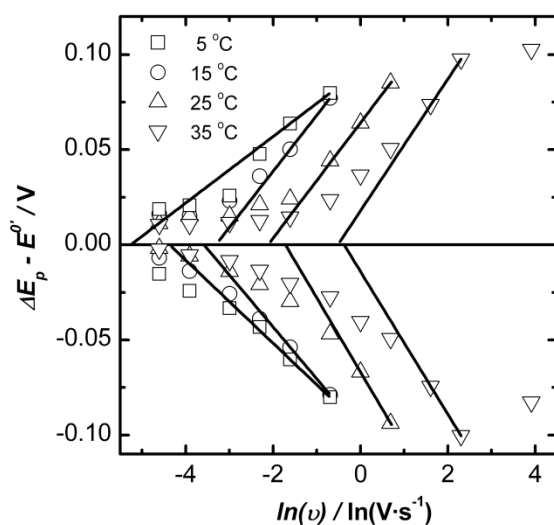


Peak current vs. scan rate at pH 13.18 at various temperatures

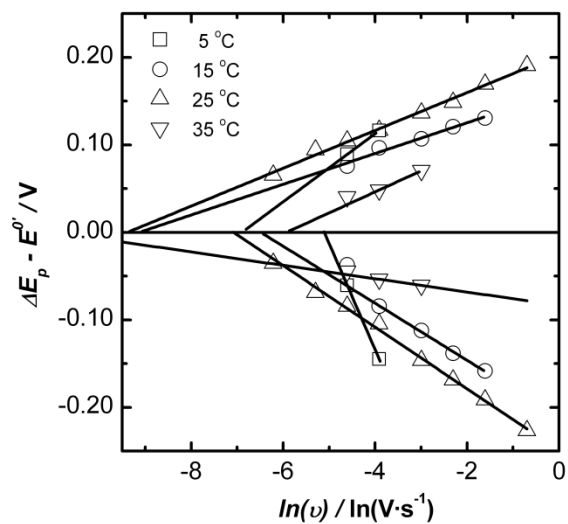
7.4 Plots of [Difference in Peak Potentials (ΔE_p) – Equilibrium Potential ($E^{0'}$)] as a function of scan rate (ν) – For SAM of 27



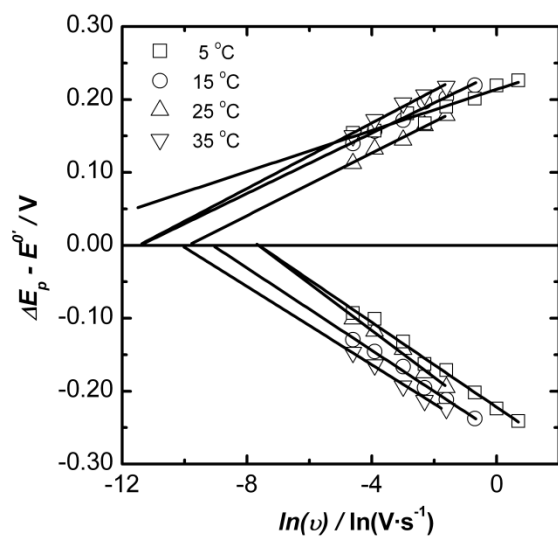
$\Delta E_p - E^{0'}$ vs. scan rate at pH 1.66 at various temperatures



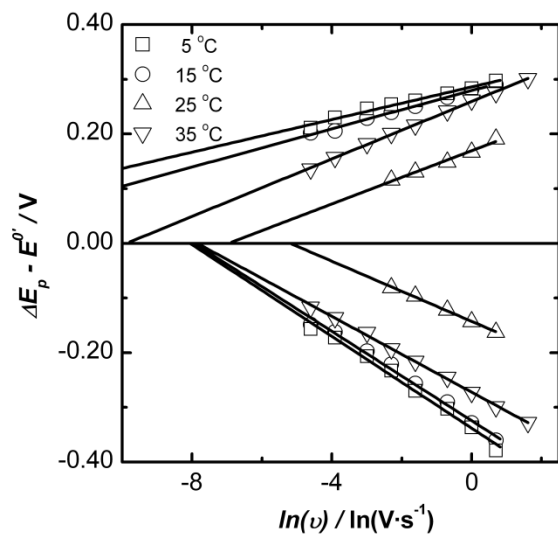
$\Delta E_p - E^{0'}$ vs. scan rate at pH 3.34 at various temperatures



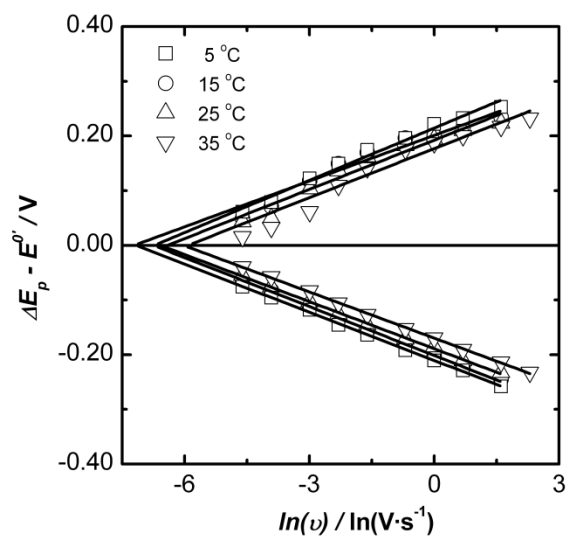
$\Delta E_p - E^{0'}$ vs. scan rate at pH 5.50 at various temperatures



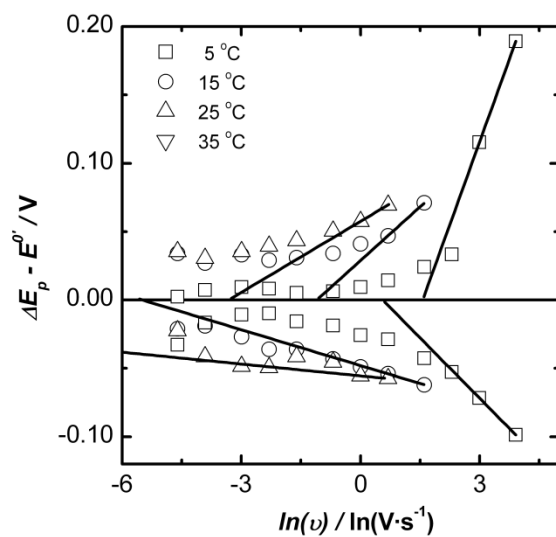
$\Delta E_p - E^{0'}$ vs. scan rate at pH 7.51 at various temperatures



$\Delta E_p - E^{0'}$ vs. scan rate at pH 9.52 at various temperatures

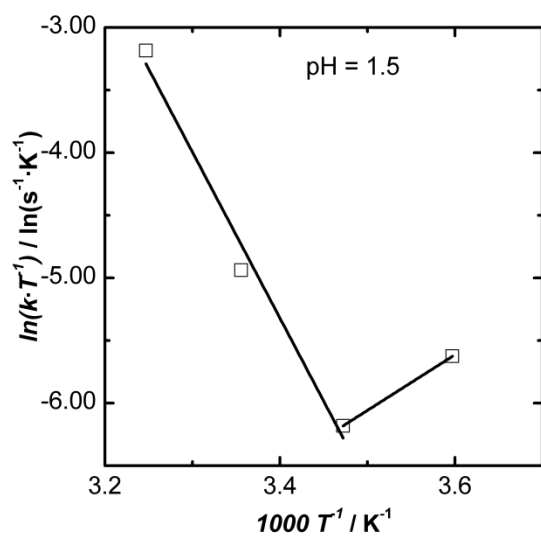


$\Delta E_p - E^{0'}$ vs. scan rate at pH 11.66 at various temperatures

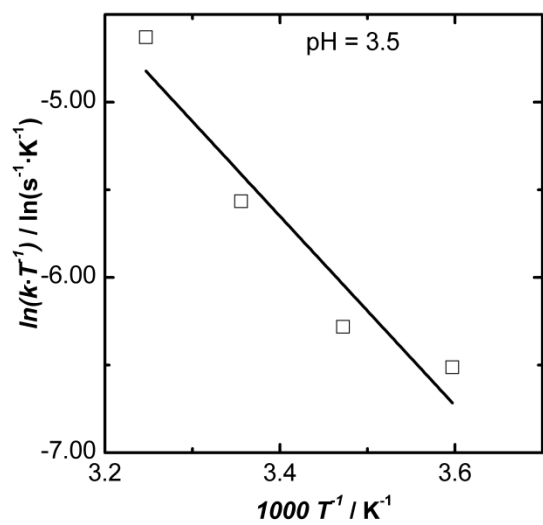


$\Delta E_p - E^{0'}$ vs. scan rate at pH 13.18 at various temperatures

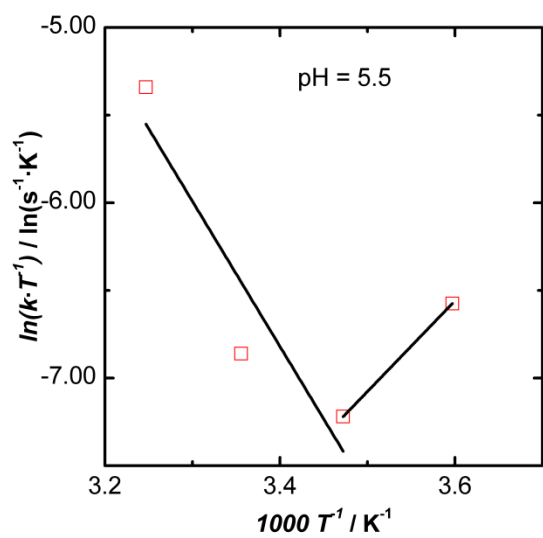
7.5 Eyring plots for SAM of 27 from EIS data



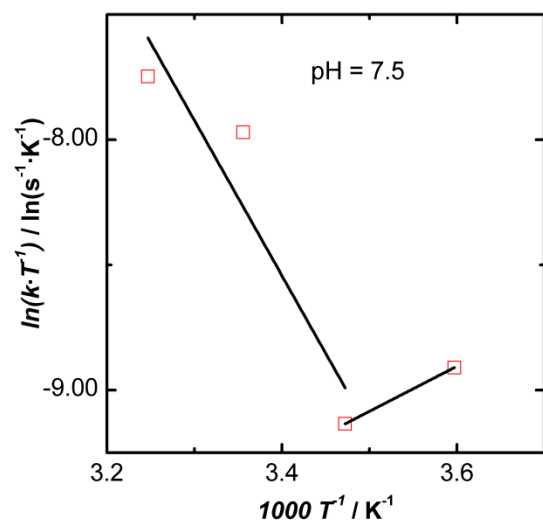
Eyring plot at pH 1.66



Eyring plot at pH 3.34



Eyring plot at pH 5.50



Eyring plot at pH 7.51

7.6 DFT coordinate files for compound EtNHAQ, EtNH₂⁺AQ, EtOAQ

Coordinates obtained in the DFT study for EtNHAQ

Center Number	Atomic Number	Atomic Type	Coordinates (Angstroms)		
			X	Y	Z
1	6	0	-1.901110	2.820076	-0.007424
2	6	0	-2.647415	1.657141	-0.007342
3	6	0	-2.017976	0.377942	-0.002344
4	6	0	-0.578491	0.325397	0.000917
5	6	0	0.153587	1.549838	0.001169
6	6	0	-0.497283	2.777866	-0.002644
7	6	0	0.130568	-0.950936	0.003651
8	6	0	1.622848	-0.948347	0.000255
9	6	0	2.354109	0.256277	0.001796
10	6	0	1.646540	1.559724	0.006035
11	6	0	2.310207	-2.170329	-0.004271
12	6	0	3.705192	-2.194712	-0.007145
13	6	0	4.430887	-0.995916	-0.005249
14	6	0	3.756264	0.224102	-0.000704
15	8	0	2.276515	2.622979	0.012717
16	8	0	-0.467538	-2.050029	0.007782
17	7	0	-2.768379	-0.749829	-0.001109
18	6	0	-4.227126	-0.792423	-0.003427
19	1	0	-2.412657	3.781848	-0.011197
20	1	0	-3.731049	1.722771	-0.011033
21	1	0	0.086619	3.693334	-0.002215
22	1	0	1.741465	-3.096402	-0.005417
23	1	0	4.229494	-3.149399	-0.010844
24	1	0	5.519769	-1.015644	-0.007377
25	1	0	4.305895	1.162380	0.000784
26	1	0	-2.239770	-1.618356	0.003168
27	1	0	-4.617999	-0.262008	0.876265
28	1	0	-4.615160	-0.274460	-0.891804
29	6	0	-4.712746	-2.239679	0.006282
30	1	0	-5.806288	-2.265370	0.004259
31	1	0	-4.359187	-2.781413	-0.877936
32	1	0	-4.362628	-2.768199	0.899788

E(RB+HF-LYP) = -822.83145148 Hartrees

Coordinates obtained in the DFT study for Reduced EtNHAQ

Center Number	Atomic Number	Atomic Type	Coordinates (Angstroms)		
			X	Y	Z
1	6	0	-1.810032	3.033016	-0.305655
2	6	0	-2.640975	1.888799	-0.358200
3	6	0	-2.135331	0.600061	-0.271490
4	6	0	-0.690287	0.406869	-0.180545
5	6	0	0.131329	1.598814	-0.000324
6	6	0	-0.462149	2.896931	-0.092605
7	6	0	-0.027976	-0.837740	-0.314799
8	6	0	1.378754	-0.945192	-0.184753
9	6	0	2.158323	0.222777	0.141368
10	6	0	1.516281	1.468959	0.223126
11	6	0	2.072964	-2.183682	-0.365958
12	6	0	3.433796	-2.276486	-0.193024
13	6	0	4.192491	-1.127484	0.171321
14	6	0	3.570795	0.087147	0.329739
15	8	0	2.321399	2.566770	0.437135
16	8	0	-0.771566	-1.935975	-0.653773
17	7	0	-3.048026	-0.473796	-0.316029
18	6	0	-3.172471	-1.332885	0.877647
19	6	0	-4.035657	-2.555553	0.580658
20	1	0	-2.255212	4.022705	-0.398031
21	1	0	-3.720410	2.016414	-0.439699
22	1	0	0.166579	3.780914	-0.020461
23	1	0	1.524406	-3.079945	-0.653330
24	1	0	3.934405	-3.232521	-0.337615
25	1	0	5.268340	-1.214323	0.315991
26	1	0	4.144661	0.970485	0.594134
27	1	0	1.889834	3.227036	1.022551
28	1	0	-0.363875	-2.772213	-0.348928
29	1	0	-3.975639	-0.107040	-0.551999
30	1	0	-3.609336	-0.760511	1.714218
31	1	0	-2.175859	-1.648385	1.186492
32	1	0	-3.579603	-3.168030	-0.203657
33	1	0	-5.037911	-2.261525	0.245762
34	1	0	-4.151978	-3.168944	1.480844

E(RB+HF-LYP) = -824.01223183 Hartrees

Coordinates obtained in the DFT study for EtNH₂⁺AQ

Center Number	Atomic Number	Atomic Type	Coordinates (Angstroms)		
			X	Y	Z
1	6	0	1.864803	2.819538	0.010281
2	6	0	2.606191	1.634321	0.010846
3	6	0	1.950015	0.408569	0.002569
4	6	0	0.539110	0.332925	-0.005385
5	6	0	-0.187173	1.544539	-0.004287
6	6	0	0.476005	2.775960	0.002668
7	6	0	-0.189470	-0.969515	-0.016515
8	6	0	-1.672565	-0.957470	-0.004428
9	6	0	-2.395634	0.253364	-0.001465
10	6	0	-1.685049	1.553871	-0.009571
11	6	0	-2.362195	-2.177915	0.003260
12	6	0	-3.757116	-2.193949	0.015175
13	6	0	-4.474581	-0.990872	0.018063
14	6	0	-3.795999	0.228203	0.009275
15	8	0	-2.297580	2.621426	-0.018357
16	8	0	0.431595	-2.037777	-0.033795
17	7	0	2.750643	-0.844588	0.003057
18	6	0	4.259280	-0.722414	0.008942
19	1	0	2.387209	3.774743	0.016265
20	1	0	3.688867	1.702089	0.017688
21	1	0	-0.109343	3.691859	0.002607
22	1	0	-1.798670	-3.107683	0.000718
23	1	0	-4.287122	-3.145314	0.022349
24	1	0	-5.563595	-1.004869	0.027323
25	1	0	-4.343349	1.167944	0.011241
26	1	0	4.536783	-0.150628	-0.879781
27	1	0	4.530950	-0.158893	0.904714
28	6	0	4.902707	-2.101957	0.004206
29	1	0	5.989014	-1.976381	0.008303
30	1	0	4.625876	-2.680583	0.891851
31	1	0	4.631582	-2.671690	-0.890921
32	1	0	2.460512	-1.408296	-0.819373
33	1	0	2.454684	-1.412549	0.821020

E(RB+HF-LYP) = -823.26308347 Hartrees

Coordinates obtained in the DFT study for Reduced EtNH₂⁺AQ

Center Number	Atomic Number	Atomic Type	Coordinates (Angstroms)		
			X	Y	Z
1	6	0	-1.806620	2.973998	-0.104680
2	6	0	-2.595483	1.812154	-0.303064
3	6	0	-2.000648	0.579870	-0.342194
4	6	0	-0.582644	0.380067	-0.210254
5	6	0	0.209861	1.584112	-0.001014
6	6	0	-0.450803	2.848230	0.053130
7	6	0	0.074707	-0.856082	-0.282071
8	6	0	1.465098	-0.977360	-0.104610
9	6	0	2.252317	0.213053	0.078465
10	6	0	1.611212	1.469433	0.119656
11	6	0	2.137457	-2.238483	-0.114047
12	6	0	3.502798	-2.310357	0.022068
13	6	0	4.278685	-1.130120	0.178923
14	6	0	3.668218	0.099187	0.212115
15	8	0	2.429956	2.538934	0.288105
16	8	0	-0.700674	-1.994708	-0.526488
17	7	0	-2.893539	-0.598478	-0.474933
18	6	0	-3.582460	-1.033783	0.813360
19	1	0	-2.281913	3.947335	-0.068256
20	1	0	-3.673061	1.907750	-0.411760
21	1	0	0.120412	3.755424	0.227258
22	1	0	1.574576	-3.164430	-0.190787
23	1	0	3.993419	-3.278549	0.021045
24	1	0	5.356145	-1.206011	0.281333
25	1	0	4.250058	1.003462	0.341979
26	1	0	-2.777271	-1.247277	1.518829
27	1	0	-4.141080	-0.168114	1.174008
28	6	0	-4.473814	-2.241405	0.567957
29	1	0	-4.950329	-2.527454	1.509528
30	1	0	-5.272178	-2.023175	-0.149632
31	1	0	-3.902199	-3.104221	0.212083
32	1	0	-2.306848	-1.391020	-0.797408
33	1	0	-3.604257	-0.410725	-1.187764
34	1	0	-0.172824	-2.671640	-0.972732
35	1	0	1.960578	3.379101	0.221434

E(RB+HF-LYP) = -824.37708537 Hartree

Coordinates obtained in the DFT study for Oxidized EtOAQ - dihedral angle 0.

Center Number	Atomic Number	Atomic Type	Coordinates (Angstroms)		
			X	Y	Z
1	6	0	-4.447014	-0.919243	0.089993
2	6	0	-3.751143	-2.135523	0.069320
3	6	0	-2.356915	-2.145231	0.021172
4	6	0	-1.639956	-0.940914	-0.002040
5	6	0	-2.341151	0.279524	0.019970
6	6	0	-3.743285	0.283565	0.063813
7	6	0	-0.142914	-0.991877	-0.058903
8	6	0	0.604536	0.291439	-0.015137
9	6	0	-0.107669	1.521259	-0.001452
10	6	0	-1.602000	1.562785	-0.005314
11	6	0	2.030194	0.340061	0.008004
12	6	0	2.684849	1.587367	0.033321
13	6	0	1.955647	2.772065	0.037592
14	6	0	0.561973	2.746067	0.021683
15	8	0	-2.202213	2.641525	-0.021252
16	8	0	0.413685	-2.089331	-0.142261
17	8	0	2.712220	-0.824194	0.009950
18	6	0	4.156056	-0.807688	0.063905
19	6	0	4.629074	-2.249040	0.077244
20	1	0	-5.535462	-0.912283	0.126353
21	1	0	-4.298284	-3.077082	0.090451
22	1	0	-1.811302	-3.084945	0.002119
23	1	0	-4.269069	1.235288	0.078271
24	1	0	3.767918	1.640404	0.049026
25	1	0	2.484909	3.723850	0.055797
26	1	0	-0.013861	3.666640	0.029194
27	1	0	4.477596	-0.278588	0.969881
28	1	0	4.544556	-0.273687	-0.812455
29	1	0	5.723098	-2.270687	0.116924
30	1	0	4.305288	-2.775973	-0.825434
31	1	0	4.240709	-2.780808	0.951169

E(RB+HF-LYP) = -842.6770309 Hartree

Coordinates obtained in the DFT study for Oxidized EtOAQ - dihedral angle 90.

Center Number	Atomic Number	Atomic Type	Coordinates (Angstroms)		
			X	Y	Z
1	6	0	7.410186	3.732200	2.269360
2	6	0	7.722298	2.383053	2.483129
3	6	0	6.856923	1.384287	2.035620
4	6	0	5.664342	1.722245	1.381688
5	6	0	5.351013	3.079277	1.168951
6	6	0	6.230615	4.077823	1.610974
7	6	0	4.767833	0.627512	0.898150
8	6	0	3.435425	1.007085	0.345405
9	6	0	3.124617	2.376929	0.133095
10	6	0	4.094413	3.459191	0.478284
11	6	0	2.443607	0.045783	0.032033
12	6	0	1.201591	0.450459	-0.475855
13	6	0	0.924143	1.797737	-0.694769
14	6	0	1.886880	2.760399	-0.391043
15	8	0	3.845858	4.638253	0.212522
16	8	0	5.146582	-0.542611	0.962415
17	8	0	2.608235	-1.292444	0.279293
18	6	0	3.174160	-2.067048	-0.807989
19	6	0	3.281101	-3.509366	-0.353955
20	1	0	8.086963	4.511592	2.616624
21	1	0	8.642490	2.110920	2.998281
22	1	0	7.095738	0.335390	2.192150
23	1	0	5.977739	5.120823	1.436093
24	1	0	0.458511	-0.316932	-0.688440
25	1	0	-0.044352	2.097293	-1.092706
26	1	0	1.684168	3.816616	-0.545721
27	1	0	4.158883	-1.658154	-1.058135
28	1	0	2.515003	-1.973435	-1.681720
29	1	0	3.692249	-4.119359	-1.165291
30	1	0	2.298402	-3.910641	-0.085706
31	1	0	3.943881	-3.593978	0.512564

$$E(\text{RB+HF-LYP}) = -842.6731134 \text{Hartree}$$

Coordinates obtained in the DFT study for Reduced EtOAQ - dihedral angle 0.

Center Number	Atomic Number	Atomic Type	Coordinates (Angstroms)		
			X	Y	Z
1	6	0	-3.306053	1.549520	-1.410792
2	6	0	-3.199290	0.128808	-1.438024
3	6	0	-2.040227	-0.487448	-1.028151
4	6	0	-0.925598	0.278537	-0.564712
5	6	0	-1.035088	1.713749	-0.530870
6	6	0	-2.255086	2.318761	-0.971138
7	6	0	0.274582	-0.344064	-0.152383
8	6	0	1.367551	0.420362	0.314368
9	6	0	1.240040	1.866342	0.375407
10	6	0	0.054178	2.477739	-0.071211
11	6	0	2.619973	-0.154140	0.759362
12	6	0	3.644191	0.626895	1.241715
13	6	0	3.481955	2.038825	1.316474
14	6	0	2.325050	2.641519	0.899552
15	8	0	-0.121252	3.845199	-0.009453
16	8	0	0.300449	-1.708173	-0.230992
17	8	0	2.709072	-1.523279	0.660534
18	6	0	3.892501	-2.207967	1.130910
19	6	0	3.671562	-3.696470	0.941271
20	1	0	-4.227332	2.026419	-1.742647
21	1	0	-4.039808	-0.468707	-1.787665
22	1	0	-1.957300	-1.570161	-1.051642
23	1	0	-2.333761	3.401844	-0.950986
24	1	0	4.578627	0.187192	1.573282
25	1	0	4.297489	2.638353	1.717698
26	1	0	2.222533	3.721063	0.976554
27	1	0	0.667346	4.328998	-0.343173
28	1	0	1.177200	-2.012422	0.076740
29	1	0	4.046508	-1.956387	2.187120
30	1	0	4.754904	-1.855484	0.552395
31	1	0	4.557793	-4.239348	1.285347
32	1	0	3.510196	-3.939636	-0.113783
33	1	0	2.810976	-4.044748	1.521373

E(RB+HF-LYP) = -843.885572Hartree

Coordinates obtained in the DFT study for Reduced EtOAQ - dihedral angle 90.

Center Number	Atomic Number	Atomic Type	Coordinates (Angstroms)		
			X	Y	Z
1	6	0	2.925215	1.207163	1.418462
2	6	0	3.116524	-0.130741	0.983050
3	6	0	2.094718	-0.844914	0.401468
4	6	0	0.787652	-0.255392	0.196120
5	6	0	0.616881	1.118686	0.639565
6	6	0	1.706959	1.813494	1.253814
7	6	0	-0.314033	-0.914365	-0.399328
8	6	0	-1.538249	-0.238398	-0.614614
9	6	0	-1.697913	1.128933	-0.173258
10	6	0	-0.621367	1.767599	0.467494
11	6	0	-2.638523	-0.859269	-1.288546
12	6	0	-3.818633	-0.191038	-1.508710
13	6	0	-3.972661	1.155223	-1.071869
14	6	0	-2.940458	1.792580	-0.428342
15	8	0	-0.695794	3.074912	0.889439
16	8	0	-0.150264	-2.210790	-0.809677
17	8	0	2.389853	-2.120305	-0.038470
18	6	0	2.121706	-3.176208	0.909925
19	6	0	2.511775	-4.497974	0.275658
20	1	0	3.751393	1.744795	1.881043
21	1	0	4.083364	-0.617021	1.100459
22	1	0	1.548916	2.835546	1.581842
23	1	0	-2.544256	-1.880628	-1.655077
24	1	0	-4.634680	-0.687876	-2.030764
25	1	0	-4.906264	1.682703	-1.260762
26	1	0	-3.067648	2.828843	-0.119398
27	1	0	2.706679	-2.986384	1.820868
28	1	0	1.056181	-3.165660	1.166850
29	1	0	2.329533	-5.315361	0.981667
30	1	0	1.921695	-4.682477	-0.627342
31	1	0	3.573485	-4.505822	0.007493
32	1	0	-1.584108	3.304310	1.239079
33	1	0	-0.994452	-2.707104	-0.810997

E(RB+HF-LYP) = -843.8728122Hartree

7.7 Potential scan EIS (Brevnov Protocol) data of SAM of 1-aminoAQ disulfide (22)

Fitting analysis results of SAM of **22** of the data acquired as a function of DC potential and frequencies at 24.8°C. Equivalent circuits (Model) for the fit are given in the last column.

E_{app} V	R_s $\Omega \cdot \text{cm}^2$	C_{dl}		R_{CT} $\Omega \cdot \text{cm}^2$	C_{ml}		R_d $\Omega \cdot \text{cm}^2$	Model
		C ($\mu\text{F} \cdot \text{cm}^{-2}$)	n		C ($\mu\text{F} \cdot \text{cm}^{-2}$)	n		
-0.40	2.5	2.00E-05	0.95	577				3-28B
-0.38	2.5	1.80E-05	0.96	777				3-28B
-0.36	2.5	1.70E-05	0.96	1080				3-28B
-0.34	2.5	1.70E-05	0.96	1606				3-28B
-0.32	2.5	1.70E-05	0.96	2411	4.30E-03	0.98	195.5	3-28C
-0.30	2.5	1.80E-05	0.96	3450	1.30E-03	0.89	953	3-28C
-0.28	2.5	1.80E-05	0.96	4670	6.80E-04	0.86	2421	3-28C
-0.26	2.5	5.30E-04	0.85	4970	1.90E-05	0.96	5580	3-28C
-0.24	2.4	4.60E-04	0.84	6830	2.00E-05	0.96	5830	3-28C
-0.22	2.4	5.70E-04	0.85	7430	2.30E-05	0.94	5980	3-28C
-0.20	2.4	6.80E-04	0.85	6020	2.80E-05	0.92	5840	3-28C
-0.18	2.3	3.80E-05	0.88	5400	8.10E-04	0.84	4970	3-28C
-0.16	2.4	7.00E-05	0.96	181.5	6.10E-05	0.86	7470	3-28C
-0.14	2.4	7.30E-05	0.96	108.8	6.30E-05	0.86	7840	3-28C
-0.12	2.4	9.10E-05	0.96	85.8	5.50E-05	0.87	9000	3-28C
-0.10	2.4	1.50E-04	0.96	71.4	4.40E-05	0.88	10980	3-28C
-0.08	2.4	2.40E-04	0.96	347	4.20E-05	0.89	14100	3-28C
-0.06	2.4	1.40E-04	0.96	2214	4.70E-05	0.89	17030	3-28C
-0.04	2.5	1.10E-04	0.96	3470	4.50E-05	0.89	22800	3-28C
-0.02	2.5	1.60E-04	0.96	1955	3.60E-05	0.91	34500	3-28C
0.00	2.5	1.10E-04	0.96	3400	3.60E-05	0.91	49100	3-28C
0.02	2.4	1.20E-04	0.96	2224	3.50E-05	0.91	71400	3-28C
0.04	2.4	1.50E-04	0.96	1750	3.60E-05	0.9	108700	3-28C
0.06	2.4	1.80E-04	0.96	1014	3.90E-05	0.89	159300	3-28C
0.08	2.4	1.40E-04	0.96	275.8	4.60E-05	0.88	229700	3-28C
0.10	2.4	8.90E-05	0.96	203.8	6.10E-05	0.86	351000	3-28C
0.12	2.3	6.90E-05	0.96	196.2	8.30E-05	0.83	611000	3-28C
0.14	2.3	7.00E-05	0.96	207.3	9.10E-05	0.83	894000	3-28C
0.16	2.3	8.30E-05	0.96	227.4	7.80E-05	0.84	763000	3-28C
0.18	2.4	1.10E-04	0.96	277.9	6.60E-05	0.85	735000	3-28C
0.20	2.3	5.70E-05	0.84					3-28A
0.22	2.3	5.00E-05	0.85					3-28A
0.24	2.3	4.50E-05	0.87					3-28A
0.26	2.4	4.30E-05	0.87					3-28A
0.28	2.4	4.20E-05	0.88					3-28A
0.30	2.4	4.10E-05	0.88					3-28A
0.32	2.4	4.00E-05	0.88					3-28A
0.34	2.3	3.90E-05	0.88					3-28A
0.36	2.3	3.90E-05	0.88					3-28A
0.38	2.3	3.80E-05	0.88					3-28A
0.40	2.3	3.80E-05	0.88					3-28A

Note: E_{app} = applied DC potential